

INFORMATION TO USERS

This manuscript has been reproduced from the microfilm master. UMI films the text directly from the original or copy submitted. Thus, some thesis and dissertation copies are in typewriter face, while others may be from any type of computer printer.

The quality of this reproduction is dependent upon the quality of the copy submitted. Broken or indistinct print, colored or poor quality illustrations and photographs, print bleedthrough, substandard margins, and improper alignment can adversely affect reproduction.

In the unlikely event that the author did not send UMI a complete manuscript and there are missing pages, these will be noted. Also, if unauthorized copyright material had to be removed, a note will indicate the deletion.

Oversize materials (e.g., maps, drawings, charts) are reproduced by sectioning the original, beginning at the upper left-hand corner and continuing from left to right in equal sections with small overlaps.

Photographs included in the original manuscript have been reproduced xerographically in this copy. Higher quality 6" x 9" black and white photographic prints are available for any photographs or illustrations appearing in this copy for an additional charge. Contact UMI directly to order.

**Bell & Howell Information and Learning
300 North Zeeb Road, Ann Arbor, MI 48106-1346 USA
800-521-0600**

UMI[®]

Delivery and verification of intensity-modulated x-ray beams in radiotherapy

by

Arthur J. Curtin-Savard

Department of Physics
McGill University, Montréal
November 1998

*A thesis submitted to the Faculty of Graduate Studies and Research
in partial fulfillment of the requirements for the degree of
Doctor of Philosophy.*

©Arthur Curtin-Savard 1998



**National Library
of Canada**

**Acquisitions and
Bibliographic Services**

**395 Wellington Street
Ottawa ON K1A 0N4
Canada**

**Bibliothèque nationale
du Canada**

**Acquisitions et
services bibliographiques**

**395, rue Wellington
Ottawa ON K1A 0N4
Canada**

Your file Votre référence

Our file Notre référence

The author has granted a non-exclusive licence allowing the National Library of Canada to reproduce, loan, distribute or sell copies of this thesis in microform, paper or electronic formats.

The author retains ownership of the copyright in this thesis. Neither the thesis nor substantial extracts from it may be printed or otherwise reproduced without the author's permission.

L'auteur a accordé une licence non exclusive permettant à la Bibliothèque nationale du Canada de reproduire, prêter, distribuer ou vendre des copies de cette thèse sous la forme de microfiche/film, de reproduction sur papier ou sur format électronique.

L'auteur conserve la propriété du droit d'auteur qui protège cette thèse. Ni la thèse ni des extraits substantiels de celle-ci ne doivent être imprimés ou autrement reproduits sans son autorisation.

0-612-50138-8

ABSTRACT

In modern radiotherapy, 3D conformal dose distributions are achieved using several beam ports each having pre-calculated planar distributions of photon beam intensity. The intensity matrix for a given beam port is generated by independent motion of the leaves of a multileaf collimator (MLC). In this thesis, we have used the *step-and-shoot* approach to intensity-modulated beam delivery, the safest and most popular approach at the moment. The first component of this thesis was to write a leaf sequence algorithm to control the MLC fitted to our Clinac 2300 C/D linear accelerator. Our algorithm is more efficient than other published *step-and-shoot* type algorithms, and takes into account the MLC transmission, MLC penumbra, and change in scatter conditions with field size.

Although sophisticated means to calculate and deliver these spatially-modulated beams have been developed by our group as well as by other medical physics research centres, means to verify their actual delivery are definitely the most problematic at the moment, making equipment and treatment quality assurance difficult to enforce. The second (and major) component of this thesis has been to investigate the use of a new portal imaging device for dosimetric verification purposes. We show that an electronic portal imaging device of the scanning liquid ionization chamber type yields images which, once calibrated from a previously-determined calibration curve, provide highly-precise planar maps of the incident dose rate distribution. For verification of an intensity-modulated beam delivered in the segmented approach with an MLC, a portal image is acquired for each subfield of the leaf sequence. Subsequent to their calibration, the images are multiplied by their respective associated monitor unit settings, and summed to produce a planar dose distribution at the measurement depth in phantom. The excellent agreement of our portal imager measurements with calculations of our treatment planning system and measurements with a one-dimensional beam profiler attests to the usefulness and relative simplicity of this method for the planar verification of intensity-modulated fields, which are produced in the segmented approach on a computerized linear accelerator equipped with an MLC.

RÉSUMÉ

Dans la radiothérapie moderne, des distributions de dose qui épousent le volume cible en 3D sont généralement produites par l'effet cumulatif de plusieurs faisceaux de rayons X dont chacune possède une intensité qui varie dans l'espace. Dans cette thèse, les matrices d'intensité sont générées par le mouvement des lamelles d'un collimateur multilames (CML) selon l'approche <<step-and-shoot>>, l'approche la plus sûre et la plus répandue aujourd'hui. La première composante de cette thèse fut de concevoir un algorithme <<step-and-shoot>> qui permettrait le contrôle informatisé du CML de notre accélérateur linéaire Varian Clinac-2300 C/D. L'algorithme que nous avons conçu est plus efficace que les autres algorithmes publiés jusqu'à présent, et tient compte de l'opacité du CML à la radiation, de sa pénombre, et de la variation du débit avec la grandeur du champ défini par le CML.

En 1998, les méthodes pour le calcul des matrices d'intensité et des techniques d'exécution à l'accélérateur thérapeutique sont hautement raffinées. Cependant, il existe présentement une importante lacune du côté de la vérification expérimentale de ces faisceaux. La deuxième composante de cette thèse fut donc d'explorer l'emploi possible d'un nouveau système d'imagerie numérique pour fin de vérification dosimétrique. À ce propos, nous démontrons qu'un système d'imagerie numérique à chambre d'ionisation liquide donne des images qui, une fois calibrées à l'aide d'une courbe de calibration préalablement déterminée, représentent fidèlement la distribution de dose dans le plan de mesure du système d'imagerie.

Pour la validation d'un faisceau de rayons X exécuté selon l'approche <<step-and-shoot>> une image numérique est acquise pour chaque segment du faisceau. Chaque image est ensuite calibrée, multipliée par sa valeur correspondante d'unités monitrices, et finalement additionnée avec la somme des autres images. Le résultat de ces opérations donne une distribution de dose qui est en excellent accord avec d'autres mesures expérimentales indépendantes, ainsi qu'avec les calculs de notre système de planification des traitements.

ORIGINAL CONTRIBUTION

The principal original contribution of this thesis regards the use of a scanning liquid ionization (SLIC) electronic portal imaging device (EPID) for dosimetric purposes. This SLIC EPID was initially designed to acquire transmission images in order to verify proper patient positioning in the X-ray therapy beam. However we have shown that, with the use of a measurement protocol described in this thesis, the SLIC EPID is ideally-suited for the dosimetric verification of intensity-modulated X-ray beams produced with a multileaf collimator (MLC) in the *step-and-shoot* approach. The SLIC EPID can thus be used both to verify the delivery of patient-specific MLC leaf sequences prior to actual patient treatment, and to perform the measurements required for the commissioning of a leaf sequence algorithm. Finally, the SLIC EPIC is also useful in the *design* of the leaf sequence algorithm since with it one may acquire all the beam parameters required for the writing of an accurate leaf sequence algorithm: the MLC transmission values, MLC leaf penumbra widths, a measure of the MLC tongue-and-groove effect, a determination of the coincidence of MLC axis of rotation with beam crosshairs, etc.

The second original contribution is the writing of a step-and-shoot leaf sequence algorithm which is more efficient than other published step-and-shoot type algorithms. Rather than assigning approximately equal doses to each subfield of the leaf sequence, our algorithm assigns the bulk of the radiation dose to the first subfield. This approach is more similar to conventional X-ray photon radiotherapy, and thus more comforting to medical personnel and to the patients. Furthermore, because fewer subfields are required in our approach, the execution of the treatment is more rapid and beam verification is simplified. We have also shown that a standard irregular-field formalism may successfully be used to account for the photon and electron scatter variations of the

MLC-defined subfields of the leaf sequence which is a further contribution of our algorithm.

The third contribution is not original but important nonetheless. As a result of the work presented in this thesis, the McGill University Hospital Centre became the first medical centre in Canada to use MLC intensity-modulated radiation therapy in patient treatment. At present, only a few centres in the United States offer this type of patient treatment.

ACKNOWLEDGEMENTS

I would like to acknowledge the help of the following people and organizations during my Ph.D. studies:

Dr. Ervin Podgorsak, my supervisor, for being a great person to work with, for upholding the tough academic standards of McGill University, and for standing behind his graduate students under all circumstances.

Michael Evans and *Katharina Sixel*, for encouraging me to undertake doctoral studies.

François Deblois, for help in computer-related issues and for being a great friend.

Karl Otto, for teaching me the basics of the AVS programming environment and *Dr. Gino Fallone* for allowing me to use this software.

William Parker and *Michael Evans*, without whose assistance the work presented in this thesis would never have been implemented clinically.

Margery Knewstubb and *Georgia Romano*, the two secretaries, for helping our Department run so efficiently.

Dr. Georges C. Savard, my father, *Mrs. Mary Curtin-Savard*, my mother, and *Liliane Beaudoin*, my girlfriend, for encouragement during the thesis writing and other difficult moments.

The *Medical Research Council of Canada* and the *Walter Sumner Foundation* for financial support during my studies.

TABLE OF CONTENTS

ABSTRACT	i
RÉSUMÉ	ii
ORIGINAL CONTRIBUTION	iii
ACKNOWLEDGEMENTS	v

CHAPTER 1: INTRODUCTION

1.1 Place of radiotherapy in management of cancer	1
1.2 Rationale for the conformal approach	2
1.3 The radiotherapy linear accelerator	3
1.4 Behaviour of megavoltage photon beams in tissue or tissue-similar materials	8
1.5 Technical requirements for conformal therapy	12
1.6 Modern conformal therapy: A patient case	16
1.7 Summary	20
1.8 References	20

CHAPTER 2: CURRENT APPROACHES TO OPTIMIZATION AND 3D CONFORMAL RADIOTHERAPY

2.1 Introduction	23
2.2 Need for computerized optimization	23
2.3 The objective function	25
2.4 Approaches to optimization	27
2.5 Approaches to 3DCRT	39
2.6 Summary	42
2.7 References	43

CHAPTER 3: USE OF THE VARIAN ELECTRONIC PORTAL IMAGING DEVICE AS A RADIATION DOSIMETER

3.1	Introduction.....	50
3.2	Dosimeters used in radiotherapy	50
3.3	General description of the Varian SLIC EPID	55
3.4	Physics of image formation in the SLIC EPID.....	57
3.5	Basic experimental investigations of the EPID	59
3.6	Basic dosimetric applications of the EPID	68
3.7	Use of the SLIC EPID for the verification of intensity-modulated beams	73
3.8	Summary	73
3.9	References.....	74

CHAPTER 4: CHARACTERIZATION OF THE VARIAN MULTILEAF COLLIMATOR

4.1	Introduction.....	77
4.2	Use of a multileaf collimator as a replacement for conventional blocks	77
4.3	Description of the Varian multileaf collimator.....	81
4.4	Multileaf collimator metrics	83
4.5	Leaf positioning for treatment	86
4.6	Leaf positioning tests.....	89
4.7	Dosimetric measurements of the MLC.....	97
4.8	Influence of the MLC on beam output	104
4.9	Summary	118
4.10	References.....	119

CHAPTER 5: THE *dynMLC* PROGRAM

5.1	Introduction.....	124
5.2	Programming platform	124
5.3	Input data for the <i>dynMLC</i> program.....	125
5.4	Determination of leaf positions.....	128
5.5	Corrections for MLC transmission and leaf penumbra.....	134

5.6	Determination of the monitor unit setting for each subfield	139
5.7	Time required to deliver a dynamically-compensated field	146
5.8	Subfield visualization	148
5.9	Summary	154
5.10	References	154

CHAPTER 6: MEASUREMENTS OF INTENSITY-MODULATED BEAMS

6.1	Introduction	155
6.2	Tests of the <i>dynMLC</i> program	155
6.3	Tests of the inverse-planning abilities of the CADPLAN TPS	170
6.4	Summary	174

CHAPTER 7: PATIENT TREATMENT

7.1	Introduction	175
7.2	Description of the first patient treatment	175
7.1	Summary	179

CHAPTER 8: CONCLUSION

8.1	Thesis summary	180
8.2	Future work	182
8.3	References	183

LIST OF FIGURES	184
------------------------------	-----

LIST OF TABLES	189
-----------------------------	-----

BIBLIOGRAPHY	190
---------------------------	-----

Section:

1.1	Place of radiotherapy in management of cancer	1
1.2	Rationale for the conformal approach	2
1.3	The radiotherapy linear accelerator	3
1.4	Behaviour of megavoltage photon beams in tissue or tissue-similar materials	8
1.5	Technical requirements for conformal radiotherapy	12
1.6	Modern conformal radiotherapy: a patient case	16
1.7	Summary	20
1.8	References	20

1.1 PLACE OF RADIOTHERAPY IN MANAGEMENT OF CANCER

It is forecast¹ that, in Canada, 130 000 new patients will be diagnosed with cancer in 1997. In the United States the number is a little over ten times greater², reflecting the roughly 10 times larger population of the United States compared to Canada. Radiotherapy is one of the three principal modes of treatment available to cancer patients, the other two being surgery and chemotherapy. Frequently radiotherapy is most advantageous to the patient when employed together with the other two modalities: for instance, the patient may first be subjected to surgery, then locally treated with radiation to sterilize cancerous cells left behind after the surgery, and also given a course of chemotherapy if distant metastatic disease is suspected. All in all, whether used as the sole mode of treatment or in conjunction with other modalities, radiotherapy is prescribed to over half of today's cancer patients^{3,4}.

1.2 RATIONALE FOR THE CONFORMAL APPROACH

Ionizing radiation is harmful not only to cancerous cells but also to normal cells. Since the discovery of X rays by Roentgen in 1895, the discipline of radiation oncology has been faced with the challenge of delivering a lethal (tumouricidal) dose to the diseased cancerous tissue while at the same time keeping the dose to surrounding healthy tissues below the level which would lead to serious radiation-induced complications. Unfortunately, with current treatment techniques, the value of the radiation dose prescription is generally limited by considerations of acceptable rates for serious complications resulting from the irradiation of tissues surrounding the tumour, rather than by considerations of the dose required to eradicate the tumour. For instance, although doses exceeding 60 Gy are often required to eradicate a cancer of the prostate, doses as low as 45 Gy to the small bowel in the vicinity of the prostate can result in radiation-induced obstruction requiring surgical intervention⁵. In the treatment of liver cancer, a dose of 50 Gy to 1/3 of the liver, a dose of 35 Gy to 2/3 of the liver, or a dose of 30 Gy to the entire liver all result in a 5-year 5% probability of liver failure^{6,7}, yet much higher doses are usually required for a cure of hepatic tumours.

Of course, all organs or tissues of the body are not equally sensitive to radiation. Therefore special attention must be given to each case depending on the site of treatment, and the risk of radiation-induced complications must be weighed against the risk of not attaining a cure for cancer when prescribed doses are too low. However, a greater ability to selectively irradiate diseased tissue and spare healthy tissues will make this evaluation of risks easier in two ways: firstly, for tumours that respond favourably to current dose levels, the probability of radiation-induced complications will be decreased and, secondly, the doses to tumours that do not respond favourably to current dose levels may be escalated while maintaining current levels of radiation-induced complications.

Radiotherapy, with the exception of total body photon irradiation, represents a localized treatment. Roughly 70% of all cancer patients have their disease confined to the original site at the time of first diagnosis⁸ and approximately two-thirds of these patients attain a cure with the current treatment protocols involving radiotherapy and/or surgery⁹. The one-third of patients who initially present solely with localized disease but are not cured may be divided approximately equally into three groups: 1) those who recur at the site of primary treatment alone, 2) those who recur both at the primary site and at a distant site, and 3) those who recur solely at a distant site¹⁰⁻¹². It is immediately obvious that improvements in the application of radiotherapy (particularly dose escalation) will be beneficial to groups 1 and 2. However, a number of publications^{13, 14} studying the temporal evolution of secondary tumours have indicated a possible causal relationship between recurrence at the primary site and the growth of distant metastatic lesions. Thus improvements to radiotherapy may be beneficial to group 3 as well.

The desire to tailor or to conform the distribution of radiation dose to the defined tumour volume is at the heart of what is commonly referred to today as *conformal radiotherapy*. Conformal radiotherapy should lead to fewer radiation-induced complications and/or better local control resulting in better cure rates. The implementation of conformal radiotherapy into clinical practice requires sophisticated medical equipment which will be discussed next.

1.3 THE RADIOTHERAPY LINEAR ACCELERATOR

A. General structure

The Varian Clinac 2300 C/D¹⁵ linear accelerator (linac) which was used for the experiments reported in this thesis is fairly typical of the state-of-the-art radiation therapy units. It produces 6 MV and 18 MV photon beams as well as electron beams with

energies of 6 MeV, 9 MeV, 12 MeV, 15 MeV, 18 MeV, and 22 MeV. Its mechanical structure consists of three main components: the *head* from which emerges the radiation beam collimated to the desired field shape; the *gantry* containing most of the power components for producing the radiation beam; and the *patient support assembly (couch)* upon which the patient is positioned for treatment. These components are shown schematically in Fig. 1.1. The collimators in the head can be rotated to assist in matching the field shape to the tumour volume. The intersection point of the collimator axis and the gantry axis is called the *isocentre*, which is generally where the centre of the tumour is placed during patient treatment. Typically, the isocentre is 100 cm from the *target*, which is the source of photon radiation. Lasers on the treatment room walls and ceiling aid in positioning the patient accurately into the radiation field.

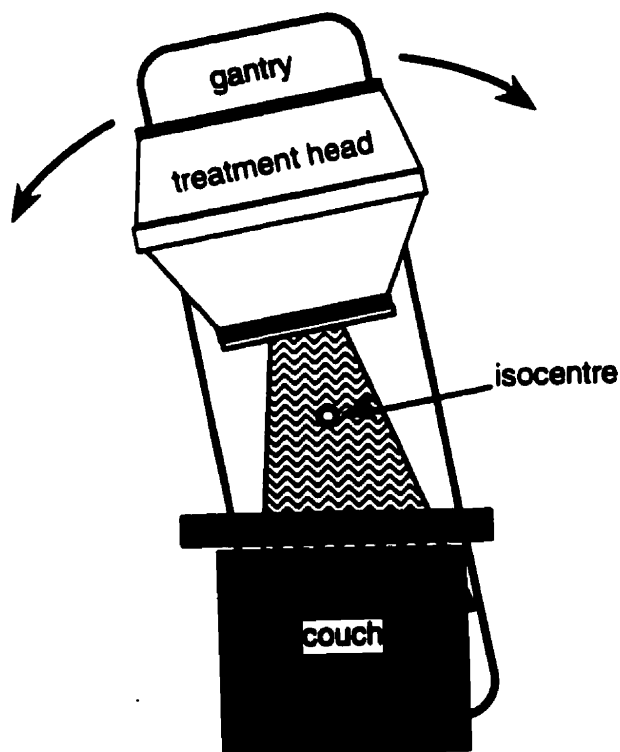


Figure 1.1. Diagram of an isocentric treatment unit showing the three basic components: head, gantry, and couch.

B. Production of X rays

In a linear accelerator a beam of X rays is produced by bombarding a metal target with a beam of high-energy electrons. The electrons are boiled off a filament, accelerated to kilo-electronvolt (keV) energies in an electron gun, and injected into a disc-loaded waveguide which receives its radiofrequency power from a klystron. The electrons emerge from the wave-guide as a roughly monoenergetic beam with an energy in the mega-electronvolt (MeV) range. This pencil electron beam, which is horizontal, passes through a 270° bending magnet so that it is directed toward the isocentre of the linac. In the photon mode, the electron beam strikes a tungsten/copper target where a broad spectrum of X rays is produced by bremsstrahlung interactions. The target is sufficiently thick to completely stop all incident electrons, and is surrounded by a tungsten shield with a circularly-symmetric aperture which serves as the primary collimator for the radiation beam.

Bremsstrahlung photons are emitted into a 4π geometry, but at mega-electronvolt energies the spatial distribution of these photons is primarily forward-peaked. This implies that the X-ray beam produced in the target has its greatest intensity on the beam central axis and must be flattened in order to achieve an acceptable uniformity of intensity over the wide area used in radiotherapy. The flattening of the beam is accomplished by a suitable, preferably low atomic number, filter having a cone-like shape. Each of the two photon beam energies is flattened by its own filter. These flattening filters are placed on a rotating carousel also containing scattering foils which are required for the electron beam mode.

Just below the flattening filter are two sealed transmission ionization chambers which serve to measure the amount of radiation delivered to the patient and to shut off the beam when the preset number of monitor units (MU) of radiation has been delivered.

Two chambers are required for safety reasons in case one of them fails. An MU is the linear accelerator's measure of the radiation that has been delivered. Generally, the sensitivity of the monitor chambers is adjusted such that 1 MU provides a dose of 1 cGy to a point at depth of maximum dose (d_{max}) in a water-equivalent phantom when the phantom surface is at isocentre of the linac and the field size is set to 10×10 cm². A typical daily MU setting for patient treatment is 300 MU; the electrometers in the Clinac 2300 accelerator which read the charge collected in the monitor chambers have a resolution of 1/256 MU. One of the monitor chambers is sectioned into four quadrants and can thus serve, in a crude way, to verify the beam's flatness as well. The Clinac 2300 C/D can operate at dose rates ranging from 100 MU/min to 600 MU/min in steps of 100 MU/min.

C. Production of electrons

When the Clinac 2300 C/D is placed into the electron mode, the target is removed from the beam line and the carousel rotated so that the photon flattening filter is replaced by the scattering foil which serves to diffuse the narrow electron beam uniformly over the maximum width of the treatment field. For equal MU rate, the beam current is reduced by a factor of approximately 100 compared to the photon mode since electrons are no longer "wasted" in the very inefficient bremsstrahlung process in the target nor are photons lost to attenuation in the flattening filter.

D. Beam-shaping system

Just below the two ionization chambers are the secondary collimators: two super-imposed pairs of movable tungsten "jaws" positioned at right angles to each other. They can be used to define rectangular apertures from 0×0 cm² to 40×40 cm² at the isocentre of the therapy unit. Since the jaws move independently, the centre of the rectangular field need not correspond to the axis of collimator rotation; this is a useful feature in some less

conventional treatment set-ups. The jaws are 7.8 cm thick, and have an X-ray transmission of approximately 1%.

In the photon mode, non-rectangular apertures can be achieved by manufacturing a custom set of metal blocks (usually made from Lipowitz's metal which is an alloy of bismuth, lead, tin, and possibly cadmium¹⁶) to be placed in an accessory tray under the secondary collimators. Non-rectangular apertures can also be produced with a multileaf collimator (MLC), which on the Varian accelerators is an optional field-shaping device bolted onto the linac head under the secondary collimators. The Varian MLC has 26 pairs of movable, opposing tungsten "leaves" which project to a width of 1 cm at the isocentre. The MLC can thus be used to define irregular apertures of maximum dimension 26×40 cm². The leaves are 6.1 cm thick and have a transmission of 2.5% at the photon energy of 6 MV and 3.5% at the photon energy of 18 MV. Both of the "tertiary" collimation systems (blocks and MLC) are placed at approximately 50 cm from the machine isocentre.

In the electron mode, the considerable scattering of the electrons as they move through the air of the treatment room requires that the tertiary collimation be placed very close to the patient's skin. This obviates the use of an MLC or blocks placed in the accessory tray. Instead, special electron cones with square apertures are used to extend the secondary collimation system down to within a few centimetres of the patient's surface. If an aperture other than square is required, custom-made metal cut-outs (lead or special alloy) approximately 1 cm thick can be inserted into the end of the electron cone close to the patient's skin. Electron beams were not used in experiments reported in this thesis and will not be discussed further.

E. Computer control

All components of the Varian Clinac 2300 C/D linear accelerator are under computer control except for the movement of the couch. This means that the position of the four secondary collimators, the individual positions of the MLC leaves, the angle of the gantry, the angle of the collimator, the energy (and type) of the radiation beam, and the duration of the irradiation may all be controlled from a keyboard located outside of the treatment room. It is also possible to load-in a computer text file and use it to control any or all of the motions of the accelerator as well as to instruct it when to turn the beam on and off. The software allowing this dynamic control of the linear accelerator is referred to as the Varian Dynamic Beam Delivery (DBD) Toolbox and has recently been acquired for our Clinac 2300 C/D.

1.4 BEHAVIOUR OF MEGAVOLTAGE PHOTON BEAMS IN TISSUE OR TISSUE-SIMILAR MATERIALS

A. Definition of dose

The radiation *dose* is the amount of energy deposited by the radiation beam in a medium per unit mass of the medium. The SI units are thus J/kg; however, the special designation of Gray (Gy) has been assigned to this quantity and $1 \text{ J/kg} = 1 \text{ Gy}$.

B. Clinical parametrization of dose

The behaviour of a single beam of radiation in a *phantom* (a block of tissue-equivalent material) can be described effectively by three dosimetric quantities: the percent depth dose (*PDD*), the off-axis ratio (*OAR*), and the machine dose output. A *percent depth dose* curve gives the variation of the central axis dose with depth in a medium, normalized to 100% at the *depth of maximum dose* d_{max} . The *PDD* curve changes with beam type and energy, as well as with field size and source-surface distance (*SSD*). The depth of maximum dose increases with beam energy because of an increasing range of the secondary electrons in the medium, and also presents a slight

variation with field size as a result of field-size dependent spectral variations of the beam. Figure 1.2 shows *PDD* curves in tissue for a $10 \times 10 \text{ cm}^2$ field for the Clinac 2300 C/D linear accelerator at 6 MV and 18 MV photon energies. The region immediately beyond the phantom surface in which the percent depth dose is rising to its maximum value is known as the dose *build-up* region. This region, which is greater for beams of higher energy, reduces the dose to the patient's skin and adjacent visceral tissues, resulting in the so-called "skin-sparing effect" which is often desirable and beneficial in treatments involving deep-seated tumours.

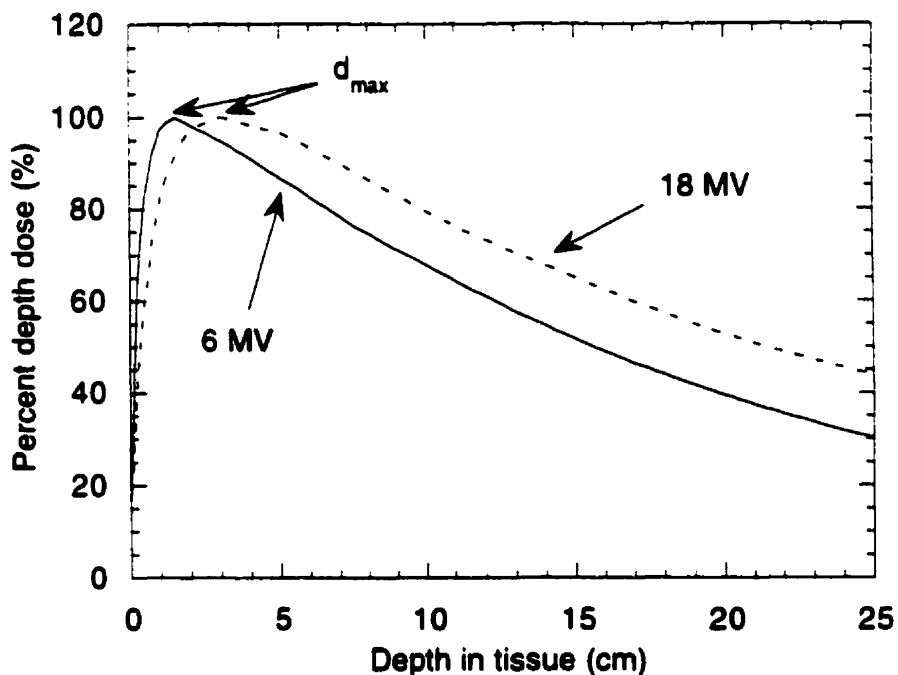


Figure 1.2. Percent depth doses of the Clinac 2300 C/D linear accelerator in tissue for a $10 \times 10 \text{ cm}^2$ field and photon energies of 6 MV and 18 MV.

The *off-axis ratio (OAR)*, also known as a *dose profile*, gives the variation of the dose in a medium perpendicular to the beam central axis at the same depth in phantom, normalized to 100% on the beam central axis. The *OARs* are measured in planes through

the field centre, either along the width or the length, and vary with field size, depth in phantom, beam energy, SSD, and size of the radiation source. Figure 1.3 shows an *OAR* plot for a 10×10 cm² field for the 18 MV beam of the Clinac 2300 C/D linear accelerator at a depth of 3.5 cm in a water phantom. The effect of a wedge filter on the beam is also shown; it reduces the overall intensity of the beam, but to a greater degree on the thick side of the wedge. Several wedges of different "strengths" serve as accessories for the two treatment units; these are used, when appropriate, to obtain more suitable distributions of dose within the patient. The strength of the wedge is expressed by the *wedge angle*, i.e. the angle formed between the isodose line at a depth of 10 cm and a line perpendicular to the beam central axis. The *wedge factor*, which characterizes the attenuation of a particular wedge on the beam central axis, is given by the ratio of the dose rates with and without the wedge, measured at depth d_{max} in phantom for an SSD of 100 cm.

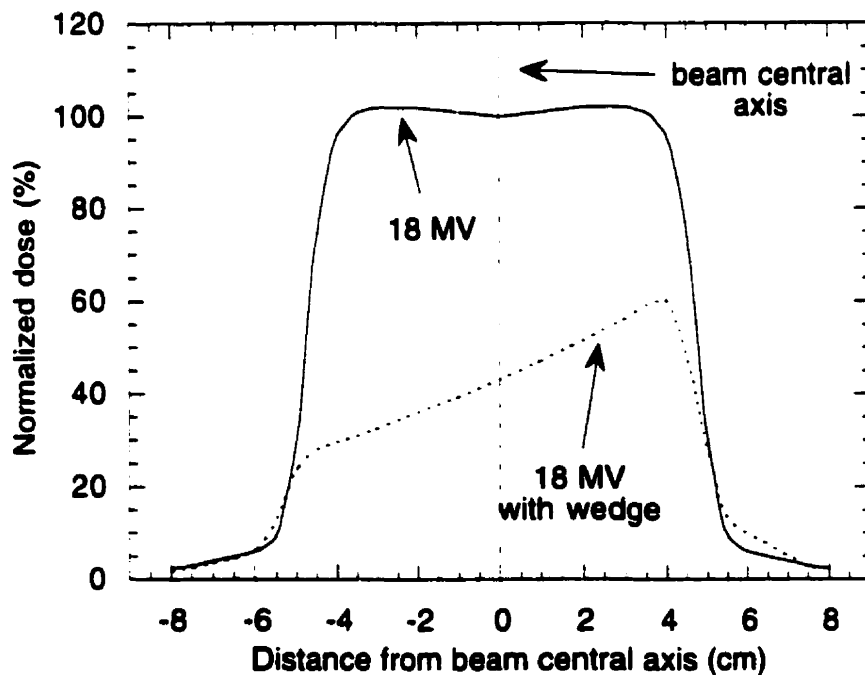


Figure 1.3. Off-axis ratio at 18 MV photon energy for a 10×10 cm² field for the Clinac 2300C/D linear accelerator at a depth of 3.5 cm in water. Also shown is the effect of a wedge with a wedge factor of 0.41 on the dose profile at the same depth in phantom.

The *output* of a radiotherapy treatment unit gives the dose rate to the d_{max} point, with the phantom surface at the isocentre. The output increases with field size for reasons described in detail in Chapter 4. Knowledge of the machine output, the PDDs, and the OARs for the range of available field sizes for a given treatment unit allows one to know the dose at any point in the phantom.

In a patient, the presence of surface obliquities or tissue heterogeneities will require point-by-point corrections to the dose matrix, which are accomplished by the computerized treatment planning system (TPS). Nowadays, TPSs perform dose calculations based on a true three-dimensional (3D) representation of the patient anatomy. TPSs are discussed further in Chapter 2.

C. Uncertainty in the delivered dose

Even slight variations in total dose delivered to the patient in photon radiotherapy can significantly alter the probability of tumour control and normal tissue complications. For this reason, the International Commission on Radiation Units and Measurements (ICRU) has recommended a goal of a $\pm 5\%$ precision in the dose delivered to the target volume¹⁷. For his M.Sc. thesis, the author performed an uncertainty analysis which tracked the uncertainty in dose delivery through the entire radiotherapy process: calibration of the secondary standard, calibration of a field instrument, output determination of the treatment unit, measurement of beam parameters, calculation of an isodose distribution, calculation of the required machine setting, and the delivery of the radiation dose to the patient on the treatment machine. The study¹⁸ found cumulative beam intensity uncertainties of $\pm 3.8\%$ (one standard deviation) and cumulative beam positional uncertainties of ± 5.5 mm (one standard deviation). These estimates were in good agreement with other previously published studies¹⁹⁻²².

1.5 TECHNICAL REQUIREMENTS FOR CONFORMAL RADIOTHERAPY

To achieve an accurate tailoring of the dose distribution to the tumour four requirements must be met: A) accurate spatial representation of the tumour in three dimensions; B) calculation of intensity profiles for a number of beams that will deliver a conformal dose distribution; C) production and delivery of the calculated intensity profiles; and 4) verification of the actual delivered dose distribution.

A. Three-dimensional representation of patient anatomy

Visualization of the anatomy of the patient is usually performed with computed tomography (CT). A CT unit consists of a couch upon which the patient lies and a halo into which the couch can be moved. The halo contains a low-energy X-ray tube and X-ray detectors. To acquire CT data, the X-ray tube is set in a rotational motion about the patient while emitting a thin fan-beam of radiation. The detectors record the radiation transmitted through the patient at each angle of the tube. A mathematical algorithm uses these projections to reconstruct axial slices of the patient anatomy with an excellent spatial resolution (~1 mm). The couch is then moved slightly to collect transmission data in the next slice. Some modern units have the possibility for helical scanning, in which the couch is in continuous linear motion during the scan. CT data can easily be transformed into an electron-density map of the patient, which is very useful for correcting patient dose distributions for the presence of tissue heterogeneities such as bone or lung. An example of a CT slice of the abdominal region is shown in Fig. 1.4.

Another imaging device which finds occasional use in radiotherapy^{23,24} is the magnetic resonance imager (MRI). The external appearance of the MRI unit is similar to that of a CT unit, consisting of a couch and a cylindrical tunnel into which the patient is inserted. Magnets located in the tunnel create a powerful, and extremely homogeneous, magnetic field oriented along the cylinder's axis. This magnetic field preferentially aligns nuclear spins in the patient and sets them into rotation at a resonance frequency

which is primarily a function of atomic species. Three weaker magnetic fields are used to establish magnetic field gradients in the cranial/caudal, anterior/posterior, and left/right directions thereby creating different resonance conditions in each voxel of the patient. The voxels are read out with a radio-frequency coil and used to reconstruct slices of the patient anatomy, typically in the sagittal plane. The main advantage of MRI over CT is superior soft-tissue contrast, contrast which can be manipulated by the selection of various read-out sequences each providing a different view of the internal composition of the patient, some of which may show the extent of disease more distinctly. However, there exists no straightforward manner to correlate the MRI data with electron densities thus, if used for dosimetric planning, the user must be willing to sacrifice the knowledge of tissue heterogeneities. Furthermore, MRI suffers from artefacts²⁵ that, in some circumstances, cast doubt upon the spatial accuracy of displayed structures. Therefore, modern application of MRI to radiotherapy imaging usually involves "registering" the MRI data set to an analogous CT data set thus providing the "fused" data with the spatial electron density resolution of the CT and the contrast resolution of the MRI.

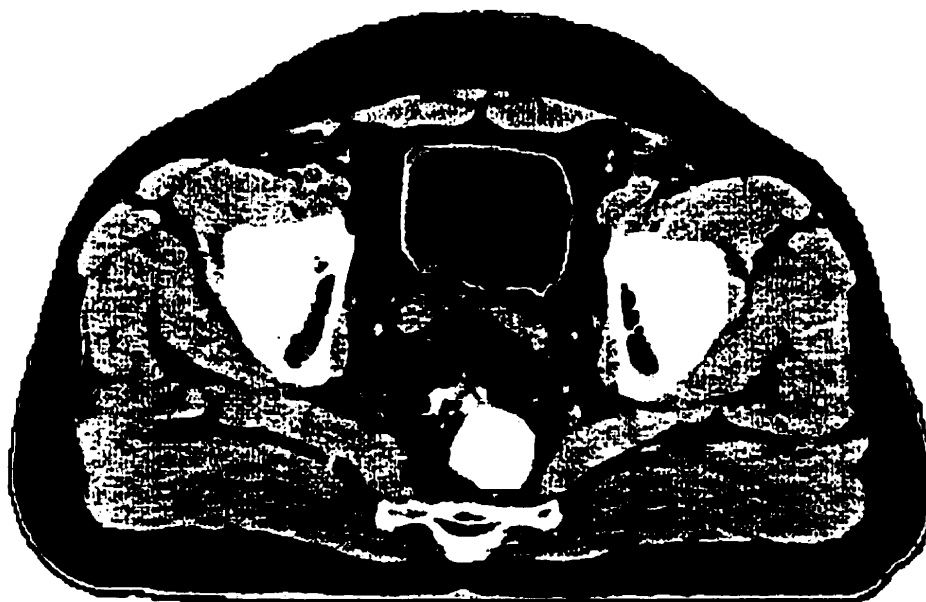


Figure 1.4. CT slice in the abdominal region. The bladder (yellow), seminal vesicles (red), and rectum (purple) have been outlined.

In certain specialized treatments ultrasonic imaging may be used for target definition. Although the images produced by this imaging modality are generally of poor quality, ultrasound units have the advantage of being entirely without hazard to the patient or personnel, and also of being small enough for use in an operating room. The ultrasound imaging modality is thus very practical for use as a guide during the implantation of radioactive prostate seeds or brachytherapy catheters.

B. Calculation of intensity profiles

Methods to calculate the intensity profiles required to obtain a desired dose distribution have been known for some time. As opposed to conventional *forward* planning in which the user attempts various beam configurations in an effort to achieve an optimal dose distribution inside the target volume by trial and error, inverse planning methods first specify the optimal dose distribution inside and outside the target volume and then work backwards, in a more or less automatic fashion, toward the beam set-up required to achieve such a dose distribution. Inverse planning methods currently in use will be discussed in detail in the next chapter. However, it is important to note that these methods, though often relatively simple conceptually, require a great deal of computation, and cannot be implemented clinically without the aid of modern high-speed computers.

C. Delivery of the intensity profiles

The calculated intensity profiles are delivered most simply through the use of compensators. These custom-made metal filters are placed in the linear accelerator accessory tray and their thickness at each ray-line point determines the transmitted beam intensity. A short-coming of compensators is that they are time-consuming to manufacture and require the radiotherapy technologist to reenter the treatment room to change the compensating filter when different filters are used for each beam port, as is usually the case. More convenient is the use of the multileaf collimator (MLC) in a

dynamic mode; in this method, the radio-opaque leaves of the MLC move independently during beam-on according to a pre-defined "leaf sequencing file" to create the desired beam intensity distribution. Faster treatment times are achieved compared to the use of compensators, since leaf sequences for all beam ports can be pre-loaded into the linear accelerator console and delivered in rapid succession. MLCs are becoming a standard on new radiotherapy accelerators and thus this practical approach to intensity-modulation is here to stay. Other more exotic approaches to the delivery of intensity-modulated beams include tomotherapy and intensity-modulated arc therapy, as discussed in Chapter 2.

D. Dose verification

Availability of accurate methods for the verification of the delivered dose distributions is the final technical requirement for accurate conformal therapy, and probably the most problematic requirement at the moment. The ideal verification tool will simultaneously record the dose distribution in a three-dimensional matrix. At present, only two dosimetric media are inherently three-dimensional: the Fricke gel dosimeter and the BANG gel dosimeter, but both, in addition to being cumbersome, possess insufficient sensitivity, reproducibility, and spatial resolution to be relied upon exclusively. For dosimetry in a plane, film (either silver halide or radiochromic) can be used as well as electronic portal imaging devices (EPIDs). Radiographic film possesses excellent spatial resolution but poor reproducibility. The radiochromic film, on the other hand, requires doses hundreds of times greater than the typical doses used in clinical practice. EPIDs have an acceptable spatial resolution as well as acceptable reproducibility. Moreover, because of the digital nature of the images they produce, they are also very practical and will be used extensively in this thesis. For point by point dosimetry, ionization chambers and thermoluminescent dosimeters (TLDs) may also be used. The latter two methods are very accurate and have good reproducibility, but the measurement of an entire three-dimensional dose distribution with either of these methods is very time-consuming and tedious.

1.6 MODERN CONFORMAL RADIOTHERAPY: A PATIENT CASE

Before describing the patient treatment process, it is important to define the terms used to describe the tumour and margins around the tumour. These are set forth in a publication of the International Commission on Radiation Units and Measurements²⁶ which clearly defines the various target volumes to be used in modern radiotherapy.

The *gross tumour volume* (GTV) is the palpable or visible (for instance by CT) extent of the tumour. It contains the greatest density of cancerous cells and forms a mass which can be clearly identified as diseased. Surrounding this mass there usually exist microscopic extensions of disease which also need to be treated. Microscopic disease may also be suspected in regional lymph nodes. The volume containing the gross tumour plus the suspected extent of microscopic disease is referred to as the *clinical target volume* (CTV). This is, ideally, the volume the physician would like to treat, i.e., raise to a tumouricidal dose.

However, unavoidable spatial inaccuracies such as lack of reproducibility in daily patient set-up, patient (or organ) motion during treatment, and small variations in the accuracy of the linear accelerator read-outs require a margin to be left around the CTV in order to ensure that the prescribed dose is actually delivered to the CTV. This margin is typically of the order of 1 cm to 2 cm. The CTV, once augmented by this geometrical margin, results in the *planning target volume* (PTV): the volume to which we must attempt to deliver the dose in order to get, in reality, a complete irradiation of the CTV.

Generally, the PTV may have quite an irregular shape and it may not be possible to fully tailor the high dose region to it with current dose calculation and delivery techniques available in the standard radiotherapy department. The volume to which a high dose is delivered is called the *treated volume*. For instance, if the PTV is ellipsoidal

and an irradiation set-up containing four beams at gantry angles of 0°, 90°, 180°, and 270° is used for the treatment, the treatment volume will be a rectangular parallelepiped. The *irradiated volume* is the volume of tissue which receives a dose that is considered significant in relation to normal tissue tolerance. Both the treated volume and the irradiated volume depend on the treatment technique used.

In a modern radiotherapy clinic the typical procedure undergone by a patient with cancer is as follows:

- 1) Special patient immobilization devices, such as alpha-cradles (for abdominal lesions), orfits (for cranial or cervical lesions), or plaster casts (for spinal lesions) are fitted to the patient. These immobilization devices greatly facilitate accurate set-up of the patient on the treatment couch permitting positional reproducibility of around ± 3 mm^{18,27}. They also immobilize the patient during the treatment with irradiation. For the superior accuracy required in radiosurgical procedures, rigid stereotactic frames bolted to the patient's skull are used for target localization as well as patient set-up on the treatment machine and immobilization during the treatment.
- 2) The patient is set up with the immobilization device on a *CT-simulator*. A CT-simulator is a conventional CT unit equipped with a high-precision graphics workstation for organ segmentation, and a set of lasers to aid in marking the isocentre of the treatment on the patient's skin. Once the CT study is completed, the physician scrolls through the CT slices and outlines the planning treatment volume PTV. Other "critical" structures especially sensitive to radiation are also outlined so that they can hopefully be avoided with the sophisticated treatment planning and dose delivery techniques available in modern radiotherapy departments.

- 3) The outlined CT slices are transferred via a computer network to a treatment planning workstation. At the treatment planning workstation the dosimetrist, medical physicist, and physician consider the best combination of beams with which to treat the PTV. This involves selecting the number of beams to be used, their energy, their point of incidence on the patient, their angle of incidence on the patient, the shape and size of their aperture, their relative weights, and the presence or absence of filters (or dynamic MLC) to spatially-modulate the beam intensity. Especially useful in defining the beam apertures is the *beam's eye view* (BEV) perspective which gives the user a view of the patient as if he or she were located at the source of radiation. An example of a BEV perspective is shown in Fig 1.5. The beam selection process may either be by trial and error or partially automated, as mentioned above. The result is an *isodose distribution*, showing a calculation of what the dose distribution in the patient will be for the particular beam set-up.
- 4) The radiation oncologist examines the isodose distribution for acceptability. Generally, the criteria for acceptability are: a) coverage of the PTV by an isodose surface of high isodose value; b) reasonable dose homogeneity within the PTV, with a $\pm 5\%$ inhomogeneity generally accepted*; and c) sufficiently low dose values to critical structures. If the calculated distribution is acceptable, the physician selects a given isodose surface to which the prescription dose of radiation is to be given. A technologist or a physicist then performs a calculation to translate the prescription dose into the appropriate machine setting (MU) for each daily treatment field.

* Except for radiosurgical procedures where the dose is usually prescribed to the lowest isodose surface still covering the PTV and an inhomogeneity of up to +100% is deemed acceptable.

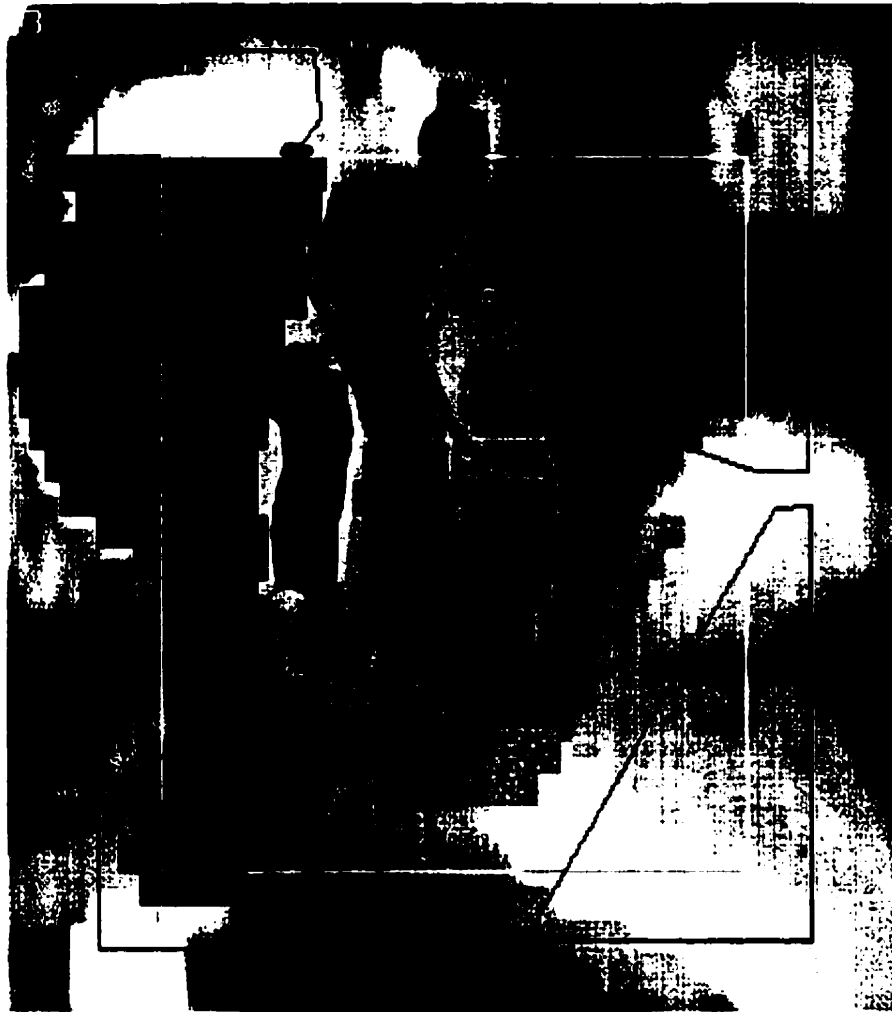


Figure 1.5. Beam's eye view for a right lateral pelvic field. The gross tumour volume (red), the planning tumour volume (yellow), the rectum (blue), the bladder (purple), and the location of shielding blocks (green outline) are shown.

- 5) The prescribed radiation is administered to the patient in small daily doses, known as *fractions*, over a period of time which is generally from three to five weeks. Fractionation of the radiation treatment, as opposed to delivery in a single dose, has been proven to result in far fewer normal tissue complications for the same level of patient cure. Check films (also known as portal images) are taken every few treatments to verify continuously the positioning of the patient in the radiation beam. During the month or so of treatment, the patient's well-being is monitored by weekly consultations with the attending physician.

1.7 SUMMARY

This chapter has discussed some of the fundamental aspects of radiation oncology: the structure of a modern high-energy therapy unit, the behaviour of a photon beam in tissue, the typical procedure undergone by a patient treated in a radiation oncology department, the rationale for a higher conformity of the radiation dose to the planning target volume, and the technical requirements to achieve such a higher dose conformity.

1.8 REFERENCES

1. Statistics Canada. *Mortality: summary list of causes 1994 (no. 84-209-xpb)*. Toronto (1994).
2. National Cancer Institute. *Web page: estimated new cancer cases and deaths by sex for all sites 1996 (<http://rex.Nci.Nih.Gov/>)*.
3. Knowlton, AH. *General principles of radiation therapy in cancer therapy*, Fisher DS and Marsh JC eds. GK Hall Medical Publishers (1982).
4. Karzmark CJ, Nunan CS, Tanabe E. *Medical electron accelerators*. McGraw-Hill (1993).
5. Cox JD. *Moss' radiation oncology: rationale, technique, results. Seventh Ed.* (1994).
6. Burman C, Kutcher GJ, Emani B, Goitein M. *Fitting of normal tissue tolerance to an analytic function*. *Int. J. Radiat. Oncol. Biol. Phys.* **21**, 123-135 (1991).
7. Ten Haken RK, Martel MK, Kessler ML, Hazuka MB, Lawrence TS, Robertson JM, Turrisi AT, Lichter AS. *Use of V_{50} and iso-NTCP in the implementation of dose escalation protocols*. *Int. J. Radiat. Oncol. Biol. Phys.* **27**, 689-69 (1993).
8. Menick HR, Garfinkel L, Dodd GD. *Preliminary report of the national cancer data base (CA 41)* (1991).

9. Myers MH, Ries LA. *Cancer patient survival rates: SEER Program results for 10 years of follow-up (CA 39) (1989).*
10. Suit HD. *Potential for improving survival rates for the cancer patient by increasing the efficacy of treatment of the primary lesion. Cancer 50, 1227-1234 (1982).*
11. Perez CA, Brady LW. *Overview in principles and practice of radiation oncology second ed. Perez Ca and Brady LW eds. JB Lippincott (1992).*
12. DeVita VT. *Progress in cancer management. Cancer 51, 2401-240 (1983).*
13. Fuks Z, Leibel SA, Kutcher GE, Mohan R, Ling CC. *Three-dimensional conformal treatment: a new frontier in radiation therapy in important advances in oncology. DeVita VT, Hellman S, Rosenberg SA eds. Lippincott (1991).*
14. Leibel SA, Ling CC, Kutcher GJ, Mohan R, Cordon-Cardo C, Fuks Z. *The biological basis of conformal three-dimensional radiation therapy. Int. J. Radiat. Oncol. Biol. Phys. 21, 805-811 (1991).*
15. Varian Oncology Systems. *Data book: high energy C-Series Clinac (part no. 01100243-02) (1995).*
16. El-Khatib EE, Podgorsak EB, Pla C. *Broad beam and narrow beam attenuation in Lipowitz's metal. Med. Phys. 14, 135-139 (1987).*
17. International Commission on Radiation Units and Measurements. *Determination of Absorbed Dose in a Patient Irradiated by Beams of X or Gamma Rays in Radiotherapy Procedures (ICRU Report No. 24) (1976).*
18. Curtin-Savard AJ, Podgorsak EB. *Dose delivery uncertainty in photon beam radiotherapy. Radiol. Oncol. 30, 218-223 (1996).*
19. Svensson GK. *Quality assurance in radiation therapy: physics efforts. Int. J. Radiat. Oncol. Biol. Phys. 10, Suppl. 1, 23-29 (1984).*
20. Leunens G, Verstraete J, Dutreix A, van der Schueren E. *Assessment of the inhomogeneity at target level by in vivo dosimetry: can the recommended 5%*

- accuracy in the dose delivered to the target volume be fulfilled in daily practice?*
Radiother. Oncol. **25**, 242-25 (1992).
21. Leunens G, Van Dam J, Dutreix A, van der Schueren E. *Quality assurance in radiotherapy by in vivo dosimetry. 2. determination of the target absorbed dose.* *Radiother. Oncol.* **19**, 73-8 (1990).
 22. Svensson H. *Quality assurance in radiation therapy: physical aspects.* *Int. J. Radiat. Oncol. Biol. Phys.* **10**, Suppl. 1, 59-65 (1984).
 23. Fraass BA, McShan DL, Diaz RF, TenHaken RK, Aisen A, Gebarski S, Glazer G, Lichter AS. *Integration of magnetic resonance imaging into radiation therapy treatment planning.* *Int. J. Radiat. Oncol. Biol. Phys.* **13**, 1897-1908 (1987).
 24. TenHaken RK, Thornton AF, Sandler HM, LaVigne ML, Quint DJ, Fraass BA, Kessler ML, McShan DL. *A quantitative assessment of the addition of MRI to CT-based, 3-D treatment planning of brain tumors.* *Radiother. Oncol.* **25**, 121-133 (1992).
 25. Leach MO. *Spatially localized nuclear magnetic resonance in the physics of medical imaging, Webb S ed.* Institute of Physics Publishing (1988).
 26. International Commission on Radiation Units and Measurements. *Prescribing, recording, and reporting photon beam therapy (ICRU Report No. 50).* Bethesda, Maryland (1993).
 27. Rabinowitz I, Broomberg J, Goitein M, McCarthy K, Leong J. *Accuracy of radiation field alignment in clinical practice.* *Radiother. Oncol.* **29**, 327-335 (1993).

2

Current approaches to dose optimization and to 3D conformal radiotherapy

Section:

2.1	Introduction.....	23
2.2	Need for computerized optimization.....	23
2.3	The objective function.....	25
2.4	Approaches to optimization	27
2.5	Approaches to 3D CRT	39
2.6	Summary.....	42
2.7	References.....	43

2.1 INTRODUCTION

This chapter will discuss: firstly, the need for computerized optimization of treatment planning; secondly, the criteria used for the optimization; thirdly, the major theoretical approaches used at present for this optimization; and fourthly, the currently used means to deliver the optimized dose distributions to the diseased site within the patient.

2.2 NEED FOR COMPUTERIZED OPTIMIZATION

Until the 1990s radiotherapy was generally considered to be a two-dimensional treatment modality. A lead wire axial contour of the patient was taken at the proposed centre of the treatment field and used to plan the disposition of the radiation beams around that "slice". It was generally assumed that all other slices of the patient in the treatment field were identical to the centre slice. Unfortunately, this sometimes caused appreciable errors in dosimetry, particularly when a slice adjacent to the central slice contained an important tissue heterogeneity or a sudden difference in the contour.

There are three reasons for the restriction of treatment planning to two dimensions. The first is that, until recently, the computer systems could not handle the computational complexity of a three-dimensional representation of the patient in a time that was reasonable for clinical use. The second reason is that the treatment units were (and still are) designed primarily to facilitate the delivery of coplanar treatments; non-coplanar treatments require the couch to be rotated, rendering the patient set-up and dose delivery more difficult. The final reason is that there has always been a shortage of CT units, although this shortage is less severe nowadays. However the upside of the quasi-universal restriction to two-dimensional treatment planning was that most calculated plans were fairly simple and could easily be "optimized" by an experienced planner.

Today, in 1998, most patients undergo a complete CT study of the affected region before treatment. Enough patient data then exists to construct a complete, and very accurate, three-dimensional model of the patient (usually referred to as the "virtual patient"). Full 3D planning can then be performed on the virtual patient with beams incident from any direction. The coverage of the PTV by any particular beam can be visualized with the "beam's eye view" (BEV) tool, and shielding may be adjusted to conform the beam to the PTV. Furthermore, on some advanced TPSs the intensity distribution across each field can be modulated to obtain a more uniform distribution of dose within the PTV. Finally, these new TPSs are not only very accurate, they also perform the three-dimensional dose calculations sufficiently fast for clinical use.

With the contemporary sophisticated treatment planning methods even an experienced planner cannot take full advantage of all the available treatment possibilities¹. Even if customized beam profiles are not allowed, there still exists the possibility of a multitude of beams (typically 3-15) incident on the patient from any direction, each having its own aperture, energy, weight and, possibly, wedge or

compensator. For normal tissues, one must consider complicated dose-volume relationships (e.g., for an abdominal lesion, is it better to irradiate one kidney to 40 Gy while sparing the other, or treat both kidneys to 20 Gy?). Additionally, there always is an impetus to minimize the integral dose (total energy) delivered to the patient. This is generally achieved by choosing beam orientations which reach the PTV after having traversed a minimum amount of healthy tissue. The great number of variables to consider render it almost impossible for a human operator to find the *optimum* treatment plan for the patient among the vast assortment of *feasible* plans. When, in addition, the possibility for intensity-modulated beam profiles is also considered, the number of variables in the problem increases tremendously since the intensity for each small "beamlet" within each beam must be determined. The optimization task now definitely requires the assistance of a computer.

2.3 THE OBJECTIVE FUNCTION

In order to select the optimum treatment plan from among a set of feasible plans, one must establish a quantitative method for evaluating the merit of a plan. The mathematical expression used to rank the plans is called the *objective function*. The objective function is generally minimized (i.e., a lower score means a better plan) but occasionally it is defined with the goal to be maximized. In the following, we will assume that the goal is to minimize the objective function. Although it may seem simplistic to reduce the entire three-dimensional treatment plan to a single number, it is important to remember that this is in fact always what one does whenever one assigns a rank to a series of items. However, it becomes imperative to specify an objective function which truly describes the "optimality" of a treatment plan.

The simpler objective functions are the *physical* objective functions which address the value of the radiation dose at specific points in the patient within the PTV and the normal tissues (particularly structures especially sensitive to radiation). They generally attempt to maximize homogeneity of dose within the PTV and minimize dose to normal structures outside the PTV. An example of an objective function F which attempts only to homogenize the dose within the PTV is:

$$F = \sum_p (D_p - D_o)^2 , \quad (2.1)$$

where D_o is the desired dose to the PTV and D_p is the dose to points p selected for scrutiny by the objective function. If we desire to include a factor to encourage sparing of normal structure K , we might change the objective function F to:

$$F = \sum_p (D_p - D_o)^2 + \sum_k (D_k)^2 , \quad (2.2)$$

where D_k is the dose to points k in the normal structure. Equations (2.1) and (2.2) are only two simple examples, and the physical objective function may be written in many other more complicated forms.

Considerably more complex are the *biological* objective functions. Instead of considering the physical distribution of dose within the patient, these functions consider the biological effects of the radiation dose, as expressed by the tumour control probability (TCP) and the normal tissue complication probability ($NTCP$). They attempt to maximize the former and minimize the latter. An example² of a biological objective function is:

$$F = P_{ic} \prod_k (1 - w_k P_{nc,k}) , \quad (2.3)$$

where P_{ic} is the probability for tumour control, $P_{nc,k}$ is the probability for normal tissue complication of organ k , given a weight w_k in the objective function. The TCP and $NTCP$ are evaluated from the doses given to various points in the PTV and the normal structures according to dose-effect relationships which at present are still very sketchy and contain large uncertainties^{3,4}. This is the principal drawback of biological objective functions.

2.4 APPROACHES TO DOSE OPTIMIZATION

We will now discuss a few of the more widely-used dose optimization techniques. Some are useful only for the optimization of beam weights, others only for finding the intensity-modulated beam profiles, and some for all variables of the treatment plan.

A. Linear or quadratic programming

Linear (or quadratic) programming algorithms express the objective function as a linear (or quadratic) function of the variables to be optimized. For instance, imagine that the task is to optimize the beam weights x_i for a set of beams whose apertures, energies, directions, etc. have already been selected. We will set up a series of equations, linear (or quadratic) in the x_i , which specify the limits on doses to normal structures as well as the maximum and minimum doses to the PTV. An additional constraint on the x_i must of course be that they are non-negative. Various well-known techniques, such as the simplex algorithm^{5,6}, the Gauss-Marquardt non-linear regression technique⁷, orthogonal matrix transformations^{8,9}, or Powell's implementation of the Goldfarb and Idnami's quadratic programming algorithm^{10,11}, can be used to find a best fit of the x_i to the

various constraints. Limitations of the programming method are, firstly, that all constraints must be linear (or quadratic) in the variables x_i and, secondly, that the methods will not provide an approximate solution if no true solution exists. A failure of this sort then requires a reformulation of the initial constraint equations.

B. Gradient methods

Gradient methods¹²⁻¹⁵ start from an initial guess of the beam weights (or beamlet weights) and find the quickest path to the bottom of the potential well in which the initial guess lies. A major shortcoming of the gradient methods is that the global minimum for objective functions containing more than one well may not be found. However, this is not a concern when the only criterion is the homogenization of the PTV dose since, in this case, the function has but one minimum, nor is it a problem if one has an alternative method for positioning the initial guess in the well containing the global minimum. The main advantage of the gradient methods is speed.

One example of a gradient approach will be presented here¹². In this example, the objective function F is formed as the product of a number of score functions relating to the TCP for the tumour and the $NTCP$ for the normal structures:

$$F = \prod_{k=0}^N S_k \quad , \quad (2.4)$$

where S_0 is the score function for TCP (it decreases if TCP increases) and S_1 to S_N are the score functions for the N various organs at risk (these decrease as $NTCP$ decreases).

Let x_i^t be the i th beam weight at iteration t . The value of this beam weight at the next iteration will then be given by:

$$x_i^{t+1} = x_i^t + \lambda \frac{\partial F}{\partial x_i} , \quad (2.5)$$

where the partial derivative $\partial F / \partial x_i$ will be calculated using a dosimetric model that computes the change of the objective function for a certain change in the beam weight x_i . The parameter λ controls the rate of change of the ray weights per iteration. In order to maximize the chance of finding the global minimum of F within the shortest possible time, λ will be made large when the partial derivative of F is small, and small when the partial derivative of F is large. Iterations which yield negative values for x_i are truncated to zero. The iterations continue until desired criteria on the dose homogeneity, TCP , $NTCP$, etc., are satisfied.

C. Filtered-projection

The filtered-projection algorithm¹⁶⁻¹⁸ for conformal radiotherapy is the procedural inverse of the filtered backprojection algorithm used in computed tomography. In computed tomography, the transmission data collected at each detector angle is filtered and then projected back onto a matrix. The sum of all backprojections yields a patient map which, at each pixel, is proportional to the linear attenuation coefficient of that pixel.

The inverse operation is to start with a desired map inside the patient (i.e., the dose distribution) and for each pre-defined beam angle project the dose distribution onto the aperture of each beam. Once filtered to compensate for lateral photon scatter and geometric blur, we have the desired beam intensity profiles. However, since the idealized dose map we have specified within the patient has a value of zero dose outside the PTV, the intensity profiles will contain negative portions, which are physically impossible to deliver. A simple truncation of the negative values to zero results in

substantial dose inaccuracies; thus, by itself, filtered-projection does not yield a feasible solution. However, subsequent iterative corrections can be applied to bring the beam intensity profiles closer to an optimum solution.

The main advantages of this method are its speed and its use of powerful and elegant image processing techniques that are extremely well-developed and familiar due to their extensive use in computed tomography.

D. Algebraic method

By performing a pixel by pixel correction to the intensity profiles rather than solving the entire problem at once, the algebraic method^{16,19-21} works backward in a very straightforward manner from a desired dose distribution to a set of intensity profiles. The algorithm is to a certain degree the inverse of the algebraic reconstruction technique used in computed tomography.

Let us start with a desired dose distribution \mathbf{D}_o attained with J beams incident on the patient. We will assign initial fluences to the beams as x_i . Choosing a particular pixel within the PTV, we calculate the dose distribution \mathbf{D} that results from the initial choice of the beam profiles. The difference between the desired and calculated dose distributions is $\mathbf{D}_o - \mathbf{D}$. We update the beamlets for each of the beam profiles contributing to the dose at the particular pixel i by a quantity proportional to $\mathbf{D}_o - \mathbf{D}$, i.e.,

$$x_i^{t+1} = x_i^t + (\mathbf{D}_o - \mathbf{D})C_j, \quad (2.6)$$

where C_j is a constant that may be different for each beam. We now proceed to the next pixel, and so forth, until all pixels in the PTV have been examined once. Because

changes in the doses delivered to other pixels may subsequently change the dose that was determined for the first pixel, we may need to repeat the entire process for a number of iterations, with the resulting calculated dose matrix \mathbf{D} each time approaching closer to the desired dose matrix \mathbf{D}_o .

The advantages of this method are that it is very simple and fast. A disadvantage is that it does not perform very well with complicated objective functions since the iterative Eq. (2.6) cannot distinguish between a dose discrepancy within the PTV and an excess dose to a normal structure.

E. Simulated annealing

The simulated annealing method²²⁻²⁶ performs a computational process analogous to the cooling of a solid from an initial high-temperature amorphous state to a final low-temperature crystalline state. The principal advantage of the simulated annealing algorithm is that it has the ability to escape local minima and thus find the global minimum of any objective function. Its drawback is that it is comparatively slow.

To start off the algorithm, an initial solution \vec{x} is proposed where \vec{x} is a vector whose components are the beam weights of all the defined beams/beamlets. At the start of the algorithm, the initial solution is the current solution. The dose distribution produced by the current solution and the corresponding value of the objective function F are calculated.

The magnitude of a displacement vector in solution space $\Delta\vec{x}$ is generated according to a generating function. Different types of generating functions have been examined by various authors. Once the magnitude of the displacement vector is determined, its components Δx_i are distributed at random. The vector $\vec{x} + \Delta\vec{x}$ is then

used in a trial solution and a dose distribution is calculated. The objective function is then calculated and its value compared to the previously obtained value. If the new trial solution represents an improvement over the previous current solution, it replaces it and becomes the new current solution. The new solution may be in a different well of the objective function so that, in a sense, the algorithm has performed a tunnelling process. If the new trial solution does not represent an improvement over the previous current solution it is not *necessarily* discarded. It will replace the current solution with a probability given by:

$$P = \exp\left(\frac{-[F(\bar{x}') - F(\bar{x})]}{T}\right) . \quad (2.7)$$

where T is a temperature parameter, to be discussed next. The non-zero probability of retaining a solution with a higher value of the objective function allows the algorithm to climb out of wells. The tunnelling and climbing features of the simulated annealing algorithm allow the algorithm to explore the entire solution space.

In analogy with the annealing process, the temperature T of the system and the magnitude of the displacement vector $\Delta\bar{x}$ both decrease with time. The initial large hops and greater potential for hill-climbing permit a coarse exploration of the topography of the objective function; the smaller final hops and more limited potential for hill-climbing permit the solution to descend slowly into the well which contains the global minimum.

F. Genetic algorithm

Genetic algorithms^{27,28} function on the basis of a "natural selection" of the "fittest" treatment plans and elimination of those plans considered less fit. The algorithm begins by defining the initial population, a set of treatment plans consisting of a number of

beams whose parameters are chosen at random within the allowed limits. An example of an individual treatment plan is the following:

<i>Beam index:</i>	34	65	21	56	99	43	39	22	84
<i>Beam weight:</i>	0.32	0.07	0.21	0.09	0.06	0.06	0.12	0.04	0.03

where each beam index specifies a unique set of parameters for energy, aperture, direction, and wedge, and the beam weight specifies the fractional weight that is assigned to that beam in the plan.

The dose distributions for all plans in the initial population are evaluated and assigned a fitness value by means of an objective function. A set of reproduction operators, which preferentially select for the fittest plans, are then used to create a new generation of plans. The reproduction operators mimic DNA crossover, cloning, mutation, as well as spontaneous generation and plan death. Each plan in the new population is again ranked according to its fitness. The process continues for a predetermined number of generations or until a certain degree of improvement is shown in the treatment plans.

G. Mixed integer

The mixed integer algorithm²⁹⁻³¹ is different from the algorithms so far presented in that its goal is to *maximize* the dose to the centre of the PTV while simultaneously respecting the set of dose-volume constraints on the sensitive organs that have been laid down.

Suppose that a set of N beams has been defined and that the weight of beam j is x_j , with x_j non-negative. Suppose also that we have a series of normal structures

denoted by the subscript k , each having M_k dose calculation points. The dose from a unit-weight beam j to the i th dose calculation point of structure k will be designated as a_{ij} . The dose-volume condition for structure k can then be expressed as:

$$\sum_{j=1}^N a_{ij} \bullet x_j \leq b_k \quad , \quad (2.8)$$

where b_k is a dose limit for normal structure k that a certain number L_k of the M_k points must satisfy to obey the imposed dose-volume constraint on organ k .

We may also wish to express a limit on the dose heterogeneity we are willing to accept within the PTV. Let there be H points on the boundary of the PTV and let c_{hj} be the dose to a particular point h for a unit-weight of beam j . Unless the PTV is exceedingly large, setting a limit on the dose heterogeneity at the PTV boundary is equivalent to (and simpler than) setting a limit on the dose heterogeneity to the entire PTV. The the heterogeneity condition can be written as:

$$\left(\frac{100-t}{100} \right) \sum_{j=1}^N d_j \bullet x_j \leq \sum_{j=1}^N c_{hj} \bullet x_j \leq \left(\frac{100+t}{100} \right) \sum_{j=1}^N d_j \bullet x_j \quad \text{with } h = 1 \text{ to } H, \quad (2.9)$$

where d_j is the dose given to the centre of the PTV for a unit-weight beam, and t is the percent heterogeneity allowed on the dose. The goal is then to maximize the dose to the centre of the PTV:

$$\sum_{j=1}^N d_j \bullet x_j \quad . \quad (2.10)$$

Simple situations having few dose points in each organ can be solved by an exhaustive enumeration of all possible combinations of the beam weight vector x which

satisfies the constraints and the selection of the one which maximizes the PTV dose. More complex problems can be solved according to the mixed integer method which requires a slight modification of Eq. (2.8) to explicitly include the fraction L_k of the M_k points that must be kept below a certain dose level.

We now rewrite Eq. (2.8) as:

$$\sum_{j=1}^N a_{ij} \bullet x_j \leq b_k + \delta_{ik} U_k \quad \text{with} \quad \delta_{ik} = 0, 1 \quad . \quad (2.11)$$

The quantity $(b_k + U_k)$ is the maximum dose that any point i_k of normal structure k is allowed to receive. However, as stated previously, L_k of these M_k points must receive less than b_k . Thus we will add the condition:

$$\sum_{i_k=1}^{M_k} \delta_{ik} \leq (M_k - L_k) \quad . \quad (2.12)$$

Equations (2.9) through (2.12) when taken together define a linear program which can be solved with standard techniques.

H. Search for a feasible solution

Two methods have been proposed in which an objective function is not used at all. Rather, a number of constraints are set up and either a random search through the space of possible solutions³² or a method of projecting the solution space onto the various constraints^{33,34} is employed. In these two methods, the first solution which satisfies the constraints is chosen. These approaches assume that all solutions satisfying the constraints are clinically acceptable and of roughly equal value. This is true only if the various constraints are set up judiciously such that the space of feasible solutions is small and relatively "flat".

I. CADPLAN's method for dose distribution optimization

Version 2.79 of the CADPLAN treatment planning system^{35,36} is not very advanced in terms of possibilities for optimization. The only aspect of a treatment plan that may be optimized is the beam profiles and this only for the case of a single beam, or for sets of parallel-opposed beams. In other words, version 2.79 of the CADPLAN software can perform dose compensation *to a plane*. It is anticipated that version 3 will have the ability to perform dose compensation *to a volume*, i.e., the ability to calculate the required dose profiles for an arbitrary number of beams that will deliver a uniform dose to the PTV.

To understand CADPLAN's algorithm for compensation to a plane, consider the radiation beam incident on the patient in Fig. 2.1. The plane in the patient at which the user desires to achieve a uniform dose is called the *compensation plane*. Presently, as shown in Fig. 2.1, the profile of the X-ray beam incident on the patient is flat (uniform) resulting in unequal doses to the five points shown on the compensation plane, with the highest dose opposite profile point x_4 since the amount of tissue traversed by the beam is the lowest at this point.

CADPLAN leaves the intensity for point x_4 unchanged and corrects the intensities opposite the other profile points by multiplying them with the reciprocal of the dose at the compensation plane. For instance, without intensity modulation, the dose point opposite x_1 receives a relative dose of 95%. To bring this in line with the relative dose opposite point x_4 , the intensity at x_1 needs to be increased by the factor $(0.95)^{-1}$. CADPLAN uses this algorithm to correct all points contained within the field limits at spatial intervals of 2.5 mm. This forms a "compensation matrix". The user is asked to specify a distance from the field edges at which the compensation will cease, to ensure

that the algorithm does not attempt to compensate in the penumbra region. CADPLAN's algorithm is not precise enough to handle adequately the compensation in the penumbra region where the dose gradient is very steep. Typically, the user should specify that the compensation is to stop approximately 1 cm from the field edge.

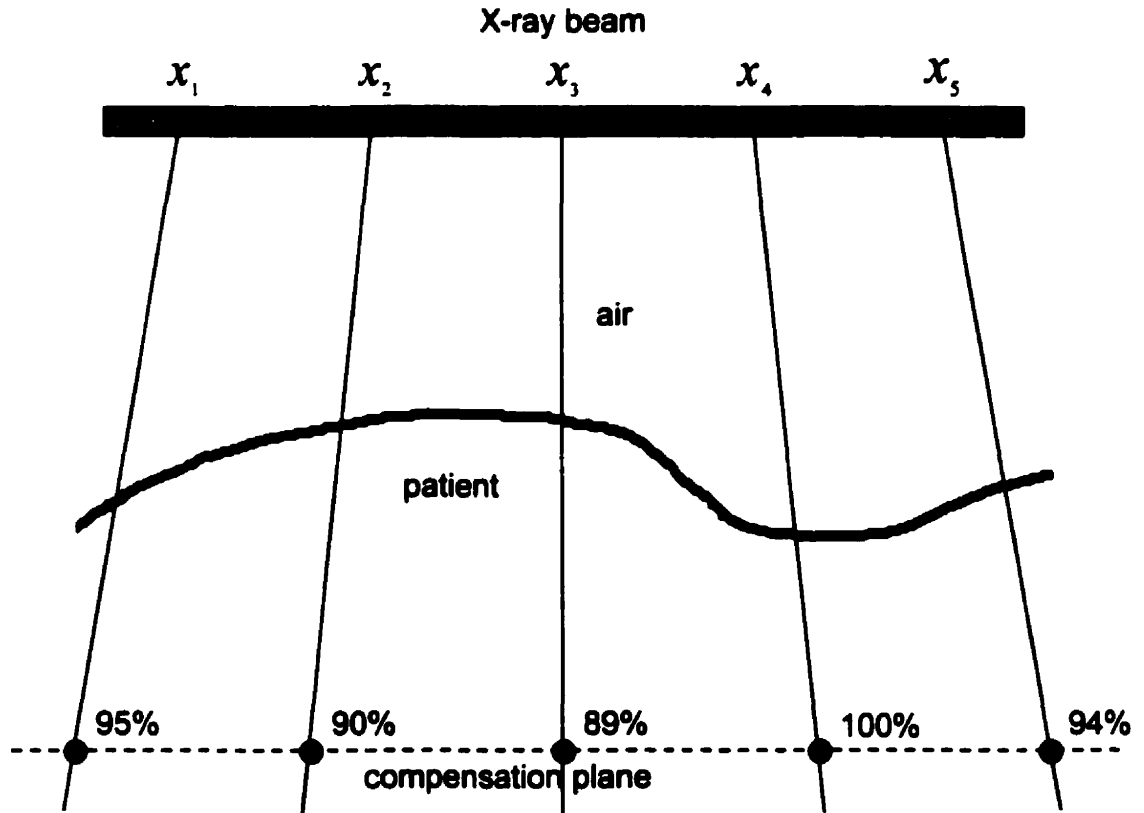


Figure 2.1. Diagram to illustrate how version 2.79 of the CADPLAN treatment planning software calculates intensity-modulated beam profiles.

If so desired by the user, the intensity matrix calculated by CADPLAN can be converted to a 3D plot of thicknesses t for a physical compensator according to a simple linear attenuation formula:

$$t = \frac{1}{\mu_{eff}} \log\left(\frac{I}{I_0}\right) , \quad (2.13)$$

where μ_{eff} is the effective linear attenuation coefficient for the compensator material and I/I_0 is the intensity at an arbitrary point of the compensation matrix relative to the maximum intensity. The plot of physical compensator thicknesses can be output in the form of a file destined to be read by a computerized milling machine.

It is evident that CADPLAN's optimization algorithm is crude and suffers from many shortcomings. Firstly, it only performs compensation to a plane and accomodates at most two beams per compensation plane. Secondly, it does not account for the fact that changes in beam intensity at one point affect neighbouring points. Some algorithms use iterative methods to account for this scatter contribution but CADPLAN simply ignores it. Thirdly, when converting the intensity values to thicknesses for a physical compensator, CADPLAN models the linear accelerator photon beam, which is composed of a wide spectrum of energies, as a monoenergetic photon beam having an effective energy given by E_{eff} and an effective attenuation coefficient μ_{eff} . This is very simplistic since, for polyenergetic beams, the shape of the energy spectrum changes with the penetration of the beam into a medium. Generally, the lower energy photons are preferentially attenuated, creating a "hardening" of the beam with increasing depth, i.e., a decrease in the effective attenuation coefficient of the beam. Tests to evaluate the performance of CADPLAN's algorithm for the calculation of beam profiles will be presented in Chapter 6.

2.5 APPROACHES TO 3D CRT

Once the parameters of an optimum treatment plan have been determined, the treatment plan must be implemented on the linear accelerator. A number of approaches for delivering the 3D dose distributions are presented below.

A. Use of physical compensators for intensity modulation

Metal compensators have been used for some time to alter the photon fluence pattern incident on the patient, particularly for single-field or parallel-opposed field configurations. To use compensators in 3D conformal treatments, the various intensity profiles calculated by the optimization routine for each field must be converted to maps of compensator thickness. A number of algorithms have been derived to perform this task^{6, 37-43}.

Conceptually, this approach is very simple but it has a major disadvantage in that it is quite time consuming⁴⁴ since for each field a compensator must be milled with a computerized milling machine and, at the time of patient treatment, the radiotherapy technologist must enter the treatment room to change the compensator for each field. Furthermore, each compensator must be documented and stored. Approaches much less demanding of the time resources of a radiotherapy department but, on the other hand, considerably more complicated have been developed for this purpose during the past few years and are briefly discussed below.

B. Use of multileaf collimators for intensity modulation

Multileaf collimators, which are described in detail in Chapter 4, are normally used for a practical delineation of irregular fields, but can also be used to achieve beam intensity modulation. A number of coplanar or noncoplanar fields are selected either by forward planning or inverse planning. Typically, the plan configuration will be similar to that used in conventional planning. However, an optimization routine will be used to

determine intensity profiles for each field to yield a desired distribution of dose within the PTV. A leaf-sequencing algorithm will then be called upon to establish the proper MLC leaf positions needed to deliver the intensity distribution for each field. The delivery of the intensity-modulated fields can be performed either in a dynamic mode or in a static mode.

In the *dynamic mode*, each set of leaf pairs moves independently according to the leaf-sequencing algorithm while the beam is on. The first field is delivered, and as the gantry and collimator rotate to bring the linear accelerator into position for the next field the beam is shut off. When the position for the second field is established, the beam is once again turned on and the leaves move according to a new leaf sequence to deliver the intensity profile for the second field. This continues until all fields of the treatment plan have been executed. The motions of the leaves as well as the gantry, collimator, and jaws are all under computer control and the treatment can be completed very rapidly. A number of leaf-sequencing algorithms have been published for use with the dynamic mode⁴⁵⁻⁵¹. However, as discussed in Chapter 3, methods for the verification of dose distributions delivered in dynamic mode are troublesome and still in their infancy. Thus the dynamic mode is used clinically only in a few centres around the world and has not yet been adopted for use in our institution.

In the *static mode*, the treatment times are slightly longer than in the dynamic mode since the leaves never move while the beam is on. Instead, the beam is temporarily shut off as the leaves move in unison from one configuration to the next, defined by the leaf-sequencing algorithm. Each static MLC configuration is referred to as a subfield; the ensemble of subfields at a given gantry angle forms the field. Otherwise, the treatment is delivered similarly to the dynamic treatment, i.e., the fields are treated sequentially under computer control. Although slightly more time-consuming to deliver,

a significant advantage of the static approach is that the dosimetry of static fields is much better understood and easier to verify than the dosimetry of dynamic fields. Algorithms for the static mode approach to intensity modulation have been given in the literature⁵²⁻⁵⁷. Our particular algorithm for dose delivery in a static mode is described in Chapter 5.

C. Tomotherapy, Peacock System, Intensity-modulated Arc Therapy (IMAT)

Three specialized approaches to intensity-modulation, namely tomotherapy, the Peacock system, and IMAT, also use a type of multileaf collimator to achieve intensity-modulation. However, they are sufficiently different from the basic MLC approach to warrant a separate discussion. All three techniques, instead of modulating the beam intensity at a number of fixed gantry angles, modulate the beam intensity simultaneously with the rotation of the gantry about the patient.

*Tomotherapy units*⁵⁸⁻⁶⁰ have been proposed as the ideal radiotherapy treatment machine, however, they are still under development and have not yet been applied to clinical use. The proposed unit resembles a modern CT unit except that, in addition to the low-energy diagnostic X-ray tube, the tomotherapy unit contains a miniature 6 MV waveguide operating in the X-band at $\sim 10^4$ MHz. The therapy beam is collimated into a 1 cm wide fan and rotates continuously about the patient while the patient couch is translating, resulting in a helical path about the patient. In order to achieve a conformal distribution of dose within the patient, intensity modulation is constantly provided by centimetre-wide tungsten vanes spanning the width of the fan beam. A very appealing property of tomotherapy units is that, due to the presence of the diagnostic tube in the unit, the patient set-up can be verified with a CT procedure each day before treatment, and even during treatment for detection of excessive patient motion.

The *Peacock system*⁶¹⁻⁶⁴, on the other hand, is a commercially available add-on package for a conventional isocentric linear accelerator. Currently, it is used only for treatment of intracranial lesions. The package consists of software for inverse treatment planning, a special multileaf collimator incorporating opposing pairs of 0.85 cm wide vanes to perform the intensity modulation, and a device for precision indexing of the couch. Patient treatment first involves rigid immobilization using a metal plate screwed into the patient's skull, and then beam delivery under continuous full gantry rotation while the opposing pairs of vane provide intensity-modulation with the couch stationary. Two 1 cm thick slices of the PTV are treated at each couch position; the couch is then translated to treat the next two slices of the PTV.

Like tomotherapy and the Peacock system, the *intensity-modulated arc therapy (IMAT)*⁶⁵ employs gantry rotation about the patient simultaneously with intensity-modulation. However, this is about as far as the resemblance goes. Contrary to the two preceding approaches, in IMAT the dose is delivered to the patient through a series of arcs rather than complete gantry rotation. Additionally, the intensity modulation is provided by a conventional multileaf collimator. The aperture of the multileaf collimator changes shape as the gantry rotates to execute the arc. The number of arcs required to treat the patient depends on the complexity of the dose distribution to be delivered and the degree of precision desired. Finally, since the full width of the PTV can be treated all at once, no movement of the couch is needed during treatment. This approach has not yet been implemented for clinical use.

2.6 SUMMARY

This chapter has discussed the currently-used means for calculating and delivering optimized beam intensity matrices. When delivered together, the sum of these

intensity-modulated fields yields a dose distribution which, in theory, will conform tightly to the target volume and produce a homogeneous dose within it, thus sparing surrounding healthy tissues.

2.7 REFERENCES

1. Oldham M, Neal A, Webb S. *A comparison of conventional forward planning with inverse planning for 3D conformal radiotherapy of the prostate.* *Radiother. Oncol.* **35**, 248-262 (1995).
2. Schultheiss TE, Orton CG. *Models in radiotherapy: definition of decision criteria.* *Med. Phys.* **12**, 183-187 (1985).
3. Mohan R, Mageras GS, Baldwin B, Brewster LJ, Kutcher GJ, Leibel S, Burman CM, Ling CC, Fuks Z. *Clinically relevant optimization of 3-D conformal treatments.* *Med. Phys.* **19**, 933-944 (1992).
4. Enami B, Lyman J, Brown A, Burman C, Coia L, Goitein M, Kutcher GJ, Munzenrider J, Solin L, Shank B, Wesson M. *Tolerance of normal tissue to therapeutic radiation.* *Int. J. Radiat. Oncol. Biol. Phys.* **21**, 109-122 (1991).
5. Rosen II, Lane RG, Morill SM, Belli JA. *Treatment plan optimization using linear programming.* *Med. Phys.* **18**, 141-152 (1991).
6. Renner WD, O'Connor TP, Bermudez NM. *An algorithm for design of beam compensators.* *Int. J. Radiat. Oncol. Biol. Phys.* **17**, 227-234 (1989).
7. Weeks KJ, Sontag MR. *3-D dose-volume compensation using non-linear least-squares regression technique.* *Med. Phys.* **18**, 474-487 (1991).
8. Starkschall G. *A constrained least-squares optimization method for external beam radiation therapy treatment planning.* *Med. Phys.* **11**, 659-665 (1984).
9. Lawson CL, Hanson RJ. *Solving least squares problems,* Prentice Hall (1974).
10. Djordjevich A, Bonham DJ, Hussein EMA, Andrew J, Hale ME. *Optimal design of radiation compensators.* *Med. Phys.* **17**, 397-404 (1990).

11. IMSL Inc. *QPROG: IMSL math library (linearly constrained minimization, quadratic programming)*, 892-894 (1988).
12. Wang X-H, Mohan R, Jackson A, Leibel SA, Fuks Zvi, Ling CC. *Optimization of intensity-modulated 3D conformal treatment plans based on biological indices*. *Radiother. Oncol.* **37**, 140-152 (1995).
13. Bortfeld T, Burkelbach J, Boesecke R, Schlegel W. *Three-dimensional solution of the inverse problem in conformation radiotherapy* in *Advanced Radiation Therapy: Tumor Response Monitoring and Treatment Planning*, Ed. Breit A, Springer-Verlag (1992).
14. Gustafsson A, Lind BK, Svensson R, Brahme A. *Simultaneous optimization of dynamic collimation and scanning patterns or compensation filters using a generalized pencil beam algorithm*. *Med. Phys.* **22**, 1141-56 (1995).
15. Hristov DH, Fallone BG. *An active set algorithm for treatment plan optimization*. *Med. Phys.* **24**, 1455-1464 (1997).
16. Bortfeld T, Ürkelbach J, Boesecke R, Schlegel W. *Methods of image reconstruction from projections applied to conformation therapy*. *Phys. Med. Biol.* **35**, 1423-1434 (1990).
17. Holmes TW, Mackie TR, Reckwerdt P. *An iterative filtered backprojection inverse treatment planning algorithm for tomotherapy*. *Int. J. Radiat. Oncol. Biol. Phys.* **32**, 1215-1225 (1995).
18. Holmes T, Mackie TR. *A filtered backprojection dose calculation method for inverse treatment planning*. *Med. Phys.* **21**, 303-313 (1994).
19. Xing L, Chen GTY. *Iterative methods for inverse treatment planning*. *Phys. Med. Biol.* **41**, 1-17 (1996).
20. Mazur EJ, Mazur AK, Yu C, Wong J. *Inverse conformal therapy planning using interpolative algebraic reconstruction technique*. *Med. Phys.* **21**, 901-913 (1994).

21. Censor Y, Altschuler MD, Powlis WD. *A computational solution of the inverse problem in rotation therapy treatment planning.* Appl. Math. Comput. **25**, 57-87.
22. Rosen II, Lam KS, Lane RG, Langer M, Morrill SM. *Comparison of simulated annealing algorithms for conformal therapy planning.* Int. J. Radiat. Oncol. Biol. Phys. **33**, 1091-1099 (1995).
23. Webb S. *Optimization of conformal radiotherapy dose distributions by simulated annealing.* Phys. Med. Biol. **34**, 1349-1370 (1989).
24. Metropolis N, Rosenbluth AW, Rosenbluth MN, Teller AH, Teller E. *Equation of state calculations by fast computing machines.* J. Chem. Phys. **21**, 1087-1092 (1953).
25. Kirkpatrick S, Gelatt CD, Vecchi MP. *Optimization by simulated annealing.* Science **220**, 671-680 (1983).
26. Mohan R, Mageras GS, Baldwin B, Brewster LJ, Kutcher GJ. *Clinically relevant optimization of 3-D conformal treatments.* Med. Phys. **19**, 933-944 (1992).
27. Ezzell GA. *Genetic and geometric optimization of three-dimensional radiation therapy treatment planning.* Med. Phys. **23**, 293-305 (1996).
28. Langer M, Brown R, Morrill S, Lane R, Lee O. *A generic genetic algorithm for generating beam intensities.* Med. Phys. **21**, 878 (1994).
29. Langer M, Brown R, Urie M, Leong J, Stracher M, Shapiro J. *Large scale optimization of beam weights under dose-volume restrictions.* Int. J. Radiat. Oncol. Biol. Phys. **18**, 887-893 (1990).
30. Benichou M, Gauthier JM, Girodet P, Hentges G, Ribiere G. *Experiments in mixed integer linear programming.* Math. Prog. **1**, 76-94 (1971).
31. Crowder H, Johnson EL, Padberg M. *Solving large-scale zero-one linear programming problems.* Op. Res. **31**, 803-833 (1983).

32. Niemierko A. *Random search algorithm (RONSC) for optimization of radiation therapy with both physical and biological end points and constraints.* Int. J. Radiat. Oncol. Biol. Phys. **23**, 89-98 (1992).
33. Lee S, Cho PS, Marks RJ II, Oh S. *Conformal radiotherapy computation by the method of alternating projections onto convex sets.* Phys. Med. Biol. **42**, 1065-1086 (1997).
34. Powllis WD, Atischuler MD, Censor Y, Buhle EL Jr. *Semi-automated radiotherapy treatment planning with a mathematical model to satisfy treatment goals.* Int. J. Radiat. Oncol. Biol. Phys. **16**, 271-276 (1989).
35. Varian Oncology Systems. *CadPlan treatment modelling workstation: external beam modelling user's manual v2.62* (1995)
36. Varian Oncology Systems. *CadPlan treatment modelling workstation: external beam modelling reference manual v2.7* (1996).
37. Butts JR, Abell GA, Morrison JC, Elson HR. *Dose uniformity from a computerized three-dimensional tissue compensating system.* Med. Dos. **22**, 113-116 (1997).
38. Mejaddem Y, Lax I, Shamsuddin Adakkai K. *Procedure for accurate fabrication of tissue compensators with high-density material.* Phys. Med. Biol. **42**, 415-421 (1997).
39. van Santvoort JP, Binnekamp D, Heijmen BJ, Levendag PC. *Granulate of stainless steel as compensator material.* Radiother. Oncol. **34**, 78-80 (1995).
40. Paliwal BR, Podgorsak MB, Harari PM, Haney P, Jursinic PA. *Evaluation and quality control of a commercial 3-D dose compensator system.* Med. Dos. **19**, 179-185 (1994).
41. Park HC, Almond PR. *Tissue compensation and verification of dose uniformity.* Med. Dos. **18**, 193-196 (1993).

42. Kutcher GJ, Burman C, Mohan R. *Compensation in three-dimensional non-coplanar treatment planning*. Int. J. Radiat. Oncol. Biol. Phys. **20**, 127-134 (1991).
43. Shragge PC, Patterson MS. *Improved method for the design of tissue compensators*. Med. Phys. **8**, 885-891 (1981).
44. Weidlich GA, Schmidt EL. *Development of methods for dynamic radiation therapy with specified dose distributions*. Med. Dos. **21**, 87-95 (1996).
45. Brahme A. *Optimization of stationary and moving beam radiation therapy techniques*. Radiother. Oncol. **12**, 129-140 (1988).
46. Källman P, Lind B, Eklöf A, Brahme A. *Shaping of arbitrary dose distributions by dynamic multileaf collimation*. Phys. Med. Biol. **33**, 1291-1300 (1988).
47. Yu CX, Symons MJ, Du MN, Martinez AA, Wong JW. *A method for implementing dynamic photon beam intensity modulation using independent jaws and a multileaf collimator*. Phys. Med. Biol. **40**, 769-787 (1995).
48. Chui CS, LoSasso T, Spirou S. *Dose calculation for photon beams with intensity modulation generated by dynamic jaw or multileaf collimators*. Med. Phys. **21**, 1237-1244 (1994).
49. Convery DJ, Rosenbloom ME. *The generation of intensity-modulated fields for conformal radiotherapy by dynamic collimation*. Phys. Med. Biol. **37**, 1359-1374 (1992).
50. Spirou SV, Chui CC. *Generation of arbitrary intensity profiles by combining the scanning beam with dynamic multileaf collimation*. Med. Phys. **23**, 1-8 (1996).
51. Stein J, Bortfeld T, Dörschel B, Schlegel W. *Dynamic X-ray compensation for conformal radiotherapy by means of multileaf collimation*. Radiol. Oncol. **32**, 163-173 (1994).
52. Bortfeld TR, Kahler DL, Waldron TJ, Boyer AL. *X-ray field compensation with multileaf collimators*. Int. J. Radiat. Oncol. Biol. Phys. **28**, 723-730 (1994).

53. Geis P, Boyer AL. *Use of a multileaf collimator as a dynamic missing-tissue compensator.* Med. Phys. **23**, 1199-1205 (1996).
54. Galvin JM, Chen XG, Smith RM. *Combining multileaf fields to modulate fluence distributions.* Int. J. Radiat. Oncol. Biol. Phys. **27**, 697-705 (1993).
55. Evans PM, Hansen VN, Swindell W. *The optimum intensities for multileaf collimator field compensation.* Med. Phys. **24**, 1147-1156 (1997).
56. Fraass BA. *Clinical use of intensity modulated radiotherapy using multi-segment treatment delivery techniques.* Med. Phys. **24**, 974 (1997).
57. Lane RG, Loyd MD, Chow CH, Ekwelundu E, Rosen II. *Custom beam profiles in computer-controlled radiation therapy.* Int. J. Radiat. Oncol. Biol. Phys. **22**, 167-174 (1991).
58. Mackie TR, Holmes T, Swerdloff S, Reckwerdt P, Deasy JO, Yang J, Paliwal B, Kinsella T. *Tomotherapy: A new concept for the delivery of dynamic conformal radiotherapy.* Med. Phys. **20**, 1709-1719 (1993).
59. Yang JN, Mackie TR, Reckwerdt P, Deasy JO, Thomadsen BR. *An investigation of tomotherapy beam delivery.* Med. Phys. **24**, 425-436 (1997).
60. Oldham M, Webb S. *Intensity-modulated radiotherapy by means of static tomotherapy: A planning and verification study.* Med. Phys. **24**, 827-836 (1997).
61. Wu A, Johnson M, Chen ASJ, Kalnicki S. *Evaluation of dose calculation algorithm of the Peacock system for multileaf intensity modulation.* Int. J. Radiat. Oncol. Biol. Phys. **36**, 1225-1231 (1996).
62. Woo SY, Grant WH III, Bellezza D, Grossman R, Gildenberg P, Carpenter LS, Carol M, Butler EB. *A comparison of intensity modulated conformal therapy with a conventional external beam stereotactic radiosurgery system for the treatment of single and multiple intracranial lesions.* Int. J. Radiat. Oncol. Biol. Phys. **35**, 593-597 (1996).

63. Carol M, Grant WH III, Bleier AR, Kania AA, Targovnik HS, Butler EB, Woo SW. *The field-matching problem as it applies to the Peacock three dimensional conformal system for intensity modulation.* Int. J. Radiat. Oncol. Biol. Phys. **34**, 183-187 (1996).
64. Carol MP. PEACOCK: *A system for planning and rotational delivery of dynamic conformal radiotherapy.* Int. J. Imaging Sys. and Tech. **6**, 56-61 (1995).
65. Yu CX. *Intensity-modulated arc therapy with dynamic multileaf collimation: An alternative to tomotherapy.* Phys. Med. Biol. **40**, 1435-1449 (1995).

3

Use of the Varian Electronic Portal Imaging Device as a Radiation Dosimeter

Section:

3.1	Introduction.....	50
3.2	Dosimeters used in radiotherapy	50
3.3	General description of the Varian SLIC EPID	55
3.4	Physics of image formation in the SLIC EPID.....	57
3.5	Basic experimental investigations of the EPID	59
3.6	Basic dosimetric applications of the EPID	68
3.7	Use of the SLIC EPID for the verification of intensity-modulated beams	73
3.8	Summary	73
3.9	References.....	74

3.1 INTRODUCTION

This chapter first presents an overview of dosimetry techniques used in photon beam radiotherapy, and then describes in detail the use of an electronic portal imaging device (EPID) for the verification of intensity-modulated beams produced by a multileaf collimator (MLC).

3.2 DOSIMETERS USED IN RADIOTHERAPY

A. Well-established techniques

The well-established dosimeters in photon beam radiotherapy are the following: the ionization chamber, the semiconductor diode, thermoluminescent dosimeters, the Fricke solution, and silver bromide film. A number of newer dosimetry techniques which are also beginning to find favour in radiotherapy include the Fricke gel, the BANG

polymer gel, and radiochromic film. We will review briefly each of these radiation dosimeters and state some of their advantages and disadvantages.

An *ionization chamber* measures the ionization produced by the radiation field in the chamber sensitive volume filled with some gas, most commonly air. The collecting volume (of dimensions typically around 1 cm³ or less) is bounded by two electrodes with a potential difference on the order of 300 V. The two most common types of ionization chambers for radiotherapy applications are the parallel-plate (end-window) chamber in which the electrodes consist of two parallel discs several millimeters apart, and the cylindrical (thimble) chamber in which the outer electrode is in the form of a thimble, with the inner electrode protruding into the thimble. The advantages of ionization chambers are the very low dependence of their response on radiation energy and the extremely high reproducibility of the measurements, making them the dosimeters most suitable for measurements of treatment machine outputs. The principal disadvantage is that dose is sampled only at a single point: measurements in a plane are thus time-consuming, and even more so in a volume.

Semiconductor dosimeters consist of a p-n junction operating in reverse bias, i.e., in diode mode. Electron-hole pairs formed in the dosimetric sensitive volume (depletion layer) by collisional interactions of the ionizing radiation yield a charge proportional to the dose received by the diode. The diode may also be operated in the photovoltaic mode without any bias at all; the diode response is smaller, but the leakage current is also reduced considerably. Volume for volume, semiconductor detectors are over 10⁴ times more sensitive than gas-filled chambers. A factor of 10³ comes from the ratio of densities and another order of magnitude comes from the energy required to create an electron-hole pair (2.7 eV for silicon in comparison to 33.97 eV, the average energy required to create an ion pair in air). Thus, for radiotherapy applications the depletion

layers of diodes can be made extremely small, typically a few tenths of a mm³ in volume, which is very practical in measurements requiring a high spatial resolution. The disadvantages of diode dosimeters are that they are generally not tissue-equivalent, their response depends significantly on their orientation with respect to the radiation beam and, like ion chambers, they sample dose at only one point. However, diode arrays for measurement of beam profiles have recently become commercially available.

Thermoluminescent dosimeters (TLDs) consist of small amounts of thermoluminescent material of volume around 1 mm³, in solid crystal or powder form. The most popular TLD material is lithium fluoride. When exposed to radiation, electrons in TLDs are promoted to higher energy levels and trapped in metastable states lying in the forbidden energy gap. These states have lifetimes ranging from seconds to years, the deeper the trap the longer its lifetime. Thermoluminescent materials can thus conserve a permanent record of the radiation dose received and this dose record can be extracted by supplying energy to the TLD in the form of heat, which causes the emission of a quantity of light proportional to the original radiation energy absorbed. In the case of lithium fluoride the emitted light falls in the blue part of the visible spectrum. The advantages of tissue-equivalent thermoluminescent materials for dosimetry are low dependence of response on radiation energy, small dosimeter size (permitting good spatial resolution of dose measurements) and reasonable reproducibility. A disadvantage is the read-out procedure of each TLD which is lengthy and tedious. The ideal use of TLD is for dose verification measurements on patients during their treatment, with one or more TLDs taped to the patient's skin or placed within body cavities.

The *Fricke dosimeter* solution is an acidic aqueous solution of ferrous sulfate. Ionizing radiation reduces the ferrous ions to ferric ions in a degree proportional to the radiation dose received by the solution. Measurement of the resultant concentration of

ferric sulfate is performed optically, i.e., by recording the change in transmission of the solution after irradiation, in the ultraviolet region at 304 nm. No *visual* change accompanies the irradiation. There are few advantages to this method except that it may be labelled as an absolute dosimetry technique provided that the energy required to oxidize a ferrous ion to a ferric ion is known. Disadvantages include the need for very careful preparation of the solution, a relatively low sensitivity, as well as dependence of dosimeter response on volume, temperature, and oxygen concentration.

Silver bromide film consists of a cellulose base to which is bound a thin emulsion of small crystals of silver bromide. The action of radiation is to reduce some of the silver atoms in the emulsion forming a "latent image" invisible to the eye; subsequent development of the film reduces the whole silver bromide crystal for those crystals containing a reduced silver atom. The development results in substantial amplification, revealing to the unaided eye a 2D "map" of the radiation distribution to which the film was subjected. Quantitative evaluation of the optical density at each point on the film is obtained with a scanning densitometer; optical density can then be converted to radiation dose if the film's characteristic curve is known. Film is an attractive dosimeter since with it one can measure radiation dose in an entire plane simultaneously with a very high spatial resolution (order of microns). However, irksome problems of film are that the response depends severely on radiation energy below energies of ~ 200 keV; that the relationship between measured optical density and radiation dose received saturates at moderate doses (~ 50 cGy); and that development conditions of the film affect the resultant optical density in a significant and quite irreproducible manner. Some investigators^{1,2} have proposed elaborate techniques to circumvent these difficulties, however, most physicists favour an approach that does not involve dubious "correction factors".

B. Recent techniques

The *Fricke gel dosimeter*³ is closely related to the Fricke ferrous sulfate solution, discussed above, except that the ferrous sulfate is now dissolved into gelatin. Because of the gel matrix, the ferric sulfate produced by the radiation field does not readily migrate, and the Fricke gel dosimeter thus records three-dimensional dose information all at once -a remarkable attribute of this new dosimeter. Contrary to the read-out of the Fricke ferrous sulfate solutions with a spectrometer, the read-out of the gels is performed in a magnetic resonance imager (MRI), exploiting the different magnetic susceptibilities of the two charge states of the iron ions. The principal drawback of Fricke gel dosimetry is the poorly-established reproducibility of the technique^{4,5}. Moreover, in order for ion migration to be truly insignificant, the Fricke gel must be read on the MRI within an hour of irradiation. This can be a serious constraint in most institutions since physics access to MRI units is often severely limited by a heavy patient load.

The same three-dimensional imaging capability exists with an even newer dosimeter: the *BANG polymer gel*⁵⁻⁸ composed of acrylamide, bis-acrylamide, and again, gelatin. Irradiation causes the bis-acrylamide to form cross-links with the acrylamide, transforming the monomer state to a polymer state to a degree proportional with the radiation dose. Quantitative read-out is performed with an MRI unit, but the dose record may also be examined qualitatively by eye, which is an agreeable feature the Fricke ferrous sulfate gel does not possess. There is no migration, as in the Fricke gel, thus the read-out need not be performed immediately after irradiation. The three-dimensional imaging capabilities of this new gel technique are very exciting and further research may make the BANG gel the cornerstone of future three-dimensional radiotherapy dosimetry.

*Radiochromic film*⁹⁻¹¹ consists of a polyester base onto which a thin emulsion of radio-sensitive dye has been deposited. Radiation turns the dye molecules a deep blue,

without any development whatsoever. Ambient office lighting has a negligible effect on the film since the radio-chemical interaction requires an energy greater than about 3 eV to proceed, but exposure to sunlight because of its ultraviolet component should be avoided. Precise read-out of the optical density of the radiochromic film is possible with a He-Ne laser densitometer and is strictly linearly proportional to dose. The advantages of radiochromic film are very low dependence of the response on radiation energy, the fact that dose may be recorded in an entire plane at once, and extreme ease of use since there is no development and no need to protect the unexposed film from ambient lighting. The disadvantages of radiochromic film are its high cost and its very low sensitivity, which implies that a large dose must be imparted to the film in order to achieve a suitable optical density range. These drawbacks make radiochromic film impractical for routine radiotherapy dose measurements, yet its low sensitivity is very useful for certain specialized applications, such as stereotactic radiosurgery verification and brachytherapy source autoradiographs.

3.3 GENERAL DESCRIPTION OF THE VARIAN SLIC EPID

Figure 3.1 is a sketch of the image detection unit (IDU) of the Varian EPID¹². The prototype of this device was built at the Netherlands Cancer Institute in the early 1980s. The IDU consists of a control unit, 256 high-voltage switches, 256 electrometers, and an ionization chamber filled with a 1 mm thick layer of a liquid hydrocarbon (isooctane). The ionization chamber is sectioned electronically into 65536 "pixels" (256×256 matrix) by 256 high-voltage polarizing electrodes and the 256 electrometer sense wires which criss-cross the chamber perpendicularly to each other. The total area of the ionization chamber is 32×32 cm², giving each pixel an area of 1.25×1.25 mm². This type of EPID is referred to as a scanning liquid ionization chamber (SLIC).

In the "standard mode" the read-out of the IDU after irradiation is performed in the following sequence¹³:

- (1) High-voltage line #1 is connected to 250 volts.
- (2) All 256 electrometers are read simultaneously to acquire the pixel values for line #1. This step is performed six times in sequence and the average is calculated digitally. Line #1 is disconnected from the power supply.
- (3) High-voltage line #2 is connected to 250 volts.
- (4) All 256 electrometers are again read simultaneously to acquire the pixel values for line #2. This step is performed six times in sequence and again the average is calculated digitally. Line #2 is disconnected from the power supply.
- (5) High-voltage line #3 is switched to 250 volts, etc. . .

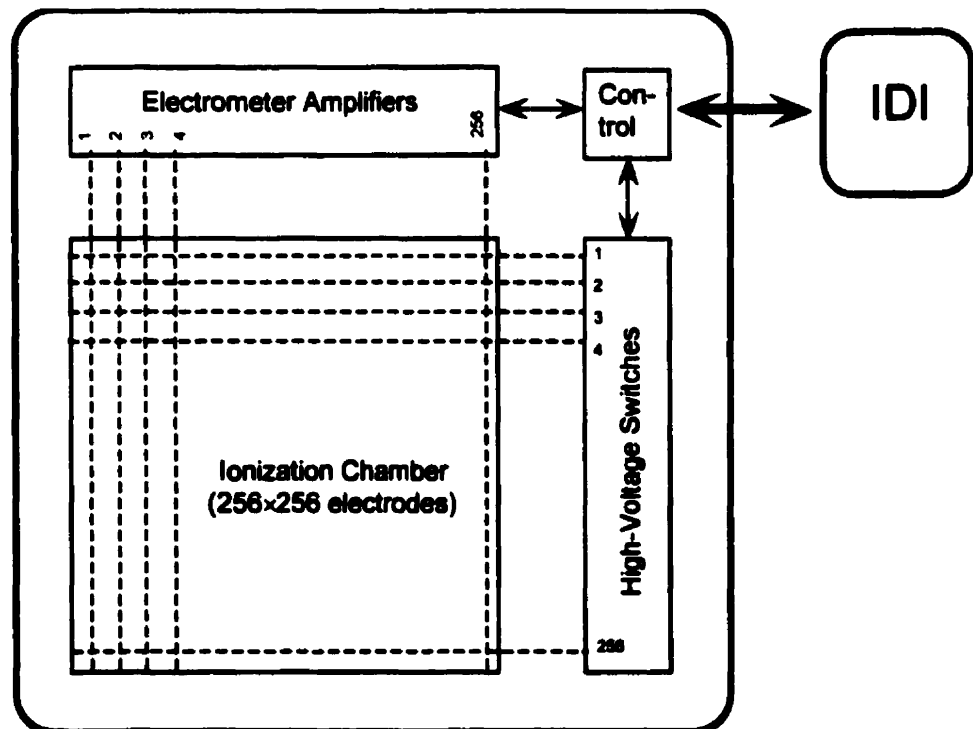


Figure 3.1. Diagram of the image detection unit (IDU) of the Varian scanning liquid ionization chamber (SLIC) EPID.

Read-out of the entire IDU takes 5.9 s in the standard mode. In the "fast mode", pairs of high-voltage lines are polarized simultaneously, which reduces the total read-out time to 2.9 s but concurrently decreases the spatial resolution by a factor of two in the direction perpendicular to the high-voltage lines.

The IDU is supported by a robotic arm with three degrees of freedom permitting source-detector-distances (SDDs) ranging from 90 cm to 200 cm, and allowing horizontal displacements of about 15 cm in all four directions. The manufacturer cautions against irradiating the electronics surrounding the ionization chamber, recommending a maximum field size at an SDD of 100 cm of 32×32 cm². When not needed, the support arm allows the IDU to be fully retracted from the radiation beam and stored next to the gantry counterweight.

Signals from the IDU are sent to the image detection interface (IDI) which contains power supplies and hardware for synchronizing the EPID with the Clinac 2300 C/D. The IDI is located outside the treatment room and is connected to an IBM-compatible PC for image processing and visualization. The PC is networked to a printer, a frame-grabber for digitization of simulator films, and to other PCs which may be used remotely to view images and perform file management.

3.4 PHYSICS OF IMAGE FORMATION IN THE SLIC EPID

Radiation striking the IDU ionizes some of the molecules within the ionization chamber, creating positive ions and free electrons. The free electrons are rapidly captured by electronegative impurities in the iso-octane liquid and thus all charged particles in the chamber sensitive volume have mobilities characteristic of moderately heavy ions¹⁴. With the relatively low ion mobility and the high density of the liquid,

recombination loss in the chamber is considerable. As a result, the ion-pair concentration in the ionization chamber rapidly reaches a steady state in which ion-pair creation by the radiation field is balanced by ion-pair recombination. The steady-state ion-pair concentration in the iso-octane layer is then sampled by the high-voltage pulses applied in turn to each pixel.

A qualitative description of the dependence of a given pixel value on dose rate (i.e., the *characteristic curve*) is easily derived as follows. Let $n(t)$ be the ion-pair concentration in the liquid. The rate of change of the ion-pair concentration will involve two terms, one positive and one negative. The positive term accounts for ion-pair creation and will be proportional to the dose rate \dot{D} impinging on the liquid in the ionization chamber. The negative term accounts for the recombination loss and, according to elementary chemical kinetics, will be proportional to the product of the positive and negative ion concentrations. The differential equation governing the ion-pair concentration is therefore given as:

$$\frac{dn(t)}{dt} = a\dot{D} - b[n(t)]^2 \quad , \quad (3.1)$$

where a and b are constants. In the steady state, $dn(t)/dt = 0$ and the ion-pair concentration, using Eq. (3.1), reaches the equilibrium value n_{eq} given by:

$$n_{eq} = \frac{\sqrt{a\dot{D}}}{b} \quad . \quad (3.2)$$

In this simplified model, the equilibrium ion-pair concentration is proportional to the square-root of the dose rate. Since the read-out of each pixel is simply a sampling of the steady-state ion-pair concentration in each pixel, one expects the pixel value to be

roughly proportional to the square-root of the dose rate at the IDU. In practice, however, the calibration curve involves higher order terms and should be determined experimentally¹⁵⁻²⁰ in the range of dose rates encountered. The calibration curve is expected to be independent of photon energy since iso-octane is composed of low atomic number elements. The preceding derivation of Eq. (3.2) is a condensed version of the derivation given by van Herk¹⁵.

3.5 BASIC EXPERIMENTAL INVESTIGATIONS OF THE EPID

The experimental investigations performed with the EPID which will be described in this section are the following:

- A. Determination of the depth of maximum dose for the EPID
- B. Determination of the characteristic curve for the EPID
- C. Reproducibility of pixel values for identical irradiation conditions
- D. Investigation of variations of the characteristic curve with field size
- E. Investigation of "memory effect" of the EPID.

All experiments reported in this section were performed in the standard acquisition mode with the EPID at a source-detector distance of 100 cm. The dose rate was selected to be 400 MU/min for both the 6 MV and the 18 MV photon beams produced by the Varian Clinac-2300 C/D linear accelerator. All stated pixel values are actually an average of the pixel values in a matrix of 9×9 pixels comprising a region of interest (ROI) at the centre of the EPID image.

A. Build-up measurements

When a choice exists as to what depth dosimetric measurements are to be performed, the depth of maximum dose d_{max} suggests itself for two reasons. The first

reason is that at d_{max} the detector will register the largest signal, thus giving the largest number of significant figures in the measurement results and the largest signal-to-noise ratio. The second reason is that the dose gradient is small in the region surrounding d_{max} ; performing measurements at depth d_{max} therefore minimizes the impact of small uncertainties in the depth.

To determine experimentally the depth of d_{max} for the Varian EPID, the field size was set to $10 \times 10 \text{ cm}^2$ and irradiations were carried out with various thicknesses of solid water placed on the IDU. Results are shown in Fig. 3.2 for the 6 MV and the 18 MV photon beams. For measurements at shallow depths in phantom, sheets of phantom material may be placed directly on the cover of the imager. However, with standard-size sheets ($30 \times 30 \text{ cm}^2$) the weight of 4 cm of phantom material will trip the EPID's collision interlocks. In order to perform experiments at greater depths in phantom, a custom jig was manufactured allowing additional sheets of solid water to be suspended above the imager surface while still making contact with those placed directly on the surface of the imager.

The results displayed in Fig. 3.2 indicate that a thickness of 1 cm of solid water and 3 cm solid water placed on the surface of the imager constitutes the depth of maximum dose for the 6 MV and 18 MV beams, respectively. It should be noted that this solid water depth is supplemental to the build-up provided by the printed-circuit board in front of the iso-octane layer, the rohacell foam cushioning the printed circuit board, and the 1 mm steel cover plate of the IDU. Our experiments showed that the depth of d_{max} varied by approximately 1 mm and 2 mm for the 6 MV and 18 MV photon beams, respectively, as the field size was changed from $5 \times 5 \text{ cm}^2$ to $20 \times 20 \text{ cm}^2$. However, since the dose varies so little with depth in the d_{max} region, we ignore this small variation and perform all our stated d_{max} measurements with the same thickness of solid

water, regardless of the field size. As evident from Fig. 3.2, this thickness is 1 cm of solid water for the 6 MV beam and 3 cm of solid water for the 18 MV beam.

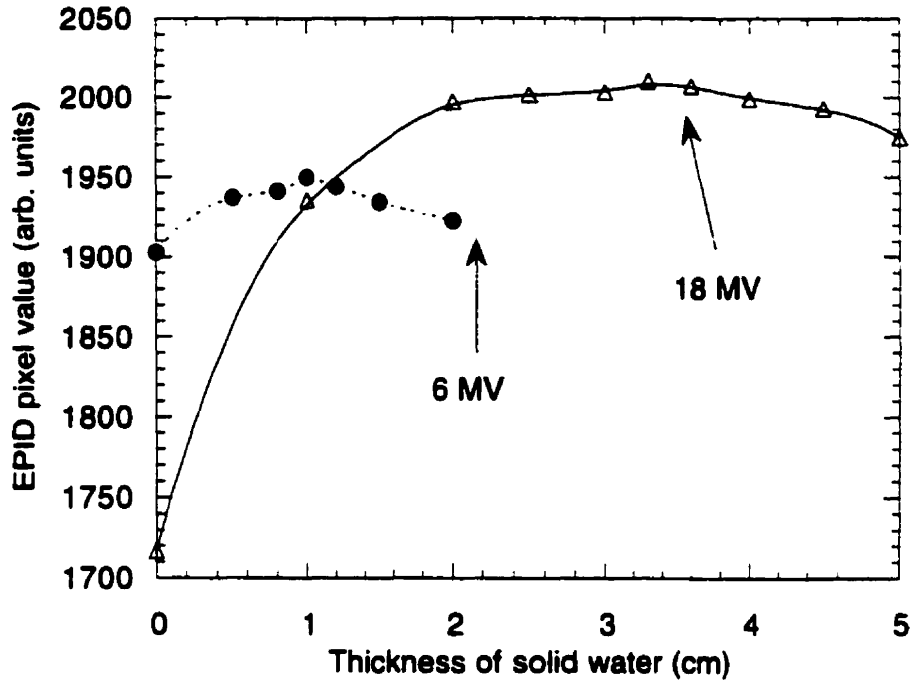


Figure 3.2. The EPID pixel value for a 10×10 cm² field at an SDD of 100 cm as a function of thickness of solid water placed on the imager surface for the 6 MV and 18 MV photon beams.

Backscatter is provided only by the lower printed circuit board, with a thickness of about 1 mm. However, photon and electron backscatter are relatively unimportant at megavoltage energies and we consider the minor correction for lack of backscatter to be included in the determination of the calibration curve of the EPID, discussed next.

B. Determination of the EPID characteristic curve

A characteristic curve relates the dose (or dose rate) received by a detector to the value of its output. The SLIC EPID is a differential dosimeter and thus we want to relate its pixel value to the incident dose rate. The dose rate at the IDU can be varied either by placing attenuators into the radiation beam or by varying the SDD of the IDU and causing the dose rate to fall off essentially according to the inverse-square law.

To determine a characteristic curve for the EPID with the attenuation method, various thicknesses of lead were placed on the upper accessory tray of the linear accelerator (distance of 58.5 cm from the X-ray source) to a maximum lead thickness of 61 mm. For each lead thickness, the average pixel value in the 9×9 ROI at the field centre was recorded. A field size of 10×10 cm² was used, centred on the IDU. In order to correlate the pixels values with the dose rate impinging on the IDU, the IDU was retracted and a calibrated Farmer chamber was positioned at the appropriate d_{max} depth in a solid water phantom with an SAD of 100 cm. The lateral dimensions of the solid water phantom were 30×30 cm², thus reproducing well the side-scatter conditions of the EPID¹⁶. The lead sheets were then removed in reverse order and the dose rates recorded.

Results are shown in Fig. 3.3 for the 6 MV and 18 MV photon beams (curves shown are not mathematical fits and are meant simply as an aid to the eye). For comparison, a characteristic curve measured at an SSD of 140 cm is also shown in Fig. 3.4. Other studies of the SLIC EPID calibration procedure have been published by Zhu¹⁷ and Yin¹⁸ and our results are similar to theirs.

To determine a characteristic curve for the EPID with the inverse-square law method, readings were taken with the EPID at various SDDs ranging from 105 cm to 180 cm. Again a field size of 10×10 cm² was used, centred on the IDU. In order to correlate the pixels values with the dose rate impinging on the IDU, the IDU was retracted and a calibrated Farmer chamber was positioned at depth d_{max} in a solid water phantom and readings were subsequently recorded at SADs ranging from 105 cm to 180 cm. Results of this experiment are shown and compared to results obtained with the lead attenuator method in Figs. 3.5 and 3.6.

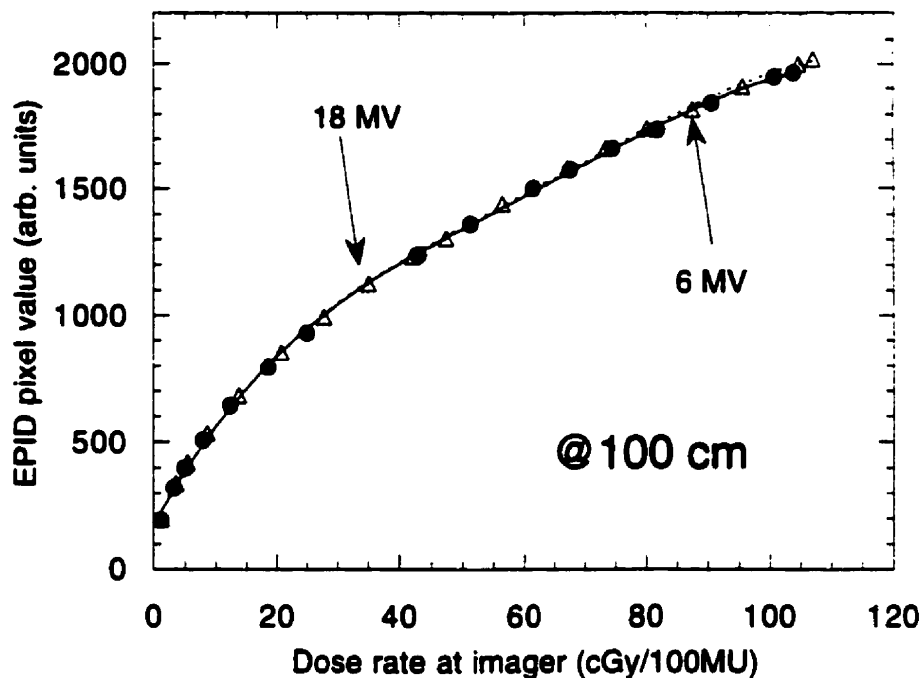


Figure 3.3. Characteristic curves for the EPID in the standard acquisition mode at an SDD of 100 cm for a field size of $10 \times 10 \text{ cm}^2$ at photon energies of 6 MV and 18 MV.

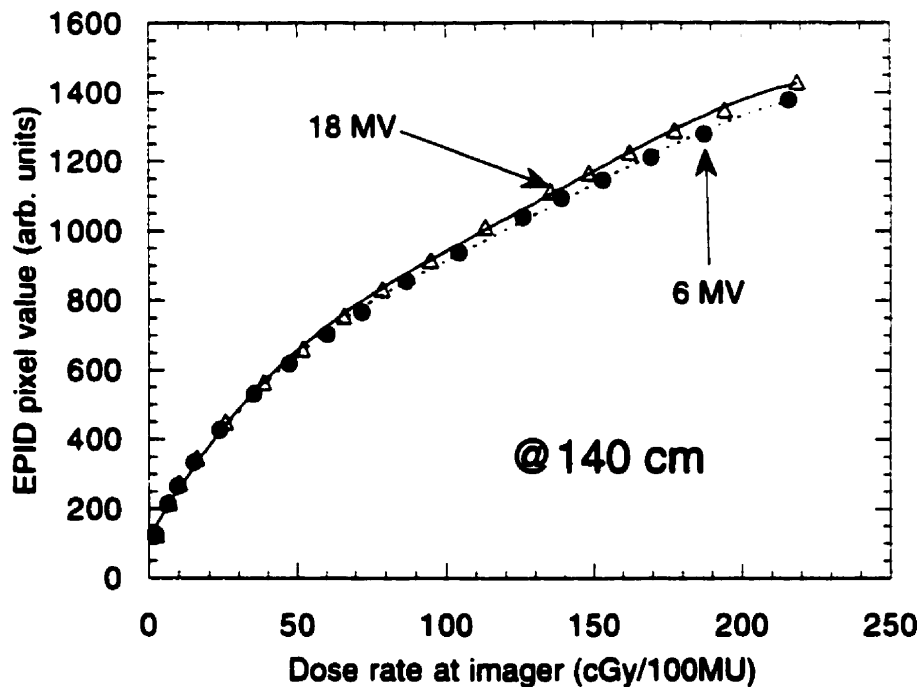


Figure 3.4. Characteristic curves for the EPID in standard acquisition mode at an SDD of 140 cm for a field size of $10 \times 10 \text{ cm}^2$ at photon energies of 6 MV and 18 MV.

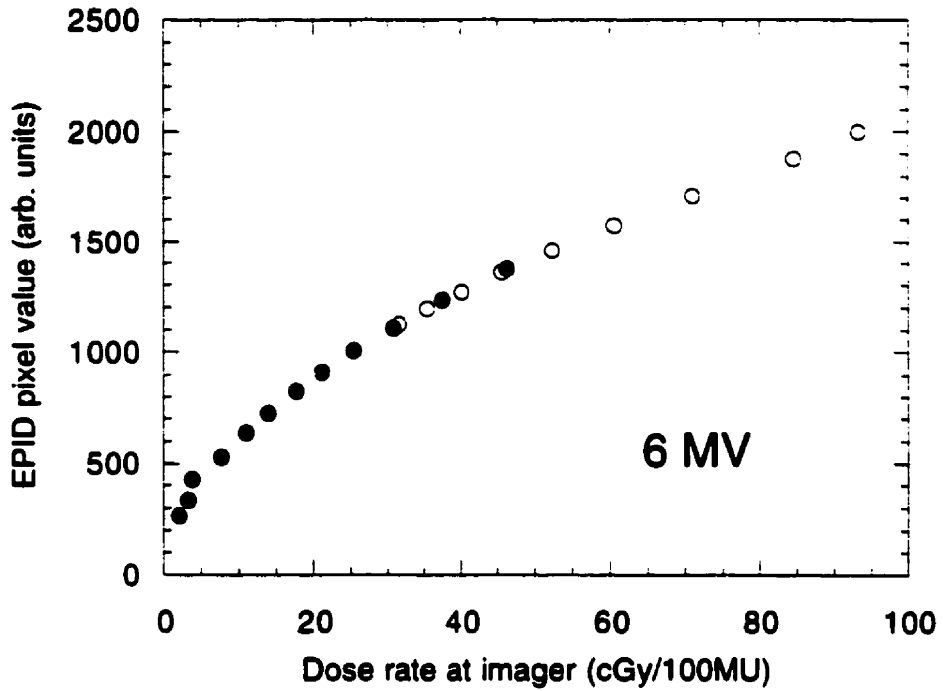


Figure 3.5. Characteristic curve for the IDU at 6 MV determined by varying the SDD (empty circles) compared to the characteristic curve obtained with the lead attenuators (solid circles).

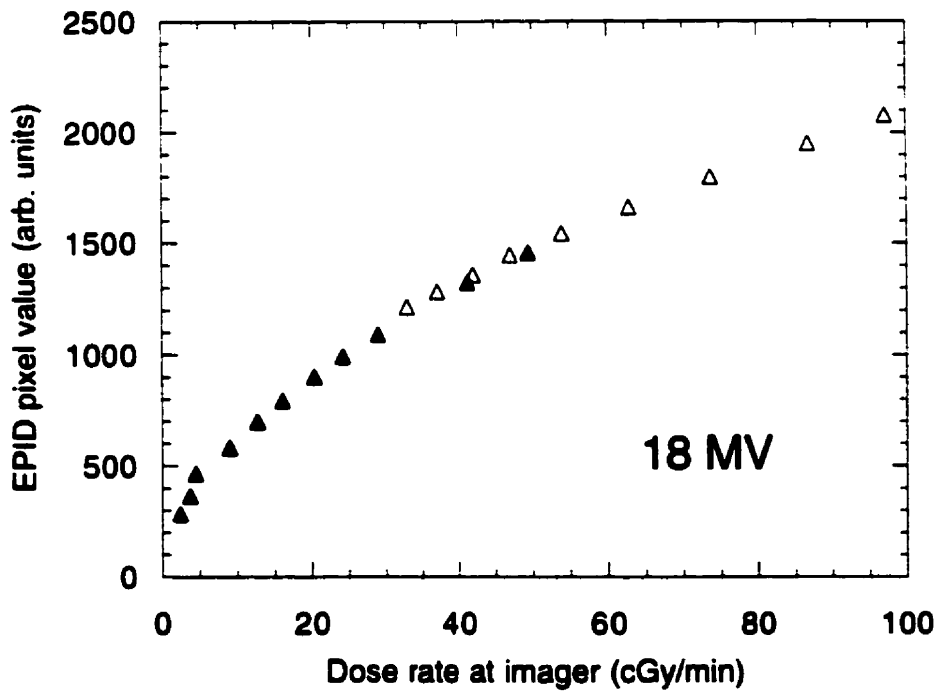


Figure 3.6. Characteristic curve for the IDU at 18 MV determined by varying the SDD (empty triangles) compared to the characteristic curve obtained with the lead attenuators (solid triangles).

Figures 3.5 and 3.6 show that the characteristic curves obtained by varying the SDD or by placing attenuators in the beam are equivalent. Furthermore, curves obtained with aluminum attenuators are identical to those obtained with lead attenuators, confirming our hypothesis that the response for the SLIC EPID is virtually energy-independent at the energies investigated. At lower energies, Boellard¹⁹ has demonstrated a significant effect of beam energy on the pixel response.

Because of various factors such as electrode shape differences, electrode surface inhomogeneities, and slight local variations in thickness of the iso-octane layer, the measured sensitivities of pixels of the IDU vary considerably for identical dose rates (up to 40%)²⁰. Since the design purpose of an EPID is to produce acceptable transmission images of patient anatomy and the radiation field limits, the response of each pixel must be adjusted in order to equalize their sensitivities, otherwise the images will be unnecessarily noisy. The simplest way to achieve this is to assume that an open beam emerging from the linear accelerator is completely uniform in intensity and then to adjust the software gain of each pixel such that the supposed uniform field yields an image with equal pixel values. This is the method Varian has adopted, and it is well-suited to imaging purposes. The manufacturer recommends that this equalization procedure be performed every two weeks, we have found that an interval of 1 month is sufficient.

However, an open field produced by a linear accelerator is *not* entirely uniform and its flatness also depends on the depth of measurement in phantom. For instance, with the Varian Clinac 2300 C/D at 6 MV there is approximately a 3% increase in the dose at points 5 cm laterally from the isocentre for measurements at a depth of d_{max} . At 18 MV, the corresponding figure is 2%. This increase in dose at d_{max} for off-axis points is referred to as the "beam horns" and is required if the dose profile is to meet the flatness specifications which are usually stated for a depth of 10 cm in a water phantom. Since

the pixel sensitivity equalization procedure adopted by Varian effectively removes the horns, they must be reinstated when measuring beam profiles with the EPID. This is achieved through a multiplication of pixel values by the appropriate off-axis ratios.

It is important to note that when performing EPID dose measurements backscatter is provided only by the lower printed circuit board (1.5 mm thick). This does not yield true in-phantom measurement conditions and lowers the recorded EPID signal by 1%-2% at megavoltage energies. However, the lack of photon and electron backscatter should be a relatively uniform percentage over the imager surface and we consider the small correction required to account for reduced backscatter to be included in the calibration curve of the EPID.

C. Reproducibility

The stability of the pixel calibration curve with time was investigated by acquiring an EPID image on a random basis (at an average interval of 2 weeks) over a period of 24 months and using the image to evaluate the dose rate of the linear accelerator. The dose rate as predicted by the EPID image was then compared to the dose rate as measured by a calibrated Farmer chamber. An agreement within $\pm 2.5\%$, one standard deviation, was found, which is slightly worse than the stability recorded by Zhu¹⁷ for the same model of EPID during a period of 2 months. Despite numerous efforts, the stability of our dose measurements obtained with the EPID could not be improved significantly; we thus conclude that the SLIC EPID is not suitable for routine output determination of a linear accelerator.

The precision of the robotic arm in positioning the liquid matrix was investigated over the same 24-month period. It was found to be better than ± 1 mm in all three dimensions.

D. Effect of field size on the characteristic curve

To determine the effect of field size on the characteristic curve, the pixel value of the IDU at the field centre was measured for square field sizes ranging from $3 \times 3 \text{ cm}^2$ to $20 \times 20 \text{ cm}^2$. These pixel values were then converted to dose rates using the characteristic curve measured above for the $10 \times 10 \text{ cm}^2$ field and normalized to the dose rate measured with a calibrated Farmer chamber for each of the field sizes. The data showed that the effect of field size on SLIC EPID response is negligible (within $\pm 1\%$), in accordance with the results of Zhu¹⁷.

E. Memory effect of the EPID at high image acquisition rates

It was suspected that the relatively low mobility²⁰⁻²² of the ions in the iso-octane of the IDU might translate into a very slow return of the imager to the pre-irradiation stable state and cause problems, particularly at very high dose rates or very high image acquisition rates. This implied that, for images acquired in rapid succession under identical conditions, the read-out EPID pixel values would increase steadily without saturation, resulting in significant errors.

To test the magnitude of this effect we acquired four series of images, each series consisting of 10 images obtained with a dose rate of 400 cGy/min and a given rest interval between successive irradiations. As in our other experiments, the mean pixel value in a 9×9 pixel matrix centered around the beam central axis was examined. In Fig. 3.7 we plot the mean pixel values of the region-of-interest as a function of the image index number (from 1 to 10) for four series with rest intervals of 6, 15, 30, and 60 seconds between successive irradiations. The mean pixel values are normalized to 100 for the first image acquired in each series. The shorter the rest interval, the steeper the error slope, amounting to $\sim 0.7\%$ per image for a 6 sec rest interval and essentially 0 for a 60 sec rest interval. Thus, at a dose rate of 400 cGy/min, a minimum rest interval of 60

sec is required to achieve reproducible results, and this equilibration time is approximately proportional to the dose rate at the imager plane (for example, the equilibration time decreases to only 15 seconds at a dose rate of 100 cGy/min).

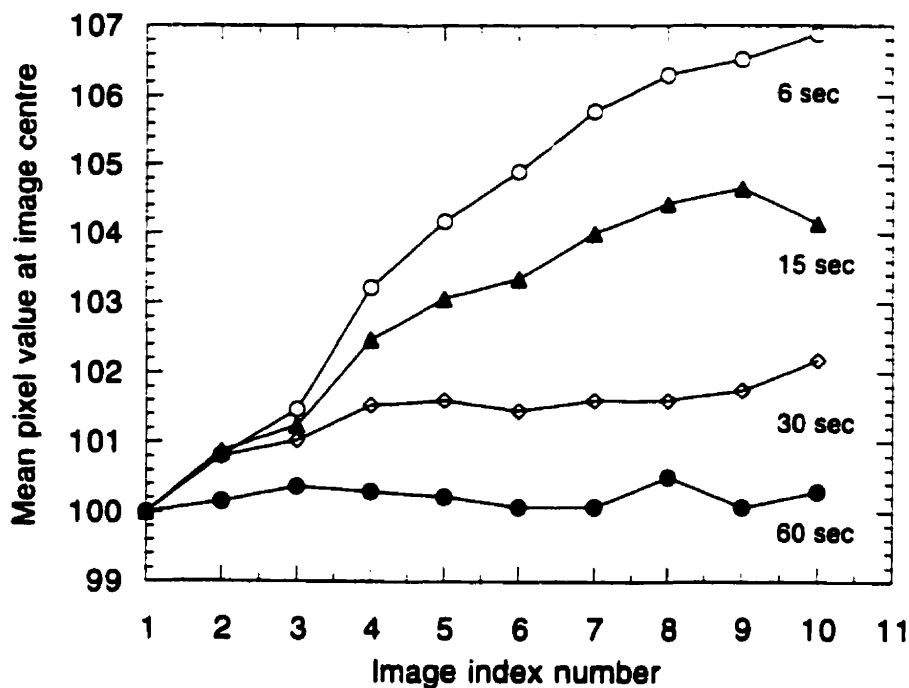


Figure 3.7. Centre pixel values for identical 6 MV EPID images taken at image acquisition intervals ranging from 6 s to 120 s.

3.6 BASIC DOSIMETRIC APPLICATIONS OF THE SLIC EPID

In order to illustrate the use of the EPID in basic dosimetric applications²³, four different measurement situations related to our subsequent work on beam intensity modulation were investigated and the results are presented below.

A. Multileaf collimator centrality

To verify that the centre of the multileaf collimator (MLC) field coincides with its axis of rotation, a narrow symmetric slit (width: 1 cm) is defined with the MLC and

irradiations are performed at collimator angles of 0° , 45° , 90° and 135° . Since the SLIC EPID is not an integrating dosimeter, a separate image must be acquired at each collimator angle. However, the resulting images may be summed numerically with standard image-processing software to yield the star-shot pattern shown in Fig. 3.8. The lines of symmetry for each of the four radiation slits can then be drawn on the star-shot image and their intersection examined very precisely with software magnification: the smaller the region of intersection, the better is the coincidence between the MLC axis of rotation and the MLC field centre. In this application, it is not necessary to convert pixel values to dose rates.

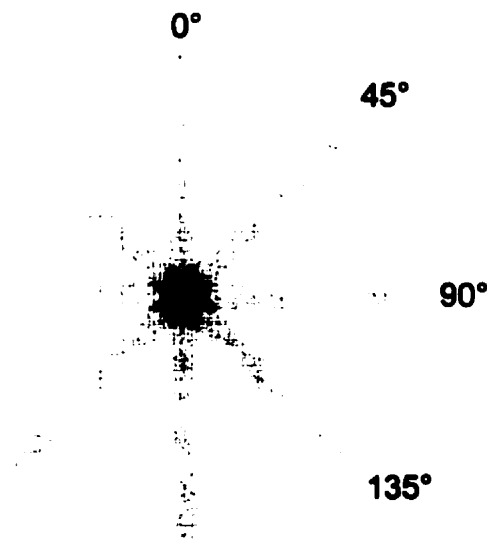


Figure 3.8 Star-shot irradiation pattern obtained from the summation of four uncalibrated EPID images of a narrow, symmetric, MLC-defined field at collimator angles of 0° , 45° , 90° and 135° .

From this example, it is easy to see how the EPID can also be used to verify the junction of abutting fields, the alignment of a halfblock, or the coincidence of radiation and light fields. In this last application, the light field measurements can be taken with respect to the crosshair and compared to the radiation field images in which the crosshair position has been recorded on the EPID images by placing a hexagonal nut at the crosshair position.

B. Multileaf collimator transmission

Measurement of MLC transmission is an application in which the EPID pixel values must be converted to dose rates in order to derive transmission values. In our experiment, an EPID image of the fully-closed multileaf collimator was acquired using the appropriate thickness of build-up material and converted to a dose rate image according to the 18 MV calibration curve for an SDD of 100 cm of Fig. 3.3. The calibrated dose rate image was analyzed numerically to obtain the transmission for the "interleaf" and "leaf end" regions, as well as for the "average" multileaf collimator transmission, as depicted in Fig. 3.9. Results are in close agreement with ionization chamber measurements. For comparison, at the photon energy of 18 MV, the average MLC transmission was measured to be 2.7% with the EPID and 2.5% with an ionization chamber.

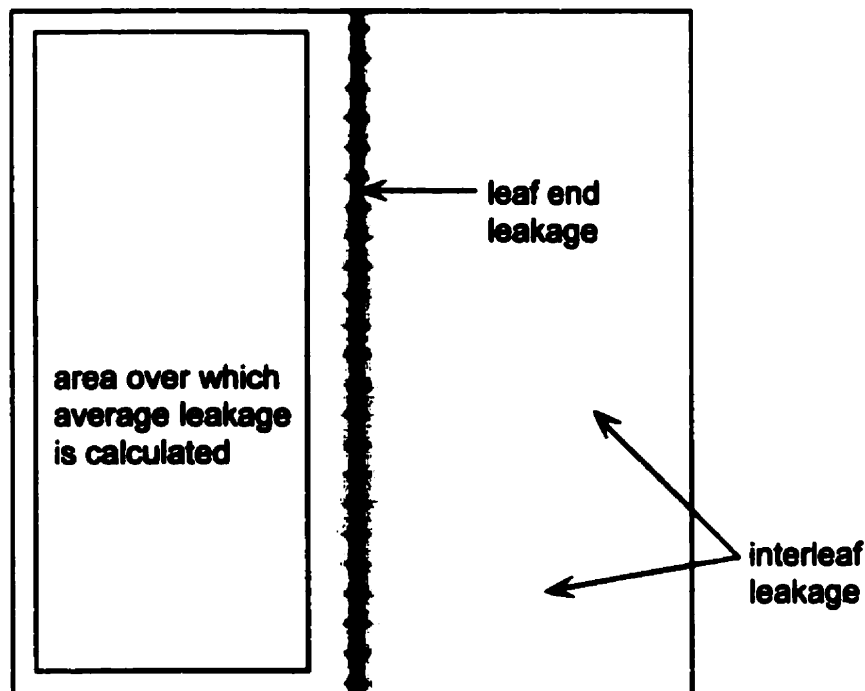


Figure 3.9. Calibrated EPID image of the transmission at 18 MV beam energy through a fully-closed MLC with illustration of the regions in which the "interleaf", "leaf end" and "average" transmission were calculated.

C. Penumbra width measurements

The EPID can also be used to measure beam penumbra. In our experiment, a 4×4 cm² MLC field was set and an EPID image acquired with the liquid matrix at an SDD of 100 cm and with an appropriate thickness of build-up material. The centre of the 4×4 cm² field was subsequently moved to numerous off-axis positions with images acquired at each of these new field positions. In this manner, the penumbra widths as a function of the field position were mapped out. The images were read into image-processing software which was instructed to superimpose the 10%, 20%, 80%, and 90% isodose lines onto the calibrated image. The images were then magnified and the 90%-10% and 80%-20% penumbral widths were measured on-screen with a ruler function. Results were in excellent agreement with film measurements. For example, at 6 MV we measured with the EPID the 80%-20% leaf-end penumbra at beam centreline to be 4.0 mm while film measurements gave 3.9 mm.

D. Compensator verification

As a final example, the EPID was used to verify the compensator calculation algorithm of our 3D CADPLAN treatment planning system. Several test phantoms, consisting of one or more inclined planes, were constructed and their contours were entered into the treatment planning system. For each phantom, a single-beam irradiation was planned which included a compensator designed to provide uniform dose at a specified depth. The compensators were then milled (by hand) according to the specifications determined by the treatment planning system.

For each phantom and compensator, four EPID images were acquired and converted to dose rate images. A profile at field centre was then extracted. The four profiles for one particular compensator test are shown in Fig. 3.10: profile (*a*) represents an image of the open beam with no phantom; profile (*b*) an image of the open beam with

the phantom in place; profile (c) an image of the compensated beam and no phantom; and profile (d) an image of the compensated field with the phantom in place. The field size for this compensator test was $10 \times 10 \text{ cm}^2$, beam energy 6 MV.

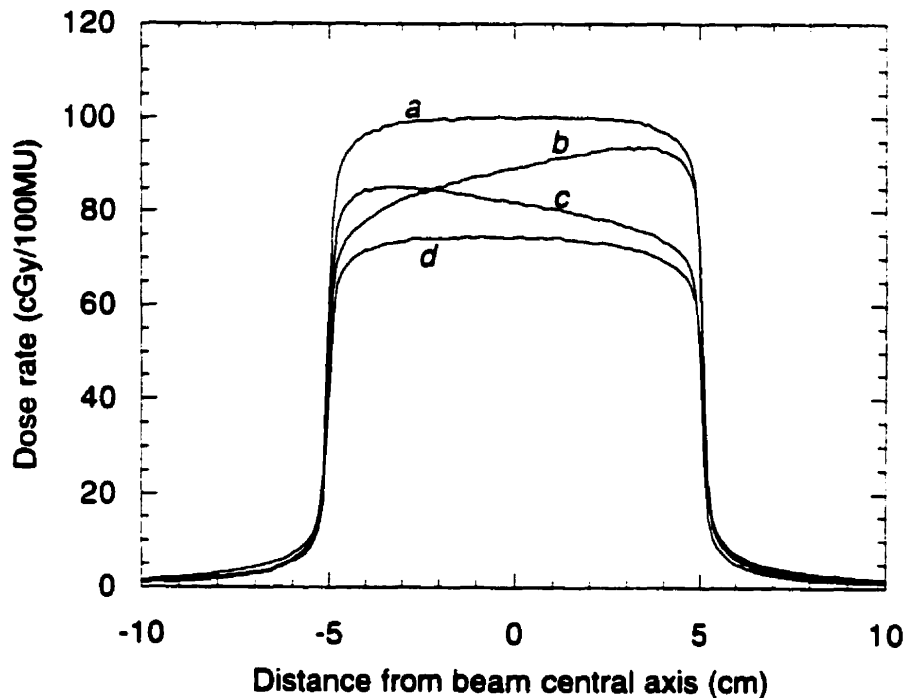


Figure 3.10. Four dose rate profiles used to test a compensator design algorithm. Profile (a) represents an image of the open beam with no phantom, profile (b) an image of the open beam with the phantom in place, profile (c) an image of the compensated beam and no phantom, and profile (d) an image of the compensated field with the phantom in place.

For a perfectly designed and manufactured compensator, profile (d) should resemble profile (a), except for an intensity scaling factor. The ratio of the dose rates on the central axis of the compensated field [profile (c)] vs open field [profile (a)] can also be used to verify the compensator transmission factor with a very good accuracy (0.820 with the EPID, compared to 0.826 measured with an ionization chamber).

3.7 USE OF THE SLIC EPID FOR THE VERIFICATION OF INTENSITY-MODULATED BEAMS

The measured data which will be acquired when the SLIC EPID is used for the verification of an intensity-modulated field consists of a series of EPID images, equal in number to the number of MLC subfields in the segmented treatment. A routine was written in the C-language to read-in the EPID image for subfield i , calibrate it according to the appropriate calibration curve, multiply the result by a weighting factor, and sum all calibrated image matrices $\mathbf{E}_{i,j}$ to produce a dose distribution \mathbf{D}_j for field j . The weighting factor used to multiply the images is the appropriate MU setting $MU_{i,j}$ corresponding to the given subfield, i.e.:

$$\mathbf{D}_j = \sum_i MU_{i,j} \mathbf{E}_{i,j} , \quad (3.3)$$

where \mathbf{E} is in units of cGy/MU and thus \mathbf{D} is in units of cGy. As described above, the calibrated image matrices \mathbf{E} are corrected by the appropriate off-axis ratio values. The dose distribution \mathbf{D} can then be compared to measurements performed with other dosimeters or to the predictions of a treatment planning computer. These comparisons are the subject of Chapter 6.

3.8 SUMMARY

This chapter has reviewed dosimeters currently used in photon beam radiotherapy and has provided a detailed description of the Varian electronic portal imaging device (EPID). Although this latter technology is relatively new, it has gained wide acceptance and an EPID is now almost a standard accessory on modern linear accelerators. A SLIC EPID combines the advantages of two-dimensional dose recording with excellent reproducibility, low dependence of response on radiation energy, and little expense

beyond the initial purchase. We therefore consider SLIC EPIDs to be the dosimeters of choice for the verification of intensity-modulated beams delivered in a step-and-shoot approach.

3.9 CHAPTER REFERENCES

1. Williamson JF, Khan FM, Sharma SC. *Film dosimetry of megavoltage photon beams: a practical method of isodensity-to-isodose curve conversion*. Med. Phys. **8**, 94-98 (1981).
2. Galvin JM, Smith AR, Moeller RD, Goodman RL, Powlis WD, Rubenstein J, Solin LJ, Michael B, Needham M, Huntzinger CJ, Kligerman MM. *Evaluation of multileaf collimator design for a photon beam*. Int. J. Radiat. Oncol. Biol. Phys. **23**, 789-801 (1992).
3. Gore JC, Yang YS, Schulz RJ. *Measurement of radiation dose distributions by NMR imaging*. Mag. Res. Im. **2**, 244-250 (1984).
4. Parker W. *Brachytherapy dosimetry with Fricke-gelatin and MRI*. M.Sc. thesis, McGill University, Montreal (1995).
5. Audet C. *NMR-dose response studies of gels used for 3-D MRI radiation dosimetry*. Ph.D. thesis, McGill University, Montreal (1996).
6. Maryanski MJ, Ibbott GS, Eastman P, Schulz RJ, Gore JC. *Radiation therapy dosimetry using magnetic resonance imaging of polymer gels*. Med. Phys. **23**, 699-705 (1996).
7. Ibbott GS, Maryanski MJ, Eastman P, Holcomb SD, Zhang Y, Avison RG, Sanders M, Gore JC. *Three-dimensional visualization and measurement of conformal dose distributions using magnetic resonance imaging of BANG polymer gel dosimeters*. Int. J. Radiat. Oncol. Biol. Phys. **38**, 1097-1103 (1997).

8. Maryanski MJ, Gore JC, Kennan RP, Schulz RJ. *NMR relaxation enhancement in gels polymerized and crosslinked by ionizing radiation: a new approach to 3D dosimetry by MRI*. *Mag. Res. Im.* **11**, 253-258 (1993).
9. Muench PJ, Meigooni AS, Nath R, McLaughlin WL. *Photon energy dependence of the sensitivity of radiochromic film and comparison with silver halide film and LiF TLDs used for brachytherapy dosimetry*. *Med. Phys.* **18**, 769-775 (1991).
10. Chiu-Tsao ST, de la Zerda A, Lin J, Ho Kim J. *High-sensitivity GafChromic film dosimetry for ¹²⁵I seed*. *Med. Phys.* **21**, 651-657 (1994).
11. McLaughlin WL, Soares CG, Sayeg JA, McCullough EC, Kline RW, Wu A, Maitz AH. *The use of a radiochromic detector for the determination of stereotactic radisurgery dose characteristics*. *Med. Phys.* **21**, 379-392, 1994.
12. Varian Oncology Systems. *Portal Vision v. 3.6 reference manual (I.D. #PV22RM)* (1995).
13. Meertens H, van Herk M, Weeda J. *A liquid ionization chamber for digital radiography of therapeutic megavoltage photon beams*. *Phys. Med. Biol.* **30**, 313-321 (1985).
14. Holroyd RA, Anderson DF. *The physics and chemistry of room-temperature liquid-filled ionization chambers*. *Nucl. Instr. and Meth.* **A236**, 294-299 (1985).
15. van Herk M. *Physical aspects of a liquid-filled ionization chamber with pulsed polarizing voltage*. *Med. Phys.* **18**, 692-702 (1991).
16. Essers M, Boellaard R, van Herk M, Lanson H, Mijnheer B. *Transmission dosimetry with a liquid-filled electronic portal imaging device*. *Int. J. Radiat. Oncol. Biol. Phys.* **34**, 931-941 (1996).
17. Zhu YZ, Jiang XQ, van Dyke J. *Portal dosimetry using a liquid ion chamber: dose response studies*. *Med. Phys.* **22**, 1101-1106 (1995).
18. Yin FF, Schell MC, Rubin P. *Input/output characteristics of a matrix ion-chamber electronic portal imaging device*. *Med. Phys.* **21**, 1447-1454 (1994).

19. Boellaard R, van Herk M, Mijnheer BJ. *The dose response relationship of a liquid-filled electronic portal imaging device.* Med. Phys. **23**, 1601-1611 (1996).
20. Essers M, Hoogervorst BR, van Herk M, Lanson H, Mijnheer BJ. *Dosimetric characteristics of a liquid-filled electronic portal imaging device.* Int. J. Radiat. Oncol. Biol. Phys. **33**, 1265-1272 (1995).
21. Boyer AL, Antonuk L, Fenster A, van Herk M, Meertens H, Munro P, Reinstein LE, Wong J. *A review of electronic portal imaging devices.* Med. Phys. **19**, 1-16 (1992).
22. Anderson DF, Holroyd RA. *High rate operation of warm-liquid ionization chambers.* Nucl. Instr. and Meth. **A260**, 343-345 (1987).
23. Curtin-Savard AJ, Podgorsak EB. *An electronic portal imaging device as a physics tool.* Med. Dos. **22**, 101-105 (1997).

4

Characterization of the Varian multileaf collimator

Section:

4.1	Introduction.....	77
4.2	Description of the Varian multileaf collimator.....	77
4.3	Use of a multileaf collimator as a replacement for conventional blocks	81
4.4	Multileaf collimator metrics	83
4.5	Leaf positioning for treatment	86
4.6	Leaf positioning tests.....	89
4.7	Dosimetric measurements of the MLC.....	97
4.8	Influence of the MLC on beam output	104
4.9	Summary.....	118
4.10	References.....	119

4.1 INTRODUCTION

This chapter describes in detail the Varian multileaf collimator (MLC) which was used in our experiments to deliver the intensity-modulated photon beams. Also presented and discussed are experiments which characterize the MLC in terms of its alignment, accuracy of leaf positioning, radiation penumbra, radiation transmission, and effect on machine output.

4.2 DESCRIPTION OF THE VARIAN MULTILEAF COLLIMATOR

Presently, there are five commercial manufacturers of MLCs: General Electric Medical Systems, Philips Medical Systems, Scanditronix, Siemens Medical Systems, and Varian Oncology Systems. The basic designs of all commercially-available MLCs are similar; however, the MLCs of these companies differ in characteristics such as the total

number of leaves, the leaf width, the shape of the leaf ends, and whether or not the leaves move perpendicularly to the beam central axis or along an arc focused at the source of radiation. The MLC installed on our Clinac 2300 C/D linear accelerator is the one manufactured by Varian as an attachment to the standard Clinac-2300 C/D and will be described in detail below. Some companies offer their MLCs as an attachment to a standard linear accelerator, others offer them as a replacement of the lower jaws in a standard linear accelerator. Attachment models are more practical because the linac may be used for standard radiotherapy during MLC malfunctions.

A. Physical characteristics of the leaves

Figure 4.1 shows an end view and a side view of an individual leaf of the Varian MLC. The leaves are machined from solid tungsten to the dimensions shown in the figure. The "tongue and groove" construction of the leaf sides reduces radiation leakage between leaves. In our particular MLC model all leaves are identical on a given side, but with minor differences between sides. There are a total of 52 leaves in all: 26 on the side of the Y1 collimator (these are referred to as the "A" leaves) and 26 on the side of the Y2 collimator (the "B" leaves). The horizontal midline of the leaves is positioned at exactly 49.9 cm from the radiation source (x-ray target), providing an effective leaf size at the isocentre of 1.00 cm.

The leaves are slightly wider at their base than at their apex resulting in focusing in the direction perpendicular to the direction of the leaf motion. The leaves are not focused in the direction parallel to the leaf motion, since focusing of the leaves along this axis would require that the leaves travel on an arc, complicating the construction of the MLC and requiring more room in the head of the linear accelerator, thus reducing clearance around the patient couch. However, linear translation of the leaves will result in important variations in beam penumbra with leaf position. To minimize this, the leaf

ends are given a rounded profile. As demonstrated by a number of investigators¹⁻⁴, the rounded leaf ends preserve a roughly constant penumbra for all leaf positions by improving the penumbra at large off-axis positions and degrading it near beam centreline. Our experimental data presented in Section 4.8 confirms this statement.

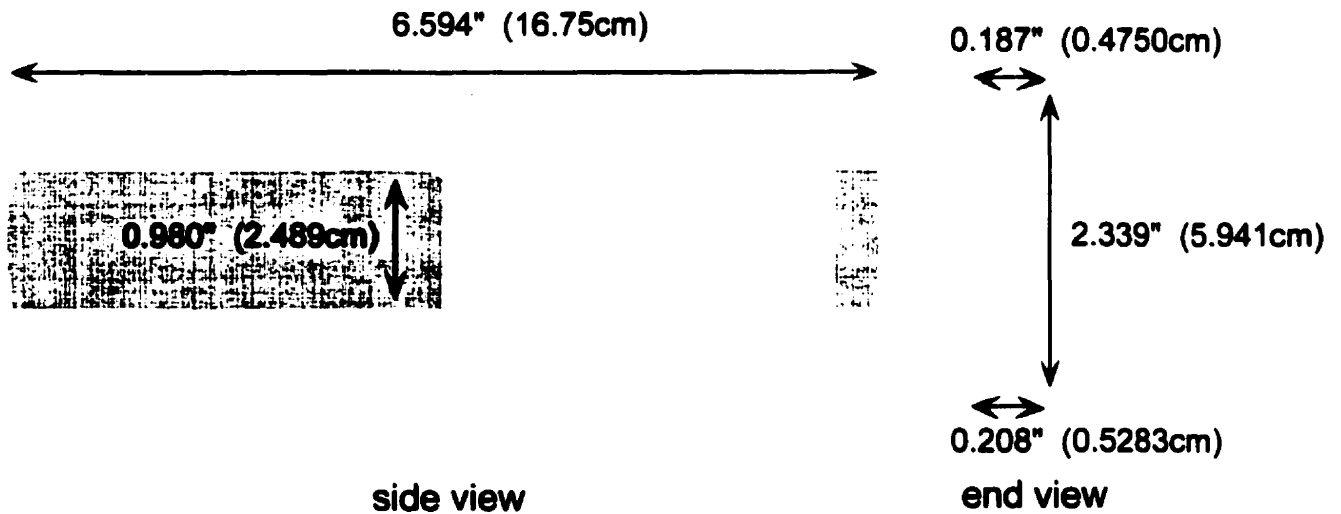


Figure 4.1. Dimensions of a Varian MLC leaf from the "A" bank of leaves.

B. Range of leaf motion

The leaves rest in a movable carriage, and the leaves on either side of the carriage can be moved either as a group by carriage motors A or B, or individually by individual leaf motors. The combination of these two motions allows the leaves to be positioned anywhere from +20 cm (fully retracted from the beam) to -16 cm (16 cm over beam centreline). However, due to the relatively short leaf length, no two leaves on the same carriage may differ in position by more than 14.5 cm; otherwise a void is created behind the most extended leaf allowing radiation to pass through. The maximum field size for an MLC-blocked field is 40×26 cm² which is sufficient to treat the overwhelming majority of target volumes which present themselves in radiation therapy^{1,5}. Note that

the MLC leaves move parallel to the X jaws regardless of the orientation of the collimator.

When the MLC is used dynamically for intensity-modulation, the present version of Varian's leaf control software does not allow carriage motion during the treatment. This implies that the maximum difference between leaf positions for leaves on the same side is 14.5 cm during the entire treatment, i.e., for all the subfields it contains.

C. Monitoring of leaf positions

The leaves are moved individually by high precision stepping motors. The accuracy of their positioning is assured by two feedback systems.

The primary position feedback mechanism involves an optical calibration, which takes place each time the accelerator is switched from a standby to ready mode. Precisely at beam centreline, and at the level of the MLC leaves, a light beam from an LED is shone through a thin slit towards a photodiode located on the opposite side. Optical calibration is achieved by slowly "touching" each leaf in turn to the light beam and noting the stepping motor count. Throughout the day, the position of a leaf is known from the number of motor counts relative to the position of the light beam. The quadrature phase encoders divide each millimetre of leaf travel at isocentre level into 598 parts (540 parts for the carriage encoders), and are thus extremely accurate. However, lack of mechanical tightness or a faulty motor can destroy the one-to-one correspondence between motor count and leaf position. Therefore secondary feed-back systems of lower accuracy have been implemented for both the leaf positions and carriage positions.

The secondary feed-back system for the leaf position relies on two strips of electric pads located on top of each leaf. Two brushes, one on each side of the leaf,

complete a different circuit depending on leaf position. This provides a positional reading which can be compared to the readings from the optical system. This secondary feed-back system has a resolution of approximately 1 mm at isocentre. The secondary feedback system for the carriage position consists of a translucent strip onto which equally-spaced parallel opaque bars (five bars per mm) have been imprinted. This strip is attached to the carriage and intercepts an optical detection system composed of an infrared LED and a photodiode. The number of dips in the photodiode signal provides an accurate record of the two carriage positions.

D. Computer interface

The signals sent to the motors, and the feedback signals received from the leaves and carriage are handled by an IBM 486 computer equipped with dedicated interface cards. Another IBM 486 computer serves as a user interface, and contains high-level software in a Windows environment for setting the desired leaf positions. A third IBM 486 computer is home to a program called an MLC Shaper, also in a Windows environment, which is used for automatically setting the leaf positions to shield the region around a given PTV. Once the leaf positions are determined by the Shaper, a data file is written to disk which can be physically brought to the MLC workstation or sent through the network. However, the Shaper is useful only for MLC blocking; an in-house developed program described in Chapter 5 is used to write the necessary computer files for MLC intensity-modulated treatments.

4.3 USE OF A MULTILEAF COLLIMATOR AS A REPLACEMENT FOR CONVENTIONAL BLOCKS

In addition to its use in intensity-modulation of photon beams, the MLC also serves the elementary purpose of providing beam blocking for tissues surrounding the PTV. It is thus important to investigate not only whether the MLC is well-suited for

beam intensity-modulation but also whether it can adequately be used as a replacement for conventional focused blocks, which traditionally are used to provide optimum shielding around the PTV.

Concerning the penumbra produced by the MLC, at first glance the projected 1 cm leaf width of the MLC, the rounded leaf ends, and the scalloping, or step-like appearance of the MLC-defined apertures would appear to provide lesser conformity to the intended target than focused blocks. However, studies^{1,2,6-8} have shown that when one considers how the molding, mounting and alignment processes affect the accuracy of apertures generated by custom blocks, and particularly the effect of daily set-up variations^{7,9,10}, the penumbræ of both the MLC and focused blocks are almost identical. For both shielding devices, the high-dose region conforms equally well to the intended target resulting in TCP and NTCP values which are essentially indistinguishable. Section 4.8 compares measured penumbral values for MLC and focused cerrobend blocks.

Section 4.7 will show that although the leakage between leaves can reach 4%, the average transmission for the MLC is significantly less than for cerrobend blocks. Section 4.10 will show that, at least for the Varian MLC, the effect of aperture size of machine output can be described in the same manner that has traditionally been used for fields shielded with blocks.

Finally, concerning ease of use, several studies¹¹⁻¹³ have shown that the use of MLCs results in a substantial reduction of in-room time for the technologists, allowing either more fields to be treated per day for each patient, or greater patient throughput. The use of an MLC eliminates the manufacturing of shielding blocks and the associated exposure of hospital workers to toxic fumes released during the manufacturing of these shielding blocks. Furthermore, the blocks are quite heavy and must be transported from

the mold room to the treatment unit and lifted into the accessory tray for each treatment. The electronic nature of the MLC files obviates this manipulation and also permits rapid modifications of a field aperture, while for blocks, any modification generally requires recasting.

4.4 MULTILEAF COLLIMATOR METRICS

Before proceeding to an investigation of the dosimetric attributes of the Varian MLC, we first examine a number of its geometric properties. These are: (A) agreement between the MLC axis of rotation and the field crosshairs; (B) agreement between the MLC centre and the field crosshairs; (C) the size of an individual leaf projected to isocentre; and (D) verification that the direction of leaf travel is parallel to the edge of the Y jaws.

A. Agreement between MLC axis of rotation and field crosshairs

To verify that the axis of rotation matches the field cross hair, the conventional star-shot pattern¹⁴ may be employed. To produce a star pattern, a narrow slit ($1 \times 20 \text{ cm}^2$) was defined with the MLC and irradiations were carried out at collimator angles of 0° , 45° , 90° , and 135° with the EPID as measuring device at an extended SSD of 140 cm to increase magnification. A hexagonal nut was placed on the EPID detector surface to record the position of the field crosshairs. The resulting EPID images for each collimator angle are then summed numerically to yield a combined image as shown in Fig. 4.2.

Image processing software was used to precisely position a bisector line at the centre of each irradiated slit. Software magnification of the region in Fig. 4.2 in which the bisectors meet, shows that the radiation isocentre is stable with collimator angle to within 0.3 mm and agrees with the crosshairs to within 0.1 mm. The uncertainty on this determination was estimated to be about $\pm 0.5 \text{ mm}$.

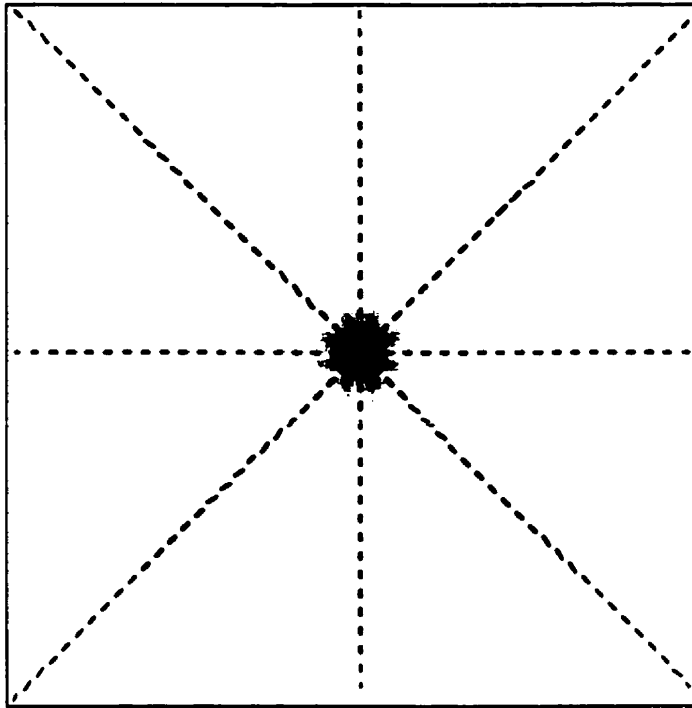


Figure 4.2. Star-shot test pattern used to establish coincidence between the MLC axis of rotation and the field crosshairs.

B. Agreement between the MLC centre and the field crosshairs

The leaves were configured in the pattern shown in Fig. 4.3 to examine three other geometric attributes of the MLC. The hatched square indicates the radiation field as defined by the upper and lower jaws; blocking within the field (white areas) results from selected leaves of the MLC being closed to midline. A small hexagonal nut was placed on the EPID at the position of the crosshairs to record its position.

By drawing a line A through the centres of the leaf ends and another perpendicular line B through the centres of the four closed leaves and comparing their intersection to the position of the nut, we can determine agreement between the crosshairs and the centre of the MLC. For the example shown in Fig. 4.3 we determined agreement to within 0.11 mm. From the conclusion of the previous test described in

Section 4.4(A), we can now also conclude that the centre of the MLC coincides with its axis of rotation.

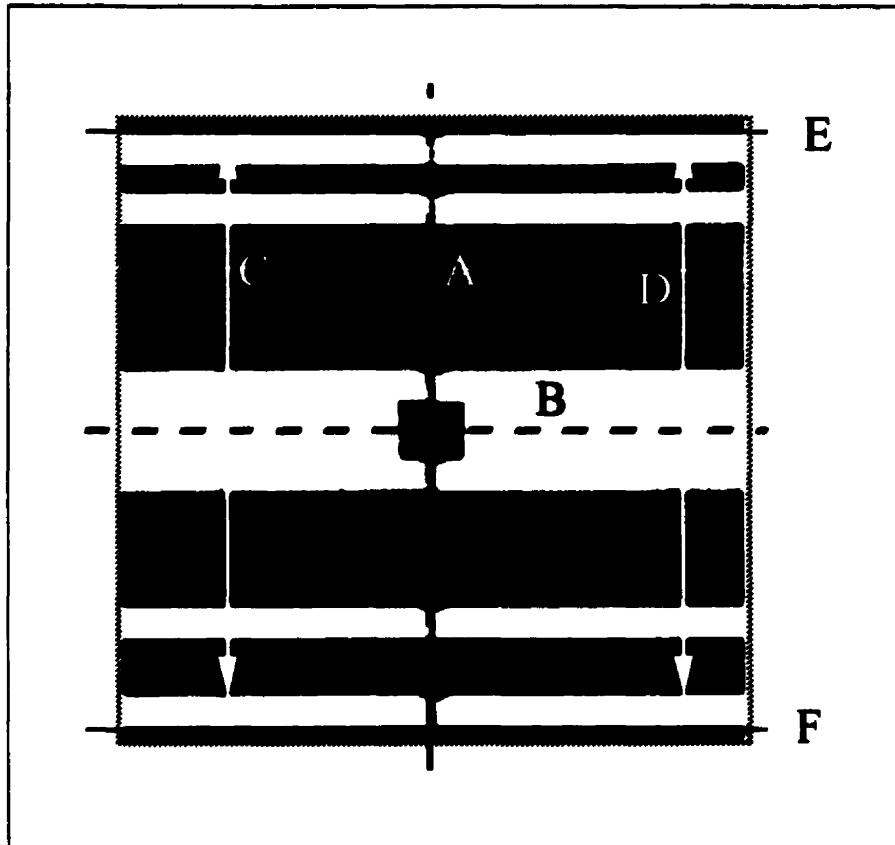


Figure 4.3. The MLC test configuration used to verify some MLC dimensions.

C. Size of an individual leaf projected at isocentre

The size of an individual leaf at isocentre may be determined from the length of the lines denoted C or D in Fig. 4.3 and adjusting for the magnification of the image. Lines C and D are drawn from the inside of one leaf pair to the outside of another pair in order to compensate for beam penumbra. We measure the leaf width at isocentre to be 1.007 cm, averaged over 20 leaves.

D. Measure of parallelness between the direction of leaf motion and Y jaws

The lines in Fig. 4.3 denoted by E and F are drawn upon a line of constant pixel value and show the direction of leaf motion. These lines can be compared to the hatched lines drawn for the jaw positions to verify that the MLC leaves travel parallel to the Y jaws. Here we determine that the MLC leaves are parallel to the Y collimator jaws to within 0.16° .

4.5 LEAF POSITIONING FOR TREATMENT

A. Leaf-tip positioning conventions

The tip of the MLC leaves can abutt with the contour of the PTV in a number of different ways, the most common of which are illustrated in Fig. 4.4. In the *in-bound* coverage, the entire width of the tip is inserted into the PTV. This maximally spares the surrounding tissues, but partially shields the target. In the *out-bound* coverage, the entire width of the leaf tip remains exterior to the PTV. The high-dose region now completely encompasses the PTV, but also extends into the healthy tissues. In the *cross-bound* coverage, the leaf tips intersect the contour of the PTV in some manner. Several types of cross-bound coverage have been proposed such as the *equal area* approach^{6,15}, the *chamfer* approach¹⁶ and the *midleaf* approach. Since the contour of the PTV is generally smooth and varies slowly, these cross-bound approaches all lead, approximately, to the same dosimetric result as if the centre of the leaf tip is set to intersect with the PTV contour (*mid-leaf* coverage). This last approach is the one that is used in our clinic when the MLC is employed for field blocking and will continue to be used for the dynamic use of the MLC. It works well, with a notable exception, as illustrated in Fig. 4.4. In this case, the equal area approach is superior.

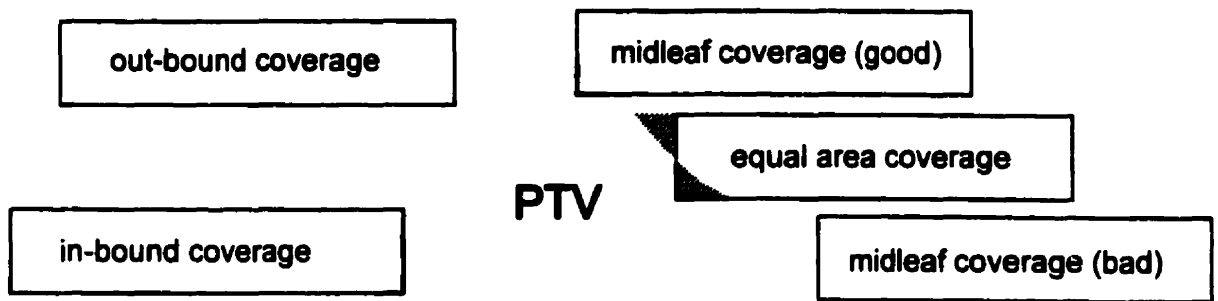


Figure 4.4. Illustration of various methods of conforming the MLC leaves to an arbitrary planning target volume.

B. Collimator orientation

Proper collimator rotation can help to optimize conformity of the high-dose region with the PTV. As demonstrated by Brahme^{15,17}, the trick is simply to use as many leaf pairs as possible to define the MLC aperture. This implies that the collimator should be rotated such that the MLC leaves travel at right angles to the largest dimension of the particular BEV of the PTV. This ideal situation is depicted in Fig. 4.5(a) and contrasted to the case in which the leaves travel parallel to the greatest dimension of the PTV in Fig. 4.5(b). This convention on collimator rotation will guarantee higher conformity for the first MLC segment in an intensity-modulated field, which generally delivers upwards of 80% of the dose for that field. It will also aid in delivering the spatial dose gradient (which is delivered with the other segments) since the 1 cm leaf width at the isocentre is the limiting factor in achieving the desired dose profile and using more leaves will allow greater spatial precision in dose delivery. An exception to the general rule for choice of collimator angle arises when a particular orientation is required to accurately shield a critical structure such as the spinal cord.

C. Jaw positions accompanying MLC-defined blocking

When the MLC is used for blocking, the X (upper) and Y (lower) jaws are positioned to form a bounding rectangle around the MLC aperture so as to minimize the transmission dose to the patient. These positions are also illustrated in Fig. 4.5. When the MLC is used for dynamic delivery, we employ the same convention for the jaw positions for the first subfield, and keep the jaws stationary in this position during the entire intensity-modulated treatment.

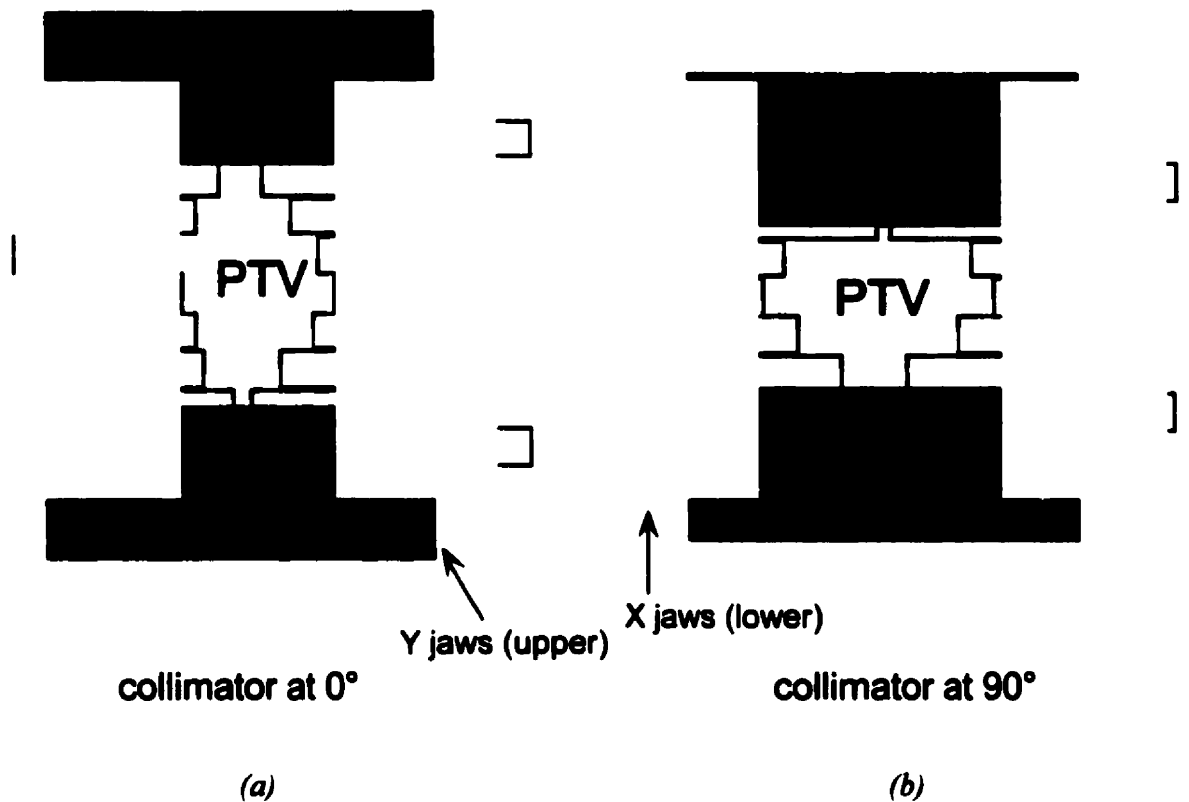


Figure 4.5. Illustration of how the choice of collimator orientation can affect the MLC coverage of the planning target volume. In (a) the ideal collimator angle, and in (b) the worst collimator angle for this PTV.

4.6 LEAF POSITIONING TESTS

Tests were performed to verify the precision (i.e., reproducibility) and also the accuracy of leaf positioning. These tests were: (A) verification of the positional reproducibility of individual leaves; (B) verification of the positional agreement of all leaves at a number of field positions; (C) measurement of the radiation-field position of one leaf compared to its digital readout; and (D) measurement of the light-field position of one leaf compared to its digital readout.

A. Positional reproducibility of individual leaves

The positional reproducibility of two leaves (leaves 12A and 17B) was measured at a gantry angle of 0° by taping a piece of graph paper to the treatment room floor at an extended SSD of 207 cm and recording the position of the leaf as measured by the light field. The positional reproducibility was better than 0.2 mm (at 100 cm) in situations where the leaf was starting from an open or closed position and situations in which the leaf was or was not extended beyond beam centreline.

The same exercise was undertaken at a gantry angle of 90° , but now the SSD was 390 cm since the graph paper could be taped to the wall of the treatment room. This allowed even greater discrimination of leaf position and allowed us to conclude that the positional reproducibility is better than 0.18 mm in situations where the leaf was starting from an open or closed position and situations in which the leaf was or was not extended beyond beam centreline. This result seems more impressive on noting that this second test was performed with the leaves oriented vertically, i.e., subjected to the influence of gravity.

B. Agreement between all leaves at a number of positions

Verification of the positional agreement of all leaves when driven as a group to the same location was accomplished by producing the irradiation pattern of Fig. 4.6(a).

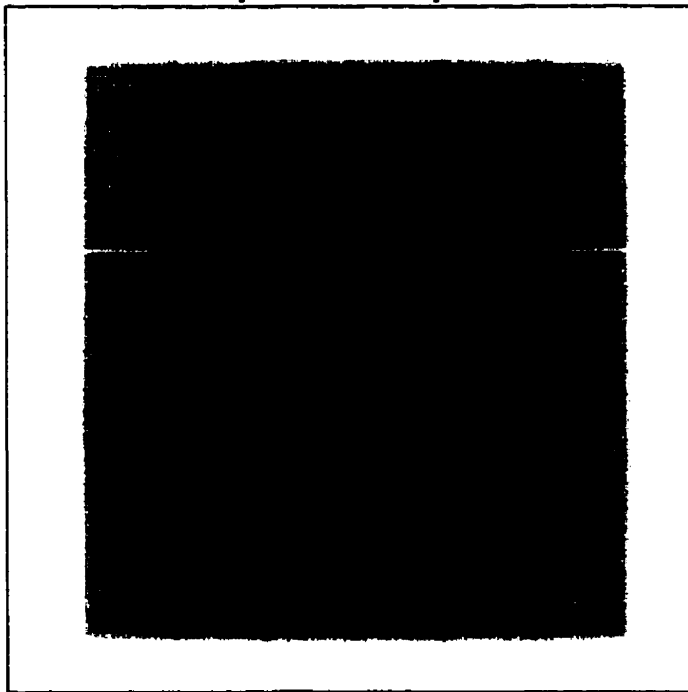
The pattern was produced by irradiating the EPID with the six MLC-defined "slits" depicted in Fig. 4.6(b) and summing the images numerically. Subsequent windowing of the cumulative image leads to Fig. 4.6(a) which shows with great detail those regions where the penumbras of the six fields overlap and provides a very sensitive measure of the agreement of leaf position. This type of test pattern can easily detect submillimetre errors in the positioning of the leaves¹⁸.

C. Radiation-field versus digital read-out

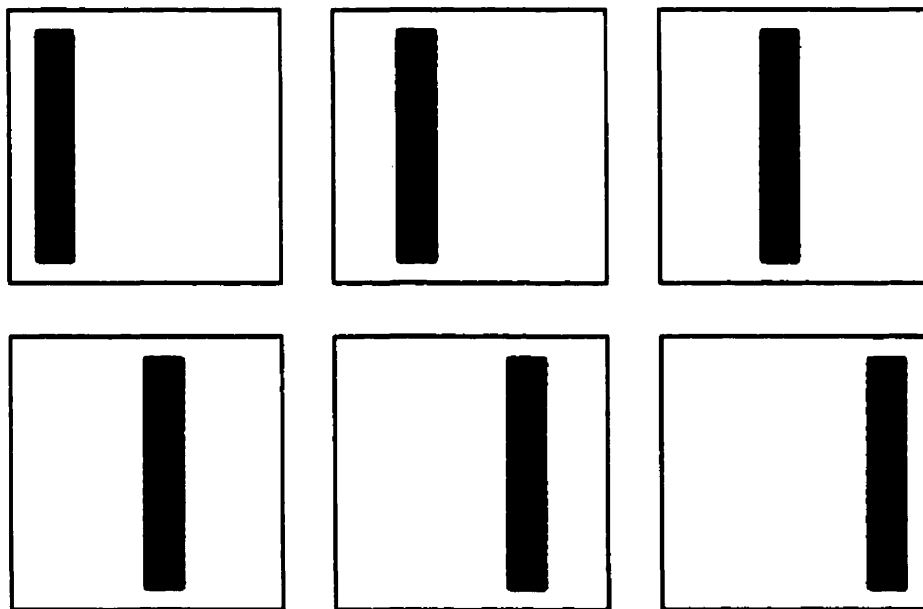
The agreement between the radiation-field position for both the MLC leaf ends and leaf sides with the readout was verified using the EPID. The surface of the detector was placed at a distance of 100 cm from the source and images were acquired for various positions of the leaf ends which were swept across the field as a group. A sufficient thickness of solid water was placed on the detector to obtain electronic equilibrium at the position of the EPID sensitive volume (cf. Section 3.5). The position of the isocentre was recorded on the images by placing a hexagonal nut at the location of the laser crosshairs.

The EPID images were first calibrated and then image processing software was used to trace the 50%, 60%, 70%, and 80% isodose lines on the images. For linear accelerator jaws, the readout position generally corresponds to the position of the 50% isodose line, but this is not necessarily the case for the MLC leaves. The leaf end data from this experiment is shown in Figs. 4.7 and 4.8 at both the 6 MV and 18 MV photon energies, respectively. Figure 4.9 depicts the data for the leaf sides. The ordinate in Figs. 4.7 through 4.9, entitled "positional difference", is obtained by subtracting the readout position from the measured position of the particular isodose line.

energies, respectively. Figure 4.9 depicts the data for the leaf sides. The ordinate in Figs. 4.7 through 4.9, entitled "positional difference", is obtained by subtracting the readout position from the measured position of the particular isodose line.



(a)



(b)

Figures 4.7 and 4.8 show that the 50% line is separated by approximately 1.0 mm and 1.5 mm from the readout position of the MLC leaf ends for the 6 MV beam and the 18 MV beam, respectively. In both figures, it is the 70% isodose line which essentially corresponds to the readout position. Using film and an MLC identical to ours, Galvin¹⁹ determined that it is the 61% isodose line which corresponds to the readout at the 6 MV and 15 MV photon energies; given the experimental uncertainties, his conclusion agrees with ours.

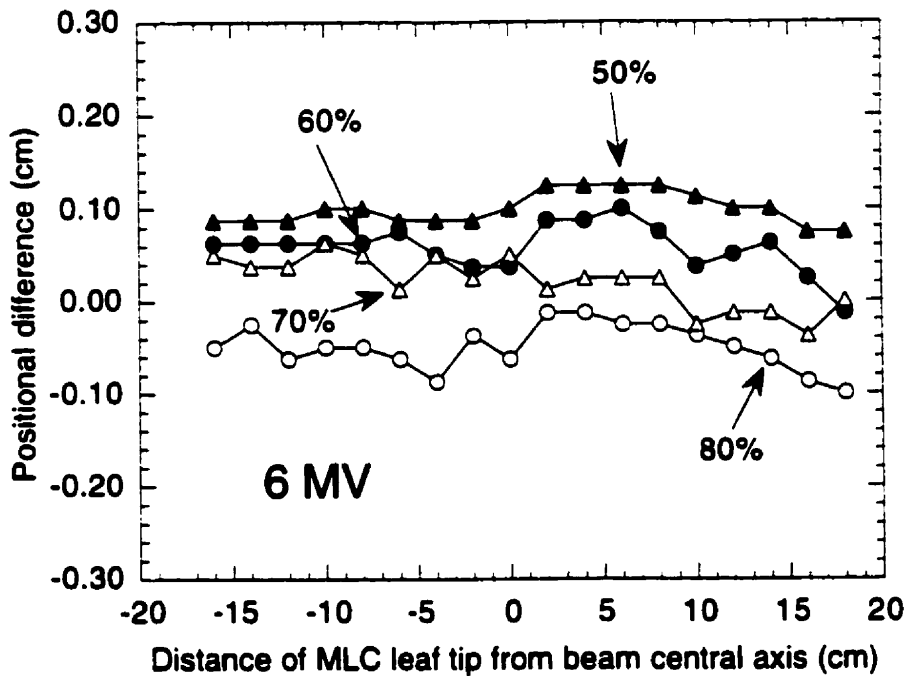


Figure 4.7. Position of the 50%, 60%, 70%, and 80% isodose lines at 6 MV photon energy as a function of the readout position of the leaf ends.

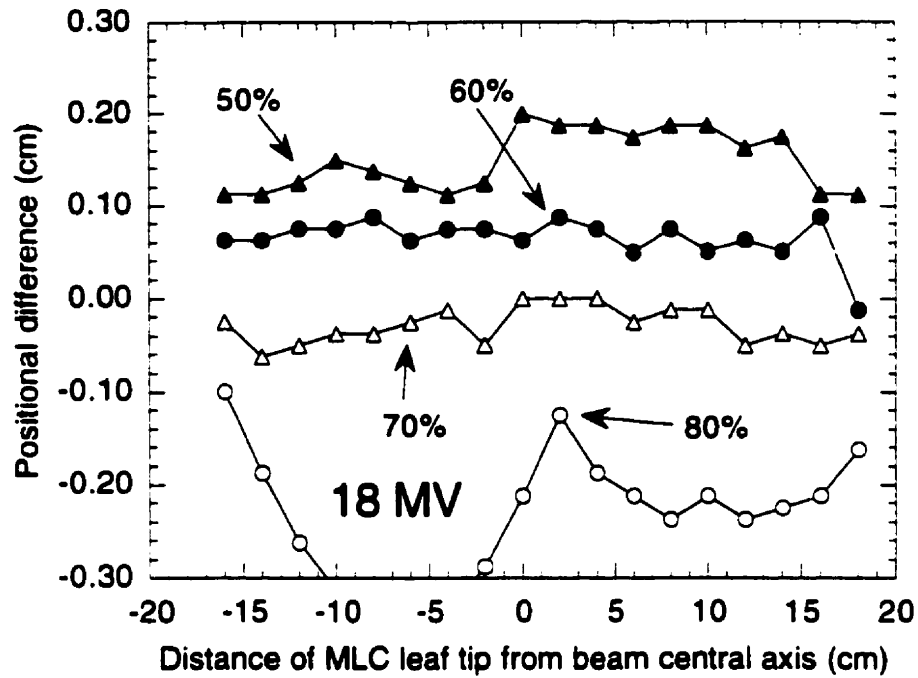


Figure 4.8. Position of the 50%, 60%, 70%, and 80% isodose lines at 18 MV photon energy as a function of the readout position of the leaf ends.

As can be observed from Fig. 4.9, the 50% isodose line for the leaf sides agrees fairly well with the readout for both the 6 MV and 18 MV photon beam energies. However, it is still approximately 0.5 mm in error for both beam energies. The 60% line, on the other hand, is also approximately 0.5 mm in error, but in the opposite direction. We can thus conclude that the 55% isodose line of the leaf sides corresponds to the readout, which is in agreement with the results obtained by Galvin¹⁹. We suspect that this is a slight design error on the part of the manufacturer since one generally tries to match the readout with the 50% isodose line.

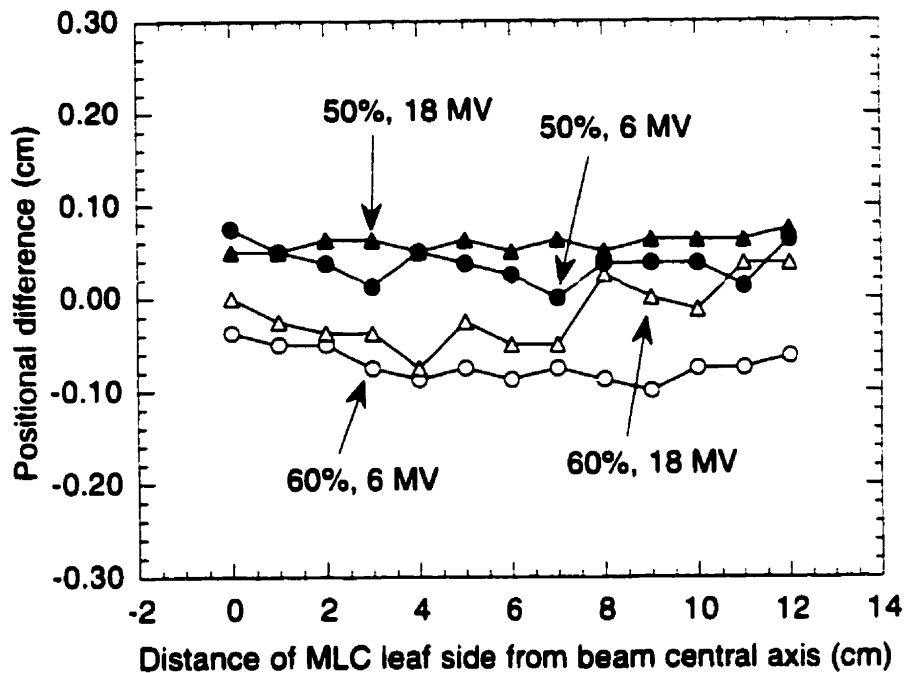


Figure 4.9. Position of the 50% and 60% isodose lines at 6 MV and 18 MV photon energies as a function of the readout position of the leaf sides.

D. Light-field versus digital read-out

The agreement between the light-field position of the leaf ends and the digital read-out of the leaf position on the MLC computer was verified by taping a piece of graph paper to the couch at an SAD of 100 cm and recording the position of the tip of leaf 13A, as shown from the light field and comparing it to the readout on the MLC computer. Results are shown in Fig. 4.10 as the solid circles. The ordinate, entitled "positional difference", is obtained by subtracting the readout position from the measured light-field position of the leaf end.

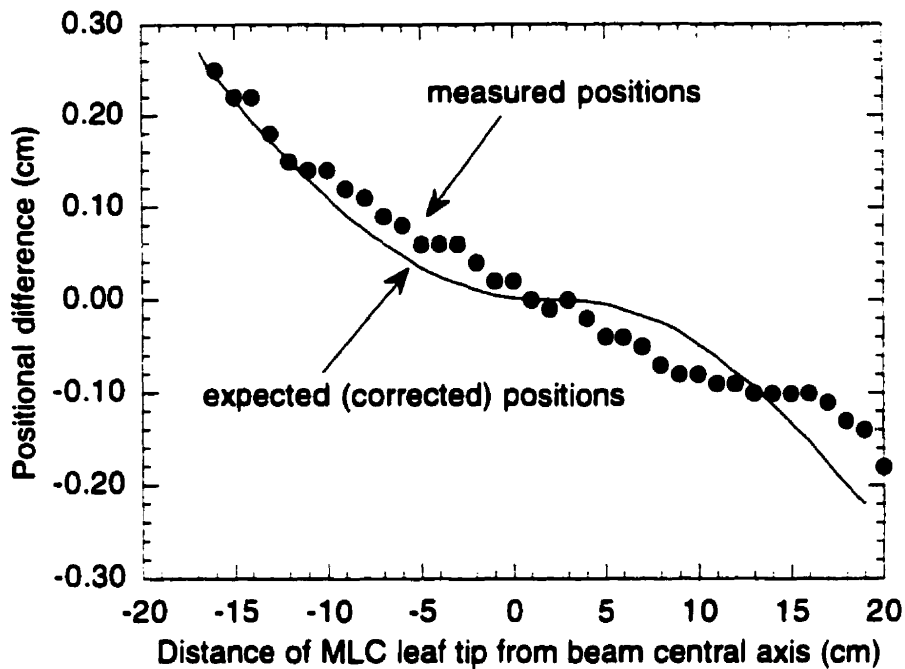


Figure 4.10. Light-field position of the leaf ends as a function of their readout position.

An observation was made that there is a systematic deviation in the light-field position of the leaf tip compared to the readout. Similar deviations have been reported previously by other investigators^{3,19,20} and explained as a simple consequence of the rounded leaf ends. As shown in Fig. 4.11, regardless of the leaf end position within the field, there is always an offset between the light-field and radiation-field positions. Since what really matters is the agreement of the digital readout with the radiation field rather than with the light-field, the Varian software adjusts on purpose the position of the leaf ends slightly from their readout positions. The solid line in Fig. 4.10 is the data contained in the correction file MLCTABLE.TXT. We thus see that the light-field position of the leaf ends follows the expected corrected positions very closely.

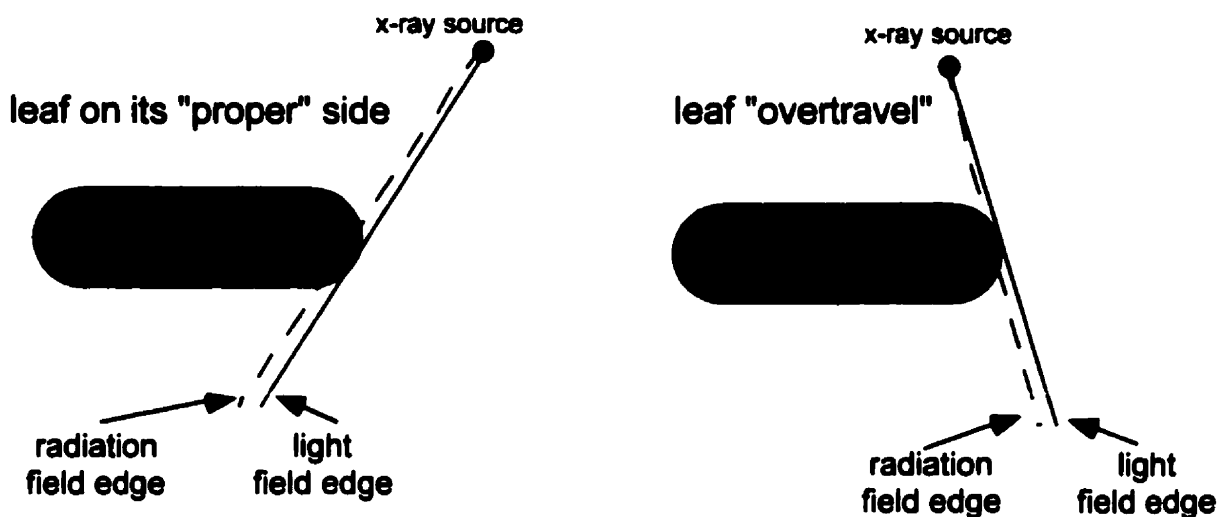


Figure 4.11. Illustration of the relative position of the light field and the radiation field for an MLC leaf end. The position of the light field source corresponds to the position of the x-ray source.

We also examined the agreement of the light-field position of the leaf sides with the readout in a similar fashion as for the leaf ends. Due to the tongue and groove construction, the position of the light field will be different depending on whether we are considering the inside of one leaf or the outside of the adjacent leaf. Data collected in this experiment is presented in Fig. 4.12 and shows that, for the leaves close to the beam centreline (e.g. leaves 12A, 13A) the average of the light-field positions for the inside of one leaf and the outside of the adjacent leaf agrees with the digital readout. However, for the leaves far from beam centreline (e.g. leaves 26A, 1B) this agreement no longer exists, and there is a discrepancy with the readout values on the order of 1 mm. This is due to the shadow projected by the tongue.

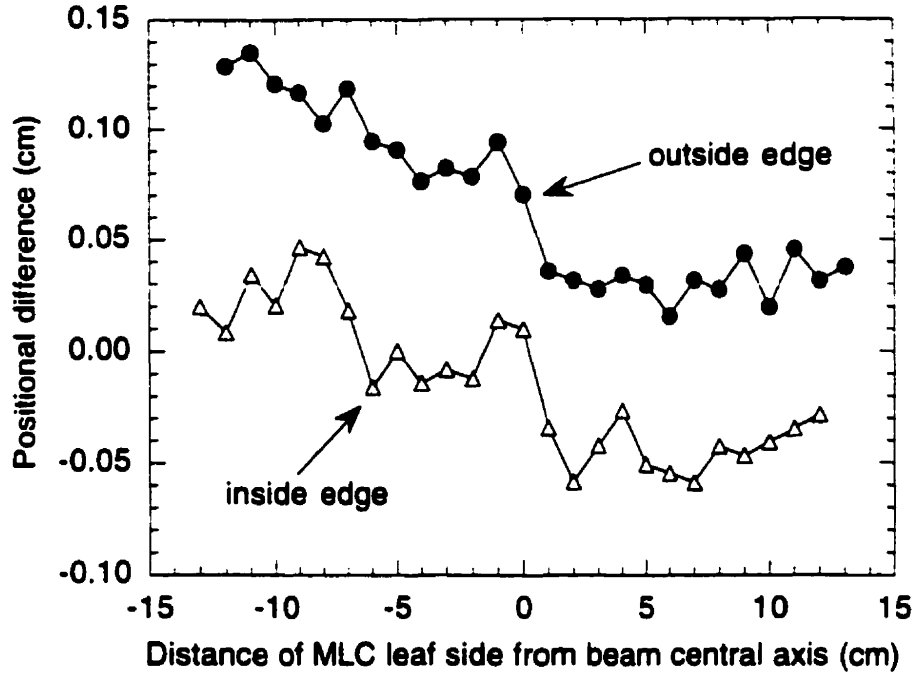


Figure 4.12. Light-field position of the leaf sides as a function of their readout position.

4.7 DOSIMETRIC MEASUREMENTS OF THE MLC

The geometric properties of our MLC are now understood and we proceed to the dosimetric measurements of the MLC, which consist of transmission measurements, an analysis of beam penumbra, and an evaluation of the tongue and groove effect. These studies were carried out with the SLIC EPID.

A. Transmission measurements

When performing intensity-modulated treatments, the MLC leaves are used to shield certain regions of the PTV for varying proportions of the total beam-on time; therefore it is essential to be aware of the transmission values of the MLC leaves for the

various photon energies at which intensity-modulation will be performed. It will then be possible, as described in Chapter 5, to incorporate the effect of leaf transmission into the calculation of the leaf sequences through accounting for the contribution of the transmitted dose to the total delivered PTV dose.

The transmission of the MLC was measured with the SLIC EPID with an SDD of 100 cm and beam energies of 6 MV and 18 MV. In order to reject electrons and low energy photons scattered from the leaves, a layer of solid water equal in thickness to the depth of dose maximum for the particular beam energy used was positioned on the sensitive area of the EPID. The leaves were closed at midline with the upper and lower linac jaws fully opened to provide a field size of 40×40 cm². The EPID image obtained is shown in Fig. 4.13. This image was calibrated and used to extract three transmission measurements, as shown in the figure: the average MLC leakage; the interleaf (or maximum) leakage; and the leaf end leakage for leaves closed at midline. In order to validate the EPID measurements, ionization chamber readings were acquired at positions A and B and used to derive an average value of the MLC transmission. Results are presented in Table 4.1.

The average transmission is a more important parameter than the maximum (interleaf) transmission since, because of the daily set-up errors (and to a lesser degree, patient motion), the peaks of interleaf transmission will move about the PTV and create a fairly uniform transmission dose. Studies²¹⁻²⁵ have shown that daily set-up errors are on the order of ±3 mm with patient motion contributing an additional ±0.5 mm to ±4 mm to the positional uncertainty, depending on treatment site. We observe that the average values for the MLC transmission obtained with the EPID are quite low and agree closely with the values obtained with the ionization chamber. Both the average and maximum transmission values fall within the specifications of the manufacturer of the MLC. The

average values also agree with values obtained by other investigators^{11,19,26} for the Varian MLC, which range from 2.0%-4.0% for the 6 MV beam and 3.5%-5.0% for the 18 MV beam. The transmission of cerrobend blocks, on the other hand, is generally about 5% for typical thicknesses used clinically.

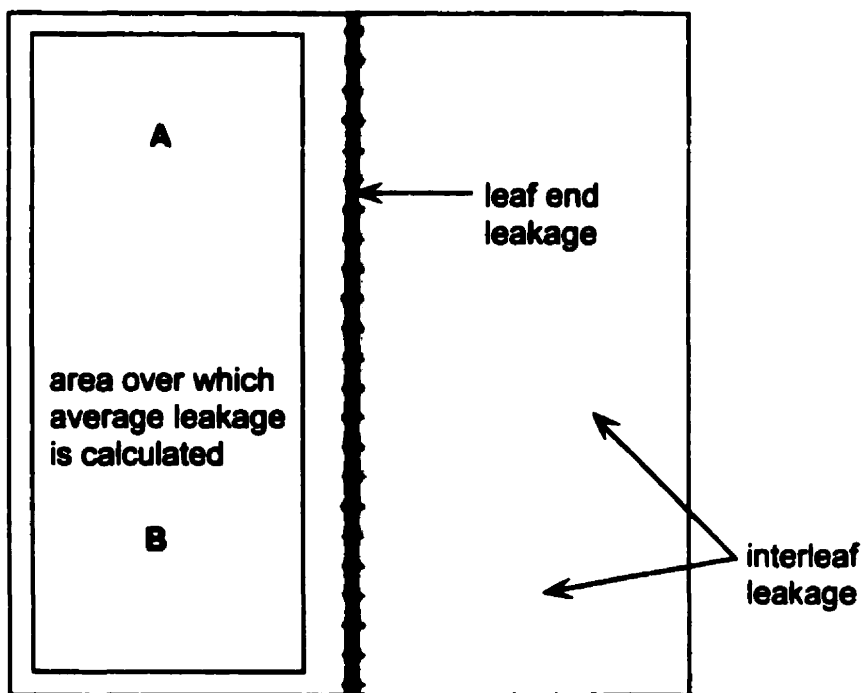


Figure 4.13. The EPID image of the transmission of the MLC. The regions used to calculate the average, interleaf, and leaf end transmission are shown.

Measurement device	6 MV photons	18 MV photons
SLIC EPID	interleaf = 3.1% average = 2.0%	interleaf = 3.6% average = 2.5%
ionization chamber	average = 2.4 %	average = 2.7%

Table 4.1. Comparison of the transmission values for the Varian MLC at 6 MV and 18 MV photon energies measured with the SLIC EPID and an ionization chamber.

The leaf end leakage is approximately 30% for both energies when the leaves are closed at midline since the leaves are not allowed by the MLC software to actually touch.

If the leaf ends are displaced from midline, the leakage falls to around 20% since photons must then pass through the gap at an angle. However, leaf end leakage is of no consequence in the approach we have taken to intensity-modulation since leaf-pairs which are "inactive" in the leaf sequence will be closed (as a rule) to positions away from midline and also behind a jaw of the linear accelerator.

B. Analysis of MLC penumbra

The penumbra of the MLC leaf ends and leaf sides was measured with the EPID as well. This was accomplished by setting up the detector surface at an SDD of 100 cm with 1 cm and 3 cm additional solid water build-up for the 6 MV and 18 MV photon beams, respectively, corresponding to a depth of d_{max} . A 4×4 cm² field was set with the MLC leaves with the linac jaws set to provide a field size of 40×26 cm². The centre of the 4×4 cm² field was moved laterally (i.e., along the direction of the leaf motion) from 0 cm to 12 cm and was also moved radially (i.e., perpendicularly to the direction of leaf motion) from 0 cm to 10 cm. At each new field position an EPID image was acquired.

The penumbral widths were then determined by reading the images into an image processing program which was instructed to calibrate the images and draw the 10%, 20%, 80%, and 90% isodose lines. The images were then magnified and the 90%-10% and 80%-20% penumbral widths were measured on screen with a ruler function. Results are shown in Figs. 4.14 and 4.15 for the leaf ends and leaf sides, respectively, at both 6 MV and 18 MV photon energies. Knowledge of these penumbral widths will play an important role in producing an accurate leaf sequencing algorithm for intensity-modulation.

The results show, first of all, that the penumbral widths for the leaf ends are constant with leaf position, as intended by the rounded design of the tips. The penumbral

widths for the leaf sides are also constant with position in the field. For the 6 MV beam, the 80%-20% penumbral width is about 4 mm for the leaf ends and slightly smaller (3 mm) for the leaf sides due to focusing in this direction. For the 18 MV beam, the 80%-20% penumbra is about 8 mm for the leaf ends and 7 mm for the leaf sides. The bulk of penumbral measurements were taken along the principal axes of the field; however, spot checks confirmed the validity of the results at arbitrary positions within the field. The results of other investigators^{19,26} measured with scanning ionization chambers or silver halide film (the response of which has been corrected for energy dependence in the penumbral region) are approximately 1 mm narrower for the 6 MV beam and 2 mm narrower for the 18 MV beam. These differences are of the order of the uncertainties for this type of measurement.

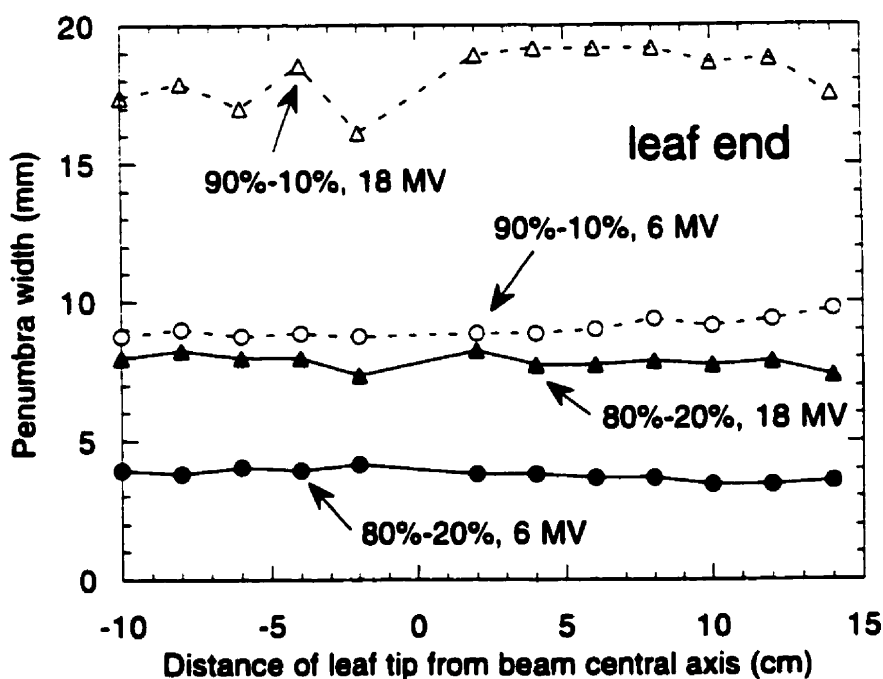


Figure 4.14. MLC leaf end penumbra widths as a function of leaf position for 6 MV and 18 MV photon energies.

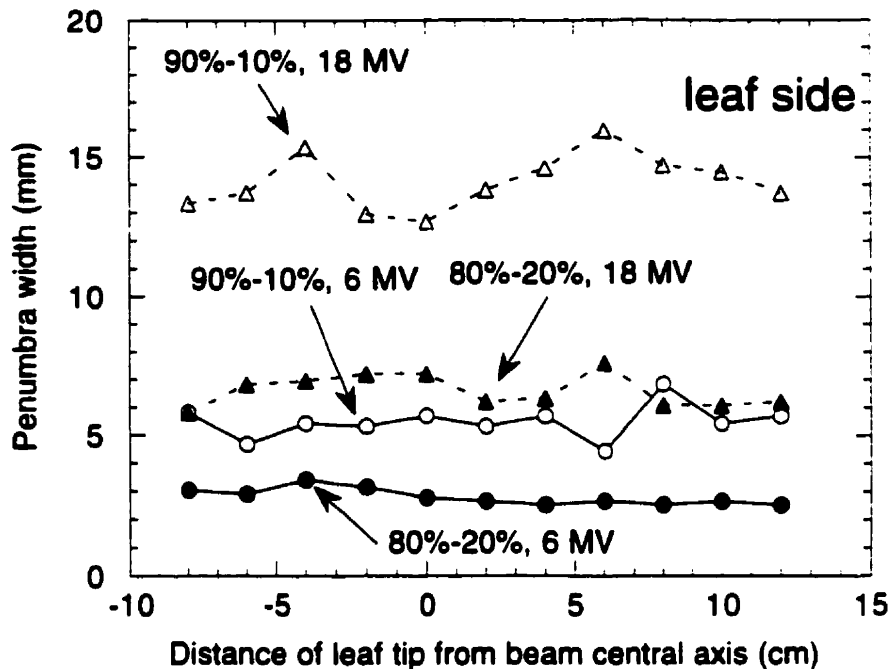
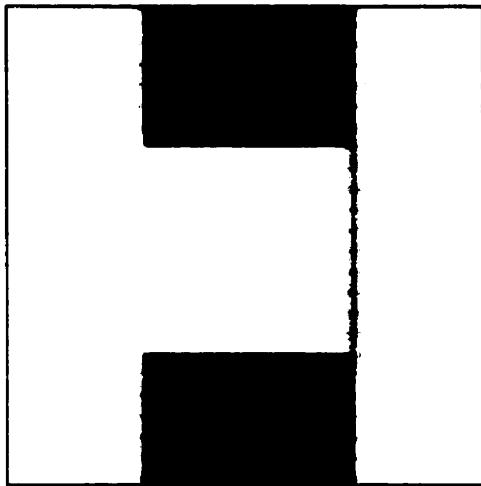


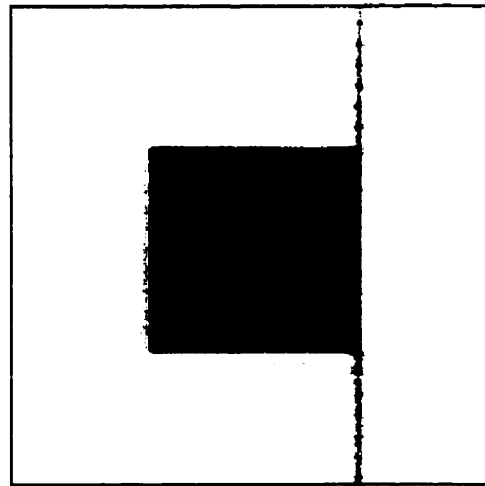
Figure 4.15. MLC leaf side penumbra widths as a function of leaf position for 6 MV and 18 MV photon energies.

C. Tongue and groove effect

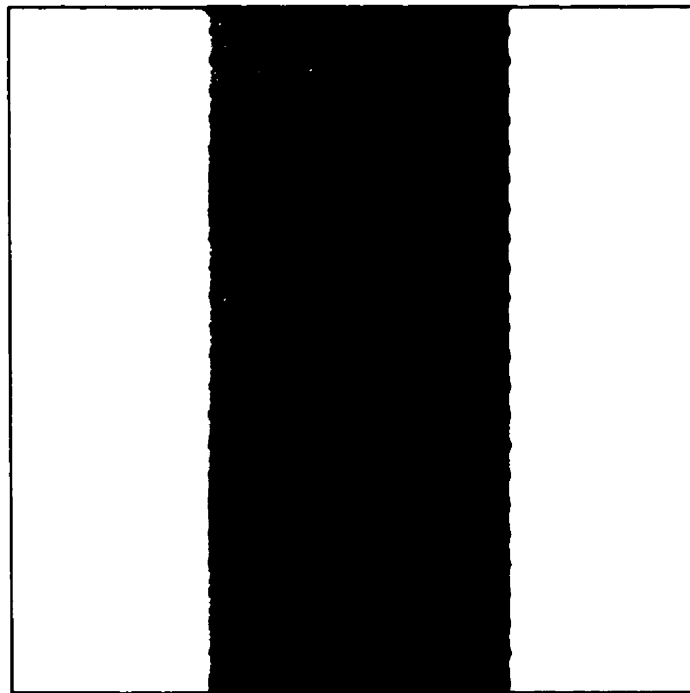
A final, and often inconsequential, dosimetric consideration when using an MLC is the tongue and groove effect, which results from the stepped profile of the leaf side. Both the tongue and groove portions of the leaf sides (drawn in Fig. 4.1) scatter photons from the beam laterally and reduce the fluence directly downstream from the tongue and groove. An example of this effect is illustrated in Fig. 4.16. The radiation fields in (a) and (b) are complements of each other and, when added together, should produce a uniform fluence. However, because of the scattering of the tongue and groove, the actual result is (c) in which there is a small underdosage directly downstream from the tongue and groove and an equal overdosage on either side. In Fig. 4.16(c), windowing has been



(a)



(b)



(c)

Figure 4.16. Depiction of the MLC "tongue and groove" effect. When added together, two complementary radiation fields (a) and (b) do not produce a fully uniform radiation fluence within the field (c).

applied to the image to visually accentuate the tongue and groove effect. In terms of absolute numbers the tongue and groove effect results in a dose decrease of

approximately 20% over about 1 mm which is the same value as that measured by Galvin¹⁹ and by van Santvoort²⁷. Although this dosimetric effect seems important, two considerations mitigate its effects. The first is that adjacent leaves generally follow each other in intensity-modulated treatments and thus do not differ too greatly in position, yet the tongue and groove effect is only important when they do differ. The second is that, similarly to the situation for the interleaf leakage (Section 4.7.A), daily set-up variations and patient motion are sufficient to uniformly spread out the underdose and overdose regions caused by the tongue and groove effect.

D. Influence of the MLC on other dosimetric parameters

A number of publications have shown that the presence of an MLC does not alter the other dosimetric parameters of the photon beam, such as the percent depth dose values^{2,26} or its characteristics in the build-up region².

4.8 INFLUENCE OF THE MLC ON BEAM OUTPUT

A. Basic theory

The output of a radiotherapy linear accelerator, for a particular collimator setting, is generally defined as the dose per MU given to a reference point in phantom when the phantom surface is at 100 cm from the source. Habitually, the reference point is taken at a depth d_{max} in phantom. Some accelerators show a deviation in dose linearity at low MU settings, but we have demonstrated that this problem does not exist on newer generation Varian Clinacs. The ratio of the output for a given field to the output of a 10×10 cm² field defined by the jaws is termed the relative dose factor (*RDF*) or output factor. The output factors or, equivalently, the *RDFs*, are generally measured for the range of square symmetric fields available on the particular treatment unit. Simple rules (described below) allow the calculation of *RDF* values for rectangular and asymmetric fields from

the symmetric square field data. The output of arbitrarily shaped fields, such as those defined by a MLC, depends largely on the characteristics of the particular MLC, and will also be discussed below.

The output of a linear accelerator (and hence the *RDF*) varies as a function of field size. The reasons for this are the following:

1. All photons emerging from the linear accelerator head do not originate from a point source. In fact, as shown in Monte Carlo studies^{28,29} and also measured by a number of investigators³⁰⁻³², a sizable percentage of photons are generated outside the nominal target region, particularly through forward-scattering in the flattening filter. The result is that, as the collimators are opened, a greater number of these "extrafocal photons" can reach the detector placed at the reference point, thus increasing the output. For the Clinac 2100 C/D which has a similar head configuration to the Clinac 2300 C/D, measurements³² indicate that approximately 8% of the photons contributing to the output originate outside the focal spot.

2. A certain percentage of photons is always back-scattered into the beam monitor chamber which, as explained in Chapter 1, measures the number of monitor units delivered. However, as the collimators are opened, the upper surface of the collimators exposed to the beam decreases and fewer photons are scattered back to the monitor chamber. This means that for larger field sizes, a smaller number of MU are counted for a given dose delivered at the reference point or, in other words, that the output is higher. For the Clinac 2300 C/D which has a thin Kapton exit window rather than a thicker metal one as in some accelerators, measurements³³ show that, as field size is increased from 5×5 cm² to 40×40 cm², the backscatter component to the output increases by 1.7 % for the 6 MV and 2.4 % for the 18 MV beam.

3. As the collimators are opened, a larger area of the collimator faces (upper and lower jaws) are exposed to the beam, scattering a greater number of photons into the reference point. Work by Ahnesjo³⁴ has shown that this effect contributes less than 1% to the total beam fluence.

4. In the phantom, a larger field size means that there is a larger volume of irradiated medium from which photons can be scattered toward the reference point. This phantom scatter increases the measured output.

The first three factors listed above as affecting the output depend on the configuration of the linear accelerator, i.e., the positions of the collimators relative to the source, the size/composition of the flattening filter, the characteristics of the monitor chamber, the beam energy, etc. Collectively, these three factors determine the "collimator scatter" or "head scatter" which differs from one unit to the next. The fourth factor, which in theory depends only on the phantom, has in fact been shown to be independent of the particular treatment unit involved³⁵ and is referred to as "phantom scatter".

Theories have been proposed to predict scatter factors in an analytical manner (i.e., without relying on beam measurements) by integrating over the area of extended source seen by the detector^{36,37}. These calculations are accurate, but complicated, and in fact depend on measured data since they require estimates of the relative contribution of scatter radiation to primary radiation as well as its spatial distribution. Another approach is the well-known sector-integration method developed by Clarkson^{38,39}, which is widely-applicable and fairly accurate. However, our aim in this section is to develop a simple theory for the calculation of relative output factors which can be applied to the specific

case of intensity-modulation performed with an MLC in the segmented approach. We will show that, under certain conditions, the collimator scatter factor is insensitive to the positions of the MLC leaves and depends only on the positions of the secondary collimators, and can be adequately predicted by interpolation in the measured tables for square, symmetric fields.

Mathematically, one separates the influence of the collimator scatter (S_c) on the output from the influence of the phantom scatter (S_p) on the output by writing the *RDF* as the product of the two factors^{26,35,40,41}:

$$RDF = S_c \times S_p \quad . \quad (4.1)$$

In what follows, we will first discuss collimator scatter in the absence of tertiary blocking, then show how the MLC affects this quantity and, finally, discuss the phantom scatter.

B. Collimator scatter (no MLC)

In order to isolate collimator scatter from phantom scatter, measurements of collimator scatter are performed in air with an ionization chamber surrounded only by sufficient build-up material for electronic equilibrium to be attained in the chamber sensitive volume. If the entire build-up is always covered by the radiation field, changes in the chamber readings as the field size is varied will reflect only the changes in collimator scatter. Typically, build-up caps for radiotherapy chambers are constructed from tissue-equivalent materials such as polystyrene or plastic; however, higher density materials, such as aluminum or copper, are sometimes required for measurements of the collimator scatter factor with very small field sizes and high photon beam energies. A graph showing collimator factors for the Clinac 2300 C/D at 6 MV and 18 MV photon

energies is shown in Fig. 4.17 for square, symmetric fields. A symmetric field is one whose field centre corresponds with the beam central axis. Like the *RDF*, the collimator factor is normalized to 1.00 for a 10×10 cm² field size.

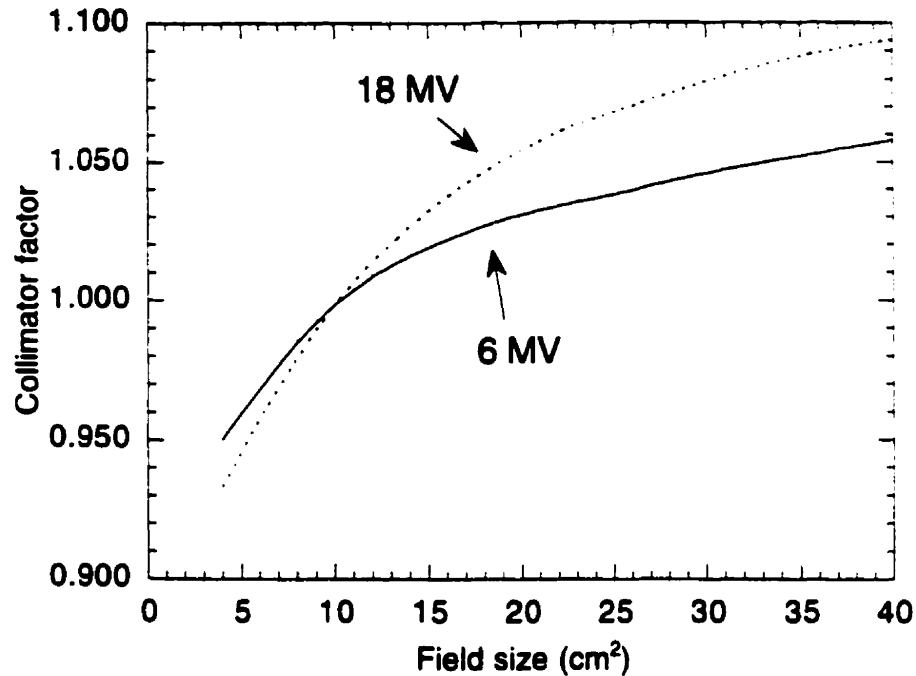


Figure 4.17. The collimator scatter factor as a function of field size for square, symmetric fields for the Clinac 2300 C/D linear accelerator at 6 MV and 18 MV photon energies.

The data in Fig. 4.17 is for square fields. When dealing with rectangular fields, one generally calculates an "equivalent square", which has similar radiation parameters as the rectangular field. The complete formula for this is given in the literature⁴². However, if the elongation ratio of the rectangular field is less than 2, the exact formula is very well approximated by:

$$s = \frac{lw}{2(l+w)} \quad , \quad (4.2)$$

where l and w are the length and width of the rectangular field, respectively.

So far, it has also been assumed that we are dealing with symmetric fields. Since modern linear accelerators such as the Clinac 2300 C/D have four independently-movable jaws, the centre of the field need not correspond with the beam axis. As was discussed in Chapter 1, as one moves away from the central axis at a constant depth in phantom the dose varies, as described by the off-axis ratio. At a depth of d_{max} , where the output is measured, the *OAR* increases as the point of measurement moves away from the beam central axis. In order to predict collimator scatter factors for asymmetric fields, one takes the S_c corresponding to the equivalent square of the aperture and then multiplies it by the *OAR* corresponding to the distance that the field centre is removed from the beam central axis.

As stated above, the dominant reason for the variation of the collimator scatter factor with field size is the differing views of the extended source presented to the point of measurement. Since the upper and lower collimators are at different distances from the source, it is not surprising that, for rectangular fields, an interchange of the X and Y jaw positions, while conserving the same field size, results in a change in the collimator scatter. And, as illustrated by Yu⁴³, changes in backscatter to the monitor chamber as the jaws are interchanged also contributes to this phenomenon, known as the "collimator exchange effect". Typically the magnitude of the effect is small, and is neglected unless the elongation of the field is very high (e.g., greater than 4). For instance, at a photon energy of 6 MV, we measured the output for a 10×30 cm² field to be 1.029 and the output of a 30×10 cm² field to be 1.011, whereas the output of the equivalent square field (15×15 cm²) is 1.033.

C. Collimator scatter (with MLC)

We now consider the effect of the MLC on the collimator scatter. If we recall the three factors which affect the collimator scatter, it is easily seen *a priori* that the addition of an MLC as a tertiary collimator as in, for example, the Varian MLC system, will not have a major impact on the output of the accelerator. Firstly, the solid angle presented to the source by the leaf ends or leaf sides is too small to generate significant scatter onto the detector plane, scatter which is already almost insignificant even from the secondary collimators. Secondly, the Varian MLC is positioned too far from the beam monitor chamber to scatter a significant portion of photons back into it³³. Thirdly, due to its large distance from the source, the ability of the MLC to shadow out portions of the extrafocal radiation is limited. It is only in situations for which the MLC aperture is very much smaller than the aperture defined by the secondary collimators that the presence of the MLC can shadow out portions of the extended source and have an effect on the collimator scatter. To illustrate this point, we consider a $w \times l$ cm² symmetric field defined by the secondary collimators and calculate the limiting symmetric field defined by the MLC for which the extended source is further shielded by the MLC and the output is affected.

Consider a detector positioned in air on the beam central axis at a distance SAD from the source as in Fig. 4.18. Initially, we assume the MLC to be retracted and the secondary collimators to define a field size of $w \times l$ cm². The opening of the jaws at the level of the jaws will be given by:

$$\text{X direction: } \frac{wd_{low}}{SAD} \quad \text{and} \quad \text{Y direction: } \frac{ld_{up}}{SAD}, \quad (4.3)$$

where d_{low} and d_{up} are the distances of the top surfaces from the x-ray target of the lower and upper jaws, respectively.

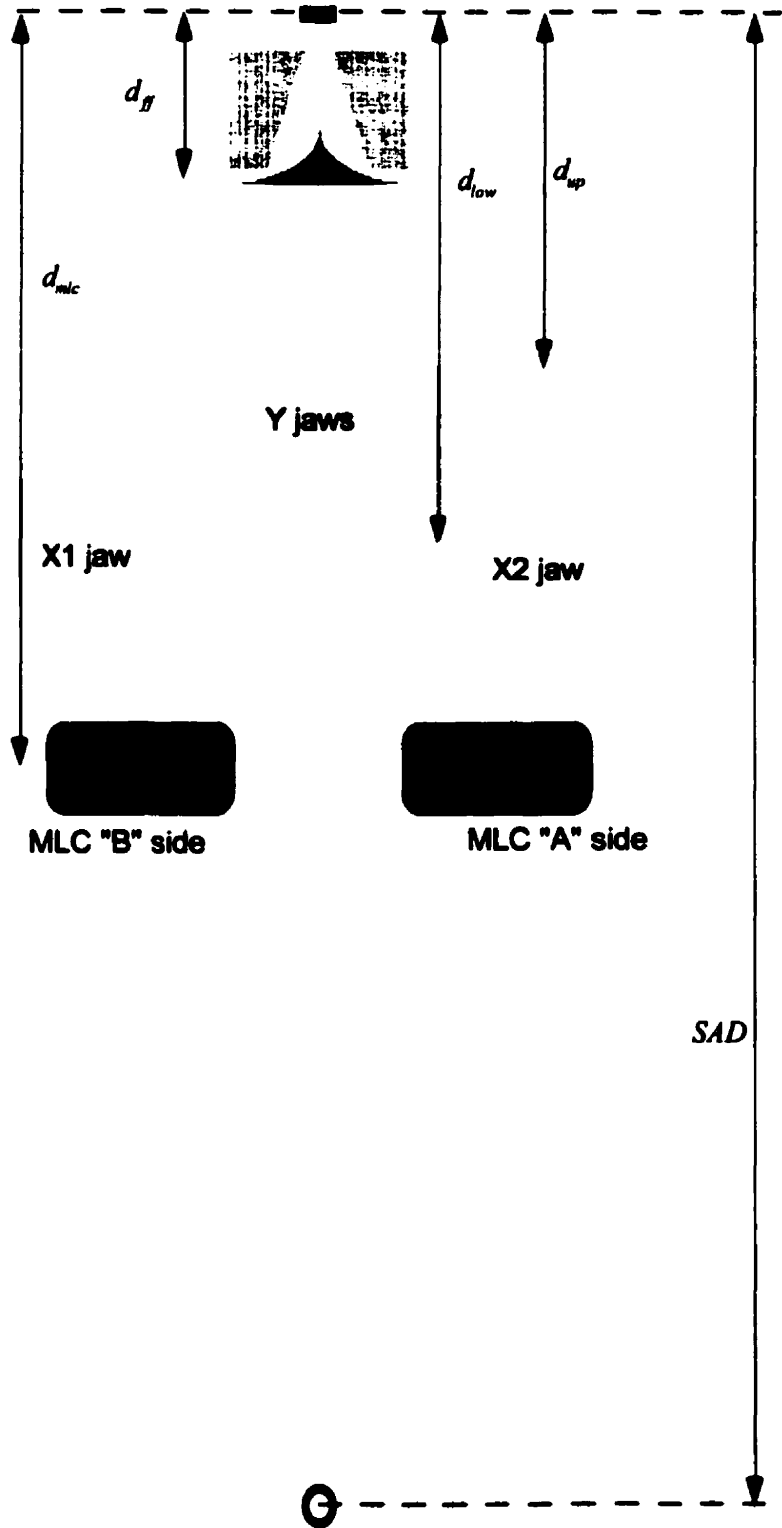


Figure 4.18. Proper scale drawing of the collimation system of the Varian Clinac 2300 C/D.

The flattening filter is the dominant source of extrafocal radiation. The area on the flattening filter from which scatter can reach the detector is a function of the two positions of the secondary collimators, calculated in Eq. (4.3). Using similar triangles, the area on the flattening filter is given by:

$$\text{X direction: } \left(\frac{wd_{low}}{SAD} \right) \left(\frac{100 - d_f}{100 - d_{low}} \right), \text{ Y direction: } \left(\frac{ld_{up}}{SAD} \right) \left(\frac{100 - d_f}{100 - d_{up}} \right), \quad (4.4)$$

where d_f is the distance from the x-ray target to the base of the flattening filter.

To obtain an equivalent projection onto the flattening filter with a field defined by the MLC, the leaves will have to define a field of size of:

$$\begin{aligned} \text{X direction: } & \left(\frac{wd_{low}}{SAD} \right) \left(\frac{100 - d}{100 - d_{low}} \right) \left(\frac{100 - d_{mlc}}{100 - d} \right) = \left(\frac{wd_{low}}{SAD} \right) \left(\frac{100 - d_{mlc}}{100 - d_{low}} \right) \text{ and} \\ & (4.5) \\ \text{Y direction: } & \left(\frac{ld_{up}}{SAD} \right) \left(\frac{100 - d}{100 - d_{up}} \right) \left(\frac{100 - d_{mlc}}{100 - d} \right) = \left(\frac{ld_{up}}{SAD} \right) \left(\frac{100 - d_{mlc}}{100 - d_{up}} \right), \end{aligned}$$

where d_{mlc} is the distance from the x-ray target to the middle of the MLC leaves.

For the particular values of d , d_{low} , d_{up} , and d_{mlc} applicable to the Clinac 2300 C/D³⁶, Eq. (4.5) reduces to:

$$\begin{aligned} \text{X direction: } & 0.298w \\ & (4.6) \\ \text{Y direction: } & 0.164l . \end{aligned}$$

This implies, for instance, that for a $10 \times 10 \text{ cm}^2$ field defined by the upper and lower jaws, the MLC can define a field as small as $3.0 \times 1.6 \text{ cm}^2$ without changing the collimator scatter of the $10 \times 10 \text{ cm}^2$ field.

To verify this hypothesis, an experiment was performed in which the linac upper and lower jaws were set to a field size of $25 \times 25 \text{ cm}^2$ and the collimator scatter factor was measured with an ionization chamber as the MLC aperture was varied from $30 \times 20 \text{ cm}^2$ to $6 \times 20 \text{ cm}^2$ and from $15 \times 26 \text{ cm}^2$ to $15 \times 6 \text{ cm}^2$ at 6 MV photon energy. The ionization chamber had the appropriate build-up cap and was placed on the beam central axis at a source-chamber distance of 100 cm. According to Eq. (4.6), the collimator scatter factor should not change significantly until either the MLC leaves are closed further than $25 \text{ cm} \times 0.298 = 7.5 \text{ cm}$ in the X direction, and $25 \text{ cm} \times 0.164 = 4.1 \text{ cm}$ in the Y direction. Although MLC fields narrower than 6 cm could not be investigated due to the large size of the chamber build-up cap, the data in Fig. 4.19 supports the hypothesis that the MLC has a negligible effect on the collimator scatter over a wide range of positions, and that it is actually the position of the upper and lower jaws which govern the collimator scatter factor.

Inverting Eq. (4.6), it can be said that insofar as the secondary collimators remain "close" to any MLC-defined field then it is the position of the secondary collimators and not the shape of the MLC aperture that dictates the magnitude of the collimator scatter. "Close" will mean, for the X-direction, that the position of X1 (or X2) will not be greater than $1/0.298 = 3.4$ times the position of the A leaves (or B leaves). In the Y-direction, the allowance is even more generous and the position of the Y1 or Y2 jaws must not be greater than $1/0.164 = 6.1$ times the opening of the MLC in the Y-direction.

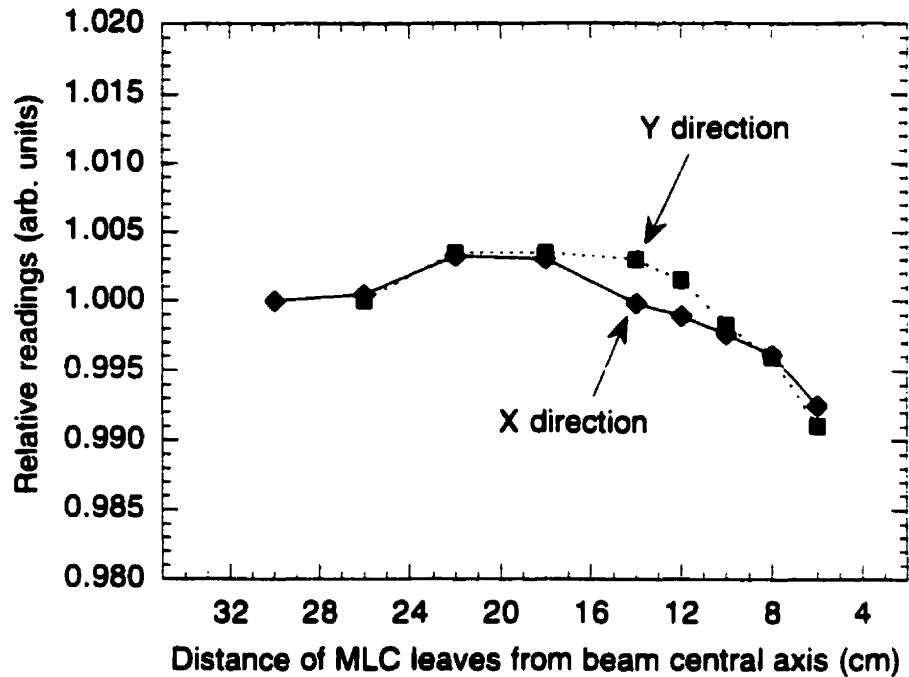


Figure 4.19. Collimator scatter factor at 6 MV photon energy illustrating the validity of the hypothesis that, for a given setting of the jaws, the positions of the MLC leaves have negligible effect on the collimator scatter factor for a wide range of MLC positions. The linac upper and lower jaws were set to $25 \times 25 \text{ cm}^2$.

In the approach we have adopted for the use of MLC-defined subfields to deliver an arbitrary intensity-modulated beam, the jaws of the treatment machine are stationary during treatment and define a bounding rectangle of the first MLC subfield. Since in the dynamic mode the largest allowable MLC field size is $14.5 \times 26 \text{ cm}^2$, the largest setting for the secondary collimators will be $15.7 \times 26.4 \text{ cm}^2$. For this setting of the jaws, only the output of MLC fields smaller than $4.3 \times 4.3 \text{ cm}^2$ will be affected. Typically, however, the secondary collimators will define much smaller fields with correspondingly smaller limiting MLC subfield sizes. Although it is possible for MLC subfields of a given leaf sequence to violate these limiting positions, such cases are relatively rare and involve only a small fraction of the total MU delivered for a beam port. They will thus be ignored similarly to methods used with success by other investigators^{40,44,45}.

D. Phantom scatter

With or without the presence of the MLC, the phantom scatter factor will depend solely on the radiation field size at the reference point. The phantom scatter factor is difficult to measure, since one must vary the amount of phantom material irradiated while keeping identical collimator scatter (i.e., identical jaw and/or MLC positions). Nonetheless, there are two methods for doing this: the first is to place shielding directly on the phantom surface thus defining a variable volume from which scatter can contribute; the second is to construct a series of phantoms of various dimensions. However, these two methods are arduous, and since both the RDF and S_c are easy to obtain experimentally, the S_p is usually calculated by division of the RDF by the S_c . Figure 4.20 shows the S_p obtained in this manner for the 6 MV and 18 MV photon beams of the Clinac 2300 C/D linear accelerator. The contribution to the 6 MV phantom scatter increases gradually with field size, while the contribution of the 18 MV phantom scatter saturates for fields larger than 15×15 cm² field size, since at these high photon energies scattering is strongly forward-peaked and a negligible percentage of photons (or electrons) are side-scattered or back-scattered into the detector from surrounding phantom material.

The data in Fig. 4.20 is for square fields. Just as for the collimator scatter factor, one can obtain the phantom scatter factor for a rectangular field quite precisely by looking up the S_p of the equivalent square of the rectangular field. However, when dealing with MLC-defined fields, the situation is more complicated since all fields are not necessarily square or rectangular. Our approach to the calculation of the equivalent square to be used for determination of the phantom scatter factor for MLC-defined fields has been to use the area/perimeter rule of thumb [Eq. (4.2)] since, in our experience, the MLC subfields are generally not too different from rectangles or ellipses, both of which obey the area/perimeter rule quite well.

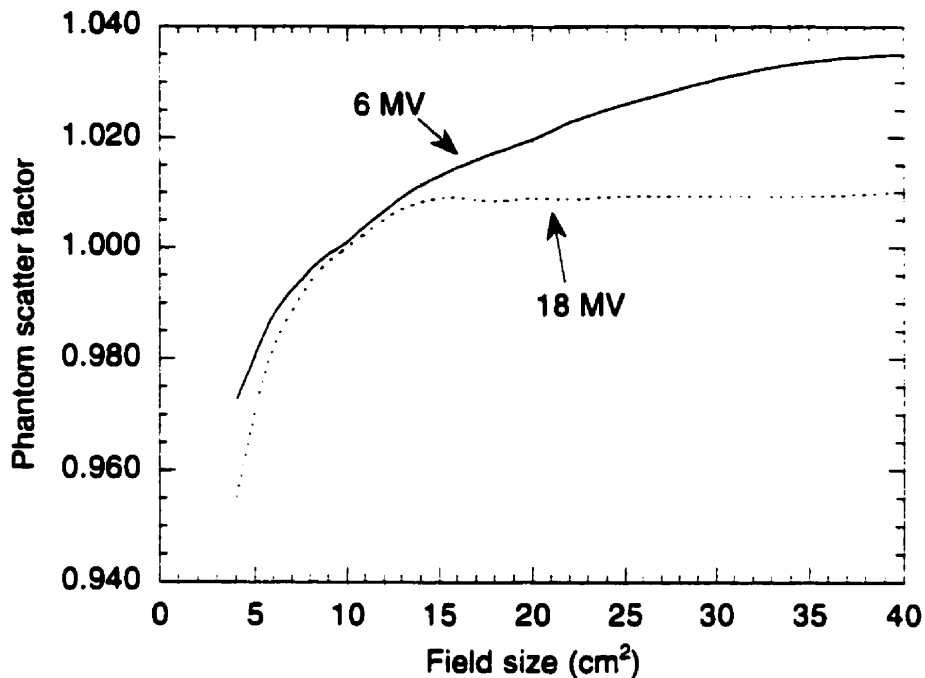


Figure 4.20. The phantom scatter factor as a function of field size for square, symmetric fields on the Clinac 2300 C/D linear accelerator at 6 MV and 18 MV photon energies.

E. Experimental verification of selected field apertures

The theory elaborated in this section for the prediction of relative dose factors was tested against measurements with an ionization chamber for various field apertures defined by the MLC. The apertures used and the resulting RDF , S_C , and S_p values are shown in Fig. 4.21 and Table 4.2, respectively. The asterixes in Fig. 4.21 denote the position of the centre of the ionization chamber, i.e., the reference point on the beam central axis. For 18 MV photons, no proper build-up cap was available in our clinic, and the collimator scatter factor was not measured. For the slit field, the width of the field was too narrow to cover even the 6 MV build-up cap and the S_C was not measured. To obtain the measured values, the RDF and S_C were measured, as discussed above, and then used to derive a "measured" value for the S_p . For the theoretical values, an S_C value for the equivalent square field of the jaw setting and an S_p value for the equivalent

square field at the phantom surface were interpolated in tables for square fields and multiplied to derive a value for the *RDF*. The agreement between experimental and theoretical values is almost always better than $\pm 2\%$ and thus considered acceptable. The worst deviations occur for the most elongated fields, since at high elongations the area/perimeter rule for determining the equivalent square is less reliable.

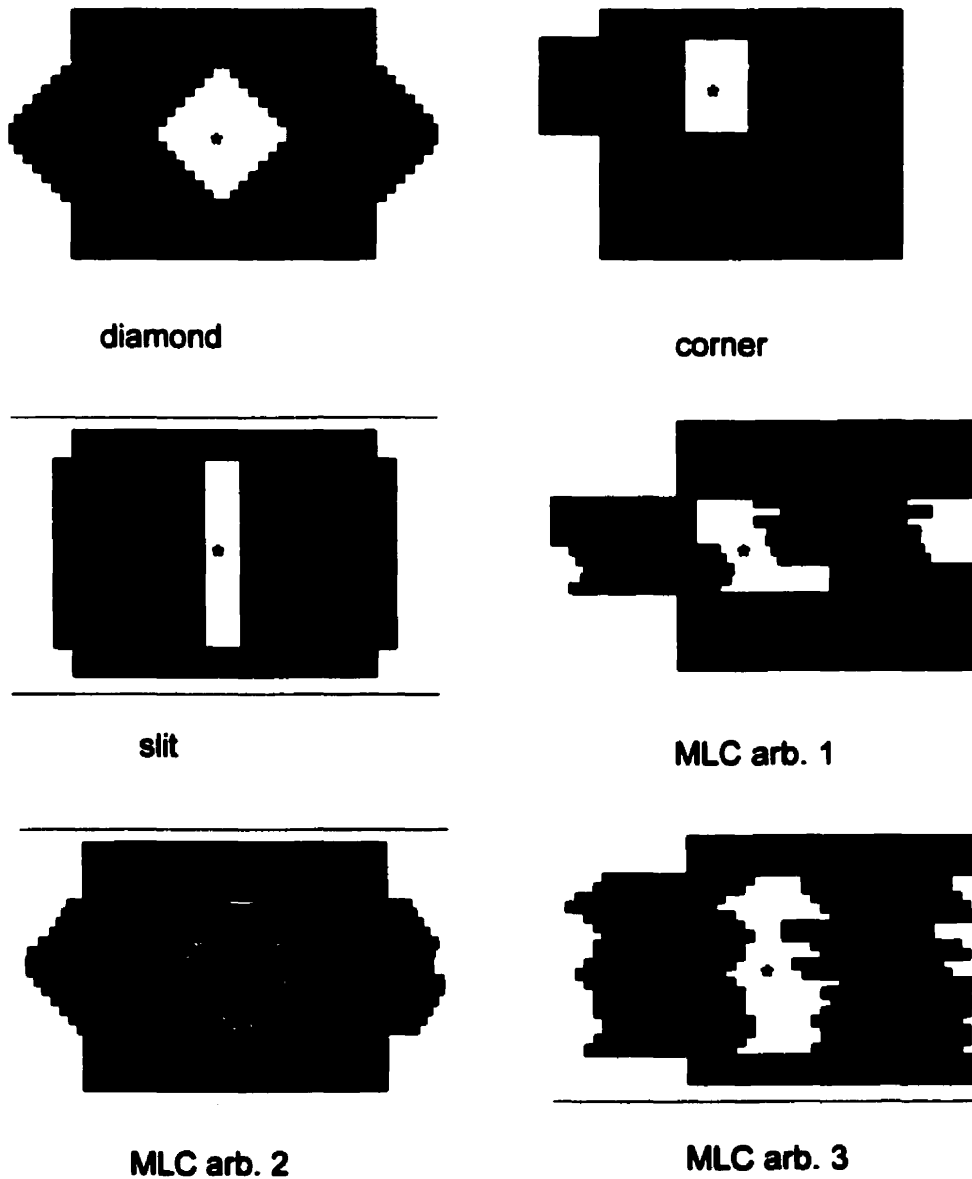


Figure 4.21. Shapes of the six MLC-defined fields used to verify the agreement between measured and calculated relative dose factors and collimator factors. The asterisk denotes the position of the ion chamber centre.

	6 MV			18 MV		
	<i>RDF</i>	<i>S_c</i>	<i>S_p</i>	<i>RDF</i>	<i>S_c</i>	<i>S_p</i>
diamond (meas.)	1.031	1.028	1.003	1.048	---	---
<i>diamond (calc.)</i>	<i>1.025</i>	<i>1.025</i>	<i>1.000</i>	<i>1.043</i>	<i>1.043</i>	<i>1.000</i>
corner (meas.)	1.050	1.055	0.996	1.054	---	---
<i>corner (calc.)</i>	<i>1.052</i>	<i>1.063</i>	<i>0.990</i>	<i>1.062</i>	<i>1.065</i>	<i>0.997</i>
slit (meas.)	1.000	---	---	1.000	---	---
<i>slit (calc.)</i>	<i>1.016</i>	<i>1.025</i>	<i>0.991</i>	<i>1.029</i>	<i>1.043</i>	<i>0.987</i>
MLC arb 1 (meas.)	1.024	1.027	0.998	1.029	---	---
<i>MLC arb 2 (calc.)</i>	<i>1.033</i>	<i>1.035</i>	<i>0.998</i>	<i>1.047</i>	<i>1.050</i>	<i>0.997</i>
MLC arb 2 (meas.)	1.030	1.029	1.001	1.047	---	---
<i>MLC arb 2 (calc.)</i>	<i>1.024</i>	<i>1.025</i>	<i>0.999</i>	<i>1.041</i>	<i>1.043</i>	<i>0.998</i>
MLC arb 3 (meas.)	1.031	1.028	1.002	1.028	---	---
<i>MLC arb 3 (calc.)</i>	<i>1.033</i>	<i>1.034</i>	<i>0.999</i>	<i>1.046</i>	<i>1.048</i>	<i>0.998</i>

Table 4.2. Comparison of measured and calculated relative dose factors and collimator factors for the six MLC-defined fields of Fig. 4.21.

4.9 SUMMARY

A thorough description of the Varian multileaf collimator (MLC) has been given in this chapter. Measurements were undertaken to evaluate its suitability for conventional beam blocking. The required beam penumbra, transmission, and leaf-positioning measurements for the development of a leaf-sequencing algorithm have also been carried out. The output of the Varian MLC has been shown to be accurately

predicted (within $\pm 3\%$) by the product of the collimator scatter factor of the jaw setting and the phantom scatter factor of the irregular field at the patient surface.

4.10 REFERENCES

1. Galvin JM, Smith AR, Moeller RD, Goodman RL, Powlis WD, Rubenstein J, Solin LJ, Michael B, Needham M, Huntzinger CJ, Kligerman MM. *Evaluation of multileaf collimator design for a photon beam*. *Int. J. Radiol. Oncol. Biol. Phys.* **23**, 789-801 (1992).
2. Huq MS, Yan Y, Chen Z-P, Suntharalingam N. *Dosimetric characteristics of a commercial multileaf collimator*. *Med. Phys.* **22**, 241-247 (1995).
3. Boyer AL, Shidong L. *Geometric analysis of light-field position of a multileaf collimator with curved ends*. *Med. Phys.* **24**, 757-762 (1997).
4. Jordan TJ, Williams PC. *The design and performance characteristics of a multileaf collimator*. *Phys. Med. Biol.* **39**, 231-251 (1994).
5. Fernandez EM, Shentall GS, Mayles WPM, Dearnaley DP. *The acceptability of a multileaf collimator as a replacement for conventional blocks*. *Radiother. Oncol.* **36**, 65-74 (1995).
6. Frazier A, Du M, Wong J, Vicini F, Taylor R, Yu C, Matter R, Martinez A, Yan D. *Dosimetric evaluation of the conformation of the multileaf collimator to irregularly shaped fields*. *Int. J. Radiol. Oncol. Biol. Phys.* **33**, 1229-1238 (1995).
7. LoSasso T, Kutcher GJ. *Multileaf collimation versus alloy blocks: analysis of geometric accuracy*. *Int. J. Radiol. Oncol. Biol. Phys.* **32**, 499-506 (1995).
8. Powlis WD, Smith AR, Cheng E, Galvin JM, Villari F, Bloch P, Kligerman MM. *Initiation of multileaf collimator conformal radiation therapy*. *Int. J. Radiol. Oncol. Biol. Phys.* **25**, 171-179 (1993).

9. Frazier A, Yan D, Du M, Wong J, Vicini F, Matter R, Joyce M, Martinez A. *Effects of treatment setup variation on beam's eye view dosimetry for radiation therapy using the multileaf collimator vs. the cerrobend block.* Int. J. Radiol. Oncol. Biol. Phys. **33**, 1247-1256 (1995).
10. Webb S. *The effect on tumour control probability of varying the setting of a multileaf collimator with respect to the planning target volume.* Phys. Med. Biol. **38**, 1923-1936 (1993).
11. Klein EE, Harms WB, Low DA, Willcut V, Purdy JA. *Clinical implementation of a commercial multileaf collimator: dosimetry, networking, simulation, and quality assurance.* Int. J. Radiol. Oncol. Biol. Phys. **33**, 1195-1208 (1995).
12. Weidlich GA, Schmidt EL. *Development of methods for dynamic radiation therapy with specified dose distributions.* Med. Dos. **21**, 87-95 (1996).
13. Heyler SJ, Heisig S. *Multileaf collimator versus conventional shielding blocks: a time and motion study of beam shaping in radiotherapy.* Radiother. Oncol. **37**, 61-64 (1995).
14. Mubata CD, Childs P, Bidmead AM. *A quality assurance procedure for the Varian multi-leaf collimator.* Phys. Med. Biol. **42**, 423-431 (1997).
15. Brewster L, Mohan R, Mageras G, Burman C, Leibel S, Fuks Z. *Three dimensional conformal treatment planning with multileaf collimators.* Int. J. Radiol. Oncol. Biol. Phys. **33**, 1081-1089 (1995).
16. Zhu Y, Boyer AL, Desobry GE. *Dose distributions of x-ray fields as shaped with multileaf collimators.* Phys. Med. Biol. **37**, 163-173 (1992).
17. Brahme A. *Optimal setting of multileaf collimators in stationary beam radiation therapy.* Strahlenther. Onkol. **164**, 343-350 (1988).
18. Chui C-S, Spirou S, LoSasso T. *Testing of dynamic multileaf collimation.* Med. Phys. **23**, 635-641 (1996).

19. Galvin JM, Smith AR, Lally B. *Characterization of a multileaf collimator system.* Int. J. Radiol. Oncol. Biol. Phys. **25**, 181-192 (1993).
20. Sun J, Zhu Y. *Study of dosimetric penumbra due to multileaf collimation on a medical accelerator.* Int. J. Radiol. Oncol. Biol. Phys. **32**, 1409-1417 (1995).
21. Enzmann DR, Pelc NJ. *Brain motion: measurement with phase-contrast MR imaging.* Radiology **185**, 653-60 (1992).
22. Huizenga H, Levendag PC, De Porre PMZR, Visser AG. *Accuracy of radiation field alignment in head and neck cancer: a prospective study.* Radiother. Oncol. **11**, 181-187 (1988).
23. Hukku S, Das KJM, Nangia S, Kumar A, Ayyagari S. *The use of portal images to study the accuracy of radiation field alignment and patient positioning in head and neck cancer.* Proceedings of the XIth International Conference on the Use of Computers in Radiation Therapy, 268-269 (1994).
24. Hunt MA, Kutcher GJ, Burman C, Fass D, Harrison L, Leibel S, Fuks Z. *The effect of set-up uncertainties on the treatment of nasopharynx cancer.* Int. J. Radiat. Oncol. Biol. Phys. **27**:, 437-44 (1983).
25. Rabinowitz I, Broomberg J, Goitein M, McCarthy K, Leong J. *Accuracy of radiation field alignment in clinical practice.* Radiother. Oncol. **29**, 327-335 (1993).
26. Boyer AL, Ochran TG, Nyerick CE, Waldron TJ. *Clinical dosimetry for implementation of a multileaf collimator.* Med. Phys. **19**, 1255-1261 (1992).
27. van Santvoort JPC, Heijmen BJM. *Dynamic multileaf collimation without "tongue-and-groove" underdosage effects.* Phys. Med. Biol. **41**, 2091-2105 (1996).
28. Chaney EL, Cullip TJ, Gabriel TA. *A Monte Carlo study of accelerator head scatter.* Med. Phys. **21**, 1383-1390 (1994).

29. Mohan R, Chui C, Lidofsky L. *Energy and angular distributions of photons from medical accelerators*. Med. Phys. **12**, 592-597 (1985).
30. Dunscombe PB, Nieminen JM. *On the field-size dependence of relative output from a linear accelerator*. Med. Phys. **19**, 1441-1444 (1992).
31. Zhu TC, Bjärngård BE, Shackford H. *X-ray source and the output factor*. Med. Phys. **22**, 793-798 (1995).
32. Jaffray DA, Battista JJ, Fenster A, Munro P. *X-ray sources of medical accelerators: focal and extra-focal radiation*. Med. Phys. **20**, 1417-1427 (1993).
33. Yu MK, Sloboda RS, Mansour F. *Measurement of photon beam backscatter from collimators to the beam monitor chamber using target-pulse-counting and telescope techniques*. Phys. Med. Biol. **41**, 1107-1117 (1996).
34. Ahnesjö A. *Collimator scatter in photon therapy beams*. Med. Phys. **22**, 267-278 (1995).
35. van Gasteren JJM, Heukelom S, van Kleffens HJ, van der Laarse R, Venselaar JLM, Westermann CF. *The determination of phantom and collimator scatter components of the output of megavoltage photon beams: measurement of the collimator scatter part with a beam-coaxial narrow cylindrical phantom*. Radiother. Oncol. **20**, 250-257 (1991).
36. Ahnesjö A. *Analytic modelling of photon scatter from flattening filters in photon therapy beams*. Med. Phys. **21**, 1227-1235 (1994).
37. Yu MK, Sloboda R. *Analytical representation of head scatter factors for shaped photon beams using a two-component x-ray source model*. Med. Phys. **22**, 2045-2055 (1995).
38. Clarkson JR. *A note on depth doses in fields of irregular shape*. Br. J. Radiol. **14**, 265-268 (1941).

39. Sharpe MB, Jaffray DA, Battista JJ, Munro P. *Extrafocal radiation: a unified approach to the prediction of beam penumbra and output factors for megavoltage x-ray beams*. Med. Phys. **22**, 2065-2074 (1995).
40. van Dam J, Bridier A, Lasselin C, Blanckaert N, Dutreix A. *Influence of shielding blocks on the output of photon beams as a function of energy and type of unit*. Radiother. Oncol. **24**, 55-59 (1992).
41. Khan FM. *The Physics of Radiotherapy*. Williams & Wilkins, (1984)
42. Day MJ, Aird EGA. *The equivalent square method for dose determinations in rectangular fields*. Br. J. Radiol. **Suppl. 17**, Appendix A, 105-114 (1983).
43. Yu MK, Murray B, Sloboda R. *Parametrization of head-scatter factors for rectangular photon fields using an equivalent square formalism*. Med. Phys. **22**, 1329-1332 (1995).
44. Tatcher M, Bjärngård BE. *Head-scatter factors in blocked photon fields*. Radiother. Oncol. **33**, 64-67 (1994).
45. Yu MK, Sloboda RS. *Effect of beam blocking on linac head scatter factors*. Int. J. Radiol. Oncol. Biol. Phys. **37**, 465-468 (1997).

5

The *dynMLC* program

Section:

5.1	Introduction.....	124
5.2	Programming platform	124
5.3	Input data for the <i>dynMLC</i> program.....	125
5.4	Determination of leaf positions.....	128
5.5	Corrections for the MLC transmission and leaf penumbra	134
5.6	Determination of the monitor unit setting for each subfield	139
5.7	Time required to deliver a dynamically-compensated field	146
5.8	Subfield visualization	148
5.9	Summary	154
5.10	References.....	154

5.1 INTRODUCTION

This chapter describes the computer program which has been written to calculate the required multileaf collimator positions for the delivery of a given intensity matrix. The program's input data, mathematical algorithm, output data, and user-interface are discussed. The intricate details of the computer code will not be discussed but can be obtained by consultation with the author.

5.2 PROGRAMMING PLATFORM

The program was written on a Hewlett Packard 700-series UNIX workstation with the aid of the Advanced Visualization Systems (AVS) software development package. The AVS package provides a sophisticated programming environment which handles many input/output procedures, and most rendering, display, and graphing

functions. It also contains a library of multi-dimensional image-processing and image-analysis tools. The basic unit in the AVS package is known as a *module*, which is a routine written in either the C or Fortran programming language, with certain additional lines of code to allow it to function in the AVS environment. Modules generally exhibit one or more input and output ports, enabling a set of modules to be "piped" together, thereby creating a dedicated application. The AVS package comes equipped with a standard set of modules, but the user may also write portions of code for his own specific purposes and compile it as an AVS module. The majority of modules used in our *dynMLC* program fall into this latter category.

5.3 INPUT DATA FOR THE *dynMLC* PROGRAM

The *dynMLC* program requires two inputs: a matrix containing beam intensity values (i.e, relative energy fluence values) as a function of position at the level of the patient isocentre (referred to as the *CADPLAN intensity file*) and a beam's-eye view (BEV) file giving the shape of the radiation field at the level of the patient surface (referred to as the *CADPLAN BEV file*). The *dynMLC* program is written to accept these two files in the format produced by the CADPLAN treatment planning system.

CADPLAN intensity file: Patient record (i.e., header) of 708 bytes containing information relative to the patient and the field for which the compensator was designed. The file then contains the calculated intensity values in a 177×177 array, ranging from a minimum value of 0 to a maximum value of 1. The resolution of the grid is 0.25 cm, thus giving a total physical size for the matrix of 44.0×44.0 cm². The intensity file has a file size of 126024 bytes and is in binary format with each intensity value occupying four bytes. In theory, values beyond the field limits should have an intensity value equal to

zero, but due to imperfections of the CADPLAN TPS this is not usually true. Therefore to handle this problem we need a second file, the CADPLAN BEV file.

CADPLAN BEV file: Patient record (i.e., header) of 240 bytes containing information relative to the patient and the field for which the BEV was defined. The file then contains X and Y coordinates for the vertices of the shielding blocks the dosimetrist may have entered. If the dosimetrist elects to use the MLC rather than blocks for shielding, the MLC leaf-end positions for the 26 leaf-pairs are stored as well. The BEV file has a file size of 9600 bytes and is in binary format with each MLC position occupying four bytes.

The *dynMLC* program presents a file browser through which the user may select the CADPLAN intensity file and BEV file for the case at hand. Once selected, the intensity file is immediately interpolated out to a 401×401 pixel matrix at a resolution of 1.00 mm. This increased resolution is useful in the calculation of the leaf sequence discussed below. Since the maximum field size attainable with the Clinac 2300 C/D is 40×40 cm², a 2 cm border around the intensity matrix can be cropped away. The BEV block file containing the coordinates of the MLC leaf ends is also cast onto a 401×401 pixel matrix at 1.00 mm resolution, similarly to the intensity matrix. Values under a leaf are assigned a value of zero; values not occluded by a leaf are assigned a value of 1.

The two input matrices, now in their new 401×401 format, are then multiplied together, pixel by pixel. This has the effect of masking out the unwanted extensions of the intensity matrix, thus limiting the intensity matrix to the region to be treated. The resultant matrix, an example of which is shown in Fig. 5.1, is presented to the user for qualitative inspection on screen as a series of contour lines. For quantitative inspection, a dashed line (also shown in Fig. 5.1) can be moved interactively through the contour plot

in both the X and Y directions. A profile of the intensity matrix at the position of the dashed line is displayed in the form of a graph as by an example in Fig. 5.2.

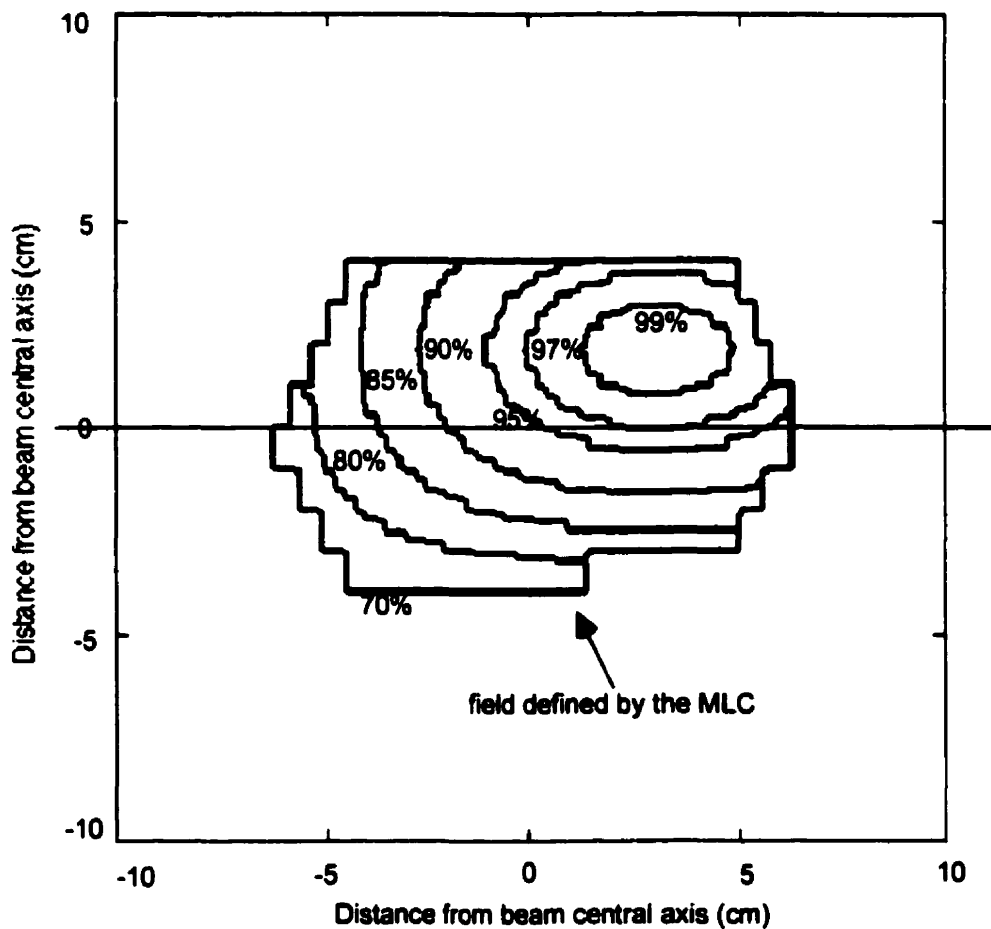


Figure 5.1. Intensity matrix presented for qualitative inspection as a series of contour lines. In this representation, the extensions of the intensity matrix which lie underneath the MLC leaves have been masked out. The data are normalized to 100%.

5.4 DETERMINATION OF LEAF POSITIONS

A. Overview

The *dynMLC* program makes use of the "static subfield" approach to beam intensity modulation. In this approach, the required intensity distribution for a given radiation field is delivered to the patient through a pre-calculated sequence of MLC-defined subfields, each having a different associated monitor unit setting. Its algorithm is similar in conception to the algorithm presented by Bortfeld^{1,2}. However, our technique is different in that it delivers the majority of the patient dose for a given field through the first MLC subfield of the leaf sequence, rather than delivering an equal dose through all subfields, as in Bortfeld's step-and-shoot leaf-sequencing algorithm. Our approach provides for a faster beam delivery, since the leaf sequence contains fewer subfields, and is also more comforting to traditionally-minded medical staff who generally view MLC leaf motion during treatment with some apprehension. In our approach, the leaves typically only rearrange themselves for the last 20% or so of the total number of monitor units delivered for a given field.

In simple terms, the calculation of the leaf sequence proceeds as follows. At 1 cm intervals throughout the intensity matrix, profiles of the intensity along the direction of leaf motion are extracted. These profiles represent the intensity to be delivered under each of the 26 leaf pairs of the MLC. Each 2D intensity profile is then partitioned, or "sliced", into a number of regularly-spaced intensity levels. The positional coordinates of the intercepts of a given intensity level with the intensity profile form a set of positions at which that particular MLC leaf pair must be placed during beam-on to deliver the given intensity level. This process is repeated for all intensity levels and then for all leaf pairs. Once completed, the resultant set of leaf pair positions is sorted to establish a sequence of subfields which can be delivered efficiently. A monitor unit

setting is calculated for each subfield from the knowledge of the particular dosimetric characteristics of the linear accelerator.

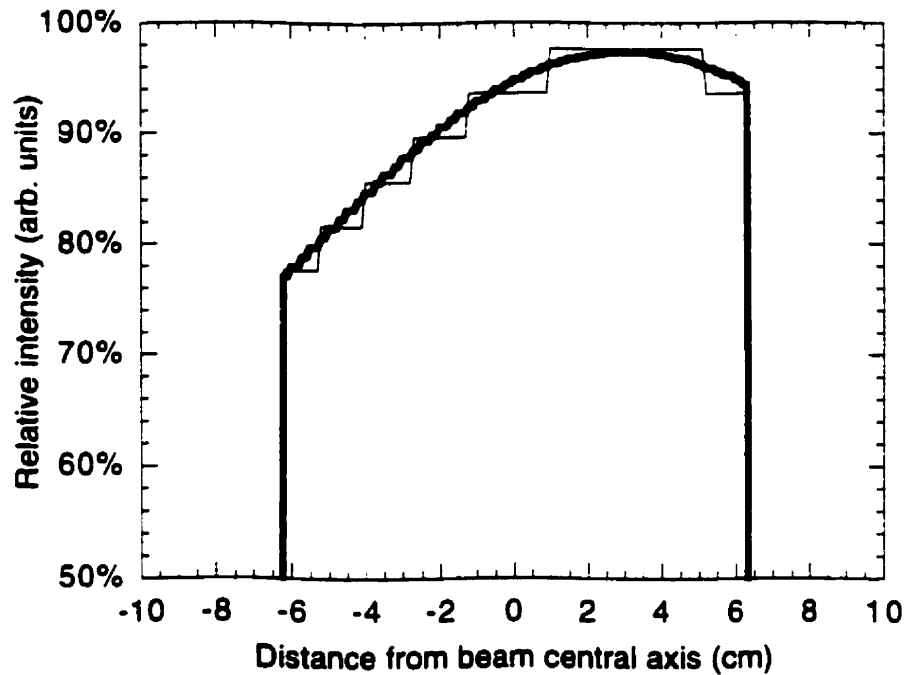


Figure 5.2. Intensity profile along the dashed line in Fig. 5.1 (thick line) and the approximate intensity distribution that will be delivered if an accuracy of $\pm 2\%$ is selected by the user (thin line).

B. Specifics

Let us now explain the procedure for determining the leaf positions in greater detail. For the moment, we will assume that the MLC leaves possess zero transmission and an infinitely sharp penumbra. The small corrections to account for these two effects will be incorporated in the next section.

Typically the intensity matrix has a lowest value close to 0.8 (the maximum value being 1.0) and all of the modulation occurs at intensity values higher than this minimum value. The reason for this high minimum intensity value is that intensity-modulated beam delivery is frequently used simply for missing tissue compensation. The photon intensity "beneath" this minimum value can be delivered in one shot with a single MLC-defined subfield. In this respect our algorithm is more efficient than the algorithm of Bortfeld which always assumes the minimum value to be zero. The first task of the program therefore is to scan the intensity profiles under all 26 leaf pairs and extract a minimum intensity value for the matrix. In the example depicted in Fig. 5.1, the minimum intensity value inside the radiation field limits is 0.756. The slicing of the intensity distribution thus starts at this minimum value, minus half of the slicing increment, and continues until the value of 1 is surpassed. The allowable, user-selected, increments for the slicing of the intensity distribution are 0.01, 0.02, 0.03, and 0.04. The selected increment specifies, with all other sources of error neglected, the accuracy of the delivered intensity distribution compared to the desired intensity distribution, which will be respectively, $\pm 0.5\%$, $\pm 1.0\%$, $\pm 1.5\%$, or $\pm 2.0\%$. The choice of the accuracy level also affects the total treatment time since the number of subfields needed to approximate the desired intensity distribution at a specified level of accuracy increases linearly with the selected accuracy level. Figure 5.2 illustrates this point for the profile under the leaf-pair indicated by the dashed line in Fig. 5.1. An accuracy level of $\pm 2.0\%$ has been chosen for this example.

Let x_i^j be the i th position under leaf-pair j corresponding to the intersection of intensity level k with the desired intensity distribution $I(u, v)$. Thus, for instance, $^{88\%}x_3^{19}$ will refer to the third intersection of the 88% intensity level with the profile of the intensity distribution under leaf-pair 19. In order to determine all of the intercepts x_i^j , the *dynMLC* program first selects a leaf pair, then an intensity level, finds all the

positional coordinates of the intercepts of that intensity level with a profile of the intensity matrix, and then exhausts all the intensity levels before switching to the next leaf-pair. All of the intercepts with an even index i correspond to rising portions of the intensity profile and thus to a position for a B side leaf. Similarly, the intercepts with an odd index i correspond to falling portions of the intensity profile and thus to a position for an A side leaf.

There are two possible types of intersections between a given intensity level and a profile of the intensity matrix. The first is for the given intensity level to fall *between* two points of the intensity profile. The second is for the given intensity level to *exactly correspond* to a point of the intensity profile. These two possible types of intersections are illustrated in Fig. 5.3.

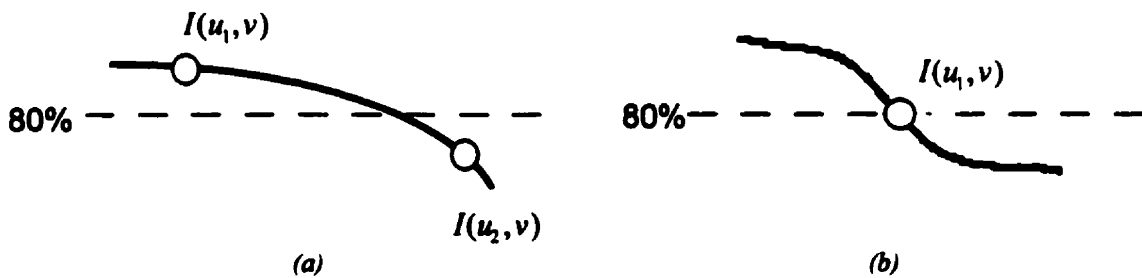


Figure 5.3. Illustration of the two possible types of intersections of a given intensity level with a profile of the intensity distribution. In (a), the intensity level falls between two points of the profile, while in (b) the intensity level intersects the profile at one of the points of the profile.

In the first type of intersection, the position of the intercept can be approximated by a linear interpolation between u_1 and u_2 such that:

$${}^i x_i^j = u_1 + (u_2 - u_1) \left(\frac{k - I(u_1, v)}{(I(u_2, v) - I(u_1, v))} \right) . \quad (5.1)$$

The second type of intersection is simpler, and results in the following simple solution:

$${}^k x_i^j = u_i \quad (5.2)$$

However, certain intersections of the second type must be excluded, as depicted in Fig. 5.4. The excluded cases are:

- a) The intensity level intersects the profile at a local extremum. This places the leaves on the A and B sides at the same position, which is redundant since radiation cannot be delivered in this configuration. Therefore, we ignore this type of intersection.
- b) The intensity level coincides with a plateau of the profile, which implies a multitude of intersection points adjacent to one another. To avoid this impractical and undesirable situation, one has the option of choosing the intersection point which neighbours either the falling or the rising end of the plateau, or any point in between the two. We choose the point which neighbours the falling end of the plateau, although it is an arbitrary decision whether to "overdose" or "underdose" the plateau region.

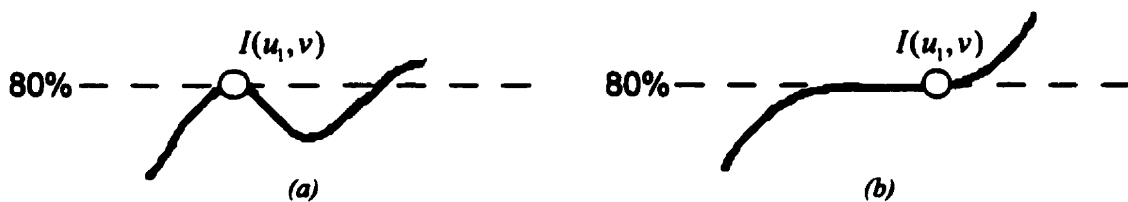


Figure 5.4. Illustration of the two cases in which the intersection of a given intensity level with a profile of the intensity distribution is problematic. In (a), the intensity level intersects with a local extremum of the profile and in (b) the intensity level coincides with a plateau of the profile.

C. Sorting of the leaf positions

Once calculated, the array ${}^k x_i^j$ of leaf positions can be sorted in one of two ways. The leaf positions can be sorted *independently* on the A and B sides in order of

increasing position in such a way that the leaves always travel from left to right. This is known as the *sliding window* delivery technique. The leaf positions can also be sorted as *pairs* of A and B leaf positions such that the B leaf of the pair always moves from left to right, but the A leaf does not necessarily. In this latter strategy, the leaves close in on each peak of the intensity distribution in what is known as the *close-in* delivery technique. Despite having different leaf sequences, both techniques yield the same intensity matrix at the level of the patient, as is depicted in the example of Fig. 5.5. Note that the first subfield is the same for both techniques, i.e., it is excluded from the sorting process.

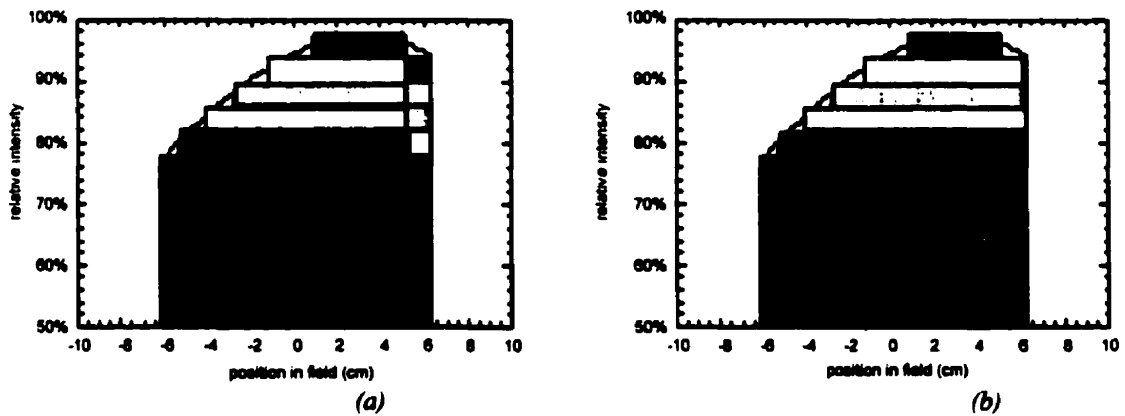


Figure 5.5. Illustration of two ways in which the leaf sequence may be sorted. The coloured bars represent the dose contributions from the individual subfields. In the sliding window technique (a), all leaves move from left to right. In the close-in technique (b), the leaves converge on each peak of the intensity distribution.

D. Required number of subfields

The number of positions calculated for a given leaf-pair will depend on the complexity of the intensity profile that must be delivered by that leaf-pair and on the user-selected accuracy level. For a given accuracy level, the leaf-pair with the maximum number of positions determines the number of subfields required for the delivery of the entire intensity matrix. Some leaf-pairs will complete their motions before the end of the

full delivery of the field and others may not be needed at all during the delivery. These "unused" leaves must be closed so as not to allow the passage of radiation. As mentioned in Section 4.7, to minimize leaf-end leakage, closed leaf-pairs are positioned completely to one side of the field, and under one of the jaws of the linear accelerator.

5.5 CORRECTIONS FOR THE MLC TRANSMISSION AND LEAF PENUMBRA

To achieve accurate dosimetry two corrections must be applied to the above calculation of the leaf sequence: one to account for photon transmission through the MLC leaves and the other to account for the penumbra width of the leaf ends.

A. Transmission through the MLC

As discussed in Section 4.7, the average transmission of the MLC is 2.5% for the 6 MV beam and 3.0% for the 18 MV beam. Ingoing this transmission will cause the actually delivered intensity to be slightly elevated compared to the desired intensity, most notably in regions that are shielded for a high proportion of the total irradiation time of a given field. For example, a point which is supposed to receive an intensity of 70% might actually receive an intensity of 75%, if it is part of a complex intensity matrix which takes a long time to be delivered.

To correct for the MLC transmission we must know the time that each point in the intensity matrix is occluded by the MLC relative to the total treatment time for the given field. However, we cannot know this until we know the leaf sequence. This therefore implies an initial run of the above algorithm to determine the approximate leaf sequence. Then, after the first pass of the leaf position calculation algorithm, we can calculate the transmitted intensity that each point in the intensity matrix would theoretically receive with the approximate leaf sequence. Subtraction of the transmitted

intensity matrix from the original intensity matrix will yield a new "corrected" intensity matrix on which we will run the leaf position calculation algorithm a second time. These new leaf positions, when delivered, will yield the desired intensity matrix in the presence of transmission. It is important to note that this method of correcting for transmission is only a first-order correction; further iterations of the method should be used to increase accuracy. For example, the intensity value of the point mentioned above which should receive 70% will be reduced to 65% to account for the 5% transmission. However, the 5% transmission value was calculated from the subfields determined by the first pass of the leaf position algorithm, not the second pass subfields which will actually be used for treatment. Thus we may not actually get 5% transmission, but only 4.9%. This source of error is always small and therefore can be neglected.

Let us assume we know the corrected intensity matrix $I'(u,v)$. If N is the number of subfields, ΔI the slicing interval of the intensity profiles, and $\min[I(u,v)]$ the minimum value of the intensity matrix, then the total relative intensity I_{tot} is:

$$I_{tot} = \min[I'(u,v)] + (N - 1)\Delta I \quad . \quad (5.3)$$

The *total relative intensity* represents the intensity (or beam-on time) required to deliver the intensity matrix with the MLC compared to a physical compensator. For single-peaked intensity matrices, the total percentage intensity will equal 100%. For multiply-peaked matrices, on the other hand, each peak must be treated separately and the total percentage intensity will exceed 100%.

The fractional time T_{occ} that a point is occluded by the leaves is equal to:

$$T_{occ} = \frac{I_{tot} - I'(u,v)}{I_{tot}} \quad , \quad (5.4)$$

while the fractional time T_{unocc} that a point is unoccluded is equal to:

$$T_{unocc} = \frac{I'(u, v)}{I_{tot}} \quad . \quad (5.5)$$

Thus the actual intensity $I_{act}(u, v)$ that the point (u, v) will receive is given by:

$$I_{act}(u, v) = I_{tot} T_{unocc} + I_{trans} T_{occ} \quad , \quad (5.6)$$

where I_{trans} is the percentage transmission of the MLC at the selected photon energy. We would like this actual intensity to be equal to the original intensity matrix $I(u, v)$, i.e.,

$$I_{act}(u, v) \equiv I(u, v) \quad . \quad (5.7)$$

This leads to the following solution for the intensity matrix corrected for the MLC transmission:

$$I'(u, v) = \frac{I_{tot} [I(u, v) - I_{trans}]}{(I_{tot} - I_{trans})} \quad , \quad (5.8)$$

and this is the formalism that we used to calculate the new leaf positions in the second pass of the algorithm.

B. Leaf penumbra

So far, our discussion has neglected the effect of the MLC leaf penumbra on the delivered intensity matrix, since we have considered that the MLC leaves possess profiles that resemble step functions.

Section 4.7 contained a detailed discussion of the MLC penumbra. It was determined that the 80%-20% *leaf-end* penumbra is approximately 4.0 mm at 6 MV and 8.0 mm at 18 MV, regardless of the position of the leaf end with respect to the beam central axis. The 90%-10% leaf-end penumbra is 9.0 mm at 6 MV and 18.0 mm at 18 MV, likewise regardless of leaf position. The discussion in Section 4.7 also established that, for the useful range of MLC positions, the readout position of a leaf end corresponds to the 70% radiation intensity level within ± 0.5 mm.

Typical measured radiation profiles of the MLC leaf-end are shown in Fig. 5.6 for the 6 MV and 18 MV photon beams. These two profiles show us that, if the leaf end is placed at the position indicated by the leaf sequence, the region under the leaf end will be slightly overdosed and the region just past the tip will be slightly underdosed. Since we are interested in treating the tumour to a high and uniform dose, the behaviour of the dose distribution in the region of the tumour is far more important than the behaviour in the low-dose region surrounding it. To this end, we will thus adjust the leaf positions so that the position indicated by the leaf sequence coincides with the 80% isodose line rather than the 70% line. For the 6 MV and 18 MV photon beams, this implies shifting the leaf-end positions by 1.0 mm and 2.0 mm, respectively. We reiterate that although this approach treats the high dose region more uniformly, it does so at the expense of the lower dose regions, which as a result are slightly over-treated.

As shown in Section 4.7, the leaf-side penumbra is slightly smaller than the leaf-end penumbra because of the focusing of the leaves in the direction perpendicular to the leaf motion. This is fortunate, since the method used to correct for the leaf-end penumbra cannot be used to correct for the leaf-side penumbra. The only way to open the leaves further in this direction is to open up an entire new pair of leaves, adding a full additional centimetre to the treated area.

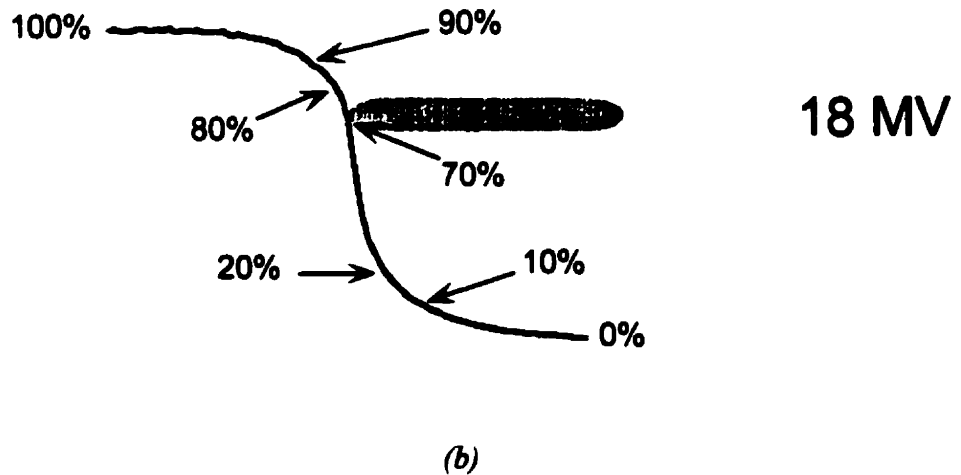
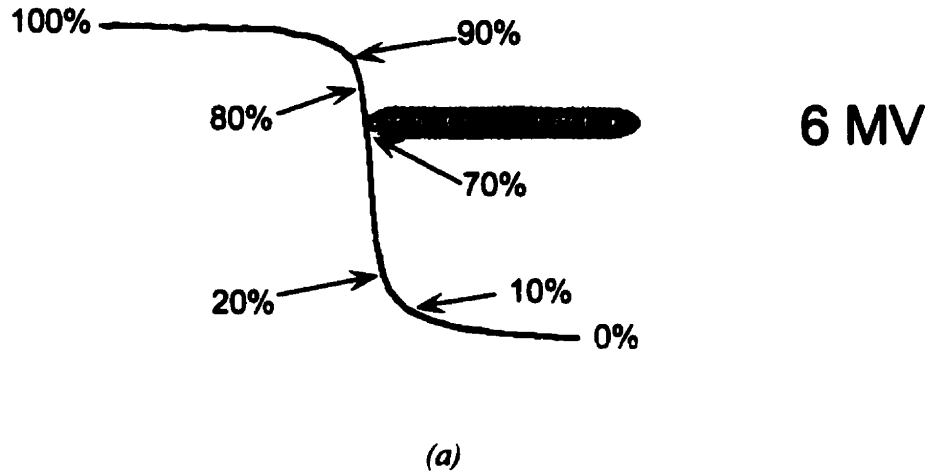


Figure 5.6. Profiles of the leaf-end penumbra at 6 MV (a) and 18 MV (b) photon energies. The readout position of the leaf end initially matches the 70% isodose line of the radiation field but is shifted to match the 80% isodose line.

Several investigators^{3,4} have devised iterative methods to account for leaf-end penumbra. Some of these methods are more accurate than ours, but have the disadvantage of being considerably more complex. Since it is impossible to correct for leaf-side penumbra, we do not believe that it is sensible to expend a substantial effort in

trying to correct rigorously for the leaf-end penumbra, so our rudimentary correction seems adequate.

5.6 DETERMINATION OF THE MONITOR UNIT SETTING FOR EACH SUBFIELD

A. Total relative intensity

As discussed above, the first subfield will deliver a relative intensity equal to the minimum intensity value in the corrected intensity distribution, plus the accuracy level. Thus, if the minimum value is 80% and the accuracy level is $\pm 1.5\%$, the relative intensity for the first subfield will be equal to 81.5%. For each subfield other than the first, the associated relative intensity is twice the accuracy level or, in other words, the slicing increment for the intensity distribution. Thus, if the accuracy level is $\pm 1.5\%$, all fields other than the first will deliver a relative intensity of 3.0%. This method results in a filling of the intensity distribution, as shown in Fig. 5.5. The maximum error in intensity due to the use of a finite number of subfields corresponds approximately to the selected accuracy level.

The intensity distribution depicted in Fig. 5.5 is single-peaked. In such a case, the total relative intensity of all subfields will yield a value of 100% (plus or minus the accuracy level of the calculation). In the case of a more general intensity distribution with multiple peaks, such as that shown in Fig. 5.7, each peak will need to be irradiated separately resulting in total relative intensities that exceed 100%. The relative intensities for each subfield are still determined in the same manner but no longer total 100%.

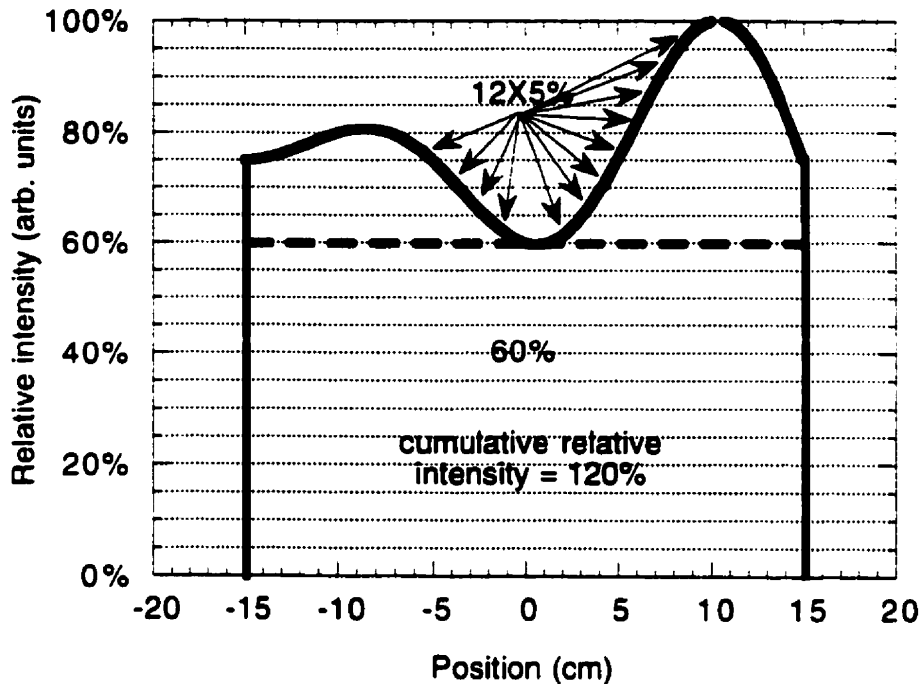


Figure 5.7. Illustration of the fact that intensity distributions containing multiple peaks will result in a total relative intensity which exceeds 100%.

B. Calculation of monitor unit settings

The doses associated with each subfield must be converted to monitor units, which are the "internal" units a linear accelerator uses to keep track of how much radiation has been delivered. A *monitor unit* is that quantity of radiation which will yield a dose of 1 cGy to a point at depth d_{max} in phantom in an SSD set-up and a field size of 10×10 cm². These conditions are known as the "calibration set-up", and the statement 1 MU = 1 cGy will generally not be true for other arbitrary conditions. Monitor units are measured by a transmission ionization chamber located in the head (nozzle) of the linear accelerator. At regular intervals a physicist uses a calibrated ionization chamber to verify that the output of the linear accelerator is equal to 100 cGy/100 MU for the 10×10 cm² field with the chamber placed at d_{max} in a water-equivalent phantom with a SSD of 100 cm. The tolerance on this determination is $\pm 2\%$; if the measurement falls beyond the

tolerance, the gain in the monitor chamber's electrometer is adjusted in such a way that the correspondence $100 \text{ cGy} = 100 \text{ MU}$ is achieved. The output of the linear accelerator (i.e., the ratio cGy/MU) increases slightly with increasing field size as described by the *relative dose factor (RDF)*. A method for obtaining the *RDF* for fields shaped with the Varian MLC was described in detail in Chapter 4.

For SAD patient set-ups (by far the most common) there are two common procedures for normalizing isodose distributions, resulting in two different methods for calculating a monitor unit setting. One procedure is called *isocentre-weighting* and takes the weights of the fields to be defined at isocentre. Thus in this method, three fields having weights of 100%, 90%, and 60% will deliver doses in a ratio of 100%, 90%, and 60% of the total dose of 250% at the isocentre of the treatment. The other method is called *TMR-weighting* (TMR = tissue maximum ratio) and takes the weights of the fields to be defined according to the reference dose delivered for that field. This reference dose is the dose at depth d_{max} in phantom with an SAD of 100 cm, which serves as the reference point. In this procedure, three fields having weights of 100%, 90%, and 60% will deliver doses in a ratio of 100%, 90%, and 60% to their respective reference points. The McGill hospitals use this latter technique.

Figure 5.8 illustrates a typical isodose distribution for a case of rectal carcinoma treated with a photon energy of 10 MV, and planned according to the TMR-weighted method. The patient slice shown is at the isocentre level. There are three radiation fields, a posterior field of dimensions $14.5 \times 20.5 \text{ cm}^2$ with a weighting of 100%, and two lateral fields of dimensions $13.5 \times 20.5 \text{ cm}^2$ with weightings of 90%. This weighting implies that if we deliver 100 cGy to the posterior reference point and 90 cGy to each of the lateral reference points, the isodose distribution, shown in Fig. 5.8, will be obtained with a dose of 222 cGy at the isocentre. The lateral fields each have a metal wedge

placed into the beam which selectively attenuates the beam toward the posterior of the patient thereby compensating for the dose fall-off of the posterior beam as well as the slope of the patient's rump as seen from the lateral fields. The use of the wedge results in a dose distribution which is more uniform in the region of the patient to be treated.

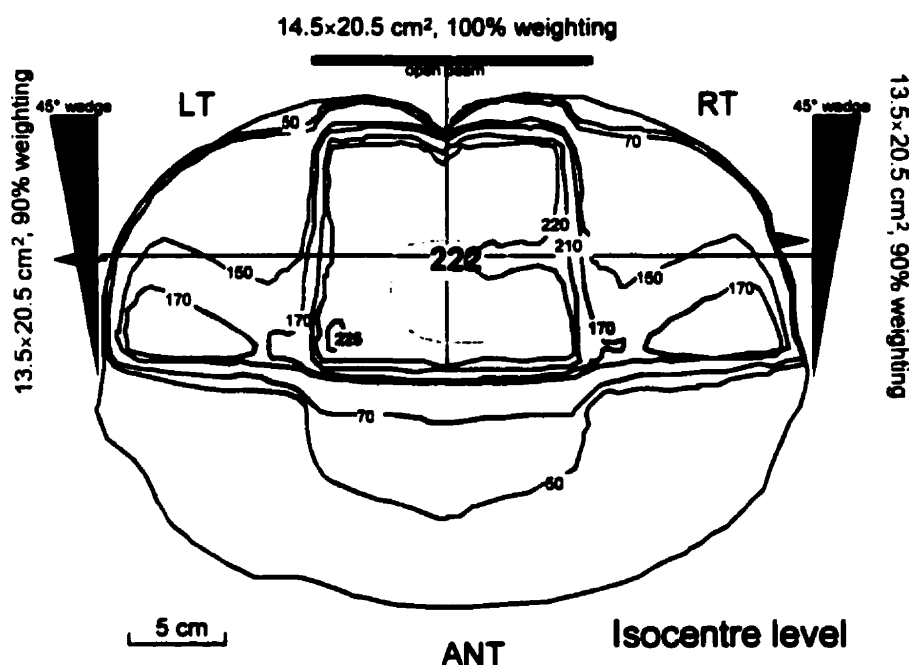


Figure 5.8. TMR-weighted isodose distribution for a three-field pelvic treatment at 10 MV photon energy. The posterior beam has a weighting of 100%; the two lateral beams contain a wedge and each has a weight of 90%.

For this particular case, the physician has prescribed a dose of 45 Gy to be delivered to the isocentre in 25 daily fractions, giving a daily dose fraction of 1.80 Gy. As stated above, the normalization of a TMR-weighted isodose distribution is such that if 100 cGy are delivered through the posterior field to the reference point and 90 cGy through each lateral field to the reference point a dose of 222 cGy will be delivered to the isocentre. Since we actually only desire 180 cGy at the isocentre, we know that the dose

for each field must be scaled by the factor (180/222), giving 81.1 cGy and 73.0 cGy for the posterior and lateral fields, respectively.

The equivalent square field size is 17.0×17.0 cm² for the posterior field which gives an *RDF* of 1.034, or an output of 1.034 cGy/MU. For the two lateral fields, the equivalent square field size is 16.3×16.3 cm² which gives an *RDF* of 1.031, or an output of 1.031 cGy/MU. We will thus require an MU setting of 78.4 MU to deliver the 81.1 cGy needed for the posterior field and an MU setting of 70.8 MU to deliver the 73.0 cGy needed for each of the two lateral fields. However, for the lateral fields, we have neglected the attenuation of the wedge, which will, through a wedge factor, increase the required MUs for the two lateral beams.

The attenuation of the wedge at the field centre is described with the *wedge factor* (*WF*) which corresponds to the transmission of the wedge on the beam central axis. It is usually measured in the calibration set-up. The wedge factor only describes the effect of the wedge on the beam central axis; the effect at positions off-axis is calculated by the computerized treatment planning system from measured beam profiles. The wedge used in our case has a factor of 0.68 which means that the MU setting must be increased from 70.8 MU to 104.1 MU to account for attenuation as the central beam passes through the wedge.

From this discussion it is evident that the MU setting for field *F*, treated in a conventional manner with a TMR-weighted isodose distribution, is given by the formula:

$$MU(F) = \frac{dose(F)}{WF(F) \times RDF(F)} \quad (5.9)$$

where $dose(F)$ is the dose for field F , $RDF(F)$ is the relative dose factor for field F , and $WF(F)$ is the wedge factor for the wedge used in field F . In the absence of a wedge, $WF(F) = 1.00$.

C. Compensated Beams

In some cases, a combination of differently-weighted beams, each of which may possibly contain a wedge, is insufficient to obtain acceptable dose uniformity within the planning target volume. It may then be desirable to use a variable thickness metal filter known as a *compensator*, which is designed and built specifically for the case at hand. A compensator may be thought of as a sophisticated wedge in which the thickness does not simply follow a ramp, but varies independently from point to point across the beam. All fields of a treatment plan may be compensated, or only the selected ones.

For such a "physical compensator" (i.e., a compensator made of some physical material such as lead) the *compensator transmission factor (CTF)* is, similarly to the wedge factor discussed above, the transmission of the compensator on the beam central axis. It is usually measured with an ionization chamber in the calibration set-up. The compensator factor is needed in dosimetric calculations because the MU setting for a compensated beam must be multiplied by the reciprocal of the compensator factor to account for the photon attenuation in the compensator, exactly as for a wedge. It is never necessary to use both a wedge and a compensator for the same field, since any desired intensity distribution can be achieved with the compensator alone.

For dynamically-compensated beams delivered with the aid of an MLC, the concept of the *CTF* can be carried over in its entirety. The compensator factor is no longer measured, instead it is given by the value of the intensity matrix on the beam central axis, before it is corrected for the MLC transmission. In order to reduce the effect

of small random variations in the intensity matrix produced by the CADPLAN, we take the compensator factor as the average of the pixel values in a 6×6 pixel ROI (pixel size = 1.0 mm) at the centre of the intensity matrix. Just as for a physically-compensated beam, the MU setting for the compensated beam must be multiplied by the reciprocal of the compensator factor to bring the dose at the reference point up to the value for the uncompensated beam. Thus, in our static approach to intensity-modulation with an MLC, the MU setting for subfield s , belonging to field F , will be:

$$MU(F_s) = \frac{dose(F_s)}{RDF(F_s) \times CTF(F)} \quad (5.10)$$

Note that the centre of a given subfield will in general not correspond with the beam central axis. It was shown in Section 4.8 that in such circumstances the equation for the MU setting should be corrected by the off-axis ratio. This, however, is unnecessary in our particular case, since the off-axis behaviour of the photon beam is already incorporated into the isodose distribution by the CADPLAN treatment planning system, and obviously does not need to be corrected for a second time.

The total MU for the field F will then be:

$$MU(F) = \sum_s MU(F_s) = \frac{1}{CTF(F)} \sum_s \frac{dose(F_s)}{RDF(F_s)} \quad (5.11)$$

In Eqs. (5.10) and (5.11) we assume that the dose (in medium) for a given subfield, $dose(F_s)$, is directly proportional to the relative intensity (in air) for that subfield. For instance, if the relative intensity for a particular subfield is 3%, the total relative intensity is 120%, and the total daily dose for the field is 100 cGy, then the daily dose for the subfield will be $(3/120) \times 100 \text{ cGy} = 2.5 \text{ cGy}$. The hypothesis of a simple

proportionality relationship between dose and intensity is not strictly valid due to photon and electron transport in the medium; however, at shallow depths in phantom the approximation is very good. The daily dose for the subfield, $dose(F_i)$, is, as we recall, defined at a depth of d_{max} .

5.7 TIME REQUIRED TO DELIVER A DYNAMICALLY-COMPENSATED FIELD

If the leaves of the MLC could move between subfields with infinite velocity, the time required to deliver the total MU for field F in a dynamically-compensated treatment would be given by the ratio of the total MU for the field Eq. (5.11) and the rate of MU delivery, MU' :

$$time_F^{dyn.} = \frac{MU(F)}{MU'} = \frac{1}{CTF(F) \times MU'} \sum_i \frac{dose(F_i)}{RDF(F_i)} \quad (5.12)$$

Typically, the total MU required for a field is of the order of 100 MU. Since our Clinac 2300 C/D is operated at 400 MU/min for patient treatment, this implies a treatment time on the order of 15 s per field. The DBD ToolBox software takes fractions of a second to drive the MLC leaves from one subfield configuration to the next adding, in total, at most a few seconds to the treatment time.

Compared to treatments in which the intensity modulation is produced by a physical compensator, intensity modulation using an MLC is generally slightly more time-consuming. For a physical compensator, the time required to deliver the total MU for field F is given by:

$$time_F^{phys.} = \frac{MU(F)}{MU'} = \frac{dose(F)}{MU' \times CTF(F) \times RDF(F)} \quad (5.13)$$

To compare this to the time needed to deliver a dynamically-compensated treatment [Eq. (5.12)], we define the *efficiency factor* (EF) which is the ratio of the time required to deliver the treatment with a physical compensator to the time required to deliver the treatment dynamically, i.e.,

$$EF = \frac{time_F^{phys.}}{time_F^{dym.}} = \frac{dose(F)}{RDF(F)} \bigg/ \sum_i \frac{dose(F_i)}{RDF(F_i)} \quad (5.14)$$

Since all RDF values are almost identical, this can be very well approximated by:

$$EF \approx \frac{dose(F)}{\sum_i dose(F_i)} \quad (5.15)$$

The EF will never exceed 1.00; however, it will be equal to 1.00 for an intensity distribution with a single peak. For an intensity distribution with multiple peaks, each peak must be irradiated separately, and this will invariably result in an EF that is less than 1.00. The EF will also decrease with an increasing depth of modulation. As an example, an intensity distribution which contains three peaks and has a minimum value of 80% will have an EF of approximately 0.7, and thus a treatment which takes 20 s with a physical compensator will take 28 s using MLC dynamic compensation, plus a few seconds for MLC motion during beam delivery. However, in this latter approach, there is no need for the technologists to enter the treatment room to replace the compensator when switching from one compensated field to another and this results in considerable saving in technologists' time and effort.

5.8 SUBFIELD VISUALIZATION

Once the subfields and their associated monitor unit settings are calculated, the user of the *dynMLC* program can view the subfields in a window showing the 52 MLC leaves drawn to scale at the top left, and three widget panels located at the bottom and on the right side. An example is shown in Fig. 5.9.

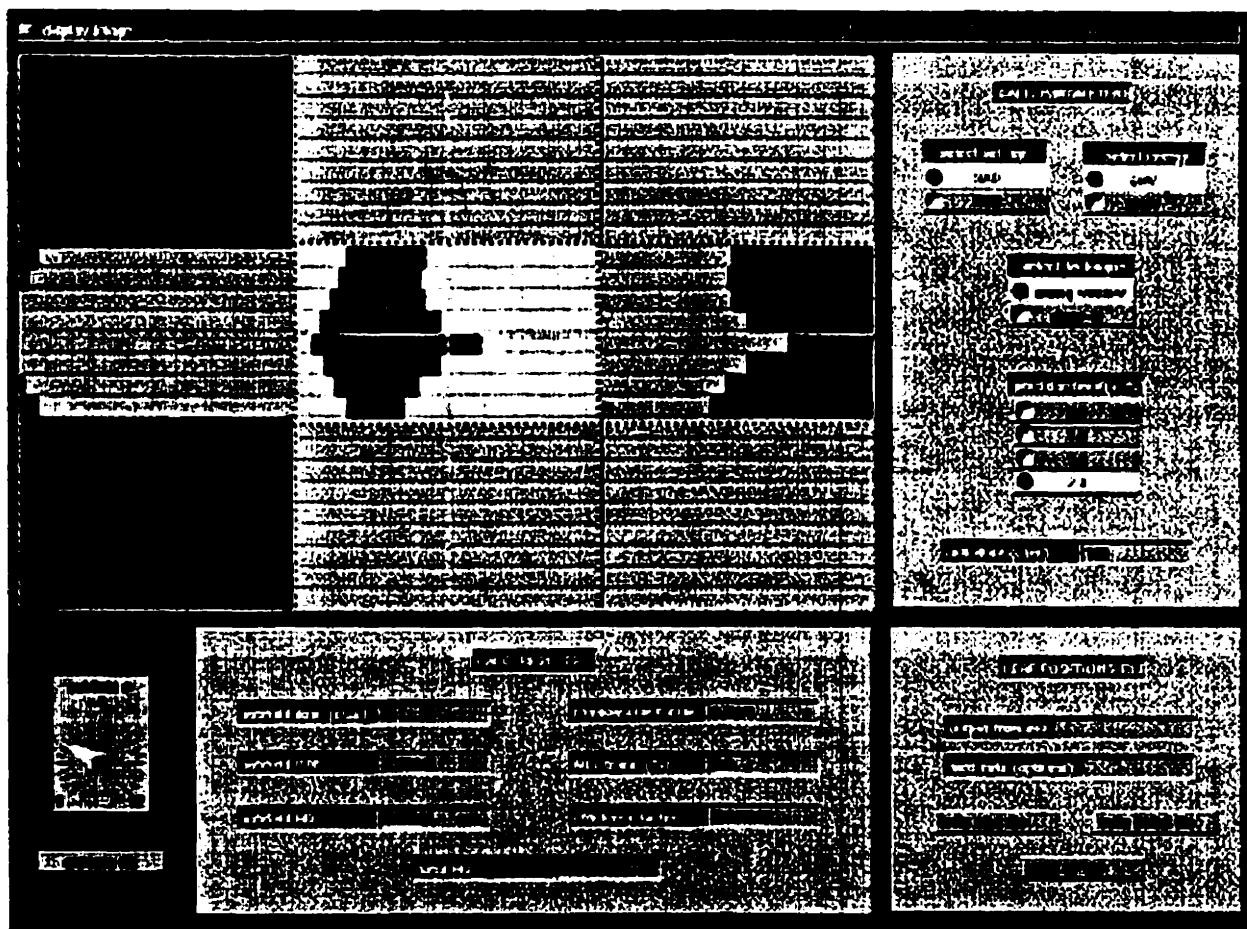


Figure 5.9. Appearance of the computer window allowing the user of the dynMLC program to visualize the MLC subfields and the associated treatment parameters.

The panel at the bottom left contains a dial allowing the user to display a particular subfield for viewing. The maximum value on the dial automatically scales to the total number of subfields in the treatment. A button labelled "animate Rx" located below the dial can be pressed to visualize the delivery of the entire sequence of subfields

in approximately real-time. The dark grey portions of the leaves are shielded by the linear accelerator jaws. The panel on the top right side contains widgets allowing the user to toggle between different calculation options. The options presented are the beam energy (6 MV or 18 MV), the treatment set-up (SAD or SSD), the precision level of the calculation ($\pm 0.5\%$, $\pm 1.0\%$, $\pm 1.5\%$, $\pm 2.0\%$, or $\pm 5.0\%$), the delivery technique (sliding window or close-in), and the daily dose to be delivered by the field. If any of these options are changed, a new set of subfields and associated MUs are immediately recalculated corresponding to the new settings. The panel on the bottom left displays some important results of the calculation such as the dose, the *RDF*, and the MU for the given subfield, and certain other results which are the same for all subfields, such as the compensator factor, the efficiency factor, the MLC transmission, and the total MUs required to deliver the field. Finally, the bottom right panel contains a space for the user to write a filename for the ASCII file which is written to control the MLC during treatment. This file is known as a DMLC (dynamic MLC) file and has ".dlc" as its extension. Pressing on "write DMLC file" button writes this file in DOS format to an external 3 1/2 inch flexi-disk.

The format of the DMLC file is as shown below. The word "Field" would more appropriately read "Subfield" in an MLC-modulated treatment but the Varian file format must be respected. The "Index" is a fractional running total of the number of MU that have been delivered. It is equal to 0 at the beginning of the delivery and 1 when the delivery is finished and the total MU count has been reached. The utility of the fractional dose is that it allows the same leaf sequence to be delivered with different total MU settings. The particular leaf sequence listed below contains 17 different subfields; however, in a segmented delivery approach the DMLC file must contain twice as many "Field" as the number of subfields actually in the leaf sequence. The reason for this is that, for every subfield, identical starting and finishing positions of the leaves must be

specified in the form of two "Fields", with only the fractional dose changing between these two "Fields".

File Rev = G
Treatment = Dynamic Dose
Last Name = DaVinci
First Name = Leonardo
Patient ID = 567567567
Number of Fields = 8
Number of Leaves = 52
Tolerance = 0.10

Field = # 1
Index = 0.0000
Carriage Group = 1
Operator = McGill University
Collimator = 0.0
Leaf 1A = -7.81
Leaf 2A = -7.81
Leaf 3A = -7.81
Leaf 4A = -7.81
Leaf 5A = -7.81
Leaf 6A = -7.81
Leaf 7A = 2.01
Leaf 8A = 2.01
Leaf 9A = 2.01
Leaf 10A = 2.01
Leaf 11A = 1.71
Leaf 12A = 1.61
Leaf 13A = 1.61
Leaf 14A = 1.62
Leaf 15A = 1.82
Leaf 16A = 2.01
Leaf 17A = 2.01
Leaf 18A = 1.52
Leaf 19A = 0.21
Leaf 20A = -0.78
Leaf 21A = -7.81
Leaf 22A = -7.81
Leaf 23A = -7.81
Leaf 24A = -7.81
Leaf 25A = -7.81
Leaf 26A = -7.81
Leaf 1B = 7.81
Leaf 2B = 7.81
Leaf 3B = 7.81
Leaf 4B = 7.81
Leaf 5B = 7.81
Leaf 6B = 7.81
Leaf 7B = 6.61
Leaf 8B = 6.61
Leaf 9B = 6.60

Leaf 10B = 6.60
Leaf 11B = 6.61
Leaf 12B = 6.61
Leaf 13B = 6.51
Leaf 14B = 6.31
Leaf 15B = 6.11
Leaf 16B = 6.01
Leaf 17B = 5.71
Leaf 18B = 5.51
Leaf 19B = 5.31
Leaf 20B = 5.21
Leaf 21B = 7.81
Leaf 22B = 7.81
Leaf 23B = 7.81
Leaf 24B = 7.81
Leaf 25B = 7.81
Leaf 26B = 7.81
Note = 0
Shape = 0
Magnification = 1.00

Field = # 2
Index = 0.8600
Carriage Group = 1
Operator = McGill University
Collimator = 0.0
Leaf 1A = -7.81
Leaf 2A = -7.81
Leaf 3A = -7.81
Leaf 4A = -7.81
Leaf 5A = -7.81
Leaf 6A = -7.81
Leaf 7A = 2.01
Leaf 8A = 2.01
Leaf 9A = 2.01
Leaf 10A = 2.01
Leaf 11A = 1.71
Leaf 12A = 1.61
Leaf 13A = 1.61
Leaf 14A = 1.62
Leaf 15A = 1.82
Leaf 16A = 2.01
Leaf 17A = 2.01
Leaf 18A = 1.52
Leaf 19A = 0.21
Leaf 20A = -0.78
Leaf 21A = -7.81
Leaf 22A = -7.81
Leaf 23A = -7.81
Leaf 24A = -7.81
Leaf 25A = -7.81
Leaf 26A = -7.81
Leaf 1B = 7.81
Leaf 2B = 7.81

Leaf 3B = 7.81
Leaf 4B = 7.81
Leaf 5B = 7.81
Leaf 6B = 7.81
Leaf 7B = 6.61
Leaf 8B = 6.61
Leaf 9B = 6.60
Leaf 10B = 6.60
Leaf 11B = 6.61
Leaf 12B = 6.61
Leaf 13B = 6.51
Leaf 14B = 6.31
Leaf 15B = 6.11
Leaf 16B = 6.01
Leaf 17B = 5.71
Leaf 18B = 5.51
Leaf 19B = 5.31
Leaf 20B = 5.21
Leaf 21B = 7.81
Leaf 22B = 7.81
Leaf 23B = 7.81
Leaf 24B = 7.81
Leaf 25B = 7.81
Leaf 26B = 7.81
Note = 0
Shape = 0
Magnification = 1.00

Field = # 3
Index = 0.8600
Carriage Group = 1
Operator = McGill University
Collimator = 0.0
Leaf 1A = -7.81
Leaf 2A = -7.81
Leaf 3A = -7.81
Leaf 4A = -7.81
Leaf 5A = -7.81
Leaf 6A = -7.81
Leaf 7A = 2.00
Leaf 8A = 2.00
Leaf 9A = 2.00
Leaf 10A = 2.00
Leaf 11A = 1.71
Leaf 12A = 1.61
Leaf 13A = 1.61
Leaf 14A = 1.61

etc..... for all other subfields.

The positions of the linear accelerator jaws during beam delivery can be set to a bounding rectangle either by manual entry at the console or under computer control from a CONFORMAL PROGRAM file which is a DOS file carrying ".cp" as its extension. An example of this file is provided below with explanatory comments prefixed by a # sign.

```

4  #NUMBER OF MOVING AXES (user-given)
   #PERMISSIBLE MOVING AXIS ARE: Gantry
   #                               Collimator rotation
   #                               all 4 jaws
   #
   #The integer codes for each clinac axis are:
   #GANTRY RTN=0
   #COLL RTN=1
   #COLL Y1=2
   #COLL Y2=3
   #COLL X2=4
   #COLL X1=5

5 4 2 3  #ORDER IN WHICH VALUES FOR MOVING
          #AXES WILL BE SPECIFIED BELOW (user-given)
          #
2        #NUMBER OF TREATMENT INSTANCES
          #
          #
#dose frac. X1 pos.   X2 pos.   Y1 pos.   Y2 pos.
0.000      7.8       6.4       5.0       5.0
1.000      7.8       6.4       5.0       5.0

```

In this example, only the four jaws are instanced. However, in a general case, the collimator and gantry orientations may also be controlled by the CP file. As for the DMLC file, pressing on "write CP file" button writes this file in DOS format to an external 3 1/2 inch flexi-disk which can be read and compiled by the Clinac 2300 C/D console computer. Once the user is finished writing the DMLC and CP files, the *dynMLC* program can be exited by choosing "Exit" from the main menu.

5.9 SUMMARY

This chapter has explained the *dynMLC* program, specifically: how the program calculates the shape of the MLC-defined subfields required to deliver a particular intensity-modulated beam, how it calculates the associated MU setting for each subfield, and how it corrects for MLC transmission and MLC leaf penumbra. The time required to deliver an intensity-modulated beam in the segmented approach on a computerized linear accelerator has also been evaluated.

5.10 REFERENCES

1. Bortfeld TR, Kahler DL, Waldron TJ, Boyer AL. *X-ray field compensation with multileaf collimators*. *Int. J. Radiat. Oncol. Biol. Phys.* **28**, 723-730 (1994).
2. Geis P, Boyer AL. *Use of a multileaf collimator as a dynamic missing-tissue compensator*. *Med. Phys.* **23**, 1199-1205 (1996).
3. Mohan R, Wu Q, Wang X, Stein J. *Intensity modulation optimization, lateral transport of radiation, and margins*. *Med. Phys.* **23**, 2011-2021 (1996).
4. Spirou SV, Chui C-S. *Generation of arbitrary intensity profiles by combining the scanning beam with dynamic multileaf collimation*. *Med. Phys.* **23**, 1-8 (1996).

6

Measurements of intensity-modulated beams

Section:

6.1	Introduction.....	155
6.2	Tests of the <i>dynMLC</i> program	155
6.3	Tests of the inverse planning capabilities of the CADPLAN TPS	170
6.4	Summary.....	174

6.1 INTRODUCTION

The bulk of this chapter is dedicated to a description of the tests performed on the *dynMLC* program to verify the precision with which it can produce a given dose distribution in a phantom. However, this chapter also describes tests designed to verify the validity of CADPLAN's inverse-planning capabilities, i.e., whether it successfully generates the intensity matrix required to produce the given dose distribution in the phantom.

6.2 TESTS OF THE *dynMLC* PROGRAM

A. Procedure used for the *dynMLC* tests

Five formal tests of the performance of the *dynMLC* program were carried out. The aim of these tests was to verify whether or not a certain planar dose distribution could be delivered to a uniform phantom, respecting not only the form of the dose distribution but also the absolute dose at each point in the plane. For all test cases, the dose distribution was measured at a depth d_{max} in phantom; for the final two cases the dose distribution was also measured at a depth of 10 cm in phantom.

The test cases are as follows: a 10×10 cm² open field; a ramp-like field, a parabolic field; an inverted parabolic field; a (cosine)²-like field; and a clinically-useful field. For all cases, the objective was to deliver a dose of 100 cGy to the d_{max} point on the central axis for an SAD 100 cm set-up with a 6 MV photon beam. The 18 MV capabilities of the *dynMLC* program were not formally tested. There are two reasons for this: firstly, beam intensity-modulation is almost never used clinically at such a high photon energy, and secondly, the 18 MV branch of the *dynMLC* program resembles the 6 MV branch in all respects except for some differences in numerical constants.

The SLIC EPID, described in Chapter 3, was used for the verification of the dose delivered by the intensity-modulated fields. As explained in Section 3.7, the EPID-measured data set consists of an image for each subfield of the leaf sequence. The images are calibrated through the measured calibration curve, multiplied by their respective associated monitor unit settings, corrected for the loss of beam horns, and summed up to yield a distribution of the dose in the phantom at the EPID measurement depth.

We compared the dose distributions measured with the EPID to the calculations of our commercial 3D treatment planning system (CADPLAN, version 2.79; Varian Associates, Palo Alto, CA). A comparison between measured dose distributions with the EPID and those obtained with the planning system is accomplished by calculating a dose distribution for a beam normally-incident on a uniform phantom; a condition which approximates the geometry of the EPID measurements. This calculation yields isodose distributions which can be suitably normalized to depict the dose in cGy in the plane of measurement of the EPID.

We also compared our EPID measurements with beam profiler measurements for the more complicated test cases (cosine² and clinically-useful cases). Our beam profiler

(model 1170; Sun Nuclear Corp., Melbourne, FL) consists of 46 radiation-sensitive diodes at intervals of 5 mm, arranged linearly. The diodes are calibrated before use to account for their slightly different dose sensitivities. When subjected to a radiation field, each diode records a charge proportional to the cumulative dose at that position. We verified that the diode array response is stable with regard to moderate changes in beam energy. In our experiments, the array of diodes was positioned at the measurement depth and sheets of phantom material were placed on top (and beneath) the profiler to simulate an in-phantom measurement. The beam profiler results were normalized to the readings obtained with a field for which the linear accelerator output (cGy/MU) is accurately known, thus allowing us to convert our charge readings directly into dose in cGy.

B. Open field

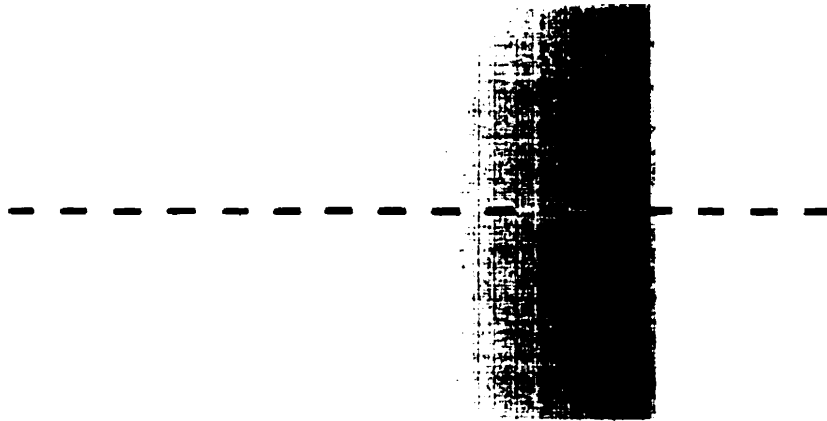
For the 10×10 cm² open field test case an intensity matrix was written which contained a value of 1 within the field limits and a value of 0 beyond the field limits. This intensity matrix was input into the *dynMLC* program, and a leaf sequence was calculated at a precision level of ±0.5%. As would be expected, the leaf sequence consisted of only one subfield, with dimensions of 10×10 cm². The monitor unit setting associated with this unique subfield was 97 MU, exactly as would be obtained from a hand calculation, if a dose of 100 cGy was desired at a depth $d_{max} = 1.5$ cm in phantom for an SAD set-up with a 6 MV photon beam.

C. Ramp-like field

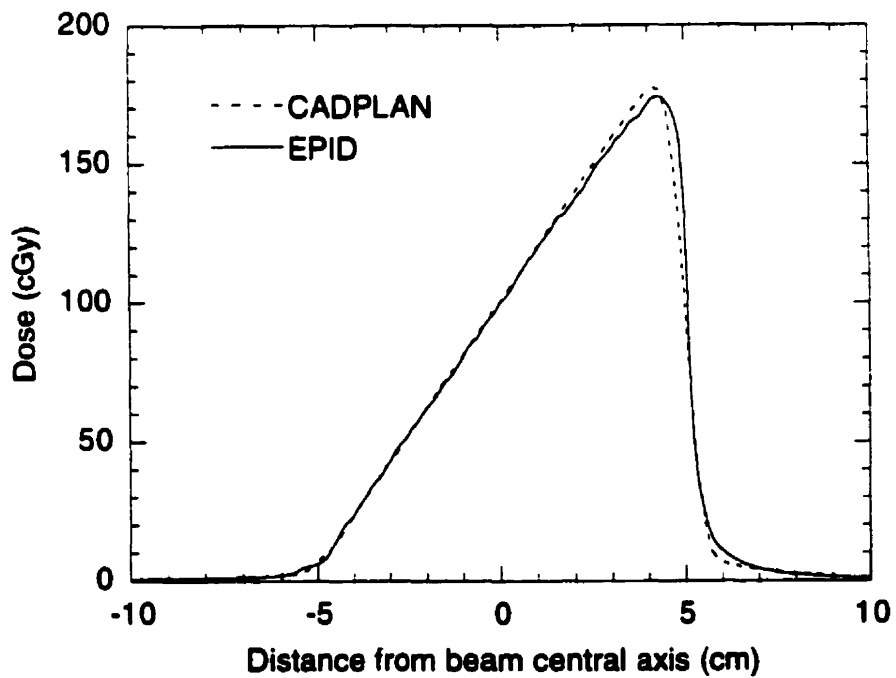
The intensity matrix for the ramp-like field, as for the open field, also had dimensions of 10×10 cm² but the beam intensity within the field limits increased linearly from left to right. The intensity gradient was such that the left side of the field had zero intensity (=0) and the right side full intensity (=1). When the leaves of the MLC were configured to move parallel to the intensity gradient, the *dynMLC* program calculated a

leaf sequence which was composed of 25 subfields. For this example, the precision level of the leaf-sequence calculation was set to allow, in theory, a maximum discrepancy of $\pm 2\%$ between the desired and delivered intensity matrices. A lower value for this inherent discrepancy could be achieved by increasing the number of MLC segments allowed in the leaf-sequence file. The EPID-measured planar dose distribution at depth d_{max} for this case is shown in Fig. 6.1(a). In Fig. 6.1(b), a profile of the EPID-measured dose distribution is extracted along the dashed line of Fig. 6.1(a) and compared to the calculation of the CADPLAN TPS. The agreement between the measured and calculated dose distributions is excellent ($\pm 0.5\%$ on central axis, $\pm 2\%$ elsewhere).

When the leaves of the MLC were configured to move perpendicularly to the intensity gradient, the *dynMLC* program calculated a leaf sequence at a precision level of $\pm 2\%$ which was composed of 10 subfields. The EPID-measured planar dose distribution at depth d_{max} for this case is shown in Fig. 6.2(a). In Fig. 6.2(b), a profile of the EPID-measured dose distribution is extracted along the dashed line of Fig. 6.2(a) and compared to the calculation of the CADPLAN TPS. The agreement between the measured and calculated dose distributions is again excellent ($\pm 0.5\%$ on central axis, $\pm 2\%$ elsewhere). The finite MLC leaf width is apparent in Fig. 6.2, illustrating that it is generally preferable to allow the leaves to move parallel to the direction of steepest gradient in the intensity matrix. Both of these ramp-like intensity-modulated fields were delivered in a "sliding window" technique.

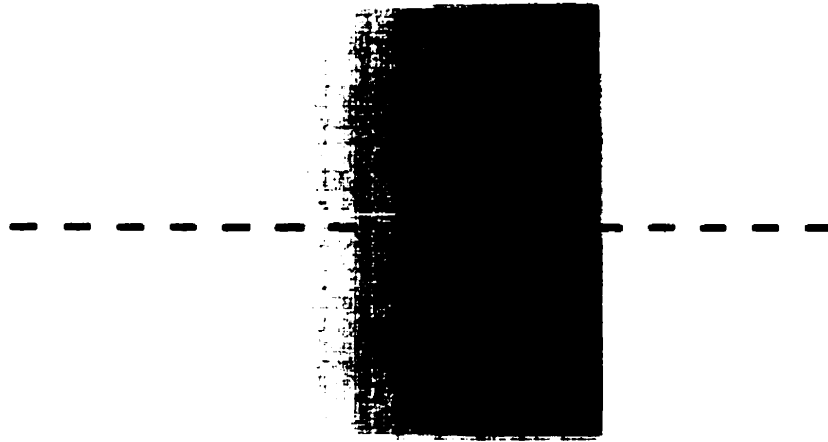


(a)

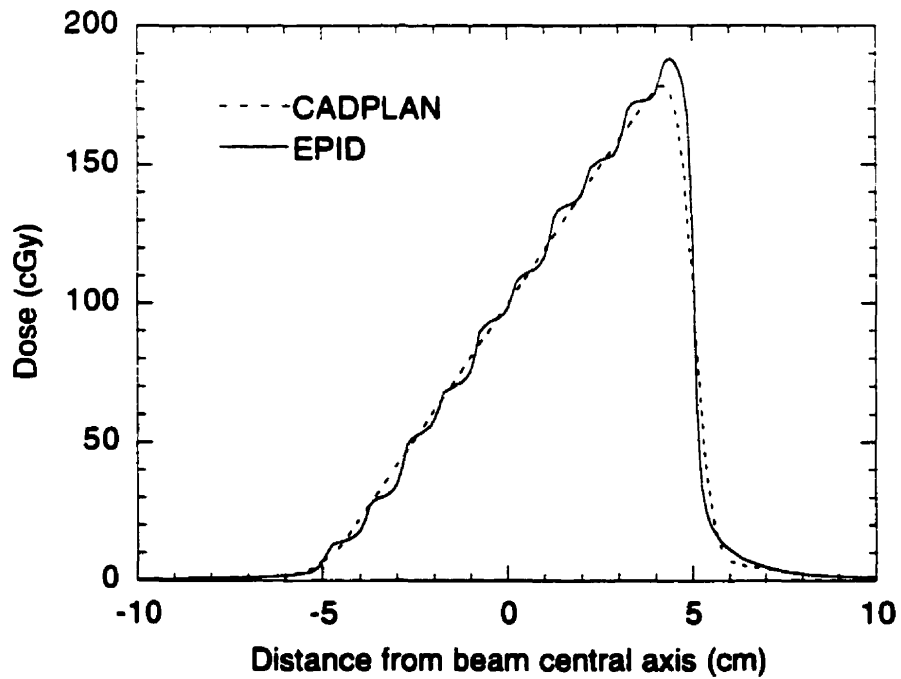


(b)

Figure 6.1. (a) EPID-measured 6 MV dose distribution for the ramp-like field at depth d_{max} for an SAD set-up. In (b), a profile of the EPID measurement (—) is extracted along the dashed line in (a) showing agreement with the calculation carried out with our treatment planning system (---). In this example, the ramp-like field was delivered with a leaf sequence in which the MLC leaves moved parallel to the intensity gradient.



(a)



(b)

Figure 6.2. (a) EPID-measured 6 MV dose distribution for the ramp-like field at depth d_{max} for an SAD set-up. In (b), a profile of the EPID measurement (—) is extracted along the dashed line in (a) showing agreement with the calculation carried out with our treatment planning system (- - -). In this example, the ramp-like field was delivered with a leaf sequence in which the MLC leaves moved perpendicularly to the intensity gradient.

D. Parabolic field

The parabolic distribution was again nominally of dimensions 10×10 cm² with a cylindrically-symmetric intensity within the field limits generated from the equation:

$$I = 1 + a(r - r_o)^2 , \quad (6.1)$$

where r is the radial spatial coordinate (in cm) measured from the beam central axis, r_o is the positional coordinate of the centre of the field, and a is a scaling factor which gives the curvature of the parabola. The leaf sequence file to deliver this intensity matrix at a precision level of ±1.5% was composed of 28 subfields for a "close-in" technique . The EPID-measured planar dose distribution at depth d_{max} for this case is shown in Fig. 6.3(a). In Fig. 6.3(b), a profile of the EPID-measured dose distribution is extracted along the dashed line of Fig. 6.3(a) and compared to the calculation of the CADPLAN TPS. The agreement between the measured and calculated dose distributions is excellent except in the penumbra region.

E. Inverted parabolic field

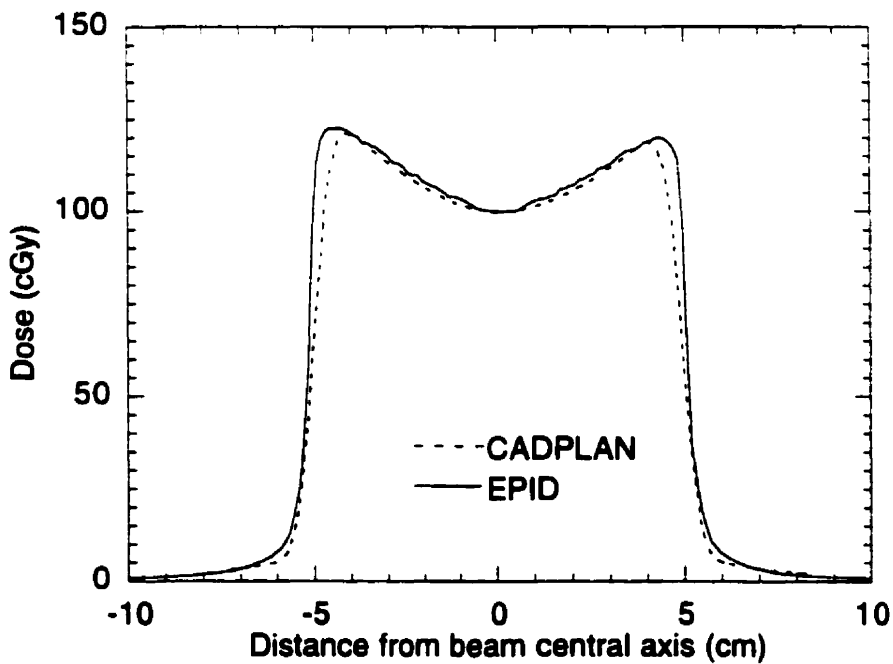
An inverted parabolic field was also tested. The intensity matrix for the inverted cap was obtained from the equation:

$$I = 1 - a(r - r_o)^2 , \quad (6.2)$$

where the variables are as defined above. At a precision level of ±1% the *dynMLC* program calculated a "close-in" technique leaf sequence file composed of 28 subfields for the delivery of this intensity matrix. The EPID-measured planar dose distribution at depth d_{max} for this case is shown in Fig. 6.4(a). In Fig. 6.4(b), a profile of the EPID-measured dose distribution is extracted along the dashed line of Fig. 6.4(a) and compared to the calculation of the CADPLAN TPS. The agreement between the measured and calculated dose distributions is excellent.



(a)

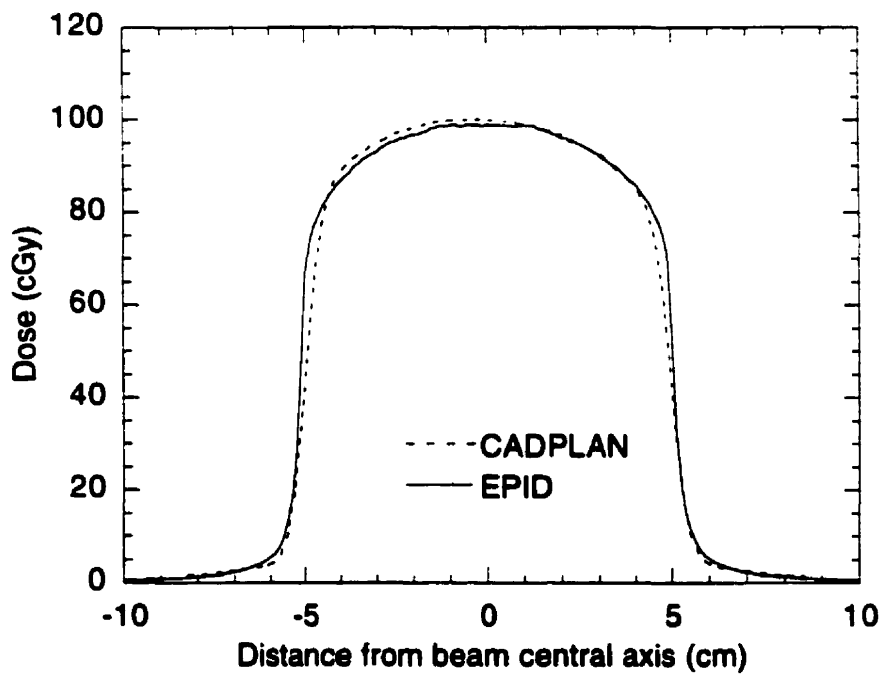


(b)

Figure 6.3. (a) EPID-measured 6 MV dose distribution for the parabolic field at depth d_{max} for an SAD set-up. In (b), a profile of the EPID measurement (—) is extracted along the dashed line in (a) showing agreement with the calculation carried out with our treatment planning system (---).



(a)



(b)

Figure 6.4. (a) EPID-measured 6 MV dose distribution for the inverted parabolic field at depth d_{max} for an SAD set-up. In (b), a profile of the EPID measurement (—) is extracted along the dashed line in (a) showing agreement with the calculation carried out with our treatment planning system (- -).

F. Cosine-squared-like field

The academic example is provided by a cylindrically-symmetric intensity function I of the form:

$$I = \cos^2 \left[\left(\frac{r}{r_o} \right) \cos \left(\frac{r}{r_o} \right) \right] ; \quad r_o = 2 \text{ cm} , \quad (6.3)$$

where r is the radial spatial coordinate (in cm) measured from the beam central axis and r_o is an arbitrary scaling factor, equal to 2 cm in our test. All values in the intensity matrix beyond a radius r of 14.0 cm were set to zero. This intensity matrix is a very demanding test case, since it possesses a high degree of modulation with maxima at $r = 0$, $r = \pi$ cm, and $r = 2\pi$ cm, a shallow minimum at $r = 1.72$ cm, and a deeper minimum ($I = 0$) at $r = 4.63$ cm. Although the intensity value at this radius (4.63 cm) is theoretically equal to zero, in-phantom scatter and transmission through the MLC will result in a non-zero *dose* measurement at this point. It is true in general that the dose at a particular point will not be strictly proportional to the intensity at that point due to in-phantom scatter. Nonetheless, the MLC transmission is corrected for in the calculation of the leaf-sequence for all points of the intensity matrix having a value greater than zero.

The leaf-sequence file required to produce the intensity matrix of Eq. 6.3 at 6 MV photon energy was composed of 88 subfields (at a precision level of $\pm 2\%$) with the intention of producing a dose of 100 cGy at depth d_{max} on the central axis in a flat phantom for an SAD set-up. The 88 MLC-defined segments were delivered with a "sliding window" technique to achieve the dose distribution shown in Fig. 6.5, at a depth of d_{max} in phantom and an SAD of 100 cm. A profile of the EPID-measured dose along the dotted line of Fig. 6.5 was extracted and is shown in Fig. 6.6(a) where it is compared to the calculation of our treatment planning system as well as the measurements with the beam profiler. The agreement between the measured and calculated dose distributions is

excellent ($\pm 0.5\%$ on central axis, $\pm 2\%$ elsewhere). The agreement along the perpendicular axis is not so good (around $\pm 10\%$ at worst) due to the 1 cm width of the MLC leaves. Figure 6.6(b) depicts the same EPID-measured dose profile as Fig. 6.8(a) but at 10 cm depth in phantom for an SAD set-up, also compared to the calculation of the planning system and to the beam profiler measurements. Agreement here is very good except in regions of steep dose gradient, which will be discussed below. A total of 348 monitor units were necessary for the delivery of this "academic" dose distribution.

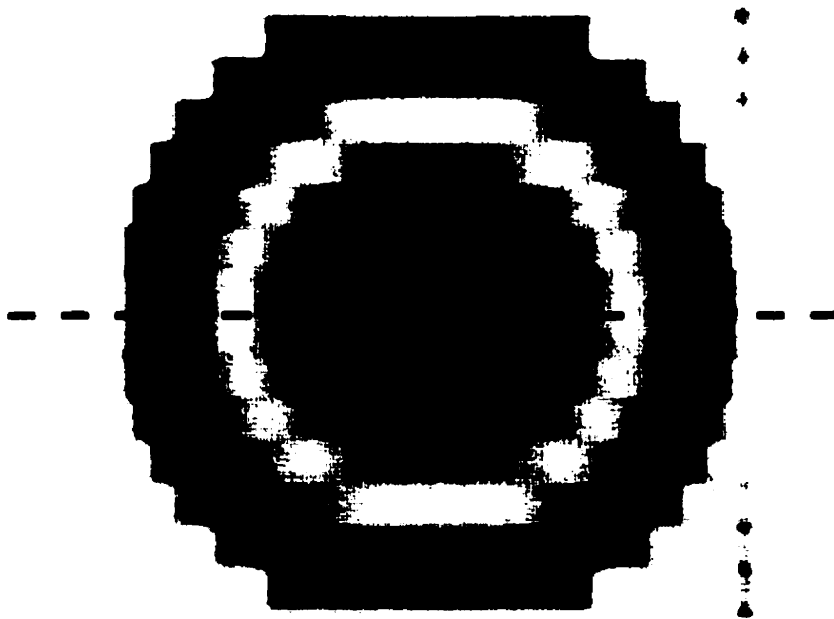
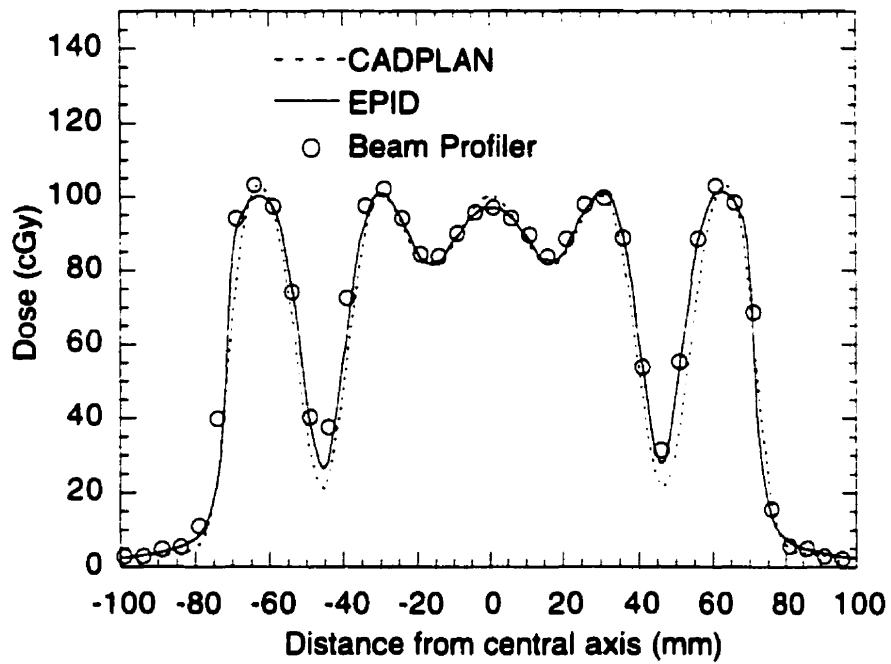
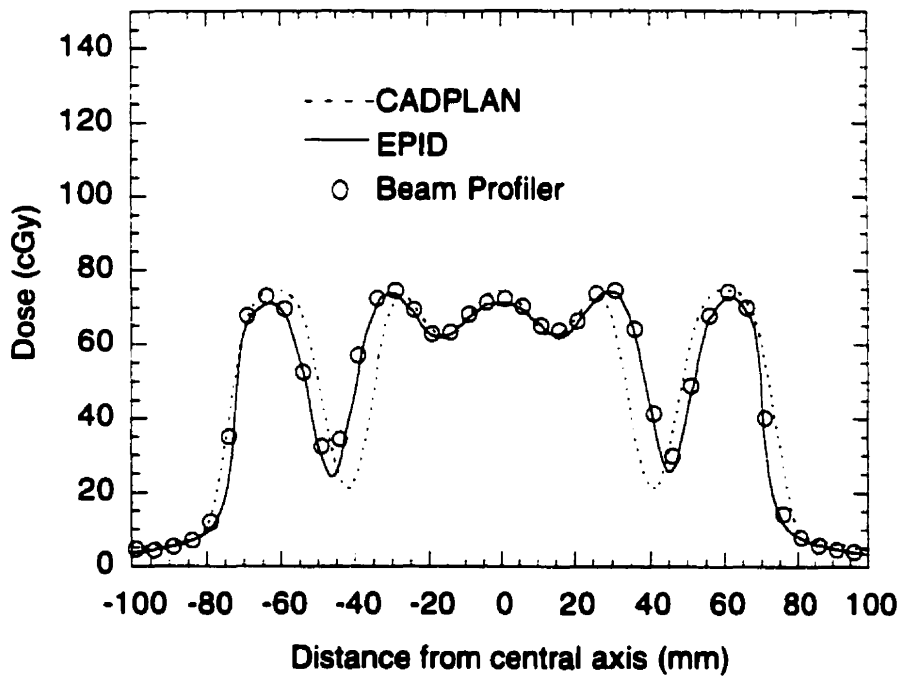


Figure 6.5. EPID-measured 6 MV dose distribution for the intensity function of Eq. 6.3 at depth d_{max} for an SAD set-up.



(a)



(b)

Figure 6.6. In (a) a profile of the EPID measurement is extracted along the dotted line in Fig. 6.5 showing agreement between the EPID measurement (—), the measurement with the beam profiler (○), and the calculation carried out with our treatment planning system (---). Part (b) represents the same dose profile as in (a), except that it is given for a 10 cm depth in phantom in an SAD set-up.

G. Clinically-useful field

In routine practice the major portion of the total radiation dose is administered to the patient through a *principal* (or *main*) field encompassing the initial PTV. However, over time the PTV will shrink due to the effect of the radiation beam or we may have reached the dose which may safely be given to certain non-diseased structures within the PTV. Thus, after several weeks of treatment a new PTV is generally defined. This second field is referred to as the *boost* field or *coned-down* field.

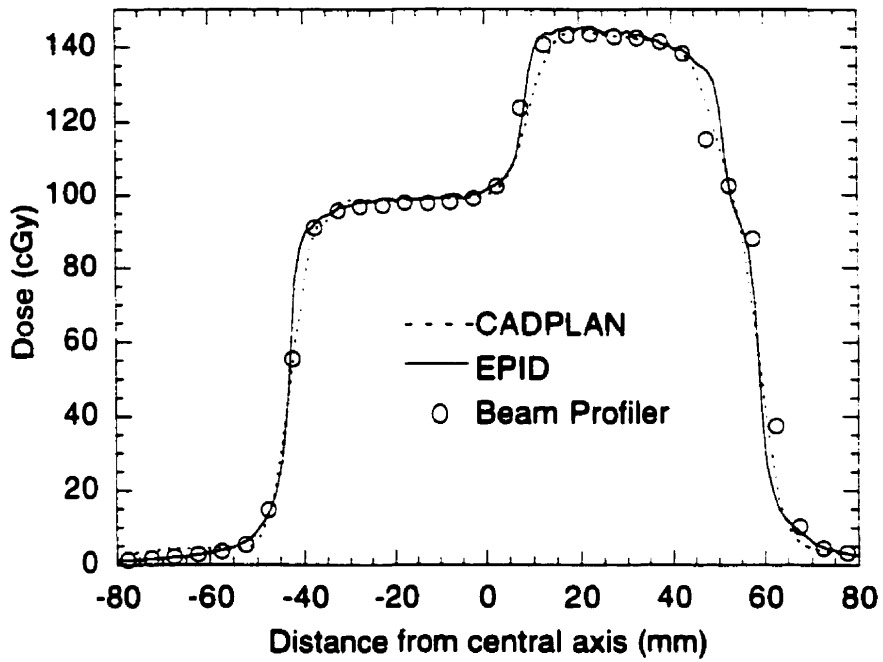
For the clinical example of MLC intensity-modulation, we experiment with the idea of delivering the boost radiation field concomitantly with the principal field, thus shortening the treatment course for the patient significantly. To illustrate this approach to treatment, we have selected a case of carcinoma of the tongue which consists of two parallel-opposed lateral 6 MV photon beams, mirror images of each other, together producing a dose of 60 Gy in the boosted volume and 45 Gy in the volume treated exclusively by the principal field. The required intensity matrices to achieve this dose distribution were calculated by our treatment planning system. The use of intensity-modulated beams in this case compensates for the non-uniform contours in the neck region and allows the administration of a lesser dose to the posterior portion of the target, keeping the spinal cord below 45 Gy, the tolerance dose for this structure.

Our segmented treatment consisted of 18 subfields for each beam, delivered according to a "close-in" technique. To test our ability to deliver the target dose prescription, we delivered a dose of 100 cGy at d_{max} to a flat phantom in an SAD set-up. For this example, the precision level of the leaf-sequence calculation was set to allow, in theory, a maximum discrepancy of $\pm 0.5\%$ between the desired and delivered intensity matrices. Figure 6.7 shows the EPID-measured dose distribution for this clinical case at depth d_{max} and SAD 100 cm. Figure 6.8(a) shows the profile of the measured dose

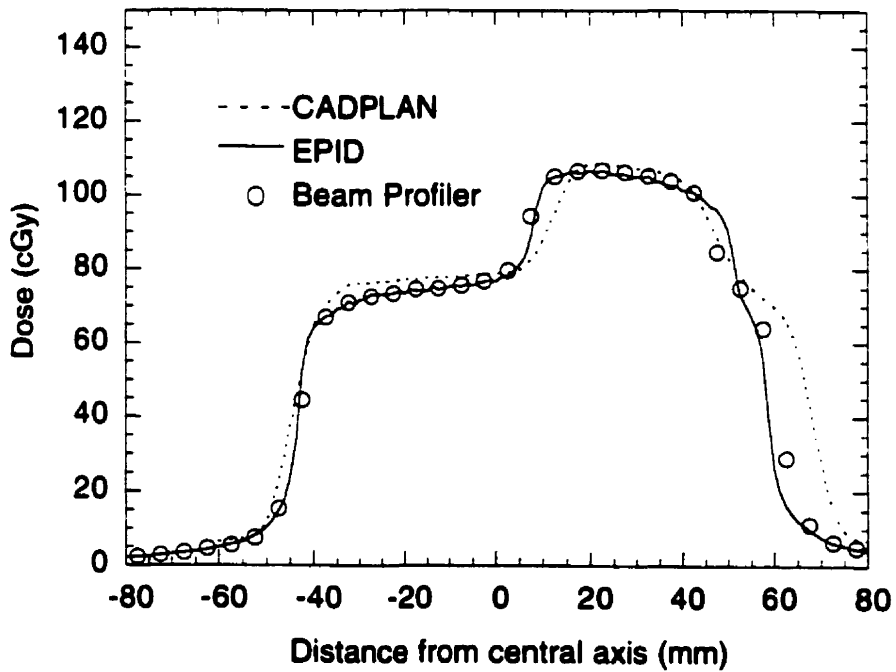
distribution along the dashed line of Fig. 6.7 compared to the calculation of our planning system and the beam profiler measurements. The agreement between the measured and calculated dose distributions is excellent ($\pm 0.5\%$ on central axis, $\pm 2\%$ elsewhere). Here the 1 cm leaf width of the MLC leaves has very little adverse effect on the dose profiles along the perpendicular axis. Figure 6.8(b) depicts the same EPID-measured dose profile as Fig. 6.8(a) but at 10 cm depth in phantom for an SAD set-up, also compared to the calculation of the planning system and to the beam profiler measurements. The agreement is slightly poorer here for reasons discussed below. For this case, beam delivery in the step-and-shoot mode required a total of 138 monitor units.



Figure 6.7. Dose distribution at 6 MV photon energy for one lateral field of the clinical case measured at depth d_{max} for an SAD set-up showing the weighted-sum of the 18 calibrated EPID images.



(a)



(b)

Figure 6.8. In (a), a dose profile along the dashed line of Fig. 6.7 showing agreement between the EPID measurement (—), the measurement with the beam profiler (○), and the calculation of our treatment planning system (---). Part (b) represents the same dose profile as in (a), except that it is given for a 10 cm depth in phantom in an SAD set-up.

H. Discussion of the test cases

The five examples presented above show that the EPID measurements agree with the beam profiler points to within $\pm 2\%$, except in regions of steep dose gradient where the agreement is ± 2 mm between corresponding isodose lines. Considering the uncertainties due to the set-up of these devices the discrepancy between the measured data is not unexpected.

Both measurement devices (EPID and beam profiler) also agree well with the calculations of the CADPLAN TPS except in regions of very steep dose gradient at large depths in phantom. We therefore conclude that the *dynMLC* program accurately and faithfully delivers a given intensity matrix. We attribute the lack of agreement between measured and calculated data in regions of steep dose gradient at significant depths in phantom to a problem with the CADPLAN TPS since we have seen this phenomenon appear in other, totally-unrelated, instances involving routine treatment planning procedures. The CADPLAN TPS cannot accurately predict the contribution of scattered radiation at these depths.

6.3 TESTS OF THE INVERSE-PLANNING ABILITIES OF THE CADPLAN TPS

In the previous section, the *dynMLC* program has been shown to produce a leaf sequence which accurately delivers a particular intensity-modulated matrix. However, in order to use intensity-modulated beams in patient treatment, we must also know whether the correct intensity matrix is calculated by the TPS for each field of the treatment plan. For the CADPLAN TPS, the correct intensity matrix is the one which provides a uniform dose to the compensation plane taking into account the particular patient geometry.

As explained in Section 2.5, CADPLAN's inverse-planning capabilities are rudimentary and limited to compensation to a plane, with a user-defined compensation plane which must be perpendicular to the beam central axis. Compensation (i.e., uniform dose) is guaranteed only at the depth of the defined plane; planes at other depths will receive only approximate compensation.

We tested CADPLAN's compensation algorithm with the aid of phantoms shown schematically in Fig. 6.9. Two wedge-shaped phantoms were constructed out of polystyrene, whereas the slab beneath them was solid water. Both polystyrene and solid water are tissue-equivalent materials. A CT study was performed on the phantom according to the routine protocol established for patients. The CT slices were then exported to the CADPLAN workstation where a 6 MV radiation beam with dimensions of 22×10 cm² was set up with the isocentre as shown in Fig. 6.9, and incident directly from above. CADPLAN was then instructed to design an intensity matrix to achieve a uniform dose at the isocentre depth. This intensity matrix was imported into the *dynMLC* program where a leaf sequence was calculated. Additionally, the intensity matrix computed by CADPLAN was converted (again by CADPLAN) to a 2D matrix of aluminum thicknesses for the fabrication of a physical compensator. This aluminum compensator was machined in our departmental machine shop.

The appropriateness of the intensity matrix calculated by CADPLAN was evaluated experimentally with the EPID. The EPID was set up with the imaging plane at 100 cm from the source. A build-up thickness of 1 cm solid water was placed on the imager (its inherent build-up thickness is 0.6 cm), and on top of this the two wedge phantoms were positioned. This set-up reproduced the arrangement shown in Fig. 6.9 with the EPID imaging plane at the isocentre depth.

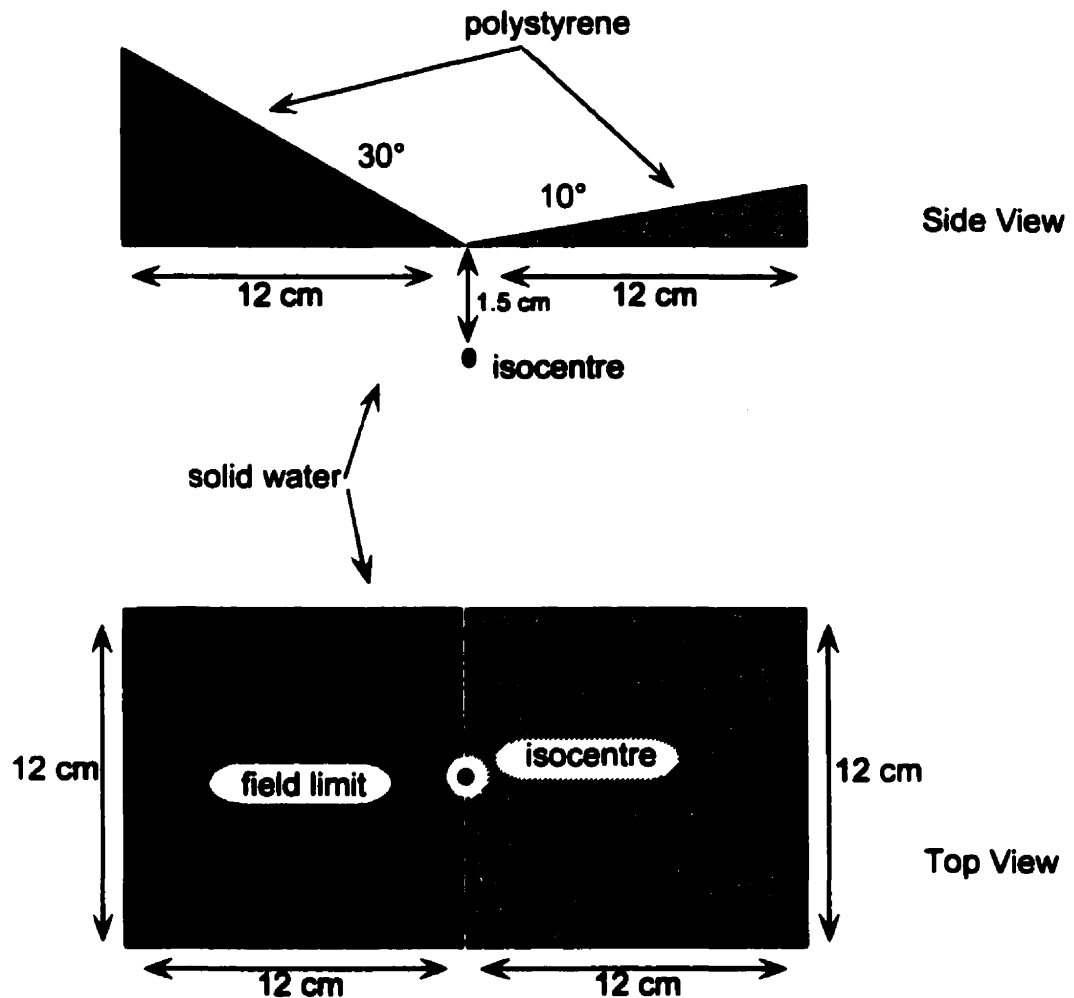


Figure 6.9. Side and top views of the phantom used to verify CADPLAN's compensation algorithm.

An EPID image was acquired for three measurement situations: (a) the open beam with only the build-up on the imager, (b) the open beam with the phantom and build-up in place, and (c) the compensated field with the phantom and build-up in place. Dose profiles were extracted from the calibrated EPID images along the field central axis for these three measurements and are shown in Fig. 6.10. In (a) we see the beam horns associated with the open beam, in (b) the effect of the uneven phantom surface on the dose profile, and in (c) the flat dose profile which results from the delivery of the compensated beam to the uneven phantom surface. In Fig. 6.10 the compensation was accomplished using the aluminum compensator; very similar results were obtained

when the intensity matrix was delivered using the leaf sequence computed by the *dynMLC* program.

CADPLAN's compensation algorithm is able to reduce the variation in dose along the profile from ~15% (curve *b*) to approximately 2% (curve *c*). This is sufficiently uniform for patient treatment. However, a number of other experiments similar to this one have demonstrated that the results presented in Fig. 6.10 are atypical. Generally, the level of dose uniformity achieved at the compensation plane is not so good. Furthermore, peculiar values of intensity are sometimes calculated, especially for pixels in the compensation matrix which do not strike the patient or, in other words, which are incident on air. Thus CADPLAN's compensation algorithm should not be used in a routine manner for patient treatment. Every intensity matrix produced by the CADPLAN TPS must be scrutinized carefully before use.

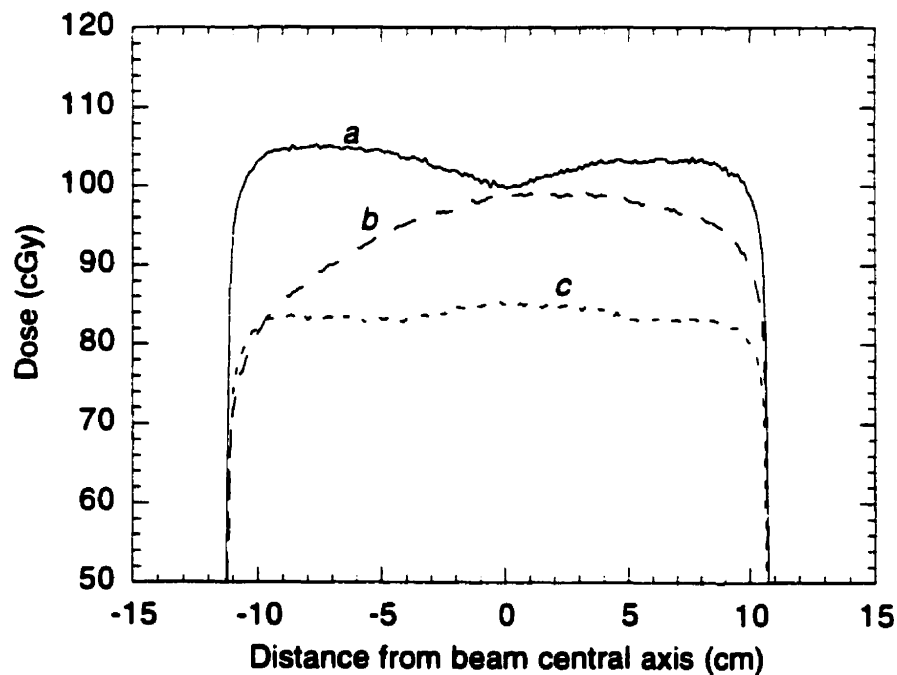


Figure 6.10. EPID-verification of CADPLAN's compensation algorithm showing dose profiles through the field centre for three cases: (a) the open beam with only the build-up, (b) the open beam with the phantom and build-up in place, and (c) the compensated field with the phantom and build-up in place.

6.4 SUMMARY

This chapter has described dosimetric measurements for a number of intensity-modulated beams. The results of these tests have allowed us to conclude that the *dynMLC* program's ability to calculate the leaf sequence required for the delivery of a given intensity-modulated beam is excellent, but that CADPLAN at present forms the weak link in our "chain" of intensity-modulation; it portrays shortcomings both in its ability to calculate the intensity matrices and in its ability to predict the dose distribution resulting from an intensity-modulated beam. Patients may nonetheless be treated with this approach, but a critical examination must be made of each case and treatment must be delivered with great care to prevent any of a large number of potential errors which may occur in the sophisticated intensity-modulated approach to conformal radiotherapy. Before the dynamic MLC option on the Clinac 2300 C/D linear accelerator can be used routinely for patient treatment, a reliable quality assurance (QA) protocol will have to be developed. The tests described in this chapter will serve as an important basis for developing this QA program.

Section:

7.1	Introduction.....	175
7.2	Description of the first patient treatment.....	175
7.3	Summary.....	179

7.1 INTRODUCTION

In this chapter we present an account of the first patient treated with MLC intensity-modulated beams in our institution.

7.2 DESCRIPTION OF THE FIRST PATIENT TREATMENT

At the McGill University Hospital Centre the first patient planned for intensity-modulation began treatment on April 29, 1998. This was a case of carcinoma of the right tonsil with extension into the skeletal muscle and surrounding soft tissue. A decision was made to treat the patient in an isocentric set-up with two parallel-opposed 6 MV photon beams with dimensions of 13×13 cm². Intensity-modulation was desirable in this case to compensate for the uneven surface of the neck region, as seen from the two lateral fields. The intensity matrices were calculated with the CADPLAN TPS with a sagittal compensation plane defined at the mid-separation depth. The BEV mode was then invoked for each beam in order to place the MLC shielding to protect the eye and nose, as well as the anterior aspect of the brain. Both the intensity matrices and the BEV files were then exported to the *dynMLC* program.

At the time of the planning for this patient's treatment, the Varian MLC software, which serves to deliver a sequence of MLC-defined subfields in rapid succession, was not yet available in our hospital. Without this software, it is still possible to deliver MLC intensity-modulated x-ray beams, but these must be executed by loading-in each MLC subfield manually and programming the desired number of MU into the Clinac 2300 C/D console for that subfield.

An intensity-modulated treatment executed in such a manner is somewhat tedious, yet, it should produce results almost identical to the more practical approach available through the dynamic MLC software option. The only two differences are that that integer MU settings must be used for each subfield (resulting in a small inaccuracy since, for instance, 4.7 MU might become 5 MU for a given subfield) and that the delivery time is slightly longer (in our case 30 s for each beam rather than 20 s). The efficiency factor thus fell from around 1 to about 0.67.

Since we did not have access to the more practical approach, we proceeded with the less sophisticated option, but limited the number of MLC subfields to five for each lateral field in order to limit the effort required by the operator of the Clinac 2300. Calculation of the leaf sequence for only five subfields per lateral beam implied setting the precision level of the *dynMLC* calculation to $\pm 5\%$, higher than would normally be tolerated, but nonetheless providing a dose distribution superior to that which could be achieved without intensity-modulation.

A dose distribution in the mid-separation sagittal plane calculated by the CADPLAN TPS, which incorporates the effect of intensity-modulation, is shown in Fig. 7.1. Although CADPLAN can provide the appropriate correction for tissue inhomogeneities, the distribution shown in Fig. 7.1 does not incorporate these corrections

since they are not routinely used in our department. The isodose lines in the figure have been normalized according to the physician's prescription to show the total dose (in cGy) that the patient will receive for each daily fraction of the treatment. The degree of dose uniformity in the treated volume is far greater than can be achieved without the use of intensity-modulated beams, where typically the dose uniformity for this type of treatment is $\pm 10\%$.

Prior to patient treatment, the leaf sequence calculated for this patient was subjected to two tests. The first was a central axis measurement with a calibrated ionization chamber of the cumulative dose from the two lateral fields at the mid-separation point (depth 7.2 cm), in a phantom approximating the patient geometry in the treatment region. The measured dose in this test was 198.2 cGy in excellent agreement with the prescribed daily dose of 200 cGy. The second test was an EPID measurement of the planar dose distribution resulting from the leaf sequence for the right lateral field performed at a measurement depth of 7.2 cm and an SAD of 100 cm. This measurement allowed us to verify the proper orientation of the field and verify that the intensity delivered to selected points was consistent with the patient thickness traversed by the beam at that point.

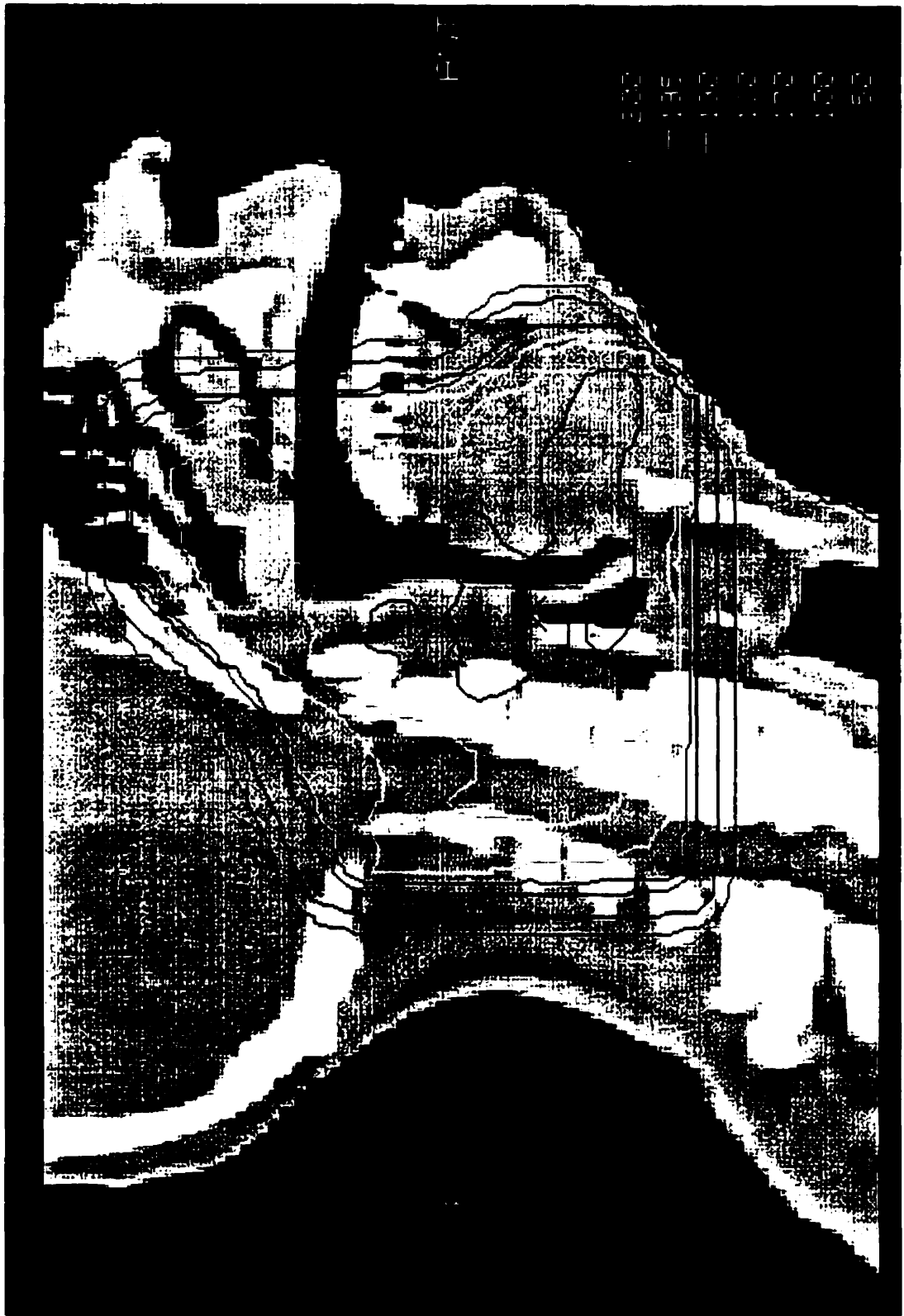


Figure 7.1. Isodose distribution in the mid-separation sagittal plane for our first patient treated with MLC intensity-modulated beams. The isodose lines are normalized to show the patient daily dose (in cGy).

7.3 SUMMARY

The treatment was completed to the entire satisfaction of the radiation oncologists who treated the patient, the medical physicists who calculated the dose distributions and beam delivery protocols, and the radiotherapists who executed the prescribed treatment. The attending physician remarked that the patient had unusually mild skin reaction -an unpleasant side effect almost invariably associated with irradiation in the head and neck region. We suspect that the more uniform distribution of dose in the treated volume that is obtained with MLC intensity-modulated treatments is to be credited for this milder skin reaction. In view of the successful first intensity-modulated treatment at McGill, planning for additional MLC intensity-modulated treatments is underway.

Section:

8.1 Thesis summary.....	180
8.2 Future work.....	182
8.3 References.....	183

8.1 THESIS SUMMARY

The objectives of this thesis were two-fold: (1) to develop and study a system for the delivery of intensity-modulated photon beams produced with a multileaf collimator (MLC) and (2) to develop a practical method for the measurement and verification of intensity-modulated photon beams. As evident from the experimental work presented in this thesis, both of these objectives have been accomplished.

The delivery aspect starts with an intensity matrix which forms the input data for the *dynMLC* leaf-sequencing algorithm. We consider this intensity matrix a "given" in our work and rely on software other than our own for its calculation. The matrices were obtained from our CADPLAN commercial treatment planning system when dealing with actual patients or, on for experimental work not presented in this thesis, from the theoretical endeavors of another graduate student in our department¹. Using the intensity matrix we write an MLC leaf sequence file, i.e., a description of the manner in which the MLC configuration will vary as a function of the monitor unit setting. In order to be sufficiently accurate for patient treatment, the leaf-sequencing algorithm must incorporate measured radiation parameters of the MLC installed on our computer-controlled Clinac 2300 C/D linear accelerator. The parameters include the MLC leaf penumbra, MLC transmission, radiation vs. light-field coincidence for the MLC leaves,

etc. Our leaf-sequencing algorithm is an adaptation of a step-and-shoot algorithm found in the literature, the practical modification being that our technique delivers the majority of the patient dose for a given field through the first MLC subfield of the leaf sequence, rather than delivering an equal dose through all subfields, as in other published step-and-shoot leaf-sequencing algorithms. Our approach provides for a faster beam delivery, since the leaf sequence contains fewer subfields. The approach is also more comforting to traditionally-minded medical staff who generally view MLC leaf motion during treatment with some apprehension. In our approach, the leaves typically only move for the last 20% or so of the monitor units delivered for a given field.

Beam verification is an essential component of the radiotherapy process since stringent demands are placed on the precision with which the dose must be delivered to the patient, and it is generally assumed that a precision better than $\pm 5\%$ is required. To this end, we have developed a new procedure using a commercially-available electronic portal imaging device (EPID) of the scanning liquid ionization chamber type (SLIC). This EPID was designed for the acquisition of images in the treatment beam in order to verify accurate patient positioning. However, we show that when a pixel to dose-rate calibration curve is measured and appropriate experimental methods are followed, the EPID can also be used successfully for the measurement of planar dose distributions at arbitrary depths in phantom. The precision of dose determination with the SLIC EPID is $\pm 2\%$. This measurement precision is sufficient to ensure a precision in dose delivery of $\pm 5\%$ to the patient, when the other sources of uncertainty in the treatment process, such as the calculation of an isodose distribution and daily set-up of the patient on the treatment unit, are considered. The EPID verification is quite rapid, requiring approximately one hour for the verification of a typical clinical beam composed of ~ 15 subfields. Thus, compared to other available dosimeters, the SLIC EPID provides an attractive compromise between rapidity of dose acquisition and precision of dose

measurements. It is also appealing that the EPID can be used both to acquire the radiation parameters of the MLC necessary for the development of a leaf-sequencing algorithm and, subsequently, to verify the delivery of the leaf sequence. We therefore consider the SLIC EPID to be ideally suited for the implementation and verification of an intensity-modulated beam delivery system in the step-and-shoot mode.

8.2 FUTURE WORK

Regarding further development of the *dynMLC* program, we recommend that it should not be pursued. Despite the fact that the *dynMLC* program incorporates a pleasant user-interface and performs very rapidly and with surprisingly few bugs for a home-made piece of software, it is, nonetheless, the work of a novice programmer and as such can never be wholly trusted. In the very near future, commercial treatment planning systems will incorporate routines allowing the writing of leaf sequences. These routines will be the work of professional programmers and therefore, one would hope, will be more robust and versatile than our *dynMLC* program. Programming is a lot of fun, but it seems counterproductive to compete on this level. The *dynMLC* program has, however, served two useful purposes: firstly, it has allowed us to investigate in detail the use of the SLIC EPID for the verification of MLC intensity-modulated x-ray beams; and, secondly, it has permitted intensity-modulated patient treatment in our department several years ahead of what otherwise would have been possible.

It is our opinion that future work should be directed toward the further study of devices serving to verify the delivery of the intensity-modulated beams. As we stated in the beginning of this thesis, development of this aspect of conformal therapy has been somewhat neglected and has lagged behind in comparison with other aspects, such as the

computation of the intensity-matrices, the writing of the leaf sequences, and the technical issues associated with beam delivery.

As we have shown, the SLIC EPID is extremely well-suited to the verification of intensity-modulated beams. Nevertheless, a few interesting questions remain. To list a few: (1) could the measurement of an intensity-modulated beam using the SLIC EPID somehow be accomplished more rapidly? (2) could the "memory effect" be minimized? (3) could the SLIC EPID be modified in order to enable the measurement of dose distributions resulting from intensity-modulated beams delivered dynamically², i.e., with components of the linear accelerator in motion while the beam is on? (4) would it be possible to use the SLIC EPID to verify the dose delivery to the patient³ during the actual treatment?

8.3 CHAPTER REFERENCES

1. Hristov D. *Development of techniques for optimization and verification of conformal radiotherapy*. Ph.D. thesis, McGill University, Montreal (1997).
2. van Herk M. *Feasibility of the Portal Vision system for verification of dynamic therapy*. Conference on Electronic Portal Imaging, Amsterdam (June 10-12, 1996).
3. Boellaard R. *In-vivo dosimetry with a liquid-filled electronic portal imaging device*. Ph.D. thesis, University of Amsterdam (1998).

LIST OF FIGURES

Figure 1.1. Diagram of an isocentric treatment unit showing the three basic components: head, gantry, and couch. (page 4 of this thesis)

Figure 1.2. Percent depth doses of the Clinac 2300 C/D linear accelerator in tissue for a 10×10 cm² field and photon energies of 6 MV and 18 MV. (page 9 of this thesis)

Figure 1.3. Off-axis ratio at 18 MV photon energy for a 10×10 cm² field for the Clinac 2300C/D linear accelerator at a depth of 3.5 cm in water. Also shown is the effect of a wedge with a wedge factor of 0.41 on the dose profile at the same depth in phantom. (page 10 of this thesis)

Figure 1.4. CT slice in the abdominal region. The bladder (yellow), seminal vesicles (red), and rectum (purple) have been outlined. (page 13 of this thesis)

Figure 1.5. Beam's eye view for a right lateral pelvic field. The gross tumour volume (red), the planning tumour volume (yellow), the rectum (blue), the bladder (purple), and the location of shielding blocks (green outline) are shown. (page 19 of this thesis)

Figure 2.1. Diagram to illustrate how version 2.79 of the CADPLAN treatment planning software calculates intensity-modulated beam profiles. (page 37 of this thesis)

Figure 3.1. Diagram of the image detection unit (IDU) of the Varian scanning liquid ionization chamber (SLIC) EPID. (page 56 of this thesis)

Figure 3.2. The EPID pixel value for a 10×10 cm² field at an SDD of 100 cm as a function of thickness of solid water placed on the imager surface for the 6 MV and 18 MV photon beams. (page 61 of this thesis)

Figure 3.3. Characteristic curves for the EPID in the standard acquisition mode at an SDD of 100 cm for a field size of 10×10 cm² at photon energies of 6 MV and 18 MV. (page 63 of this thesis)

Figure 3.4. Characteristic curves for the EPID in standard acquisition mode at an SDD of 140 cm for a field size of 10×10 cm² at photon energies of 6 MV and 18 MV. (page 63 of this thesis)

Figure 3.5. Characteristic curve for the IDU at 6 MV determined by varying the SDD (empty circles) compared to the characteristic curve obtained with the lead attenuators (solid circles). (page 64 of this thesis)

Figure 3.6. Characteristic curve for the IDU at 18 MV determined by varying the SDD (empty triangles) compared to the characteristic curve obtained with the lead attenuators (solid triangles). (page 64 of this thesis)

Figure 3.7. Centre pixel values for identical 6 MV EPID images taken at image acquisition intervals ranging from 6 s to 120 s. (page 68 of this thesis)

Figure 3.8 Star-shot irradiation pattern obtained from the summation of four uncalibrated EPID images of a narrow, symmetric, MLC-defined field at collimator angles of 0°, 45°, 90° and 135°. (page 69 of this thesis)

Figure 3.9. Calibrated EPID image of the transmission at 18 MV beam energy through a fully-closed MLC with illustration of the regions in which the "interleaf", "leaf end" and "average" transmission were calculated. (page 70 of this thesis)

Figure 3.10. Four dose rate profiles used to test a compensator design algorithm. Profile (a) represents an image of the open beam with no phantom, profile (b) an image of the open beam with the phantom in place, profile (c) an image of the compensated beam and no phantom, and profile (d) an image of the compensated field with the phantom in place. (page 72 of this thesis)

Figure 4.1. Dimensions of a Varian MLC leaf from the "A" bank of leaves. (page 79 of this thesis)

Figure 4.2. Star-shot test pattern used to establish coincidence between the MLC axis of rotation and the field crosshairs. (page 84 of this thesis)

Figure 4.3. The MLC test configuration used to verify some MLC dimensions. (page 85 of this thesis)

Figure 4.4. Illustration of various methods of conforming the MLC leaves to an arbitrary planning target volume. (page 87 of this thesis)

Figure 4.5. Illustration of how the choice of collimator orientation can affect the MLC coverage of the planning target volume. In (a) the ideal collimator angle, and in (b) the worst collimator angle for this PTV. (page 88 of this thesis)

Figure 4.6. MLC test pattern to verify, at once, the positional agreement of all MLC leaves at once for a number of field positions. In (a) we show the sum of the individual images; in (b) the six individual slit images. (page 91 of this thesis)

Figure 4.7. Position of the 50%, 60%, 70%, and 80% isodose lines at 6 MV photon energy as a function of the readout position of the leaf ends. (page 92 of this thesis)

Figure 4.8. Position of the 50%, 60%, 70%, and 80% isodose lines at 18 MV photon energy as a function of the readout position of the leaf ends. (page 93 of this thesis)

Figure 4.9. Position of the 50% and 60% isodose lines at 6 MV and 18 MV photon energies as a function of the readout position of the leaf sides. (page 94 of this thesis)

Figure 4.10. Light-field position of the leaf ends as a function of their readout position. (page 95 of this thesis)

Figure 4.11. Illustration of the relative position of the light field and the radiation field for an MLC leaf end. The position of the light field source corresponds to the position of the x-ray source. (page 96 of this thesis)

Figure 4.12. Light-field position of the leaf sides as a function of their readout position. (page 97 of this thesis)

Figure 4.13. The EPID image of the transmission of the MLC. The regions used to calculate the average, interleaf, and leaf end transmission are shown. (page 99 of this thesis)

Figure 4.14. MLC leaf end penumbra widths as a function of leaf position for 6 MV and 18 MV photon energies. (page 101 of this thesis)

Figure 4.15. MLC leaf side penumbra widths as a function of leaf position for 6 MV and 18 MV photon energies. (page 102 of this thesis)

Figure 4.16. Depiction of the MLC "tongue and groove" effect. When added together, two complementary radiation fields (a) and (b) do not produce a fully uniform radiation fluence within the field (c). (page 103 of this thesis)

Figure 4.17. The collimator scatter factor as a function of field size for square, symmetric fields for the Clinac 2300 C/D linear accelerator at 6 MV and 18 MV photon energies. (page 108 of this thesis)

Figure 4.18. Proper scale drawing of the collimation system of the Varian Clinac 2300 C/D. (page 111 of this thesis)

Figure 4.19. Collimator scatter factor at 6 MV photon energy illustrating the validity of the hypothesis that, for a given setting of the jaws, the positions of the MLC leaves have negligible effect on the collimator scatter factor for a wide range of MLC positions. The linac upper and lower jaws were set to 25×25 cm². (page 114 of this thesis)

Figure 4.20. The phantom scatter factor as a function of field size for square, symmetric fields on the Clinac 2300 C/D linear accelerator at 6 MV and 18 MV photon energies. (page 116 of this thesis)

Figure 4.21. Shapes of the six MLC-defined fields used to verify the agreement between measured and calculated relative dose factors and collimator factors. The asterix denotes the position of the ion chamber centre. (page 117 of this thesis)

Figure 5.1. Intensity matrix presented for qualitative inspection as a series of contour lines. In this representation, the extensions of the intensity matrix which lie underneath the MLC leaves have been masked out. The data are normalized to 100%. (page 127 of this thesis)

Figure 5.2. Intensity profile along the dashed line in Fig. 5.1 (thick line) and the approximate intensity distribution that will be delivered if an accuracy of ±2% is selected by the user (thin line). (page 129 of this thesis)

Figure 5.3. Illustration of the two possible types of intersections of a given intensity level with a profile of the intensity distribution. In (a), the intensity level falls between two points of the profile, while in (b) the intensity level intersects the profile at one of the points of the profile. (page 131 of this thesis)

Figure 5.4. Illustration of the two cases in which the intersection of a given intensity level with a profile of the intensity distribution is problematic. In (a), the intensity level intersects with a local extremum of the profile and in (b) the intensity level coincides with a plateau of the profile. (page 132 of this thesis)

Figure 5.5. Illustration of two ways in which the leaf sequence may be sorted. In the sliding window technique (a), all leaves move from left to right. In the close-in technique (b), the leaves converge on each peak of the intensity distribution. (page 133 of this thesis)

Figure 5.6. Profiles of the leaf-end penumbra at 6 MV (a) and 18 MV (b) photon energies. The readout position of the leaf end initially matches the 70% isodose line of the radiation field but is shifted to match the 80% isodose line. (page 138 of this thesis)

Figure 5.7. Illustration of the fact that intensity distributions containing multiple peaks will result in a cumulative relative intensity which exceeds 100%. (page 139 of this thesis)

Figure 5.8. TMR-weighted isodose distribution for a three-field pelvic treatment at 10 MV photon energy. The posterior beam has a weighting of 100%; the two lateral beams contain a wedge and each has a weight of 90%. (page 142 of this thesis)

Figure 5.9. Appearance of the computer window allowing the user of the dynMLC program to visualize the MLC subfields and the associated treatment parameters. (page 148 of this thesis)

Figure 6.1. (a) EPID-measured 6 MV dose distribution for the ramp-like field at depth d_{max} for an SAD set-up. In (b), a profile of the EPID measurement (—) is extracted along the dashed line in (a) showing agreement with the calculation carried out with our treatment planning system (- - -). In this example, the ramp-like field was delivered with a leaf sequence in which the MLC leaves moved parallel to the intensity gradient. (page 159 of this thesis)

Figure 6.2. (a) EPID-measured 6 MV dose distribution for the ramp-like field at depth d_{max} for an SAD set-up. In (b), a profile of the EPID measurement (—) is extracted along the dashed line in (a) showing agreement with the calculation carried out with our treatment planning system (- - -). In this example, the ramp-like field was delivered with a leaf sequence in which the MLC leaves moved perpendicularly to the intensity gradient. (page 160 of this thesis)

Figure 6.3. (a) EPID-measured 6 MV dose distribution for the parabolic field at depth d_{max} for an SAD set-up. In (b), a profile of the EPID measurement (—) is extracted along the dashed line in (a) showing agreement with the calculation carried out with our treatment planning system (- - -). (page 162 of this thesis)

Figure 6.4. (a) EPID-measured 6 MV dose distribution for the inverted parabolic field at depth d_{max} for an SAD set-up. In (b), a profile of the EPID measurement (—) is extracted along the dashed line in (a) showing agreement with the calculation carried out with our treatment planning system (- - -). (page 163 of this thesis)

Figure 6.5. EPID-measured 6 MV dose distribution for the intensity function of Eq. 6.3 at depth d_{max} for an SAD set-up. (page 165 of this thesis)

Figure 6.6. In (a) a profile of the EPID measurement is extracted along the dotted line in Fig. 6.5 showing agreement between the EPID measurement(—), the measurement with the beam profiler (○), and the calculation carried out with our treatment planning system (- - -). Part (b) represents the same dose profile as in (a), except that it is given for a 10 cm depth in phantom in an SAD set-up. (page 166 of this thesis)

Figure 6.7. Dose distribution at 6 MV photon energy for one lateral field of the clinical case measured at depth d_{max} for an SAD set-up showing the weighted-sum of the 18 calibrated EPID images. (page 168 of this thesis)

Figure 6.8. In (a), a dose profile along the dashed line of Fig. 6.7 showing agreement between the EPID measurement (—), the measurement with the beam profiler (○), and the calculation of our treatment planning system (-.-). Part (b) represents the same dose profile as in (a), except that it is given for a 10 cm depth in phantom in an SAD set-up. (page 169 of this thesis)

Figure 6.9. Side and top views of the phantom used in to verify CADPLAN's compensation algorithm. (page 172 of this thesis)

Figure 6.10. EPID-verification of CADPLAN's compensation algorithm showing dose profiles through the field centre for three cases: (a) the open beam with only the build-up, (b) the open beam with the phantom and build-up in place, and (c) the compensated field with the phantom and build-up in place. (page 173 of this thesis)

Figure 7.1. Isodose distribution in the mid-separation sagittal plane for our first patient treated with MLC intensity-modulated beams. The isodose lines are normalized to show the patient daily dose (in cGy). (page 178 of this thesis)

LIST OF TABLES

Table 4.1. Comparison of the transmission values for the Varian MLC at 6 MV and 18 MV photon energies measured with the SLIC EPID and an ionization chamber. (page 99 of this thesis)

Table 4.2. Comparison of measured and calculated relative dose factors and collimator factors for the six MLC-defined fields of Fig. 4.21. (page 118 of this thesis)

BIBLIOGRAPHY

- Ahnesjo A. *Collimator scatter in photon therapy beams*. Med. Phys. **22**, 267-278 (1995). (cited on page 106 of this thesis)
- Ahnesjo A. *Analytic modelling of photon scatter from flattening filters in photon therapy beams*. Med. Phys. **21**, 1227-1235 (1994). (cited on pages 106,112 of this thesis)
- Anderson DF, Holroyd RA. *High rate operation of warm-liquid ionization chambers*. Nucl. Instr. and Meth. **A260**, 343-345 (1987). (cited on page 67 of this thesis)
- Audet C. *NMR-dose response studies of gels used for 3-D MRI radiation dosimetry*. Ph.D. thesis, McGill University, Montreal (1996). (cited on page 54 of this thesis)
- Benichou M, Gauthier JM, Girodet P, Hentges G, Ribiere G. *Experiments in mixed integer linear programming*. Math. Prog. **1**, 76-94 (1971). (cited on page 33 of this thesis)
- Boellard R. *In-vivo dosimetry with a liquid-filled electronic portal imaging device*. Ph.D. thesis, University of Amsterdam (1998). (cited on page 183 of this thesis)
- Boellaard R, van Herk M, Mijnheer BJ. *The dose response relationship of a liquid-filled electronic portal imaging device*. Med. Phys. **23**, 1601-1611 (1996). (cited on page 65 of this thesis)
- Bortfeld T, Burkelbach J, Boesecke R, Schlegel W. *Three-dimensional solution of the inverse problem in conformation radiotherapy* in Advanced Radiation Therapy: Tumor Response Monitoring and Treatment Planning, Ed. Breit A, Springer-Verlag (1992). (cited on page 28 of this thesis)
- Bortfeld T, Ürkelbach J, Boesecke R, Schlegel W. *Methods of image reconstruction from projections applied to conformation therapy*. Phys. Med. Biol. **35**, 1423-1434 (1990). (cited on pages 29,30 of this thesis)
- Bortfeld TR, Kahler DL, Waldron TJ, Boyer AL. *X-ray field compensation with multileaf collimators*. Int. J. Radiat. Oncol. Biol. Phys. **28**, 723-730 (1994). (cited on pages 41,128 of this thesis)
- Boyer AL, Antonuk L, Fenster A, van Herk M, Meertens H, Munro P, Reinstein LE, Wong J. *A review of electronic portal imaging devices*. Med. Phys. **19**, 1-16 (1992). (cited on page 67 of this thesis)
- Boyer AL, Ochran TG, Nyerick CE, Waldron TJ. *Clinical dosimetry for implementation of a multileaf collimator*. Med. Phys. **19**, 1255-1261 (1992). (cited on pages 99,101, 104,107 of this thesis)
- Boyer AL, Shidong L. *Geometric analysis of light-field position of a multileaf collimator with curved ends*. Med. Phys. **24**, 757-762 (1997). (cited on pages 79,85 of this thesis)
- Brahme A. *Optimal setting of multileaf collimators in stationary beam radiation therapy*. Strahlenther. Onkol. **164**, 343-350 (1988). (cited on page 87 of this thesis)

- Brahme A. *Optimization of stationary and moving beam radiation therapy techniques*. *Radiother. Oncol.* **12**, 129-140 (1988). (cited on page 40 of this thesis)
- Brewster L, Mohan R, Mageras G, Burman C, Leibel S, Fuks Z. *Three dimensional conformal treatment planning with multileaf collimators*. *Int. J. Radiol. Oncol. Biol. Phys.* **33**, 1081-1089 (1995). (cited on pages 86,87 of this thesis)
- Burman C, Kutcher GJ, Emani B, Goitein M. *Fitting of normal tissue tolerance to an analytic function*. *Int. J. Radiat. Oncol. Biol. Phys.* **21**, 123-135 (1991). (cited on page 2 of this thesis)
- Butts JR, Abell GA, Morrison JC, Elson HR. *Dose uniformity from a computerized three-dimensional tissue compensating system*. *Med. Dos.* **22**, 113-116 (1997). (cited on page 39 of this thesis)
- Carol M, Grant WH III, Bleier AR, Kania AA, Targovnik HS, Butler EB, Woo SW. *The field-matching problem as it applies to the Peacock three dimensional conformal system for intensity modulation*. *Int. J. Radiat. Oncol. Biol. Phys.* **34**, 183-187 (1996). (cited on page 42 of this thesis)
- Carol MP. *PEACOCK: A system for planning and rotational delivery of dynamic conformal radiotherapy*. *Int. J. Imaging Sys. and Tech.* **6**, 56-61 (1995). (cited on page 42 of this thesis)
- Censor Y, Altschuler MD, Powlis WD. *A computational solution of the inverse problem in rotation therapy treatment planning*. *Appl. Math. Comput.* **25**, 57-87. (cited on page 30 of this thesis)
- Chaney EL, Cullip TJ, Gabriel TA. *A Monte Carlo study of accelerator head scatter*. *Med. Phys.* **21**, 1383-1390 (1994). (cited on page 105 of this thesis)
- Chiu-Tsao ST, de la Zerda A, Lin J, Ho Kim J. *High-sensitivity GafChromic film dosimetry for ¹²⁵I seed*. *Med. Phys.* **21**, 651-657 (1994). (cited on page 54 of this thesis)
- Chui C-S, Spirou S, LoSasso T. *Testing of dynamic multileaf collimation*. *Med. Phys.* **23**, 635-641 (1996). (cited on page 90 of this thesis)
- Chui CS, LoSasso T, Spirou S. *Dose calculation for photon beams with intensity modulation generated by dynamic jaw or multileaf collimators*. *Med. Phys.* **21**, 1237-1244 (1994). (cited on page 40 of this thesis)
- Clarkson JR. *A note on depth doses in fields of irregular shape*. *Br. J. Radiol.* **14**, 265-268 (1941). (cited on page 106 of this thesis)
- Convery DJ, Rosenbloom ME. *The generation of intensity-modulated fields for conformal radiotherapy by dynamic collimation*. *Phys. Med. Biol.* **37**, 1359-1374 (1992). (cited on page 40 of this thesis)
- Cox JD. *Moss' radiation oncology: rationale, technique, results*. *Seventh Ed.* (1994). (cited on page 2 of this thesis)
- Crowder H, Johnson EL, Padberg M. *Solving large-scale zero-one linear programming problems*. *Op. Res.* **31**, 803-833 (1983). (cited on page 33 of this thesis)

- Curtin-Savard AJ, Podgorsak EB. *An electronic portal imaging device as a physics tool.* Med. Dos. **22**, 101-105 (1997). (cited on page 68 of this thesis)
- Curtin-Savard AJ, Podgorsak EB. *Dose delivery uncertainty in photon beam radiotherapy.* Radiol. Oncol. **30**, 218-223 (1996). (cited on page 11 of this thesis)
- Day MJ, Aird EGA. *The equivalent square method for dose determinations in rectangular fields.* Br. J. Radiol. Suppl. **17**, Appendix A, 105-114 (1983). (cited on page 108 of this thesis)
- DeVita VT. *Progress in cancer management.* Cancer **51**, 2401-240 (1983). (cited on page 3 of this thesis)
- Djordjevich A, Bonham DJ, Hussein EMA, Andrew J, Hale ME. *Optimal design of radiation compensators.* Med. Phys. **17**, 397-404 (1990). (cited on page 27 of this thesis)
- Duncombe PB, Nieminen JM. *On the field-size dependence of relative output from a linear accelerator.* Med. Phys. **19**, 1441-1444 (1992). (cited on page 105 of this thesis)
- El-Khatib EE, Podgorsak EB, Pla C. *Broad beam and narrow beam attenuation in Lipowitz's metal.* Med. Phys. **14**, 135-139 (1987). (cited on page 7 of this thesis)
- Enami B, Lyman J, Brown A, Burman C, Coia L, Goitein M, Kutcher GJ, Munzenrider J, Solin L, Shank B, Wesson M. *Tolerance of normal tissue to therapeutic radiation.* Int. J. Radiat. Oncol. Biol. Phys. **21**, 109-122 (1991). (cited on page 27 of this thesis)
- Enzmann DR, Pelc NJ. *Brain motion: measurement with phase-contrast MR imaging.* Radiology **185**, 653-60 (1992). (cited on page 98 of this thesis)
- Essers M, Hoogervorst BR, van Herk M, Lanson H, Mijnheer BJ. *Dosimetric characteristics of a liquid-filled electronic portal imaging device.* Int. J. Radiat. Oncol. Biol. Phys. **33**, 1265-1272 (1995). (cited on pages 59,62,65,67 of this thesis)
- Evans PM, Hansen VN, Swindell W. *The optimum intensities for multileaf collimator field compensation.* Med. Phys. **24**, 1147-1156 (1997). (cited on page 41 of this thesis)
- Ezzell GA. *Genetic and geometric optimization of three-dimensional radiation therapy treatment planning.* Med. Phys. **23**, 293-305 (1996). (cited on page 32 of this thesis)
- Fernandez EM, Shentall GS, Mayles WPM, Dearnaley DP. *The acceptability of a multileaf collimator as a replacement for conventional blocks.* Radiother. Oncol. **36**, 65-74 (1995). (cited on page 79 of this thesis)
- Fraass BA, McShan DL, Diaz RF, TenHaken RK, Aisen A, Gebarski S, Glazer G, Lichter AS. *Integration of magnetic resonance imaging into radiation therapy treatment planning.* Int. J. Radiat. Oncol. Biol. Phys. **13**, 1897-1908 (1987). (cited on page 12 of this thesis)
- Fraass BA. *Clinical use of intensity modulated radiotherapy using multi-segment treatment delivery techniques.* Med. Phys. **24**, 974 (1997). (cited on page 41 of this thesis)
- Frazier A, Du M, Wong J, Vicini F, Taylor R, Yu C, Matter R, Martinez A, Yan D. *Dosimetric evaluation of the conformation of the multileaf collimator to irregularly*

shaped fields. Int. J. Radiol. Oncol. Biol. Phys. 33, 1229-1238 (1995). (cited on pages 82,86 of this thesis)

Frazier A, Yan D, Du M, Wong J, Vicini F, Matter R, Joyce M, Martinez A. *Effects of treatment setup variation on beam's eye view dosimetry for radiation therapy using the multileaf collimator vs. the cerrobend block*. Int. J. Radiol. Oncol. Biol. Phys. 33, 1247-1256 (1995). (cited on page 82 of this thesis)

Fuks Z, Leibel SA, Kutcher GE, Mohan R, Ling CC. *Three-dimensional conformal treatment: a new frontier in radiation therapy in important advances in oncology*, DeVita VT, Hellman S, Rosenberg SA eds. Lippincott (1991). (cited on page 3 of this thesis)

Galvin JM, Chen XG, Smith RM. *Combining multileaf fields to modulate fluence distributions*. Int. J. Radiat. Oncol. Biol. Phys. 27, 697-705 (1993). (cited on page 41 of this thesis)

Galvin JM, Smith AR, Lally B. *Characterization of a multileaf collimator system*. Int. J. Radiol. Oncol. Biol. Phys. 25, 181-192 (1993). (cited on pages 92,93,95,99,101,104 of this thesis)

Galvin JM, Smith AR, Moeller RD, Goodman RL, Powlis WD, Rubenstein J, Solin LJ, Michael B, Needham M, Huntzinger CJ, Kligerman MM. *Evaluation of multileaf collimator design for a photon beam*. Int. J. Radiat. Oncol. Biol. Phys. 23, 789-801 (1992). (cited on pages 53,79,82 of this thesis)

Geis P, Boyer AL. *Use of a multileaf collimator as a dynamic missing-tissue compensator*. Med. Phys. 23, 1199-1205 (1996). (cited on pages 41,128 of this thesis)

Gore JC, Yang YS, Schulz RJ. *Measurement of radiation dose distributions by NMR imaging*. Mag. Res. Im. 2, 244-250 (1984). (cited on page 54 of this thesis)

Gustafsson A, Lind BK, Svensson R, Brahme A. *Simultaneous optimization of dynamic collimation and scanning patterns or compensation filters using a generalized pencil beam algorithm*. Med. Phys. 22, 1141-56 (1995). (cited on page 28 of this thesis)

Heyler SJ, Heisig S. *Multileaf collimator versus conventional shielding blocks: a time and motion study of beam shaping in radiotherapy*. Radiother. Oncol. 37, 61-64 (1995). (cited on page 82 of this thesis)

Holmes T, Mackie TR. *A filtered backprojection dose calculation method for inverse treatment planning*. Med. Phys. 21, 303-313 (1994). (cited on page 29 of this thesis)

Holmes TW, Mackie TR, Reckwerdt P. *An iterative filtered backprojection inverse treatment planning algorithm for tomotherapy*. Int. J. Radiat. Oncol. Biol. Phys. 32, 1215-1225 (1995). (cited on page 29 of this thesis)

Holroyd RA, Anderson DF. *The physics and chemistry of room-temperature liquid-filled ionization chambers*. Nucl. Instr. and Meth. A236, 294-299 (1985). (cited on page 57 of this thesis)

Hristov D. *Development of techniques for optimization and verification of conformal radiotherapy*. Ph.D. thesis, McGill University, Montreal (1997). (cited on page 180 of this thesis)

- Hristov DH, Fallone BG. *An active set algorithm for treatment plan optimization*. Med. Phys. **24**, 1455-1464 (1997). (cited on page 28 of this thesis)
- Huizenga H, Levendag PC, De Porre PMZR, Visser AG. *Accuracy of radiation field alignment in head and neck cancer: a prospective study*. Radiother. Oncol. **11**, 181-187 (1988). (cited on page 98 of this thesis)
- Hukku S, Das KJM, Nangia S, Kumar A, Ayyagari S. *The use of portal images to study the accuracy of radiation field alignment and patient positioning in head and neck cancer*. Proceedings of the XIth International Conference on the Use of Computers in Radiation Therapy, 268-269 (1994). (cited on page 98 of this thesis)
- Hunt MA, Kutcher GJ, Burman C, Fass D, Harrison L, Leibel S, Fuks Z. *The effect of set-up uncertainties on the treatment of nasopharynx cancer*. Int. J. Radiat. Oncol. Biol. Phys. **27**:, 437-44 (1983). (cited on page 98 of this thesis)
- Huq MS, Yan Y, Chen Z-P, Suntharalingam N. *Dosimetric characteristics of a commercial multileaf collimator*. Med. Phys. **22**, 241-247 (1995). (cited on pages 79,82,104 of this thesis)
- Ibbott GS, Maryanski MJ, Eastman P, Holcomb SD, Zhang Y, Avison RG, Sanders M, Gore JC. *Three-dimensional visualization and measurement of conformal dose distributions using magnetic resonance imaging of BANG polymer gel dosimeters*. Int. J. Radiat. Oncol. Biol. Phys. **38**, 1097-1103 (1997). (cited on page 54 of this thesis)
- IMSL Inc. *QPROG: IMSL math library (linearly constrained minimization, quadratic programming)*, 892-894 (1988). (cited on page 27 of this thesis)
- International Commission on Radiation Units and Measurements. *Determination of Absorbed Dose in a Patient Irradiated by Beams of X or Gamma Rays in Radiotherapy Procedures (ICRU Report No. 24)* (1976). (cited on page 11 of this thesis)
- International Commission on Radiation Units and Measurements. *Prescribing, recording, and reporting photon beam therapy (ICRU Report No. 50)*. Bethesda, Maryland (1993). (cited on page 16 of this thesis)
- Jaffray DA, Battista JJ, Fenster A, Munro P. *X-ray sources of medical accelerators: focal and extra-focal radiation*. Med. Phys. **20**, 1417-1427 (1993). (cited on page 105 of this thesis)
- Jordan TJ, Williams PC. *The design and performance characteristics of a multileaf collimator*. Phys. Med. Biol. **39**, 231-251 (1994). (cited on page 79 of this thesis)
- Källman P, Lind B, Eklöf A, Brahme A. *Shaping of arbitrary dose distributions by dynamic multileaf collimation*. Phys. Med. Biol. **33**, 1291-1300 (1988). (cited on page 40 of this thesis)
- Karzmark CJ, Nunan CS, Tanabe E. *Medical electron accelerators*. McGraw-Hill (1993). (cited on page 1 of this thesis)
- Khan FM. *The physics of radiotherapy*. Williams & Wilkins (1984). (cited on page 107 of this thesis)

- Kirkpatrick S, Gelatt CD, Vecchi MP. *Optimization by simulated annealing*. Science **220**, 671-680 (1983). (cited on page 31 of this thesis)
- Klein EE, Harms WB, Low DA, Willcut V, Purdy JA. *Clinical implementation of a commercial multileaf collimator: dosimetry, networking, simulation, and quality assurance*. Int. J. Radiol. Oncol. Biol. Phys. **33**, 1195-1208 (1995). (cited on pages 82,99 of this thesis)
- Knowlton, AH. *General principals of radiation therapy in cancer therapy*, Fishter DS and Marsh JC eds. GK Hall Medical Publishers (1982). (cited on page 1 of this thesis)
- Kutcher GJ, Burman C, Mohan R. *Compensation in three-dimensional non-coplanar treatment planning*. Int. J. Radiat. Oncol. Biol. Phys. **20**, 127-134 (1991). (cited on page 39 of this thesis)
- Lane RG, Loyd MD, Chow CH, Ekwelundu E, Rosen II. *Custom beam profiles in computer-controlled radiation therapy*. Int. J. Radiat. Oncol. Biol. Phys. **22**, 167-174 (1991). (cited on page 41 of this thesis)
- Langer M, Brown R, Morrill S, Lane R, Lee O. *A generic genetic algorithm for generating beam intensities*. Med. Phys. **21**, 878 (1994). (cited on page 32 of this thesis)
- Langer M, Brown R, Urie M, Leong J, Stracher M, Shapiro J. *Large scale optimization of beam weights under dose-volume restrictions*. Int. J. Radiat. Oncol. Biol. Phys. **18**, 887-893 (1990). (cited on page 33 of this thesis)
- Lawson CL, Hanson RJ. *Solving least squares problems*, Prentice Hall (1974). (cited on page 27 of this thesis)
- Leach MO. *Spatially localized nuclear magnetic resonance in the physics of medical imaging*, Webb S ed. Institute of Physics Publishing (1988). (cited on page 13 of this thesis)
- Lee S, Cho PS, Marks RJ II, Oh S. *Conformal radiotherapy computation by the method of alternating projections onto convex sets*. Phys. Med. Biol. **42**, 1065-1086 (1997). (cited on page 35 of this thesis)
- Leibel SA, Ling CC, Kutcher GJ, Mohan R, Cordon-Cardo C, Fuks Z. *The biological basis of conformal three-dimensional radiation therapy*. Int. J. Radiat. Oncol. Biol. Phys. **21**, 805-811 (1991). (cited on page 3 of this thesis)
- Leunens G, Van Dam J, Dutreix A, van der Schueren E. *Quality assurance in radiotherapy by in vivo dosimetry. 2. determination of the target absorbed dose*. Radiother. Oncol. **19**, 73-8 (1990). (cited on page 11 of this thesis)
- Leunens G, Verstraete J, Dutreix A, van der Schueren E. *Assessment of the inhomogeneity at target level by in vivo dosimetry: can the recommended 5% accuracy in the dose delivered to the target volume be fulfilled in daily practice?* Radiother. Oncol. **25**, 242-25 (1992). (cited on page 11 of this thesis)
- LoSasso T, Kutcher GJ. *Multileaf collimation versus alloy blocks: analysis of geometric accuracy*. Int. J. Radiol. Oncol. Biol. Phys. **32**, 499-506 (1995). (cited on page 82 of this thesis)

Mackie TR, Holmes T, Swerdloff S, Reckwerdt P, Deasy JO, Yang J, Paliwal B, Kinsella T. *Tomotherapy: A new concept for the delivery of dynamic conformal radiotherapy*. Med. Phys. **20**, 1709-1719 (1993). (cited on page 41 of this thesis)

Maryanski MJ, Gore JC, Kennan RP, Schulz RJ. *NMR relaxation enhancement in gels polymerized and crosslinked by ionizing radiation: a new approach to 3D dosimetry by MRI*. Mag. Res. Im. **11**, 253-258 (1993). (cited on page 54 of this thesis)

Maryanski MJ, Ibbott GS, Eastman P, Schulz RJ, Gore JC. *Radiation therapy dosimetry using magnetic resonance imaging of polymer gels*. Med. Phys. **23**, 699-705 (1996). (cited on page 54 of this thesis)

Mazur EJ, Mazur AK, Yu C, Wong J. *Inverse conformal therapy planning using interpolative algebraic reconstruction technique*. Med. Phys. **21**, 901-913 (1994). (cited on page 30 of this thesis)

McLaughlin WL, Soares CG, Sayeg JA, McCullough EC, Kline RW, Wu A, Maitz AH. *The use of a radiochromic detector for the determination of stereotactic radisurgery dose characteristics*. Med. Phys. **21**, 379-392, 1994. (cited on page 54 of this thesis)

Meertens H, van Herk M, Weeda J. *A liquid ionization chamber for digital radiography of therapeutic megavoltage photon beams*. Phys. Med. Biol. **30**, 313-321 (1985). (cited on page 56 of this thesis)

Mejaddem Y, Lax I, Shamsuddin Adakkai K. *Procedure for accurate fabrication of tissue compensators with high-density material*. Phys. Med. Biol. **42**, 415-421 (1997). (cited on page 39 of this thesis)

Menick HR, Garfinkel L, Dodd GD. *Preliminary report of the national cancer data base (CA 41)* (1991). (cited on page 3 of this thesis)

Metropolis N, Rosenbluth AW, Rosenbluth MN, Teller AH, Teller E. *Equation of state calculations by fast computing machines*. J. Chem. Phys. **21**, 1087-1092 (1953). (cited on page 31 of this thesis)

Mohan R, Chui C, Lidofsky L. *Energy and angular distributions of photons from medical accelerators*. Med. Phys. **12**, 592-597 (1985). (cited on page 105 of this thesis)

Mohan R, Mageras GS, Baldwin B, Brewster LJ, Kutcher GJ, Leibel S, Burman CM, Ling CC, Fuks Z. *Clinically relevant optimization of 3-D conformal treatments*. Med. Phys. **19**, 933-944 (1992). (cited on page 27 of this thesis)

Mohan R, Mageras GS, Baldwin B, Brewster LJ, Kutcher GJ. *Clinically relevant optimization of 3-D conformal treatments*. Med. Phys. **19**, 933-944 (1992). (cited on page 31 of this thesis)

Mohan R, Wu Q, Wang X, Stein J. *Intensity modulation optimization, lateral transport of radiation, and margins*. Med. Phys. **23**, 2011-2021 (1996). (cited on page 138 of this thesis)

Mubata CD, Childs P, Bidmead AM. *A quality assurance procedure for the Varian multi-leaf collimator*. Phys. Med. Biol. **42**, 423-431 (1997). (cited on page 83 of this thesis)

Muench PJ, Meigooni AS, Nath R, McLaughlin WL. *Photon energy dependence of the sensitivity of radiochromic film and comparison with silver halide film and LiF TLDs used for brachytherapy dosimetry.* Med. Phys. **18**, 769-775 (1991). (cited on page 54 of this thesis)

Myers MH, Ries LA. *Cancer patient survival rates: SEER Program results for 10 years of follow-up (CA 39)* (1989). (cited on page 3 of this thesis)

National Cancer Institute. *Web page: estimated new cancer cases and deaths by sex for all sites 1996 (<http://rex.Nci.Nih.Gov/>)* (1996). (cited on page 1 of this thesis)

Niemierko A. *Random search algorithm (RONSC) for optimization of radiation therapy with both physical and biological end points and constraints.* Int. J. Radiat. Oncol. Biol. Phys. **23**, 89-98 (1992). (cited on page 35 of this thesis)

Oldham M, Neal A, Webb S. *A comparison of conventional forward planning with inverse planning for 3D conformal radiotherapy of the prostate.* Radiother. Oncol. **35**, 248-262 (1995). (cited on page 24 of this thesis)

Oldham M, Webb S. *Intensity-modulated radiotherapy by means of static tomotherapy: A planning and verification study.* Med. Phys. **24**, 827-836 (1997). (cited on page 41 of this thesis)

Paliwal BR, Podgorsak MB, Harari PM, Haney P, Jursinic PA. *Evaluation and quality control of a commercial 3-D dose compensator system.* Med. Dos. **19**, 179-185 (1994). (cited on page 39 of this thesis)

Park HC, Almond PR. *Tissue compensation and verification of dose uniformity.* Med. Dos. **18**, 193-196 (1993). (cited on page 39 of this thesis)

Parker W. *Brachytherapy dosimetry with Fricke-gelatin and MRI.* M.Sc. thesis, McGill University, Montreal (1995). (cited on page 54 of this thesis)

Perez CA, Brady LW. *Overview in principals and practice of radiation oncology second ed.* Perez Ca and Brady LW eds. JB Lippincott (1992). (cited on page 3 of this thesis)

Powlis WD, Atschuler MD, Censor Y, Buhle EL Jr. *Semi-automated radiotherapy treatment planning with a mathematical model to satisfy treatment goals.* Int. J. Radiat. Oncol. Biol. Phys. **16**, 271-276 (1989). (cited on page 35 of this thesis)

Powlis WD, Smith AR, Cheng E, Galvin JM, Villari F, Bloch P, Kligerman MM. *Initiation of multileaf collimator conformal radiation therapy.* Int. J. Radiol. Oncol. Biol. Phys. **25**, 171-179 (1993). (cited on page 82 of this thesis)

Rabinowitz I, Broomberg J, Goitein M, McCarthy K, Leong J. *Accuracy of radaition field alignment in clinical practice.* Radiother. Oncol. **29**, 327-335 (1993). (cited on pages 17,98 of this thesis)

Renner WD, O'Connor TP, Bermudez NM. *An algorithm for design of beam compensators.* Int. J. Radiat. Oncol. Biol. Phys. **17**, 227-234 (1989). (cited on pages 27,39 of this thesis)

- Rosen II, Lam KS, Lane RG, Langer M, Morrill SM. *Comparison of simulated annealing algorithms for conformal therapy planning*. Int. J. Radiat. Oncol. Biol. Phys. **33**, 1091-1099 (1995). (cited on page 31 of this thesis)
- Rosen II, Lane RG, Morill SM, Belli JA. *Treatment plan optimization using linear programming*. Med. Phys. **18**, 141-152 (1991). (cited on page 27 of this thesis)
- Schultheiss TE, Orton CG. *Models in radiotherapy: definition of decision criteria*. Med. Phys. **12**, 183-187 (1985). (cited on page 26 of this thesis)
- Sharpe MB, Jaffray DA, Battista JJ, Munro P. *Extrafocal radiation: a unified approach to the prediction of beam penumbra and output factors for megavoltage x-ray beams*. Med. Phys. **22**, 2065-2074 (1995). (cited on page 106 of this thesis)
- Shragge PC, Patterson MS. *Improved method for the design of tissue compensators*. Med. Phys. **8**, 885-891 (1981). (cited on page 39 of this thesis)
- Spirou SV, Chui C-S. *Generation of arbitrary intensity profiles by combining the scanning beam with dynamic multileaf collimation*. Med. Phys. **23**, 1-8 (1996). (cited on pages 40,138 of this thesis)
- Starkschall G. *A constrained least-squares optimization method for external beam radiation therapy treatment planning*. Med. Phys. **11**, 659-665 (1984). (cited on page 27 of this thesis)
- Statistics Canada. *Mortality: summary list of causes 1994 (no. 84-209-xpb)*. Toronto (1994). (cited on page 1 of this thesis)
- Stein J, Bortfeld T, Dörschel B, Schlegel W. *Dynamic X-ray compensation for conformal radiotherapy by means of multileaf collimation*. Radiol. Oncol. **32**, 163-173 (1994). (cited on page 40 of this thesis)
- Suit HD. *Potential for improving survival rates for the cancer patient by increasing the efficacy of treatment of the primary lesion*. Cancer **50**, 1227-1234 (1982). (cited on page 3 of this thesis)
- Sun J, Zhu Y. *Study of dosimetric penumbra due to multileaf collimation on a medical accelerator*. Int. J. Radiat. Oncol. Biol. Phys. **32**, 1409-1417 (1995). (cited on page 95 of this thesis)
- Svensson GK. *Quality assurance in radiation therapy: physics efforts*. Int. J. Radiat. Oncol. Biol. Phys. **10**, Suppl. 1, 23-29 (1984). (cited on page 11 of this thesis)
- Svensson H. *Quality assurance in radiation therapy: physical aspects*. Int. J. Radiat. Oncol. Biol. Phys. **10**, Suppl. 1, 59-65 (1984). (cited on page 11 of this thesis)
- Tatcher M, Bjärngård BE. *Head-scatter factors in blocked photon fields*. Radiother. Oncol. **33**, 64-67 (1994). (cited on page 114 of this thesis)
- Ten Haken RK, Martel MK, Kessler ML, Hazuka MB, Lawrence TS, Robertson JM, Turrisi AT, Lichter AS. *Use of V_{eff} and iso-NTCP in the implementation of dose escalation protocols*. Int. J. Radiat. Oncol. Biol. Phys. **27**, 689-69 (1993). (cited on page 2 of this thesis)

TenHaken RK, Thornton AF, Sandler HM, LaVigne ML, Quint DJ, Fraass BA, Kessler ML, McShan DL. *A quantitative assessment of the addition of MRI to CT-based, 3-D treatment planning of brain tumors.* Radiother. Oncol. **25**, 121-133 (1992). (cited on page 12 of this thesis)

van Dam J, Bridier A, Lasselin C, Blanckaert N, Dutreix A. *Influence of shielding blocks on the output of photon beams as a function of energy and type of unit.* Radiother. Oncol. **24**, 55-59 (1992). (cited on pages 107,114 of this thesis)

van Gasteren JJM, Heukolom S, van Kleffens HJ, van der Laarse R, Venselaar JLM, Westermann CF. *The determination of phantom and collimator scatter components of the output of megavoltage photon beams: measurement of the collimator scatter part with a beam-coaxial narrow cylindrical phantom.* Radiother. Oncol. **20**, 250-257 (1991). (cited on pages 106,107 of this thesis)

van Herk M. *Feasibility of the Portal Vision system for verification of dynamic therapy.* Conference on Electronic Portal Imaging, Amsterdam (June 10-12, 1996). (cited on page 183 of this thesis)

van Herk M. *Physical aspects of a liquid-filled ionization chamber with pulsed polarizing voltage.* Med. Phys. **18**, 692-702 (1991). (cited on page 59 of this thesis)

van Santvoort JP, Binnekamp D, Heijmen BJ, Levendag PC. *Granulate of stainless steel as compensator material.* Radiother. Oncol. **34**, 78-80 (1995). (cited on page 39 of this thesis)

van Santvoort JPC, Heijmen BJM. *Dynamic multileaf collimation without "tongue-and-groove" underdosage effects.* Phys. Med. Biol. **41**, 2091-2105 (1996). (cited on page 104 of this thesis)

Varian Oncology Systems. *CadPlan treatment modelling workstation: external beam modelling reference manual v2.7* (1996). (cited on page 36 of this thesis)

Varian Oncology Systems. *CadPlan treatment modelling workstation: external beam modelling user's manual v2.62* (1995). (cited on page 36 of this thesis)

Varian Oncology Systems. *Data book: high energy C-Series Clinac (part no. 01100243-02)* (1995). (cited on page 3 of this thesis)

Varian Oncology Systems. *Portal Vision v. 3.6 reference manual (I.D. #PV22RM)* (1995). (cited on page 55 of this thesis)

Wang X-H, Mohan R, Jackson A, Leibel SA, Fuks Zvi, Ling CC. *Optimization of intensity-modulated 3D conformal treatment plans based on biological indices.* Radiother. Oncol. **37**, 140-152 (1995). (cited on page 28 of this thesis)

Webb S. *Optimization of conformal radiotherapy dose distributions by simulated annealing.* Phys. Med. Biol. **34**, 1349-1370 (1989). (cited on page 31 of this thesis)

Webb S. *The effect on tumour control probability of varying the setting of a multileaf collimator with respect to the planning target volume.* Phys. Med. Biol. **38**, 1923-1936 (1993). (cited on page 82 of this thesis)

- Weeks KJ, Sontag MR. *3-D dose-volume compensation using non-linear least-squares regression technique*. Med. Phys. **18**, 474-487 (1991). (cited on page 27 of this thesis)
- Weidlich GA, Schmidt EL. *Development of methods for dynamic radiation therapy with specified dose distributions*. Med. Dos. **21**, 87-95 (1996). (cited on pages 39,82 of this thesis)
- Williamson JF, Khan FM, Sharma SC. *Film dosimetry of megavoltage photon beams: a practical method of isodensity-to-isodose curve conversion*. Med. Phys. **8**, 94-98 (1981). (cited on page 53 of this thesis)
- Woo SY, Grant WH III, Bellezza D, Grossman R, Gildenberg P, Carpentar LS, Carol M, Butler EB. *A comparison of intensity modulated conformal therapy with a conventional external beam stereotactic radiosurgery system for the treatment of single and multiple intracranial lesions*. Int. J. Radiat. Oncol. Biol. Phys. **35**, 593-597 (1996). (cited on page 42 of this thesis)
- Wu A, Johnson M, Chen ASJ, Kalnicki S. *Evaluation of dose calculation algorithm of the Peacock system for multileaf intensity modulation*. Int. J. Radiat. Oncol. Biol. Phys. **36**, 1225-1231 (1996). (cited on page 42 of this thesis)
- Xing L, Chen GTY. *Iterative methods for inverse treatment planning*. Phys. Med. Biol. **41**, 1-17 (1996). (cited on page 30 of this thesis)
- Yang JN, Mackie TR, Reckwerdt P, Deasy JO, Thomadsen BR. *An investigation of tomotherapy beam delivery*. Med. Phys. **24**, 425-436 (1997). (cited on page 41 of this thesis)
- Yin FF, Schell MC, Rubin P. *Input/output characteristics of a matrix ion-chamber electronic portal imaging device*. Med. Phys. **21**, 1447-1454 (1994). (cited on pages 59,62 of this thesis)
- Yu CX, Symons MJ, Du MN, Martinez AA, Wong JW. *A method for implementing dynamic photon beam intensity modulation using independent jaws and a multileaf collimator*. Phys. Med. Biol. **40**, 769-787 (1995). (cited on page 40 of this thesis)
- Yu CX. *Intensity-modulated arc therapy with dynamic multileaf collimation: An alternative to tomotherapy*. Phys. Med. Biol. **40**, 1435-1449 (1995). (cited on page 42 of this thesis)
- Yu MK, Murray B, Sloboda R. *Parametrization of head-scatter factors for rectangular photon fields using an equivalent square formalism*. Med. Phys. **22**, 1329-1332 (1995). (cited on page 109 of this thesis)
- Yu MK, Sloboda R. *Analytical representation of head scatter factors for shaped photon beams using a two-component x-ray source model*. Med. Phys. **22**, 2045-2055 (1995). (cited on page 106 of this thesis)
- Yu MK, Sloboda RS, Mansour F. *Measurement of photon beam backscatter from collimators to the beam monitor chamber using target-pulse-counting and telescope techniques*. Phys. Med. Biol. **41**, 1107-1117 (1996). (cited on pages 105,110 of this thesis)

Yu MK, Sloboda RS. *Effect of beam blocking on linac head scatter factors*. Int. J. Radiol. Oncol. Biol. Phys. **37**, 465-468 (1997). (cited on page 114 of this thesis)

Zhu TC, Bjärngard BE, Shackford H. *X-ray source and the output factor*. Med. Phys. **22**, 793-798 (1995). (cited on page 105 of this thesis)

Zhu Y, Boyer AL, Desobry GE. *Dose distributions of x-ray fields as shaped with multileaf collimators*. Phys. Med. Biol. **37**, 163-173 (1992). (cited on page 86 of this thesis)

Zhu YZ, Jiang XQ, van Dyke J. *Portal dosimetry using a liquid ion chamber: dose response studies*. Med. Phys. **22**, 1101-1106 (1995). (cited on pages 59,62,66,67 of this thesis)